UNIVERSITY OF SOUTHAMPTON

Faculty of Engineering and Physical Science
School of Electronics and Computer Science

Near- and far-field wave shaping for optofluidic particle manipulation

by

Shengqi Yin

ORCiD: 0000-0003-1087-1507

A thesis for the degree of
Doctor of Philosophy

April 2023

Abstract

University of Southampton
Faculty of Engineering and Physical Science
School of Electronics and Computer Science

Doctor of Philosophy

Near- and far-field wave shaping for optofluidic particle manipulation

by Shengqi Yin

Optofluidic particle manipulation provides a powerful and versatile technological platform for on-chip sensing. Embedded planar nanophotonic devices can shape electromagnetic fields in fluidic channels, allowing for a high level of control over particles. This thesis reports my research contribution to designing optofluidic nanostructures for several different kinds of on-chip particle manipulation that are detailed as below.

I have numerically demonstrated plasmonic nanoparticle routers that can guide and route nanospheres in a microfluidic channel. I have analyzed the power flow and the corresponding optical force on the nanosphere, and have derived the Maxwell stress tensor utilized in the finite element analysis solver. I also identified the relationship between the relative refractive index of the nanospheres and the magnitude of the generated optical force. The results suggest a new method for next-generation plasmo-fluidic sensing.

I have designed dielectric metalenses with phase profiles that can be coherently controlled. The Mie scattering field from the meta-atoms of the metalens can be tailored dynamically, in which the output Bessel beam sweeps in a range from –1.37° to 1.36°. I have further analyzed particle routing in a continuous flow.

I have numerically demonstrated a metalens-based microfluidic microsphere sorter that enables automatic sphere sorting based on fluorescent color. The sorting originates from the metalens' ability to focus fluorescent light back onto the target sphere, creating self-induced optical tweezers. Because the embedded metalens doublet eliminates the need for any additional sorting mechanism, the technique can be referred to as FEACS (Fluorescence-Enabled Automatic Cell Sorting) to highlight its self-sorting capability.

List of Publications

Journal Publications:

[1] S. Yin, F. He, N. Green, and X. Fang, "Nanoparticle trapping and routing on plasmonic nanorails in a microfluidic channel," Opt Express 28, 1357-1368 (2020).

[2] S. Yin, F. He, W. Kubo, Q. Wang, J. Frame, N. G. Green, and X. Fang, "Coherently tuneable metalens tweezers for optofluidic particle routing," Opt Express 28, 38949-38959 (2020).

[3] J. Liu, X. Fang, F. He, S. Yin, W. Lyu, H. Geng,X. Deng, and X. Zheng."Directional conversion of a THz propagating wave into surface waves in deformable metagrating", Optics Express 29, 21749-21762 (2021).

[4] W. Lyu, J. Liu, S. Yin, X. Deng, X. Fang, H. Geng, and X. Zheng, "Deep-subwavelength gap modes in all-dielectric metasurfaces for high-efficiency and large-angle wavefront bending", Optics Express 30, 12080-12091 (2022).

[5] S. Yin, N. G. Green, and X. Fang, "Metalens doublet for self-tracing and self-guiding of particles in a microfluidic channel", under review.

[6] S. Chen, J. Huang, S. Yin, M. M. Milosevic, H. Pi, J. Yan, H. M. H. Chong, and X. Fang, "Metasurfaces integrated with a single-mode waveguide array for off-chip wavefront shaping", postprint.

Conference Publications:

[1] S. Yin, F. He, N. Green, and X. Fang, "Optical routing of nanospheres on plasmonic rails," CLEO/Europe-EQEC 2019, Munich, Germany, 22-26 Jun 2019.

[2] S. Yin, F. He, N. Green, and X. Fang, "Metalens-based Particle Routing in Continuous-flow Microchannels," CLEO/Europe-EQEC 2021, online meeting, 21-25 June 2021.

[3] S. Yin, N. G. Green and X. Fang, "Metalens-based microfluidic sorter", EIMC, online meeting, 20-21 July 2021.

[4] S. Yin, N. G. Green and X. Fang, "Metalens Doublets for Self-sorting of Fluorescent Particles", CLEO 2022, online meeting, 15-20 May 2022.

Declaration of Authorship

I declare that this thesis and the work presented in it is my own and has been generated by me as the result of my own original research.

I confirm that:

1. This work was done wholly or mainly while in candidature for a research degree at this University;
2. Where any part of this thesis has previously been submitted for a degree or any other qualification at this University or any other institution, this has been clearly stated;
3. Where I have consulted the published work of others, this is always clearly attributed;
4. Where I have quoted from the work of others, the source is always given. With the exception of such quotations, this thesis is entirely my own work;
5. I have acknowledged all main sources of help;
6. Where the thesis is based on work done by myself jointly with others, I have made clear exactly what was done by others and what I have contributed myself;
7. Parts of this work have been published as the journal papers and conference contributions in the list of publications.

Signed:..... Date:.....

Contents

List of Figures

List of Tables

Acknowledgements

Words cannot express my gratitude to my supervisors, Dr. Xu Fang and Dr. Nicolas Green. Dr. Xu Fang provided me with numerous invaluable opportunities and constant support, and he acted as a role model for me not only academically but also personally. Without his support, this research and others not covered in this thesis would have never been completed. Dr. Nicolas Green's prompt inspiration, timely suggestions, kindness, enthusiasm, and dynamism have enabled me to complete my thesis.

I am also grateful to my collaborators, especially my office mates, who provide precious advice and technical support to help my research. I would also like to thank my seniors, Dr. Fei He, Dr. James Frame, Dr. Yu Feng, Dr. Hailong Pi, and Dr. Xiangming Xu, for sharing their numerical simulation expertise and nanofabrication experiments. I also want to thank Dr. Ziwei Liu, Wangke Yu, Yue Fan, Peng Li, Wen Lv and Jiaming Liu, who motivate my research idea. I would also like to thank Dr. Bruce Ou, who kindly provided an optical measurement device for measuring my fabricated sample in my final year. Without his help, I would not have been able to present the actual optical images in this thesis.

I also want to thank my juniors, Jianzhi Huang, Zihang Zheng, Siyu Chen, Chuang Sun, for discussing many promising research realms and helping in daily life. All members of the Sustainable Electronic Technology Group I have had the pleasure of working with during my PhD. I also want to thank the techniques in the SNC, TRC and IPC cleanrooms, Dr. Owain Clark, Dr. Kiang Kian Shen, Dr. Libe Arzubiaga Totorika, Dr. Anushka Gangnaik, Neil Sessions and Xiangjun Wang, for training and supporting nanofabrication in the cleanroom.

I also want to thank my friends Dr. Shenghao Liu, Dr. Wei Cao, Dr. Weiwei Zhang, Dr. Tanchao Pu, Shumeng Wang, Bing Xue, Meijing Liu, Jiaqi Wang, Chen Wei, Gaoce Han, Jiale Zeng and Weilin Jin enrich my fun leisure time for scientific research.

Thanks must go to my family, especially my parents, Hongxia Sun and Long Yin. They try their best to support and encourage me to live and research in a foreign country. Without their support, I would never have had a chance to start and complete my PhD. I want to thank them for understanding and tolerating that I have not been home for three and half years during the pandemic.

Finally, I would like to thank my wife, Xinyang Li. She came to Southampton with me and established a preferable environment that allowed me to focus on my research without distraction. When I ran into a bottleneck, she would try to help me sort out my thoughts, even though her major is not in nanophotonics. Without her accompany, it would have been hard for me to spend four years of research life, significantly when three years of them were affected by Covid-19.

To my lovely wife, Xinyang Li, who gave me tremendous encouragement and unconditional support to fulfill my PhD journal.

Definitions and Abbreviations

ARROW	Anti-resonance reflecting optical waveguides
DFB	Distributed feedback
DFOFL	Distributed fiber optofluidic laser
ER	Extinction ratio
EWOD	Electrowetting-on-dielectrics
FDTD	Finite-difference time-domain
FEM	Finite element method
FP	Fabry Perot
FRET	Forster resonance energy transfer
FSR	Free spectral range
FWHM	Full width at half maximum
FZP	Fresnel zone plate
HOF	Hollow core optical fiber
ICP	Inductively coupled plasma
LCOS-SLM	Liquid Crystal Silicon Spatial Light Modulator
LSPR	Localized surface plasmon resonance
MMI	Multimode interference
MTF	Modulation transfer function
NIR	Near infrared
OAM	Orbital angular momentum
OFRR	Optofluidic ring resonator laser
OPO	Optical parameter oscillator
OSEMC	Optical-switch-enabled microfluidic chip
PBS	Polarization beam splitter
PDMS	Poly-dimethyl-siloxane
POT	Plasmon-based optical tweezers
PS	Polystyrene
SAM	Spin angular momentum
SERS	Surface-enhanced Raman spectroscopy
SHMOF	Simplified hollow-core microstructured optical fiber
SPPs	Surface plasmon polaritons
SPR	Surface plasmon resonance

TIR	Total internal reflection
WGMs	Whisper garllary modes

Chapter 1

Introduction to Thesis Structure

As a research and technology area, optofluidics is at the intersection of optics and microfluidics regions. Optofluidics enables advanced applications in minimized lab-on-a-chip and biosensing regions [1]. Based on the interaction between photons and fluidic medium at the nano- and micro-scale, optofluidic devices can be classified into two groups that explore light-on-fluid and fluid-on-light actions, respectively [2, 3]. The former enables optical sensing, marking, and manipulation for performing automatic functions such as particle sorting and separation in a microfluidic medium [4, 5]. This integration provides several unique characteristics that can be leveraged for biological and chemical analysis.

Optical force can be exploited to transport particles between the laminar flows, allowing for devices such as optofluidic switches, optofluidic microscope, optical-based droplet manipulation and integrated optical tweezers [2, 6, 7]. This thesis shows how nanophotonic devices can be integrated with microfluidic systems as a lab-on-a-chip routing and sorting system. Embedded nanophotonic devices for guiding dielectric particles in the near-field and the far-field [8, 9] could be helpful for biosensing in terms of controlling test samples. The contents of each following chapter are summarized below.

- In Chapter 2, I provide a review of different interactions between light and fluid, optofluidic applications, and optical tweezers used in a microfluidic channel.
- In Chapter 3, I numerically demonstrate novel plasmonic nanorails with a Y-branch junction for continuous near-field particle routing [8]. The evanescent field can be controlled by adjusting the incident wavelength, and it can transport nanoparticles injected into the microchannel toward a determinated terminal.
- In Chapter 4, I numerically demonstrate a new approach for long-range trapping of dielectric spheres by using a coherent controllable metalens [9]. The output beam from a phase gradient metamaterial surface can be tuned by using coherent control. This tuning enables Rayleigh- / Mie-sized spheres guiding and routing in optofluidic systems.

- In Chapter 5, I numerically demonstrate a metalens doublet for sorting fluorescent particles in microchannels. A pair of metasurfaces structured on the opposite sides of a silica layer is analyzed. The doublet focuses fluorescent light back onto a source particle, which may lead to automatic cell sorting. The doublet has wavelength selectivity, giving rise to self-sorting of a different fluorescent microspheres.
- In Chapter 6, I summarize the main achievement of my PhD research and propose future work that can be derived from this thesis.

Chapter 2

Introduction to Optofluidics

Optofluidics has emerged as a vibrant research topic in recent years [2, 10]. Fluid, a material that continually deforms under an applied external force, shows flexibility and reconfigurability. Fluidic replacement and modification result in tunable optical systems using the microfluidic framework to generate highly compact and integrated optics devices [1]. Microfluidic devices can provide a controlled environment for photon-to-liquid interaction; simultaneously, in sensing applications, they only require small volumes of analyzed samples and can enhance detection efficiency. Following these concepts, various types of devices are adopted in miniaturized lab-on-a-chip applications, such as optofluidic lasers [11, 12], adaptive optical lenses [13, 14] and optofluidic microscopes [6]. In addition, optofluidics has demonstrated a wide variety of achievements in biosensing and chemical analysis, such as optically actuated routers [8, 9], optical cell manipulation [7, 15], and DNA analysis [16]. This chapter attends on the interaction between photonics and microfluidics, especially tunable optical force in near-field and far-field at visible and near-infrared [17–19], which is directly related to the research of this thesis.

At present, optofluidic devices are often used to complete light ray control by modifying the refractive index of liquid mediums or by changing droplets injected into the fluid environment [10, 20]. By changing the parameters of solvents in the microfluidic channel, an optofluidic system is capable of affecting the embedded optical system in interference and scattering. In addition, light from photonic devices in a microfluidic system can excite, actuate, and analyze the target particle (e.g. single cells, dielectric beads, and fluorescent spheres) suspended in the microfluidic system. Based on these mechanisms of interaction between light and fluidic medium, optofluidics can be classified into two categories: fluidic action on light and optical action on fluid. In the latter, the term fluid also covers particles inside a fluid.

2.1 Fluidic action on light

In conventional solid photonic structures (e.g. those made of metal, silicon, and fused silica), in which the whole geometries are fixed after fabrication, optofluidic can exploit changeable fluidic mediums to reconfigure optical parameters after embedding these photonic structures into a microfluidic device. Therefore, microfluidics is not an afterthought to an optofluidic device but an essential component. The synthesized photonic-microfluidic devices show merits with advanced adaptivity, liquidity, and re-moldability. Furthermore, by manipulating the fluid parameters in refractive indices or solvent types, optofluidics can develop light generation, light routing, and light discrimination [2]. The main aim is to generate a photonic device whose function is mostly determined by a fluid.

The first example is an optical system for generating laser light from a pump source. Laser (i.e. light amplification by stimulated emission of radiation) is usually exploited as an optical source due to its high temporal coherence, directivity, and monochromaticity, as compared with LED sources and fluorescence sources. Three components are often considered to constitute a laser source: incident pump light, a suitable amplification medium, and frequency-selective feedback in an optical cavity. In the context of optofluidics, except for the external excitation pump light, the rest two components can be compactly integrated into a lab-on-a-chip system. It can incorporate novel frequency tuning mechanisms, like mechanical stretching [21] and pneumatically actuation [22, 23], which depends on an elastic solid-type poly-dimethylsiloxane (PDMS) air cell. Previous reports have introduced a wide variety of on-chip dye-laser with controllable microfluidic systems [11, 23–28]. Microdroplet with a refractive index higher than that of the surrounding liquid medium, can form an optical microcavity that results in whispering gallery modes (WGMs) [11]. An array of nozzles, shown in **Fig. 2.1 a**, integrated in a microfluidic channel injects oil droplets with a diameter ranging from 115 to 475 μm. These droplets support high Q-factor ($> 10^6$) WGMs with lasing thresholds as low as 0.63 $\mu J/mm^2$ [26]. In **Fig. 2.1 b**, an on-chip tunable laser with a corrugated sidewall structure forms a distributed feedback (DFB) grating, which can be switched on and off using a pneumatic cell This leads to an 8.84 dB attenuation of laser emission with a pressure of 50 psi on the pneumatic cell [23]. In addition, optofluidic lasers have demonstrated a lower lasing threshold at 113 nJ/mm^2 by using a high Q-factor Fabry-Pérot (FP) resonator [12, 27, 29], a microring resonator (shown as **Fig. 2.1 c**) [27, 28, 30, 31], a hollow-core fiber (in **Fig. 2.1 d**) [25, 32] and förster resonance energy transfer (FRET) [25, 29, 33]. These examples demonstrate that optofluidic dye lasers are superior in low threshold and reconfigurable functionalities.

The second example is to route and shape the light beam guided into microfluidic systems. In conventional optics, a solid-state integrated optical waveguide can be used to transport light from one point to another. The principle is that light wave can be confined by the total internal reflection (TIR) for mediums with different refractive indices. Simultaneously, structured waveguides have been used to achieve spatial multiplexing and demultiplexing. These properties are highly relevant to optofluidic devices because liquid mediums in optofluidics

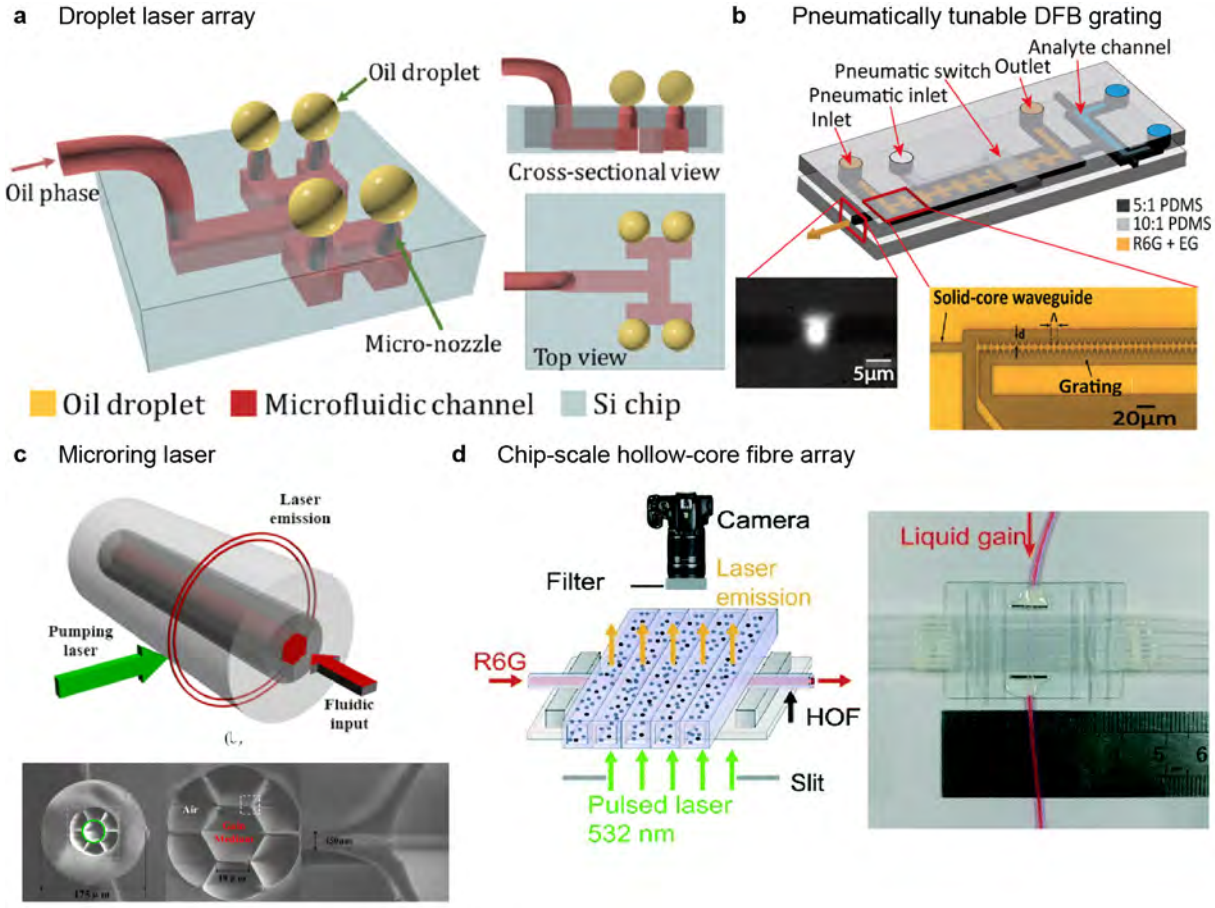

Fig. 2.1. On-chip dye-lasing. (a) Schematic diagram of a droplet laser array on a silicon chip. The oil channel splits into 4 identical branches to route the oil into the 2×2 micro-nozzle, shown in the perspective view, cross section view, and top view. The generated oil droplets as microcavities are immersed in the surrounding water channel (not indicated in this panel). (b) Schematic of a PDMS optofluidic DFB dye laser chip built with corrugated sidewalls. Ethylene glycol and water, with dissolved rhodamine 6G as gain medium, is injected into the microfluidic channel with a solid-core waveguide shown in the zoom-in view at the bottom right. A pneumatic control over a segment of the DFB grating can operate the laser operation by the tuning pneumatic pressure. The emission laser exits the microchannel via the waveguide shown at the bottom left. (c) Three-dimensional schematic diagram of a hollow-core microstructured optical fiber and its SEM photographs (bottom row). A liquid-core with gain medium and 6 symmetric segments air-cores constitute this hollow-core fiber. (d) Schematic and photo of the chip-scale hollow-core fibre array. A liquid-core fiber is located beneath 5 microfluidic channels with the test samples. The figures are reproduced (a) from [26]; (b) from [23]; (c) from [31]; (d) from [25].

can be dynamically reconfigurable and contain the sample to be tested. This allows optical waveguides embedded into the liquid medium to achieve on-chip detection. **Figs. 2.2 a-c** demonstrate three different optofluidic routers to guide light into chip-scale systems, all are compatible with planar on-scale integration and have unique advantages. **Fig. 2.2 a** shows an aerogel-based micro-photoreactor that confines both the aqueous core liquid and the guided light [34]. Total internal reflection (TIR), enables this single liquid-filled channel to function as an optofluidic waveguide. This phenomenon occurs due to the refractive index of the cladding ($n_{aerogel} = 1.06$) is smaller than that of the core liquid. Both liquid-liquid and liquid-air combinations have been used to put this principle into practice [35–37]. A second possibility is to use a solid-core rib waveguide under a liquid-core waveguide, in which light is confined to the guide modes of the solid core surrounded by a fluidic core [38]. This principle is illustrated in **Fig. 2.2 b**, where a hollow waveguide, i.e. liquid-core waveguide, covers solid waveguides [39, 40]. In this integrated hollow-core anti-resonant reflecting optical waveguides (ARROW), the light from a 633 nm single mode laser is coupled to the rib solid-core waveguide. It is used to detect fluorescent microbeads injected into the hollow-core waveguide, which has achieved multiplexed routing and detection with an optical throughput of 9.1% and an average signal per bead of 15 counts/ms. The other possibility is to exploit a coupled cavity localized near a waveguide to control the transmittance spectrum and the reflectivity in the waveguide [41, 42]. A plasmonic metal-dielectric-metal slit waveguide-based tunable wavelength filter with an optofluidics pump system is shown in **Fig. 2.2 c**. In this research, a surface plasmon polaritons (SPPs) based waveguide achieves wavelength filter by coupling a side slit segment with the fluidic channel. It is possible to control the liquid-air interface in the slit segment by using an optofluidics pump system [43]. In addition, microlenses in an optofluidic system allow for very compact optical systems, that can focus light [11, 44]. Three typical optofluidic lenses on different configurations are introduced in **Fig. 2.2 d** [14]. Firstly, a liquid-liquid or liquid-air interface is established by using different materials, and this interface can be controlled by electrowetting [45], the pneumatic actuator [46], and voltage [47]. In the research of K. Mishra *et al.*, an external voltage is exploited to reshape an oil-water interface from a spherical profile to a perfect aspherical profile for eliminating longitudinal spherical aberration [44]. Unfortunately, gravity significantly affects the shape of the liquid-liquid (-air) interface, which causes the incident light to diverge [48]. Secondly, a fluid-solid interface relies on elastic membranes that can be manufactured into various lens types and are more resistant to external inertial disturbance. The shape of elastomer-liquid lenses can be changed by pumping fluid into the lens chamber [44], and by pneumatic actuating [49]. Thirdly, modulating the refractive indices of the materials that make up optical fluidics is another way to achieve tunable refractive power. Liquid gradient refractive index lenses and adaptive liquid crystal lenses are two example applications [50, 51].

The third example is to tune light beams for sensing via controllable medium-to-medium interface, e.g. liquid-air, liquid-liquid and air-elastic solid interfaces [14]. Through a number of methods, such control has been introduced to optofluidics, demonstrating the design flexibility gained by integrating non-solid materials into solid-state photonic environments. In this

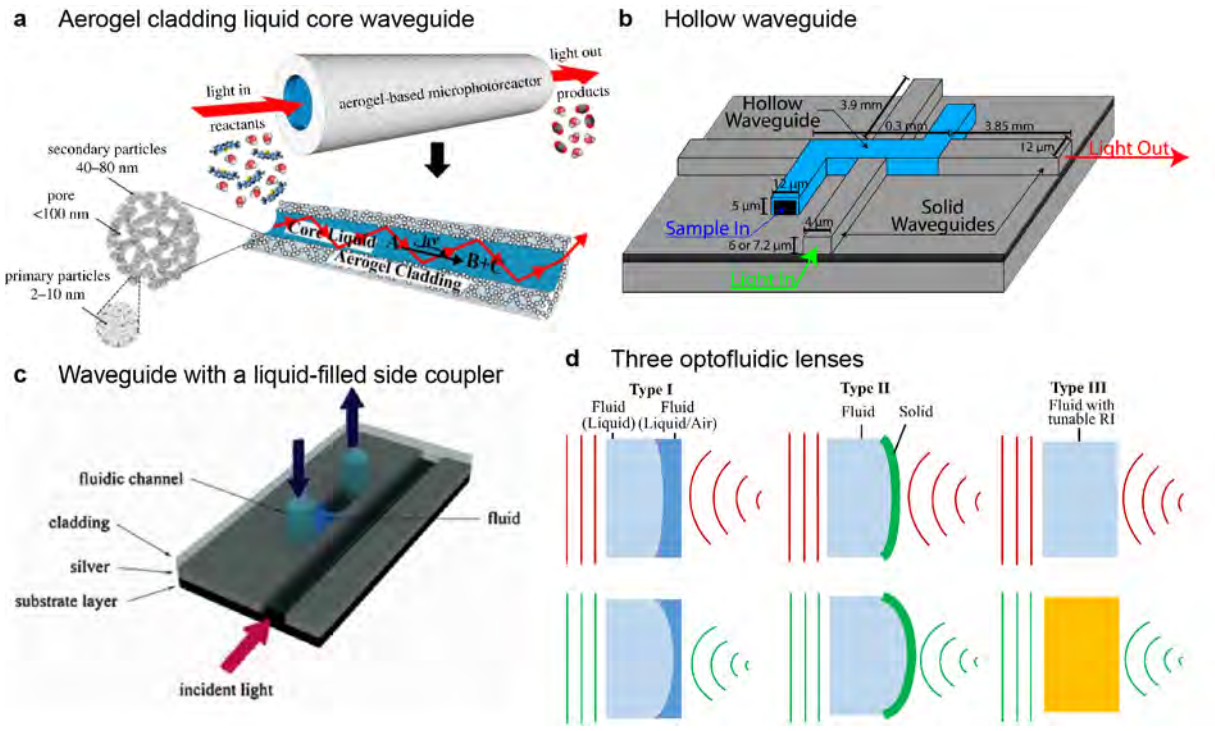

Fig. 2.2. On-chip optofluidic router. (a) A schematic diagram shows an aerogel-based liquid-core waveguide and its corresponding cross sectional view of light guiding in the liquid by total internal reflection. (b) Illustration of an integrated solid-core and liquid-core waveguide based on an antiresonance reflection optical waveguide. Light in the solid-core waveguide is guided into the liquid-core hollow waveguide, where the sample is injected to be detected. (c) A surface plasmon polariton-based waveguide with a side coupler that is filled with controllable fluid. (d) Three types of optofluidic microlenses, that is, two-phase interface lens (Type I), membrane lens (Type II), and refractive index-based lens (Type III). Plane waves illuminate these microlenses from the left and generate focusing beams on the right. The figures are reproduced (a) from [34]; (b) from [39]; (c) from [43]; from [14].

context, three characteristic devices are shown in **Figs. 2.3 a-c**, which are beam splitter, beam router, and beam switch, respectively. A polarization beam splitter based on an optofluidic ring resonator is illustrated in **Fig. 2.3 a**. Its operation depends on the birefringence of light passing through. At the resonance wavelength, only one polarization can travel while the other does not; hence the light with TE and TM polarizations will be extracted by the microfiber and the fiber tip, respectively [52]. A tunable liquid-liquid (-air) interface is often chosen to realize a controllable optofluidic switch [53–56]. In **Fig. 2.3 b**, a fluidic chamber containing three different liquids can create routing and power distribution; an electrowetting dyed liquid can distribute light to two outputs at any ratio between 0% and 100% [45]. With a voltage of 55 V, the dyed liquid spreads and covers the output lightpath to realize a "switch off". In addition, the low Young's modulus of PDMS ($759KPa$) [57] enables a much more straightforward tuning method, that is, air (liquid)-elastomer controlling. By using a pneumatic actuator or a pumping system, pressure applied to the fluid alters the contours of the elastic material to achieve TIR or change the radius of microlens curvature [13, 37, 48, 58]. **Fig. 2.3 c** demonstrates a pneumatically tunable 2×2 optofluidic switch that is fabricated on a PDMS chip and controlled by air pressure [46]. At the PDMS-air interface of the air-gap mirror, the two incident beams can be

deflected entirely when the applied pressure reaches 1.2 bar.

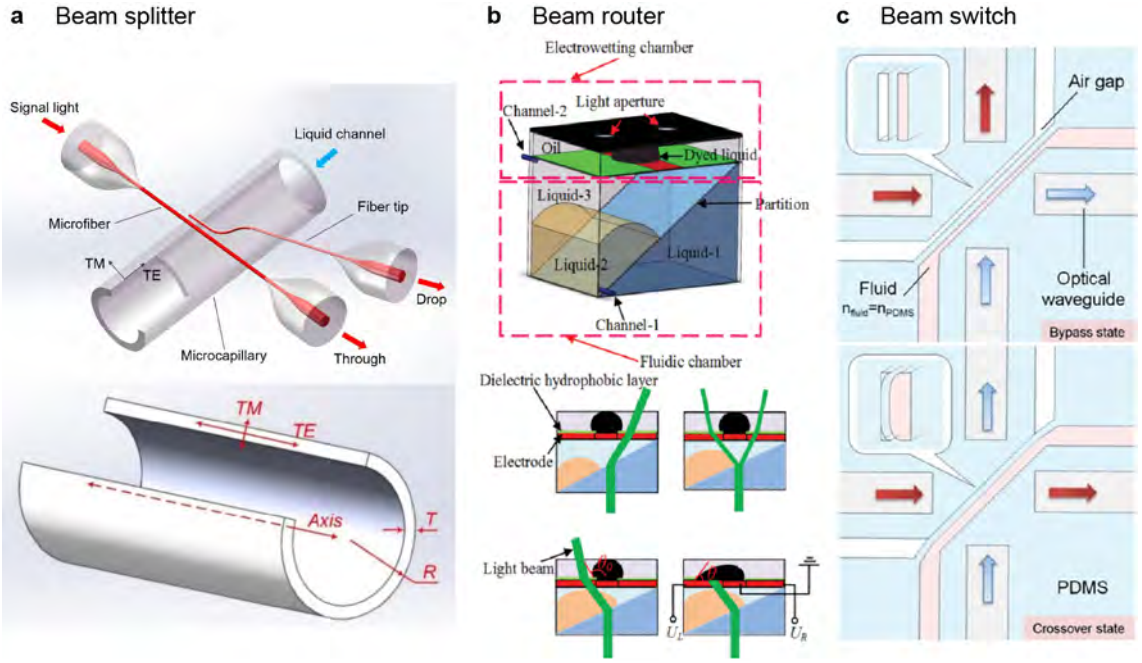

Fig. 2.3. On-chip optofluidic beam controller. (a) A schematic illustration of a polarization beam splitter based on an optofluidic ring resonator (top) and the illustration of enhanced birefringence in the optofluidic ring resonator (bottom). (b) Schematic structure of a beam router (top), controlling three different liquids in a fluidic chamber and electrowetting dyed liquid. The bottom portion demonstrates the light route tuned at the liquid-1/ liquid-2 interface. Additional external voltages applied on electrodes switch between the "on" and "off " states. (c) Top view of a 2×2 beam switch, which can tune "Bypass state" (top row) and "Crossover state" (bottom row) by regulating the pressure applied on the fluid to bounce PDMS membrane using a pneumatical controller. The figures are reproduced (a) from [52]; (b) from [45]; (c) from [46].

In conclusion, optofluidic devices bring unique tunability. Furthermore, the incorporation of fluidics assists the implementation of multiplexing into photonic devices. In multiplexed analysis, the advantage of lab-on-a-chip devices is the small sample volume and reagent needed. More innovative optofluidic methods for shaping and imaging beams are currently emerging. Examples include color-tunable pressure sensors by using nanostructured polymer membranes [49], laser interferometry based on nanoporous membranes [59] and broadband laser routers based on liquid-filled hollow-core photonic crystal fiber [60].

2.2 Optical action on fluid

Currently, analytical techniques based on microfluidics have become essential for chemical and biological analysis. Novel applications and prospects in cell- and molecule-level detection have emerged. Especially in cell study, high compatibility of microchannel dimensions and cells, which is possible to simulate the cellular environment in vivo, can be achieved in vitro [61, 62]. Simultaneously, optical detection has high sensitivity and is easily integrated with a

microfluidic chip, making it more suitable for the real-time detection of live cells. Based on the optical method, the optical detection technology used in microfluidics can be classified as an off-chip detection system and an on-chip detection system. As compared with off-chip optical systems, an on-chip optical system in microfluidics shows advanced properties in automation, portability, integration, and programmable tunability [3, 10]. By combining a compatible photonic detector and a microchannel, optofluidics can expand the detection function of a microfluidic chip. Besides, it can more sensitively detect and analyze the experimental result in the chip. Because it incorporates sample preparation and transport with the analytical process, optofluidics is particularly well-suited for real-time biological/ chemical detection and analysis in tiny detection volumes (femtoliters to nanoliters).

In past decades, optofluidic devices have substantially influenced biomedical and chemical applications. A previous research paper has reviewed the applications of optofluidic devices with different photonic components detecting cells, pathogens, protein biomarkers, and nucleic acids [63]. Several optical characteristics, such as refractive index (RI), fluorescence, Raman scattering, absorption, and polarization, can be used individually or in combination. The detection can be grouped as follows: fluorescence detection, surface-enhanced Raman spectroscopy detection, RI detection, and surface plasmon resonance (SPR) detection. For example, a multiplexing wide waveguide based on multimode interference (MMI) ARROW can confine light into sample flow and output fluorescence signal, as shown in **Fig. 2.4 a** [64]. In addition, waveguide [65], fiber [66] is also commonly used as as optical device for fluorescence detection based on optofluidics. It is used to establish a optofluidic point-of-care testing platform [67] and a lab-in-a-fiber system [68]. As compared with fluorescence detection, optofluidic detection based on Raman spectroscopy shows higher reproducibility [66, 69]. In recent studies, a number of SERS-active components, such as silver nanoparticles colloid [70], nanometric gold layer [71], and gold nanorods [72, 73], are used to further improve the sensitivity of Raman spectra via surface resonance enhancement. By including extra plasmonic components, surface-enhanced Raman spectroscopy (SERS), a highly sensitive molecular analysis technique, may achieve non-destructive detection of molecular bond by "fingerprint" recognition, allowing the identification of the analyte's constituent component. As **Fig. 2.4 b** shows, an on-chip parallel detector is available to inject a two-phase segmented flow for transporting target analyte and flower-shaped gold nanoparticles to the detection region [74]. Simultaneously, plasmonic materials are also used to create a surface plasmon resonance (SPR) detector with an integrated microfluidic channel [75]. Unlabeled real-time monitoring of biomolecular interactions at the interface is the key property of SPR detection, and signals of biomolecular interactions may be acquired by monitoring dynamic changes in SPR while biological reactions take place [76–78]. As shown in **Fig. 2.4 c**, localized SPR-based gold nanorods as plasmonic gel films can detect the enzymatic reaction [79]. Unlike the previous detection method, the introduced refractive index detection can deal with non-fluorescent, no-absorption, and dielectric analytes [80, 81]. In the research of Barshilia *et al*. [82], a glass planar waveguide (as **Fig. 2.4 d** shown) is exploited as a portable RI detection system to detect the microchannel above the waveguide. In addition, polymer bent ridge waveguides [83], cascade-microlens [84], Bragg

microcavities [85], and photonic crystal fibers [75, 78] are used in microfluidic channels to create rapid, high-throughput, low-cost sensors based on RI detection.

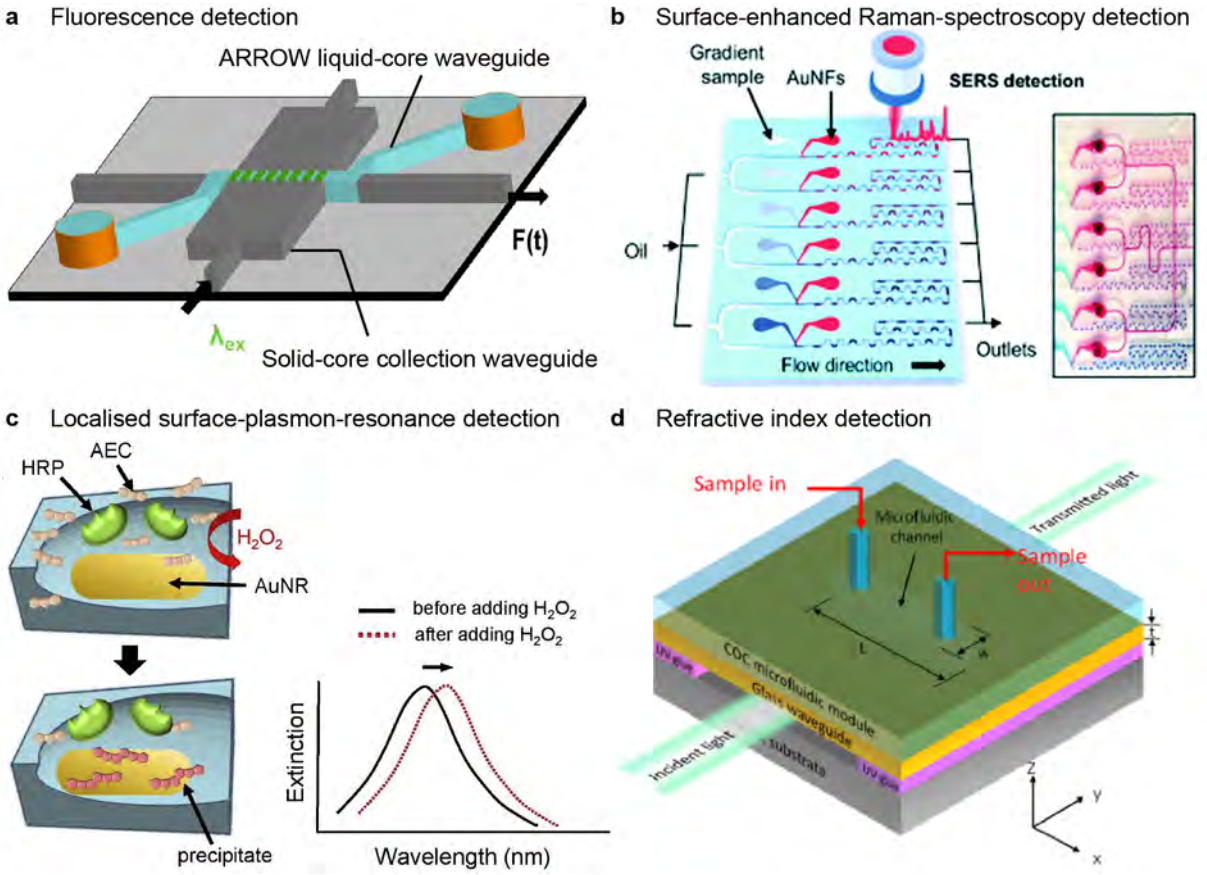

Fig. 2.4. Detection technologies based on optofluidics. (a) Schematic diagram of an MMI-ARROW device, in which light is confined by a solid-core MMI waveguide. Analyte with biomarkers are transported in an ARROW liquid-core waveguide and output fluorescence signals are extracted by a perpendicular collection waveguide. (b) Illustration of a parallel SERS detector that mixes flower-patterned gold nanoparticles and gradient samples for detection. (c) Schematics of gold gel films based on gold nanorods and the corresponding spectrum of peak shifting before (black straight curve) and after (red dot) adding H_2O_2 solution. (d) A wide waveguide-based refractive index detector shows the incident light transport beneath the microfluidic channel, and the transmitted light through the waveguide is used for real-time analysis. The figures are reproduced (a) from [64]; (b) from [74]; (c) from [79]; (d) from [82].

Sample analysis requires diversified operations, such as preconcentration, sorting, and trapping. When compatible photonic components are integrated inside microchannels, it is possible to efficiently manipulate a group of cells or a single cell by using external optical force. At typical flowrates in microfluidic systems is often laminar because the viscous force of the fluid in a microchannel is often significantly stronger than the inertia force. By utilizing the geometric regularity of laminar flow, ordered arrangement of cells in a microchannel may be achieved [10]. The laminar flow occurs when a fluid flow in a channel, its mass point moves in a smooth straight line parallel to the channel axis, as shown in **Fig. 2.5 a** [86]. By controlling injected velocities of the fluid into a microchannel, the laminar flow effect can effectively limit the trajectory of the analyte and selectively transport and trap the analyte to the specified

detector through embedded photonic elements. As **Fig. 2.5 b** shows, an optofluidic platform can demonstrate a series of single-cell analysis processes, which includes manipulation, treatment, and detection [4]. In this approach, microfluidic platforms provide stable transport, while photonic devices perform a range of tasks by applying additional forces on a single cell. Furthermore, integrated photonic devices make it possible to realize multi-cellular manipulation simultaneously [80, 87]. In **Fig. 2.5 c**, a planar waveguide embedded under a microfluidic channel shows the possibility to transport particles perpendicular to the flow direction as a conveyor belt [88]. Particles can be collected and transported along the excited waveguides while altering the energy coupled to the waveguide can switch its capture and release states [88, 89]. The interaction between light and particles provides the possibility of particle sorting by exploiting on-chip photonic devices. A mechanism for enhancing the size-based particle sorting technique is shown in **Fig. 2.5 d**, which separates polystyrene microspheres with three different diameters of 2, 5, and 10 μm [5]. At present, existing particle separators are able to achieve separation purity greater than 95% [90, 91], even reaching 100% [92].

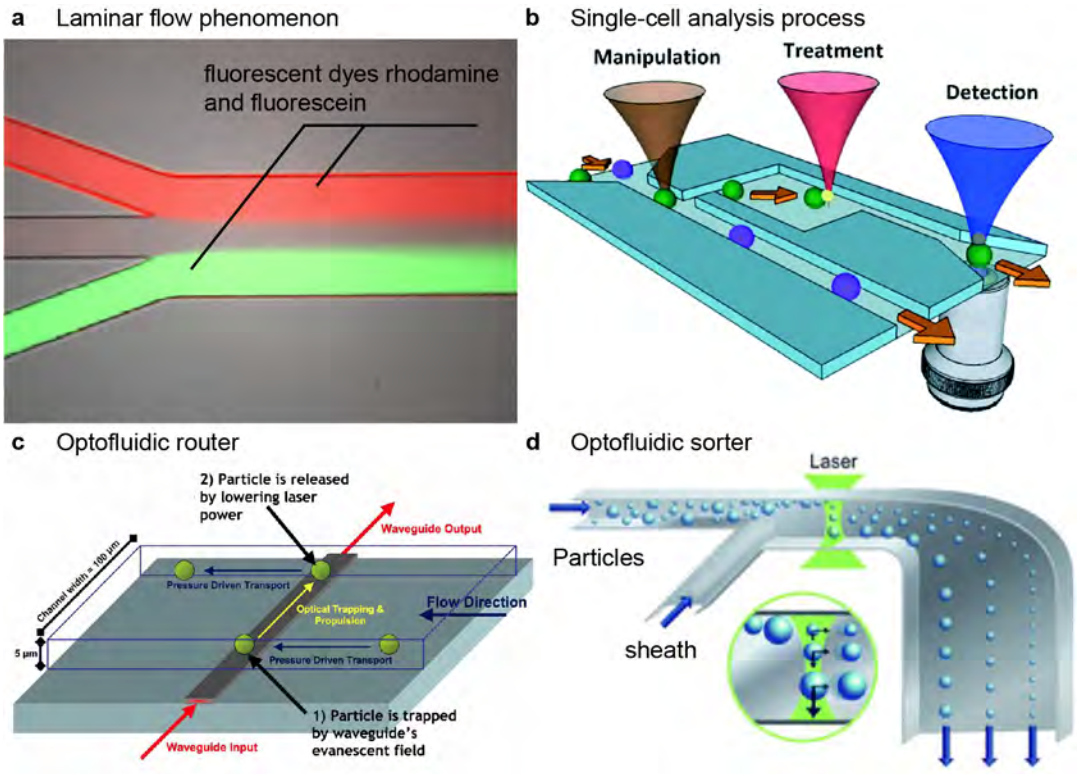

Fig. 2.5. Optofluidic platforms for optical manipulation. (a) An illustration of the laminar flow phenomenon shows a three-input microfluidic channel, in which the two outer channels contain fluorescent dyes rhodamine and fluorescein, for visualization. (b) A schematic diagram of an optofluidic platform for the single-cell analysis process. It consists of manipulation, treatment, and detection functions. (c) The schematic diagram of a planar waveguide-based optofluidic router can manipulate the trajectories of trapped particles. The particles are transported by liquid flow where the flow direction is perpendicular to the waveguide. (d) Illustration of an optofluidic enhanced sorting system with two inputs containing particles and sheath. Laser light pushes the particle along the beam propagation direction. The figures are reproduced (a) from [86]; (b) from [4]; (c) from [88]; (d) from [5].

This section reviews the benefits of incorporating photonic devices into microfluidics devices in detecting and manipulating analytes. In general, the advantages of photonic deceives and microfluidic devices are complementary to each other in optofluidics. In the following three sections, optical manipulation of small particles is discussed in detail, as it directly relates to my PhD work.

2.3 Optical manipulation

Since the pioneering work of Ashkin *et al*. on optical trapping [93], a wide range of optical manipulation methods have been developed. Single beam gradient force trapping, known as optical tweezers uses a highly focused laser beam to trap and manipulate micro- and submicron-scale objects using a highly focused laser beam. The principle of optical tweezers is that the light field will push a transparent object in a highly focused light field to the location with the maximum light intensity [86, 94]. It combines gradient force and radiation pressure, as shown in **Fig. 2.6 a**. Gradient force is precise the polarization of an object in an electric field that draws the object to where the electric field is the greatest. Simultaneously, scattering induces radiation pressure because photons have momentum and push objects along the direction of light. Stable optical capture is achieved when the gradient force is balanced with the radiation pressure. The optical force can penetrate transparent and semi-transparent objects to identify the structure's liquid content and mechanical properties [95, 96]. Since the experiment can be carried out without physical contact, tissue damage can be avoided. Optical tweezers possess a wide range of applications in biological systems, from manipulating luminous nanoscale objects to pathogens such as cells, and bacteria [15]. The optical trapping potential of a single laser is determined by the relation between the incident light's wavelength and the particle's size, the refractive index of the particle, and several parameters (e.g. densities, refractive indices, and viscosities) of the surrounding medium [97]. When the particles size is considerably larger than the laser wavelength, the geometric optical model can be used to predict the optical gradient force, and the relation between refractive index and momentum transfer can also be explored, as shown in **Fig. 2.6 b** [1, 98]. In contrast, if the particle's size is substantially smaller than the laser wavelength, it is considered a dipole in an inhomogeneous electromagnetic field and can be analyzed using the Rayleigh scattering theory [99, 100].

Moreover, many optical tweezers controlled objects are in biological tissue in liquid media. The viscosity and Brownian force of the liquid can be used to estimate optical trap force and optical trap properties. **Fig. 2.6 c** illustrates the Brownian motion of an optically trapped particle [1]. An optical trap produced by two orthogonally polarized beams propagating opposite to each other traps a 3 μm particle. A 3-dimensional map shows the optical potential energy, and the particle position under the Brownian motion is recorded. Under this condition, the mean square displacement curve tends to be stable after 1 ms, while the maximum value of the displacement is less than 10^{-15} m^2. As mentioned above, particles in the optical trap will be

exposed to both gradient force and radiation force, and particle manipulation may be accomplished by balancing the two. A gradient force larger than the radiation pressure is required to attract particles, especially under the influence of Brownian motion in an optofluidic device. This is possible with a high numerical aperture (NA) objective lens, which can highly focus the laser beam to form a diffraction-limited focal point, enhancing the gradient of the field amplitude. Because the gradient force is proportional to the gradient of the field amplitude, it can produce a force of several hundred pico-newton force [15, 101].

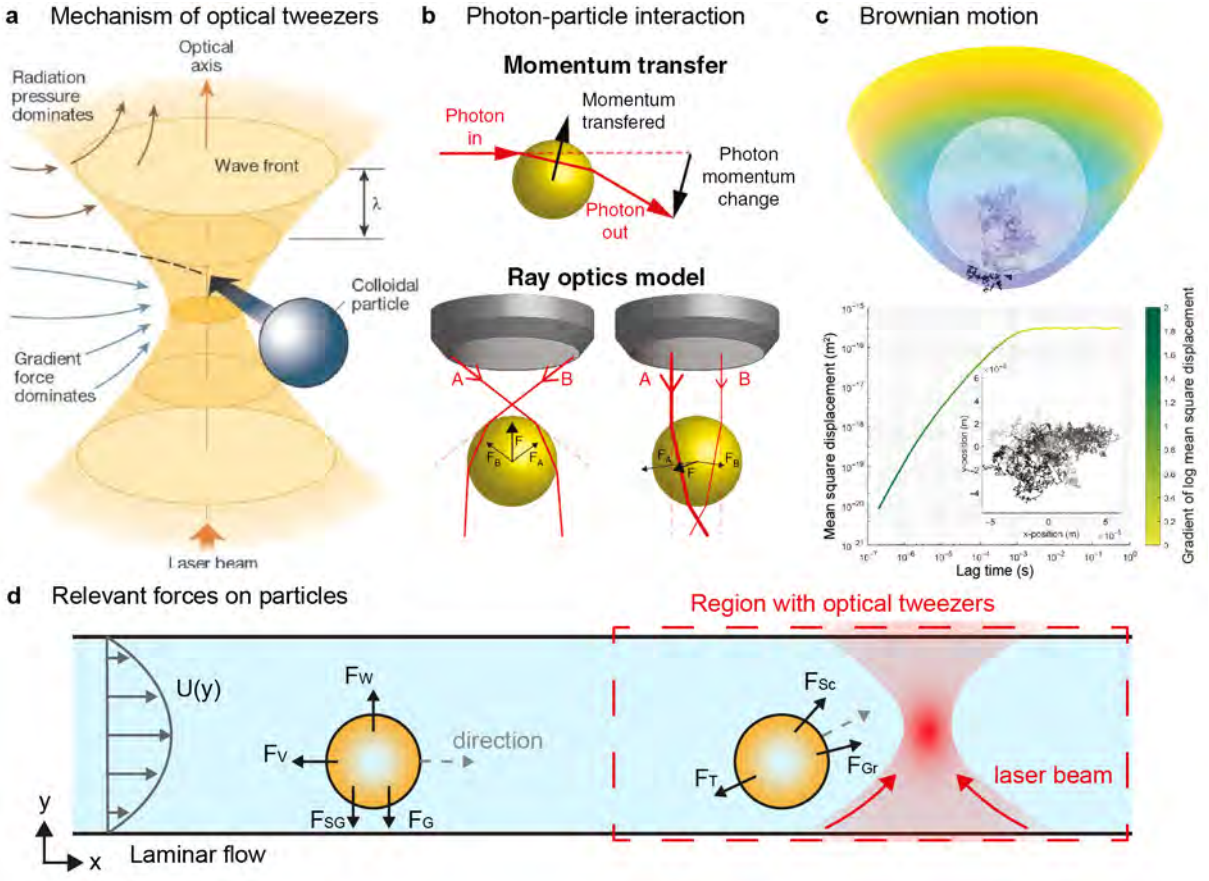

Fig. 2.6. Schematic diagrams of the confinement of optical tweezers. (a) Intensity gradients in the converging beam can push a colloidal particle towards the focal waist. Meanwhile, the radiation pressure of the laser beam pushes the particle along the positive optical axis. (b) Illustration showing how a particle gains momentum as a photon refracts inside it, shown in the top row. The bottom row shows the ray optics model for symmetric and asymmetric beams and corresponding gradient forces F. (c) The confinement of an optically trapped particle moves under Brownian motion, where the particle trajectory is shown as the black line. The bottom row shows the mean square displacement of a particle in optical tweezers. In the inset, the Brownian motion of a trapped micro-scale particle is depicted, with shading corresponding to the sample point. (d) Schematic diagram showing various forces on particles in a laminar flow. The grey parabolic curve represents the flow profile of the laminar flow in a microchannel, and the solid grey arrows represent corresponding flow velocities U. The dashed arrows show the direction of movement. When the particle moves close to optical tweezers, only the forces induced by the laser beam are shown for clarity. The forces acting on the particles are: wall-induced lift force F_W, shear gradient lift force F_{SG}, gravity force F_G, viscous force F_V, scattering force (i.e. radiation pressure) F_{Sc}, optical gradient force F_{Gr}, and optical-induced thermophoretic force F_T. The figures are reproduced (a) from [86]; (b) and (c) from [1].

Forces that can act on the particles in an optofluidic platform are shown in **Fig. 2.6 d**. For a particle far away for the focus of optical tweezers, gravity force will push the particles toward the bottom. The wall-induced lift force pushes the particles away from the wall, while the shear gradient lift force drives the particles away from the center of the flow [102].Under these forces, the particles transfer laterally to an equilibrium position where the net force is zero [102]. The viscous force appears in the opposite direction of the particle movement while the particle is at equilibrium position. In addition, due to the thermal convection generated by the laser beam, thermophoretic force tends to drive the particle away from the heat source. Based on the force analysis above, the effect of fluidic force on optical manipulation can be eliminated by placing the photonics devices below the equilibrium position of the microchannel. In previous research, the trapping stiffness increases linearly with the increase of laser power, which means that the enhancement of gradient force is sufficient to overcome the increase of thermophoretic force when the incident energy increases [103]. In later chapters, only the contribution of light forces acting on particles is considered.

Optical tweezers are minuscule "tweezers" that manipulate particle movement and rotation. As the first example, optical tweezers-based tractors [95, 104], shown as **Figs. 2.7 a-b**, can move particles without using high NA lenses. Based on the principle of optical force, the motion of a particle in an unfocused beam follows the forward scattering of light because only radiation pressure existed. However, the optical tractor could indeed transport the particle in reverse. **Fig. 2.7 a** illustrates a tunable angle-based optical tractor, which is can pull and push particles of a 410 nm radius by adjusting the angle of wave vectors between two incident beams. The pulling force exists while the angle is between 152° and 180° [105]. An optical tractor also depends on the polarization of the tractor beam, as shown in **Fig. 2.7 b**. More specifically, a gold-coated glass sphere shows forward motion in a radially polarized beam, while it moves backward in an azimuthally polarized beam [106]. Radial polarization can be generated in several methods. A common method is to use q-plates [107] or liquid crystals [108] to convert a light beam from circular polarization to radial polarization. As the second example, optical tweezers created using vortex light can provide angular momentum to induce orbit rotation and spin in trapped particles [109–111]. **Fig. 2.7 c** shows the coefficients of spin angular momentum (SAM) and orbital angular momentum (OAM) on a sphere with a radius of 250 nm [112]. Both radial and circular polarized vortex beam can exert OAM and SAM on the trapped particle, causing it to spin while orbiting the optical axis. Such structured beams show the possibility of optical tweezers performing complex and multiplex manipulations on microscopic objects, such as confinement, conveyance, and rotation.

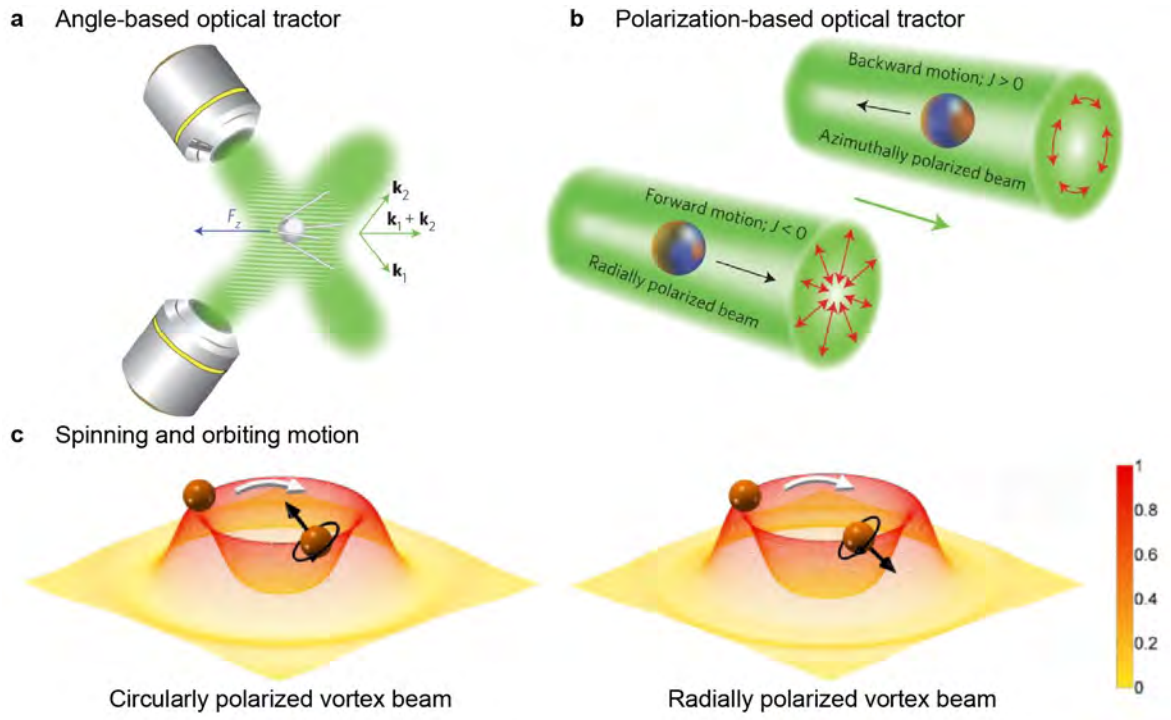

Fig. 2.7. Optical manipulation with structured light. (a) Illustration of two plane waves with tunable wave vectors. A particle located in the two beams is dragged in reverse along the resultant vector of the two wave vectors. (b) Schematic diagrams of polarization-based optical tractors demonstrating the forward and backward movement of semitransparent spheres. The green arrow represents light propagation, and the black arrows represent motion tendency. (c) A schematic diagram of spin and orbital torque vectors on a particle in the focusing fields of a vortex beam with topological charges of $m = -5$. The white arrows represent the orbiting motion, the black circles around the particle with arrows represent the directions of spinning motion, and the black arrows represent the spin torque vectors. The figures are reproduced (a) from [105]; (b) from [106]; (c) from [112].

2.4 Optical manipulation in the near-field

Methods of using optofluidics for trapping single cells or even molecules, cell transport, and sorting cells of various sizes have all become novel research subjects [7, 20]. Conventional optical-based tweezers [86, 113] trap and manipulate micron-scale objects by concentrating a laser beam and using the optical force at the focal spot. Although optical tweezers can manipulate sub-micron-scale samples, they require significant optical power because of the diffraction limit of laser focusing. Optical tweezers require a large numerical aperture to provide a strong gradient force against radiation pressure to achieve stable trapping. Thermal effects, such as heating from the laser beam and thermal convection [114] in liquid, may affect the trapping efficiency. Furthermore, conventional optical tweezers often need large equipment and are often difficulty for batch operation. It is thus worth considering novel near-field optical manipulation technology for sub-micron target samples. Recently, advanced near-field optical manipulation has been used, which employs waveguides [88], optical resonators [115], and

plasmonic tweezers [116]. These near-field optical tweezers are often extremely small, allowing for large-scale integration on a single optofluidic chip. In this section, several tweezers based on surface plasmon resonance (SPR) are reviewed.

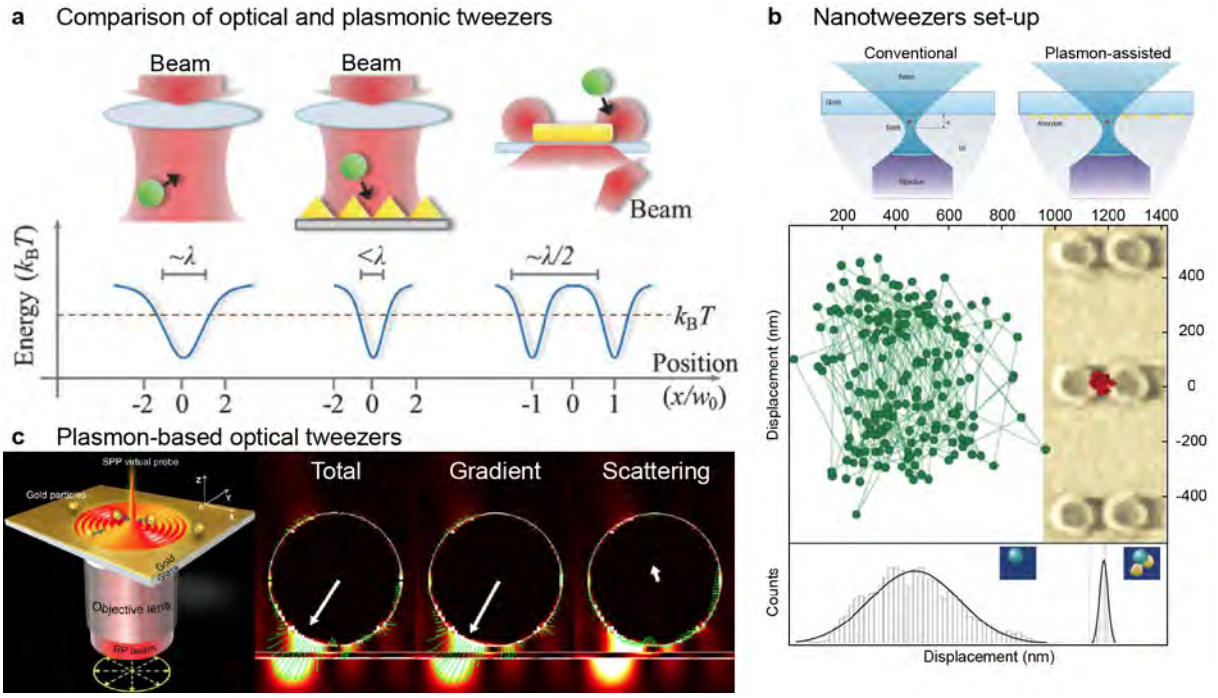

Fig. 2.8. The development of optical tweezers for trapping. (a) Schematic diagrams show conventional optical tweezers (left) and plasmonic-based optical tweezers (center, right). Ellipses represent lenses, green circles represent trapped particles, black arrows denote particle motions, and yellow triangles and rectangles represent structured plasmonic materials. (b) An illustration of optical tweezers and plasmon-assisted tweezers with a nanostructured substrate. A light beam focuses on the substrate through an objective lens immersed in oil. In the bottom row, green and red spots record the trajectories of a particle trapped by conventional optical tweezers and plasmon-assisted optical tweezers, respectively. Two black curves represent the number of particles at different positions under relevant conditions. (c) Perspective view of plasmonic trapping and generated forces on a 1-diameter particle. A schematic of a beam focused on the glass-gold film (left figure) generates an SPP. The electric field intensity is shown in the background, while the white circles and white lines represent the particles and gold films, respectively. Three white arrows represent the resultant forces of the total, gradient, and scattering (green arrows). The figures are reproduced (a) from [101]; (b) from [117]; (c) from [118].

Conventional far-field optical tweezers show a crucial restriction known as the diffraction limit [119]. The trapping potential is restricted by the focal spot size. As the left segment in **Fig. 2.8 a** shows, optical tweezers stably trap and manipulate particles of a size similar to the beam wavelength. In contrast, plasmon-assisted and plasmon-based optical tweezers (POTs) demonstrate the potential to overcome the diffraction limit, shown as the central and right segments in **Fig. 2.8 a**, respectively. Grigorenko *et al*. published an article in 2008 on using a nanostructured substrate to enhance the tapping of conventional optical tweezers [117]. In this research, the trapped particles are immersed in oil. Due to the Brownian motion, they are free to move randomly within a range. By adding an array of nanodots on the glass substrate, as shown in **Fig. 2.8 b**, the displacement of trapped particles with a 200 nm diameter

in plasmonic-assisted optical tweezers is ten times smaller than in conventional optical tweezers. It is because, light illuminating the nanodots can activate the localized surface plasmonic resonance (LSPR) [120, 121] at the nanodots, and the LSPR can enhance the electric field intensity to increase the trapping potential. According to the lightning rod effect [122], the enhanced electric field tends to concentrate in the gap of such nanocavities [116, 123], which is referred to as a "hotspot". Trapped particles prefer to concentrate at these spots. In addition to plasmon-assisted optical tweezers, plasmonic tweezers based on surface plasmon-polaritons (SPPs) and localized surface plasmon (LSP) can manipulate subwavelength particles as well. In **Fig. 2.8 c**, an SPP virtual probe is generated on a gold film under the illumination light from an object lens, and the interaction between the virtual probe and a nano-scale gold particle moves the particle [118]. It is worth noticing that the scattering force and gradient force show different distributions in the trapping. Whereas the scattering force pushes the gold particle up and toward the light axis, the gradient force drives the particle moves toward the position illuminated by the focusing beam. A POT based on a thin gold layer [118, 124] has been used to trap and manipulate gold particles with a diameter ranging from 0.5 - 2.2 μm when the surface plasmon is excited by a radially polarized cylindrical vector beam. Min *et al*. has observed that when a high numerical aperture objective lens is used, the SPP wavefront can propagate toward the center of the focus [118]. Overcoming the diffraction limit of traditional optics has been a breakthrough for plasmonic tweezers [125], and the measured optical force enhancement can be larger by up to 40 times at resonance when compared to non-resonance conditions [124]. Therefore, POTs are promising for applications of in-vitro cell detection [126].

Many different plasmonic nanostructures have been used to manipulate subwavelength particles. These POTs can realize intense energy trapping with a dramatic optical gradient at the dielectric-to-plasmonic interface, promising novel applications in switching [127], sensing [128], scattering microscopy [129], and trapping [116, 120, 125, 130]. Although homogeneous plasmonic films can trap subwavelength-scale particles, stable trapping requires a strong stiffness and a strong trapping potential. This can be achieved by creating plasmonic nanostructures on a substrates. Several POTs with nanostructures are shown in **Figs. 2.9 a-c** as examples.

A stiff trap, which can be constructed using a metal pattern, is required for trapping particles stably at specific locations on the metal surface. Righimi *et al*. have designed a gold micro-disk on a glass substrate to achieve surface plasmonic tweezers [131]. In their study, a 4.88-μm-diameter PS bead can be trapped on a gold micro-disk by a linearly polarized laser at 710 nm. The incident laser intensity is more than two orders of magnitude lower than the minimum intensity used in conventional OTs to confine similar beads [126]. Subsequently, two-dimensional square lattices of gold nanostructures consisting of four-nanodisks arrays, shown in **Fig. 2.9 a**, have realized trapping and guiding nanoparticles with 100 - 500 nm diameters [131]. Chen *et al*. have used nanodisks for achieving particle trapping of multiple nanospheres, all with a diameter of 500 nm. Under 4.75 mW illumination, the particles were stacked to form a closely packed structure. The illumination lasted 34 s and was then turned off, and the structure dispersed and the particles escaped the trap.

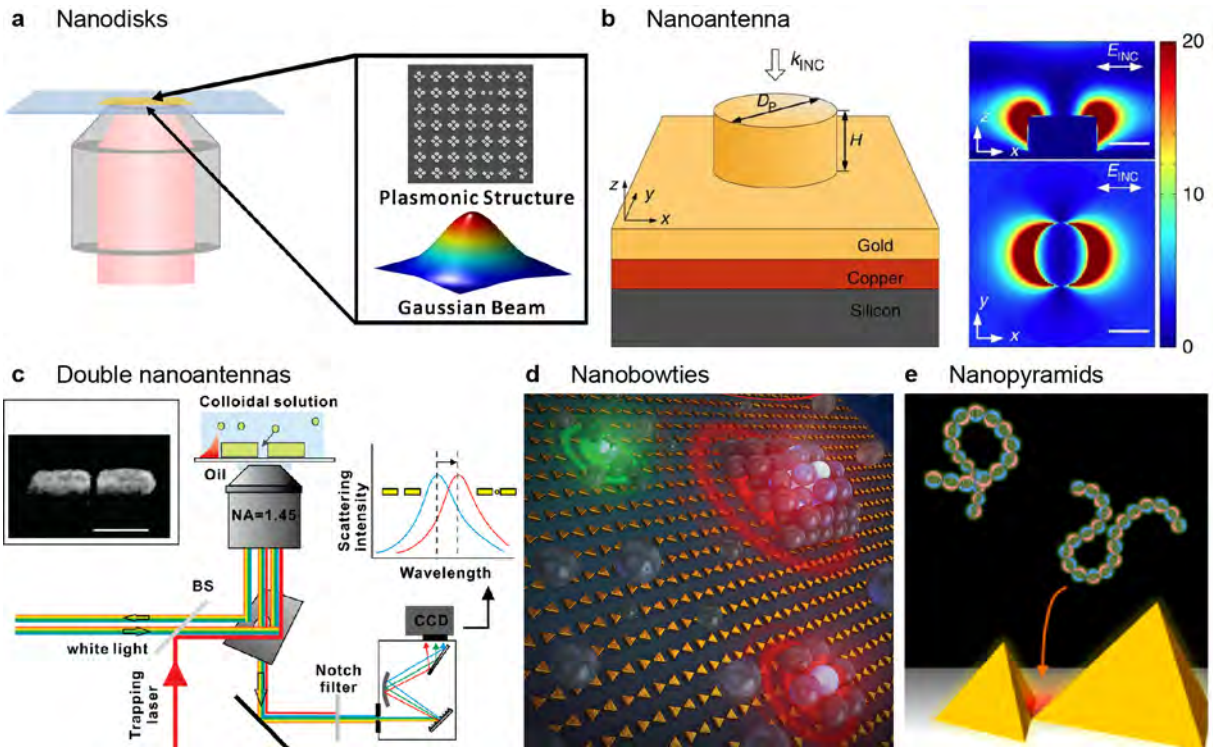

Fig. 2.9. Plasmon-based optical tweezers utilizing different metallic geometries. (a) A Gaussian beam illuminates a two-dimensional square lattice of gold nanostructures on an ITO-coated cover glass. Each cell of the nanostructure consists of four nanodisks. (b) An illustration of a gold nanoantenna developed on a gold-copper-silicon layer with a linearly polarized beam from the top. Distributions of field intensity in the xz-plane and xy-plane shown on the right column demonstrate the intensity enhancement surrounding the excited nanoantenna. (c) Experiment setup and double nanoantenna design. Double dipole antennas are created on a substrate, and a white light illuminates from the bottom. The inset figure is an SEM image of the nanofabricated antennas with a 10-nm gap. (d) A perspective view of a bowtie nanostructure array with trapped single particles and stacked multiple particles. (e) A schematic diagram of the evanescent field on pyramids for trapping λ-DNAs. The figures are reproduced (a) from [131]; (b) from [132]; (c) from [133]; (d) from [134]; (e) from [135].

Metallic nanoantennas are among the most intriguing plasmonic geometries, because they can confine light to a localized "hotspot". As compared to nanodisks, nanoantennas are often more suitable for trapping objects orders of magnitude smaller. In Wang *et al.*'s research, a structured layer consisting of gold nanopillars with a diameter of 280 nm and a height of 130 nm is analyzed [132]. In this experiment, the LSPR-based POTs concentrate the electromagnetic field on two sides of the nanopillar along the polarized direction of the incident beam. The maximum enhancement of the electromagnetic field intensity reaches 490 times of that of the incident beam, as **Fig. 2.9 b** shows. This enhanced electric field can trap PS beads with a diameter of 110 nm [132]. In addition, this nanoantenna also demonstrates the possibility of rotating trapped PS beads by manually rotating the linear polarized beam or exploiting a circularly polarized illumination.

Simultaneously, nanoantennas can achieve real-time detection of such small particles based

on resonance shift, because the field enhancement caused by LSPR can lead to surface-enhanced Raman scattering enhancement [136]. Zhang *et al*. have reported using novel plasmonic dipole antennas to trap and detect gold nanoparticles with diameters as small as 10 nm. As shown in **Fig. 2.9 c**, two rectangular nanoantennas with a 10-nm-gap demonstrate the possibility of trapping a 20-nm-diameter gold particle under white light illumination. At the same time, the Rayleigh scattering spectra appear to have a 50-nm red shift when such a particle is trapped [133]. Such duel nanoantennas can further confine electromagnetic field into the gap where it can realize stable trapping [117, 133, 137]. Bowtie nanostructure, composed of two symmetric triangular structures facing each other but separated by a gap, has attracted significant interest in nanophotonics [134]. This geometry appears to have higher sensitivity than a pair of nanoantennas [138], while it can confine light in a single spot inside the gap. Although the bowtie nanostructures can not concentrate the energy of the electromagnetic field as much as the nanoantenna [132, 139], the former can generate multiple potential wells at the external edges of the triangles [140]. By exploiting the advantages of bowtie nanostructures, Roxworthy *et al*. have excogitated bowtie arrays of two equilateral triangles, each with a 120 nm tip-to-base height and separated by a 20 nm gap for optical trapping, stacking, and sorting [134]. In their experiments, gold bowtie arrays can achieve single micro- and nano-particle trapping at an input power of approximately 100 μW, as well as multiple particle stacking at an input power of less than 1 mW, as shown in **Fig. 2.9 d**. In the same year, this research group also utilized a femtosecond input source to realize both Rayleigh and Mie particle trapping in gold bowtie nanoantenna arrays. 300-nm-diameter fluorescent PS spheres and 80-nm-diameter silver spheres can be trapped and manipulated using a 50 μW input power [139, 141].

Another nanostructured worth mentioning is the pyramidal nanostructure. It provides optical trapping at nano-valleys between adjacent pyramids, allowing for photo-luminescence quenching and enhancement based on the LSPR and SERS effect [142]. Nano-pyramids (shown in **Fig. 2.9 e**) can create stable trapping of quantum dots [142], polymer chains [143], and λ-DNA [135]. In 2017, Yan *et al*. fabricated graphene-gold nanopyramids to achieve self-aligned trapping of molecules, in which evanescent fields were generated on the two sides of the nanopyramids and a strong attraction force ($> 10^{11}$ N/m^3) was detected [144]. In nanofabrication, it is impossible to obtain the ideal sharp edges. Although the sharpness of edges edge can affect field distribution, the influence is not normally considered in numerical simulation [131–135]. The experimental results are usually consistent with modeling based on sharp edges.

Instead of using protruding structures in a metal film, trapping can also be achieved by etching apertures in the metallic film [116]. As early as 1928, an aperture in a metallic plate was proposed to realize high spatial resolution beyond the diffraction limit [145]. Plasmonic nanoapertures have been confirmed to confine electromagnetic fields into subwavelength volumes. The enhanced local field intensity and strong trapping potential can lead to nanoscale manipulation with low input power. Juan *et al*. have fabricated a self-induced back-action

cylindrical nanoaperture with a diameter of 310 nm to trap a single 100-nm-diameter PS particle in water using 1 mW incident power, as shown in **Fig. 2.10 a**. This power requirement is one-twelfth of that used to trap PS particles with a diameter of 109 nm [94]. This experiment indicates that a real-time sensor could be accomplished by utilizing the substantial influences of dielectric loading on the nanoaperture transmission [120, 146–148]. In 2018, a gold plasmonic nanohole array was demonstrated to be able to trap 30-nm-diameter PS particles by integrating a nano-slot with the nanoholes [149]. A co-axial nanoaperture has also been employed to achieve optical trapping due to enhanced transmission efficiency [150]. A silver plasmonic co-axial aperture with a 25-nm-width silica ring can trap a 10-nm-diameter dielectric particle with a refractive index $n = 2$ using a 20 mW linearly polarized plane wave [151]. As **Fig. 2.10 b** demonstrates, Yoo *et al*. has used an optical trapping array with resonant coaxial nanoapertures to realize stable trapping of 30-nm-diameter PS particles and streptavidin molecules with laser power as low as 4.7 mW [152]. In addition, a grating structure can concentrate the incident light energy and transfer it in a specified direction [153]. Based on these properties of gratings, a fiber-based coaxial nanoaperture with flanked gratings, namely Bull's eye, can decrease the input power of stable optical trapping from 1 W (without gratings) to 100 mW (with grating) [154]. In the experiment, a fiber with silver or gold tips, as **Fig. 2.10 c** shows, is equipped to trap 10-nm-diameter PS beads under illumination at wavelengths of 695 nm or 770 nm [154], respectively.

Most plasmon-based optical tweezers exhibit rotational symmetry. Nevertheless, a nanoaperture structure with non-rotational symmetric, for example the C-shape aperture, possesses unique characteristics in trapping, guiding, and sorting of nanoscale dielectric particles [155–157]. In 2003, Shi *et al*. demonstrated a novel nanoaperture with a C-shape pattern, as shown in **Fig. 2.11 a**, which could generate 3 orders of magnitude more power in throughput than a conventional square aperture. They claim that a C-shape nanoaperture can achieve a high spatial resolution of 0.1 λ as well as a high power throughput (> 1) at 6 GHz [158]. It is worth mentioning that the power throughput, which shows the net power capturing capability (not transmission efficiency), can be defined as the ratio of the power transmission cross section and the aperture area [159]. For subwavelength apertures at resonance, the power transmission cross section can be larger than the aperture area giving a power throughput larger than unity.

The following year, the same research group explained the principle of designing a C-shape aperture and its resonant-transmission properties while demonstrating the possibility of scaling to other wavelengths [159]. In the same year, Matteo *et al*. showed that C-shape apertures could enhance transmission by 13-22 times in the visible regime as compared to square apertures of the same volume [160]. Based on these benefits, a nano-optical conveyor belt has been fabricated to achieve stable trapping of PS particles with a diameter of 200 nm, by using a plane wave with an intensity of 1 $\mathrm{mW}/\mu\mathrm{m}^2$ [161]. Simultaneously, C-shape apertures appear to have high wavelength sensitivity because they are LSPR-based structures. Hansen *et al*. used the asymmetric light scattering force of a C-shape aperture to limit the escape direction of the

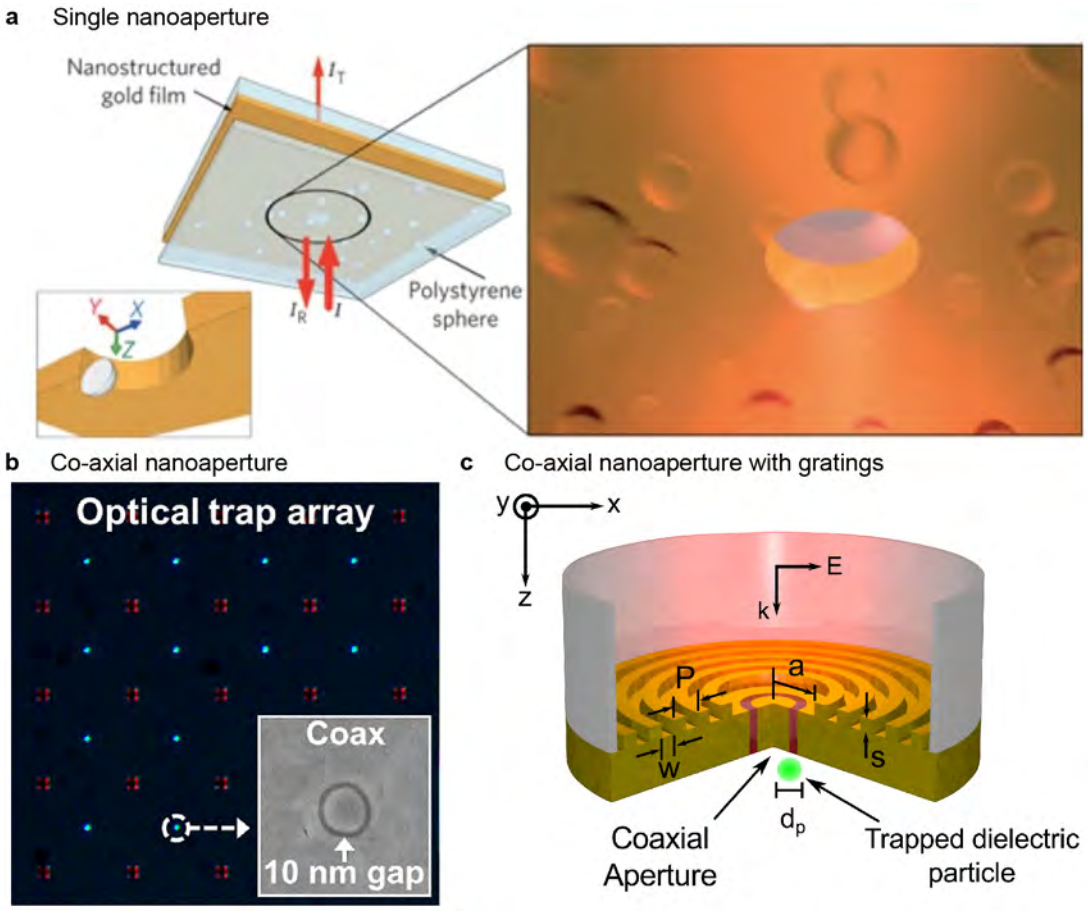

Fig. 2.10. Optical trapping using nanoapertures. (a) Illustration of trapping using a 310-nm-diameter cylindrical aperture in a 100-nm-thick gold film. (b) Cross sectional schematic of an optical trap array with co-axial nanoapertures on an 80-nm-thick gold film.(c) A schematic diagram of the fiber-based plasmonic tweezers. The nanoaperture is fabricated on a metal-coated fiber tip, while the flanked gratings of the nanoaperture are integrated at the metal/fiber interface. A green sphere represents the trapped dielectric particle. The figures are reproduced (a) from [146]; (b) from [152]; (c) from [154].

particles, producing a conveyor belt consisting of C-shape apertures with two different characteristic scales to transfer and sort PS particles with diameters of 200 nm and 400 nm along the guidance trajectory, as shown in **Fig. 2.11 b** [161]. Furthermore, the researchers demonstrated a switching operation for handing-off 400-nm-diameter particles between adjacent C-shaped apertures by utilizing the influence of an incident laser's polarization angle on the scattering field distribution of the aperture, as shown in **Fig. 2.11 c** [162]. Due to the advantages of C-shape apertures, it can realize label-free nanoparticles guiding and sorting via the plasmonic near-field trap and asymmetric field distribution. In addition, it is possible to overcome the range restriction of conventional plasmonic traps by employing electrophoresis force to attract nanoparticles to the area of the plasmonic trap [163]. This approach combines far-field manipulation and near-field manipulation.

Plasmon-based optical tweezers (POTs) can manipulate a wide range of nanoscale particles [164, 165], including dielectric particles, biomolecules [123], and living cells. As compared to

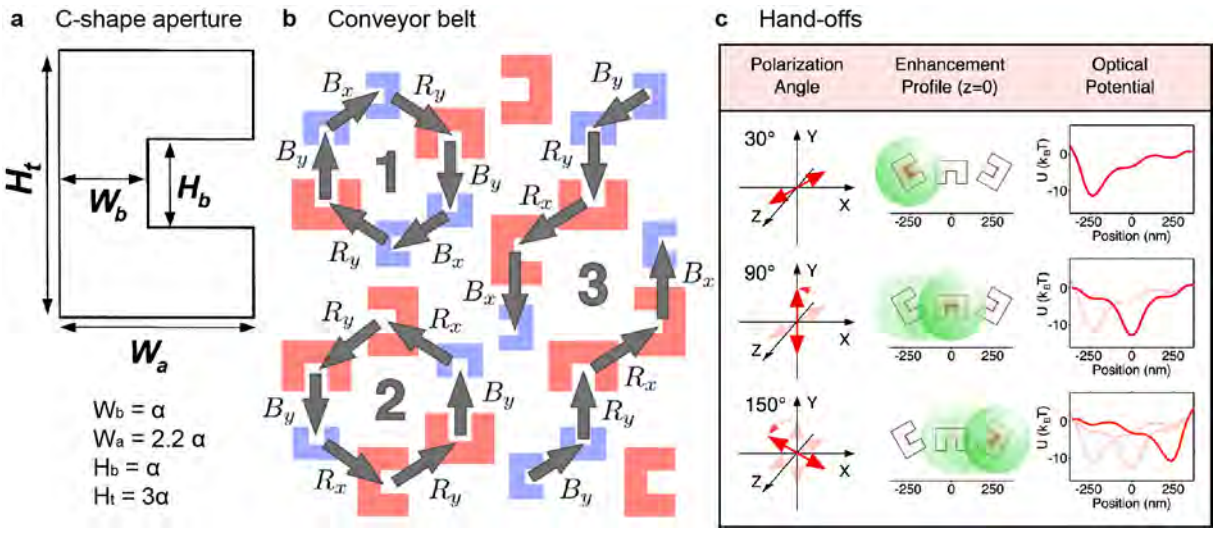

Fig. 2.11. Design principle of a C-shape aperture and its applications. (a) A design of a C-shape aperture with a characteristic size α. (b) Illustration of a two-dimensional conveyor belt using two scaled aperture with $\alpha = 40$ nm (blue patterns) and $\alpha = 60$ nm (red patterns). B_x, B_y, R_X, and R_y represents four illuminate conditions, that is, 979 nm x-polarized beam, 979 nm y-polarized beam, 1181 nm x-polarized beam, and 1181 nm y-polarized beam, respectively. Three trajectory protocols with grey arrows represent the particle motions. (c) Schematic diagrams of a polarization-controlled conveyor belt and corresponding potential wells (right column). Red arrows on the left column represent polarized directions, and green semi-transparent beads in the middle column represent 400-nm-diameter particles. The figures are reproduced (a) from [159]; (b) from [161]; (c) from [162].

conventional optical tweezers, POTs technology combines low power consumption and the concept of nano-optics, which can be useful for biological, biochemistry, and nanoscience research [157, 166].

2.5 Optical manipulation in the far-field

Although plasmonic tweezers demonstrate exceptional properties in deep subwavelength-scale manipulation due to their ability to overcome the diffraction limit, they face challenges in provide trapping dynamically and with a high degree of freedom. Another issue is the efficiency. Because the enhanced evanescent field of plasmonic structures has a limited range, often just a few dozens of nanometers [125, 132], only particles adjacent to the plasmonic structure can be affected. Although far-field optical tweezers are restricted by the diffraction limit, OTs often provide a high degree of freedom for optical manipulation in optofluidics [10]. At present, a technology named Liquid Crystal Silicon Spatial Light Modulator (LCOS-SLM) can be used to achieve far-field optical trapping. It can be utilzed for beam steering, splitting, and focusing. It can also convert a Gaussian beam into many "advanced tweezers", e.g. vortex beam with orbital angular momentum to drive particles spin up, and Bessel beam with no diffraction [167, 168]. LCOS-SLM can also generate multiple three-dimensional optical traps. In 2018, Smalley *et al*. showed that, the OTs can trap fluorescent particles as holographic image

pixels and manipulate the trapped particles to display 3D images [169]. Observers can see a true 3D image from any angle as shown in **Fig. 2.12 a**. Accordingly, simultaneously trapping and manipulating multiple particles in three dimensions is possible by utilizing light in the far field. An emerging method is to use metalens [170–172], which for example can generate multiple foci in latitudinal (**Fig. 2.12 b**) [173, 174] and longitudinal (**Fig. 2.12 c**) [175, 176] directions at the same time.

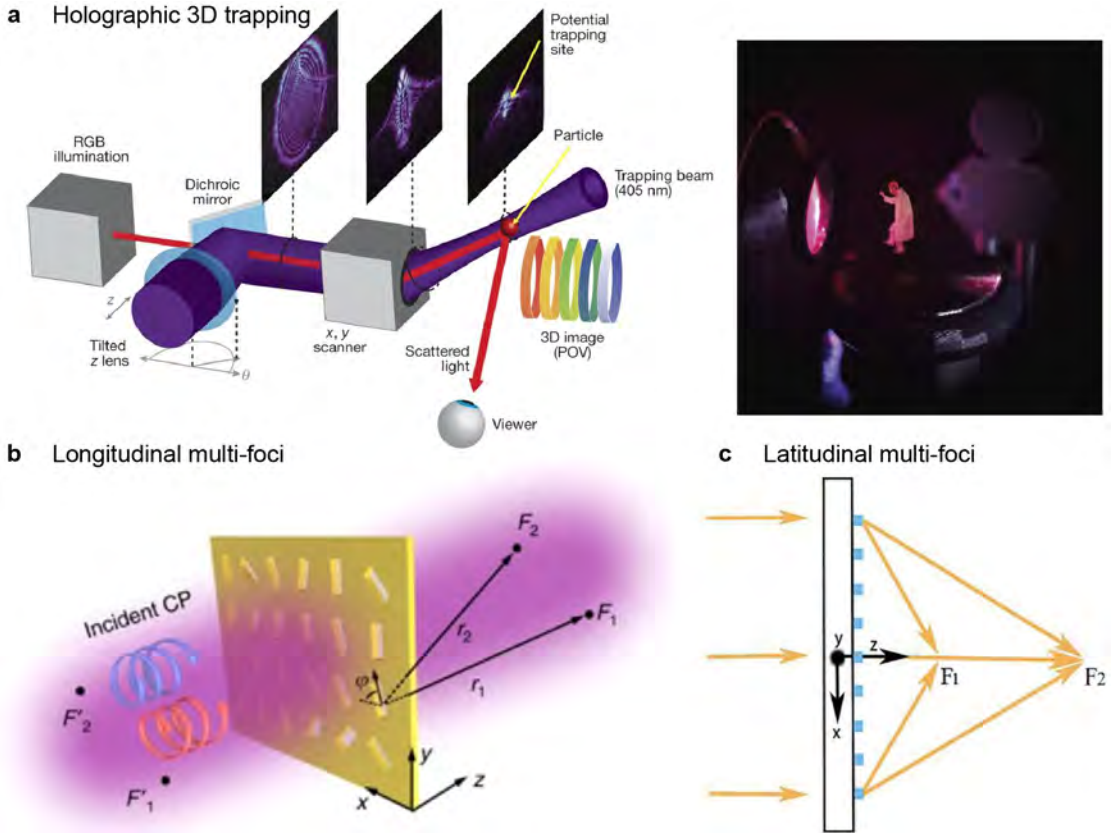

Fig. 2.12. Illustration of holographic trapping and multi-foci. (a) An experiment setup where a low-visibility light-trapped particle is used to scan a volume. Close-up of the projected image is shown on the right. (b) Illustration of a metalens consisting of nanoslit with two foci under the illumination of circularly polarized light. (c) Schematic diagram of a designed bifocal metalens that produces two different focal points. The figures are reproduced (a) from [169]; (b) from [174]; (c) from [176].

A metalens, or two-dimensional metamaterial surface, is an optics device that uses artificial subwavelength meta-atoms to modify polarization, phase, and amplitude of output light. As compared to conventional optics lenses, which require bulk equipment to correct chromatic aberration, a well-designed metalens can focus the entire visible spectrum, from 470 nm to 670 nm in wavelength, by a planar structure [177]. In the context of optofluidics, metalenses retain the far-field particle manipulation capabilities of conventional optical tweezers (i.e. optical tweezers that rely on the used microscope objectives with a high numerical aperture). At the same time, it leverages the nanoscale light-shaping capabilities provided by nanophotonics devices.

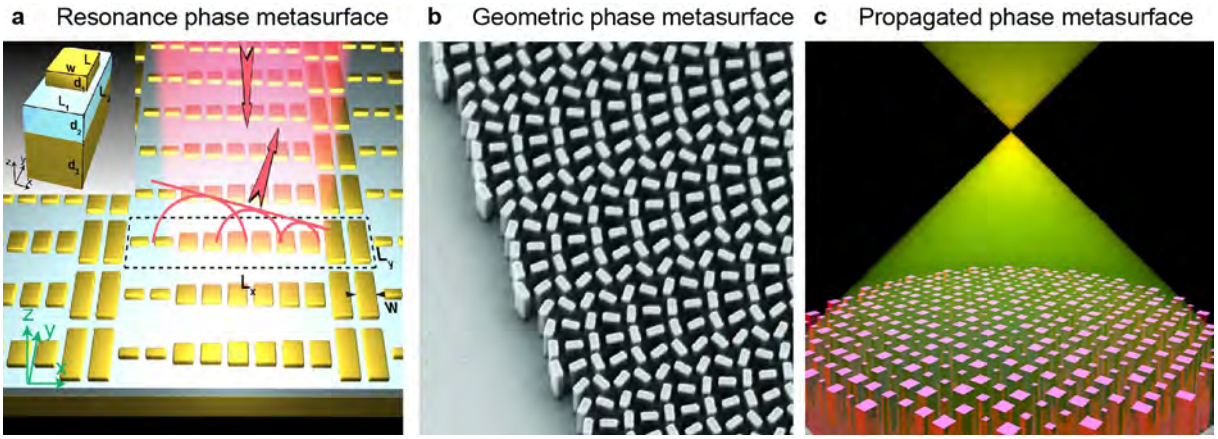

Fig. 2.13. Three categories of metamaterial surface, based on different approaches to generate optical phase modulation. (a) Perspective view and mechanism of a metasurface. A unit-cell (inset) of the designed metamaterial surface consists of a continuous gold film and a gold rectangular nanoantenna separated by a MgF_2 layer. A super-cell is composed of 10 unit cells. Red arrows indicate the incident and reflected light, and red lines indicate retailored wavefronts. (b) SEM image of a geometric phase metasurface with fixed-size, varying angles, and periodic distribution of nanofins. (c) Illustration of a propagation phase metasurface consisting of TiO_2 square nanopillars with a 600-nm height on a substrate. The phase can be controlled by modifying the side length of the nanopillar cross section. The light illuminates from the top (not indicated) and the reflected beam focuses in free space. The figures are reproduced (a) from [178]; (b) from [179]; (c) from [180].

A two-dimensional planar metalens, acting as a diffractive optical lens, utilizes light scattered by nanostructures to imitate the phase front generated by a conventional refractive lens. Based on the approach of optical phase modulation, metamaterial surfaces can be divided into three categories, that is, resonance phase metasurface [178], geometric phase metasurface [179, 181, 182], and propagation phase metasurface [180, 183, 184], as shown in **Fig. 2.13 a-c**. The first category, the resonant phase-modulated metasurface, is often made of metal components, and its phase delay is caused by structural resonance, resulting in a restricted operational bandwidth [178, 180]. Such resonance-based metasurface often has high light absorption and low efficiency. Geometric phase modulation can achieve phase control by utilizing nanostructures with a changeable rotation angle.

The last category, i.e. the propagation phase category, the optical path difference formed during the propagation of electromagnetic waves is employed to create the output phase. The output phase of a nanostructure can be modulated using several methods: by varying the height of nanostructures and by spatially varying the equivalent refractive index [185]. For a planar metasurface with a fixed thickness, the cross sectional dimension in each unit cell of the metasurface can be adjusted, hence changing the relative refractive index. Based on this principle, metalenses can employ phase-matched subwavelength structures to apply a designated phase delay against the incident plane wave, achieving the effect of focusing the light field.

Once the nanostructures of a metamaterial surface are fabricated, it is often difficult to

change their geometry or dimension, rendering it challenging to tune their focusing performance in real-time. Nevertheless, through the real-time modulation of metasurface using mechanical [186], thermal [187, 188], electrical [189], and optical [190] controls, tunable metasurface lenses have been developed. Here I highlight optical control of metalenses [191]. As an example shown in **Fig. 2.14**, a structured gold nanofilm works as a metalens and can tune focused SPP beam toward four different directions under 632 nm, 670 nm, 710 nm, and 750 nm incident wavelength. Simultaneously, the polarization of the incident light can also modify the direction of the focusing SPP.

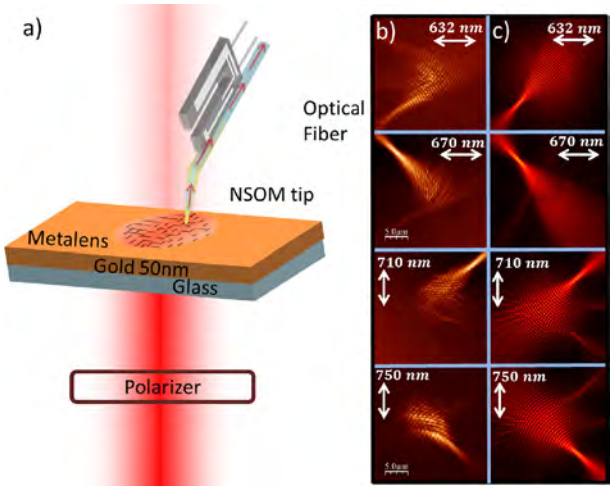

Fig. 2.14. Wavelength-based tunable metalenses. (a) Illustration of the experiment setup. A patterned gold film with a 50 nm thickness is deposited on a glass substrate, and a linearly polarized beam illuminates it from the bottom. A metal-coated, tapered optical fiber interacts with the SPP and is used to collect light. (b) and (c) Experimental and simulated results demonstrate field distribution with the polarization of light indicated by white arrows. Four wavelengths of the incident light are analyzed. The figure is reproduced from [191].

Geometric and propagation phase metalenses can exhibit sensitivity to the polarization of incident light. For the geometric phase approach, metalenses consisting of well-designed rotated nanofins can demonstrate focus shift. Badloe *et al.* presented a two-layer system with a top metasurface lens and a bottom liquid crystals layer. Collimated light illuminates from the bottom of the system [192]. Controlling the bias voltage on the liquid crystals affects the orientation of the liquid crystals, which changes the polarization of the light transmitted through the liquid crystals. As a result, the light from the metalenses layer will focus on two different preset locations following the polarized condition, as shown in **Fig. 2.15 a** [192]. The essence of optical modulation here is to control the rotation direction of the incident circular polarization light to shift the focus point of the metalenses.

As another example, a metalens composed of three concentric circles can generate three focal points with different longitudinal distances, as shown in **Fig. 2.15 b** [170]. The first and the third focal points correspond to the RCP incident light, while the second focus corresponds to the LCP incident light. These three focal points exist simultaneously under a linearly polarized light, because the linearly polarized beam can be decomposed into LCP and RCP, which provides an opportunity to control the generated foci by adjusting the weight of the LCP and RCP

component. **Fig. 2.15 c** shows another example, where a geometric phase metalens exhibits unique spin-decoupled characteristics [193]. Two RCP foci are generated under the illumination of LCP waves, while two LCP focal points can be observed for the incident RCP waves. In addition, the intensity between two RCP foci and two LCP foci can be modulated by controlling different weights of LCP and RCP waves [193]. This phenomenon allows for dynamic particle trapping and manipulation by modulating the convergence of the metalenses, which is achieved by changing the polarization condition of the incident light. In the fourth example, a planar silicon metalens can generate two foci at different longitudinal positions under two different linearly polarized states, i.e. x-polarized and y-polarized, for trapping the particles in the vicinity of the focal points [194]. Trapped particles can be transferred between the two foci by switching between two polarization conditions, as shown in **Fig. 2.15 d**.

Coherent control is an alternative approach which uses optical modulation in Chapter 4. It allows for efficient control of two incident electromagnetic waves by utilizing a single-layer metamaterial surface. In the coherent control, an optical standing wave is created via the interference of two input light waves. For a metasurface in the standing wave, phase retardation caused by the film thickness may be omitted when the metasurface is seen as a vanishingly thin film to the standing wave field [197]. Each meta-atom can be seen as exposed under the same electromagnetic field. As shown in **Fig. 2.16 a**, the metasurface can switch between the electric field node (i.e. magnetic field antinode) and electric field antinode (i.e. magnetic field node) of the standing wave [198]. The coherent control approach can actively tune the metasurface absorption efficiency from 0% to 100% (**Fig. 2.16 a**) [199]. It can also modulate transmission, reflection, and polarization.

A number of research teams [196, 200] have demonstrated light-with-light control on a metallic metamaterial surface for realizing logical operations. For example, Papaioannou *et al*. have conducted an experiment with two incident beams shaped by marks and their relative phase modulated by a phase modulator. They utilized a CCD camera to observe output light, as **Figs. 2.16 b,c** show. The relative phase of the two counter-propagation beams can be tuned to establish interference in the area where images overlap (see **Fig. 2.16 c**), giving rise to various logical operations. It is worth noting that the optical modulation is a linear optical phenomenon. Although the metasurface in **Fig. 2.16** exhibits complex logical operations, the input and output are still linear superpositions of the two coherent, counter-propagating waves.

Our research team has recently designed a coherently controlled dielectric metasurface for LIDAR and machine vision systems [190]. As **Fig. 2.17 a** shows, a gradient metasurface is illuminated by two coherent, counter-propagating electromagnetic waves. All the six coherent conditions can be easily specified by the field ratio between the magnetic fields of the incident light from the glass (B_S) and the free space (B_f), which leads to tuned field distribution shown in **Fig. 2.17 a**. By changing the standing wave condition from the electric field node to the antinode, this design shows continuous output beam steering across an angular range of around 9 degrees. After two years, my group presented another metalens design, which achieved the tunable focusing of a dielectric metalens by coherent control, i.e., modulating localized electric

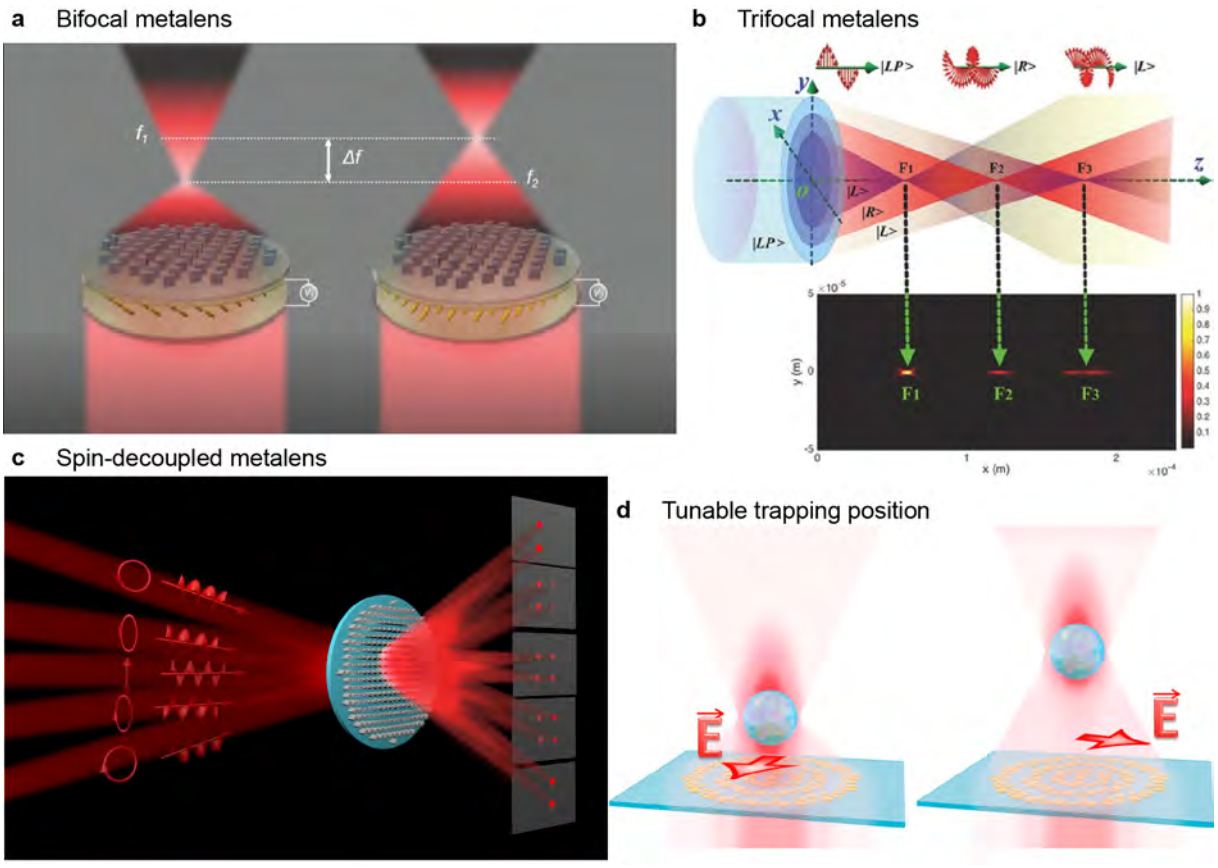

Fig. 2.15. Polarization-based tunable metalenses. (a) Illustration of the bifocal metalens. A metasurface lens array is fabricated on the upper layer, while the liquid crystal cells are placed on the lower layer. The orientation of the liquid crystals generates a shift in RCP and LCP light, resulting in a change of focal length from $f_1 = 7.5$ mm to $f_2 = 3.7$ mm. (b) Schematic diagram of the metasurface lens and its focusing performance under three different illuminations. Three focal points are highlighted by f_1, f_2, and f_3, respectively. A perspective view of three different polarized conditions, linear polarization, left circular polarization, and right circular polarization, shown on the top row. (c) Schematic illustration of the spin-decoupled metalens and the corresponding tunable multiple foci. Different foci are generated under LCP, RCP, LP, and two incident beams with different weights of LCP and RCP incidence. (d) Schematic views of the multiple focal points of a metalens. (Left) Polarization of the electric field is along the y axis and metalens generates a lower focal point. (Right) The orthogonal polarization generates a higher focal point. The figures are reproduced (a) from [192]; (b) from [170]; (c) from [193]; (c) from [194].

fields in a planar metalens, without adjusting the physical and geometric conditions of nanostructures and surrounded media [201]. Coherent switching metalens achieves longitudinal focus shift in both spherical and axicon lens, as shown in **Fig. 2.17 b**. Simultaneously, the metalens can switch between spherical and axicon types [201]. Other examples include coherent spin-orbit angular momentum conversion [202], dual band coherent absorption [203], coherent wavefront manipulation [199], and coherent large angle diffraction grating [204].

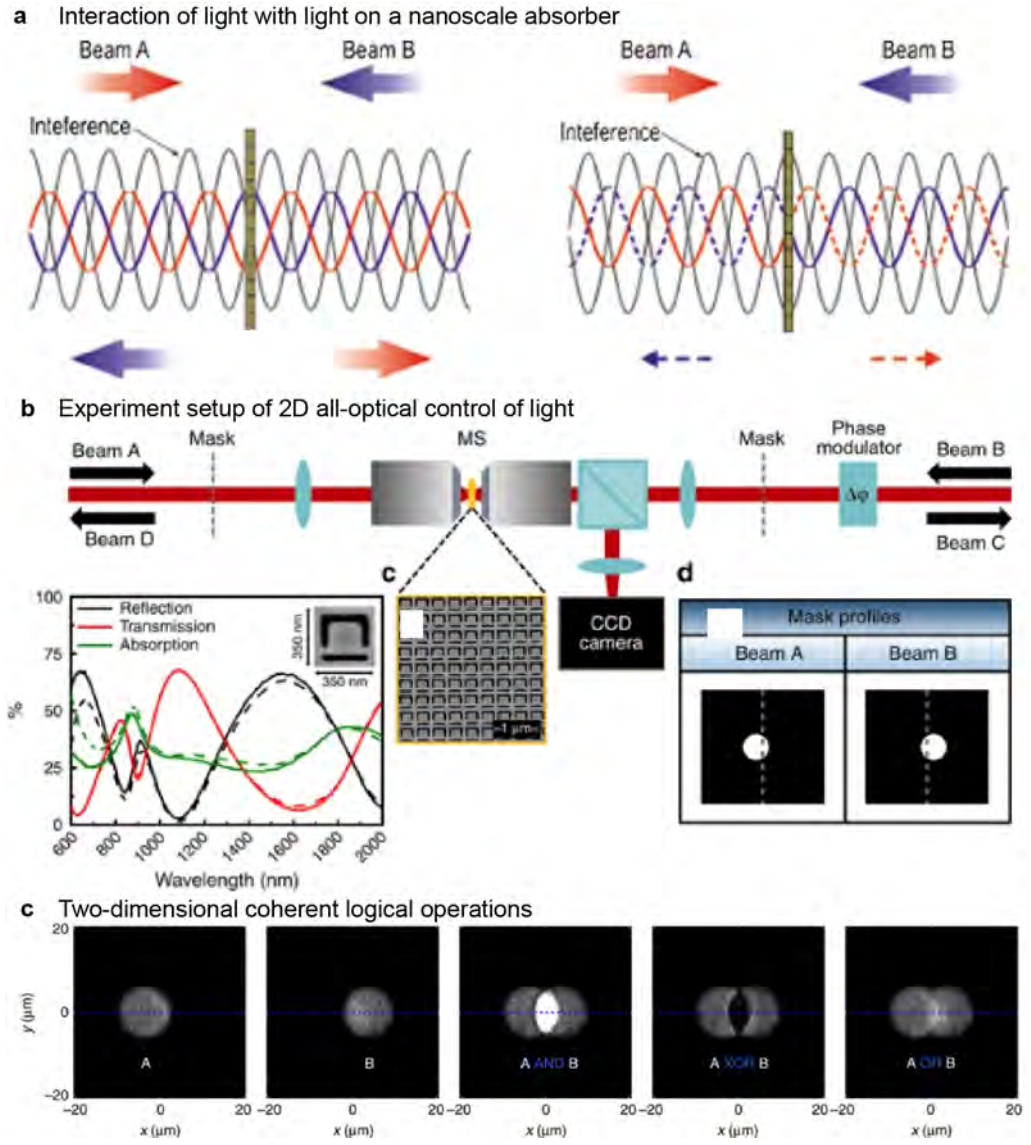

Fig. 2.16. Coherent control on structured films. (a) Light-to-light interaction on a nanoscale structured film. Two coherent counter-propagating beams, A and B, illuminate a sub-wavelength-thick film, a lossy plasmonic metasurface array. By tuning the relative phase between the two incident beams, the beams at the metasurface interact destructively or constructively. (b) Illustration of an experimental setup with two coherent beams, A and B, in which masks enable two-dimensional spatial modulation and a phase modulator provides temporal modulation. The output field is observed by a CCD camera. Insets exhibit reflection, transmission, and absorption of the well-designed gold metasurface, scanning electron microscopy of the metasurface, and mask profiles for spatial modulating two incident beams, respectively. (c) Images of metasurface illuminated by only beam A, only beam B, and three other logical operations of beams A and B, respectively. The figures are reproduced (a) from [195]; (b) and (c) from [196].

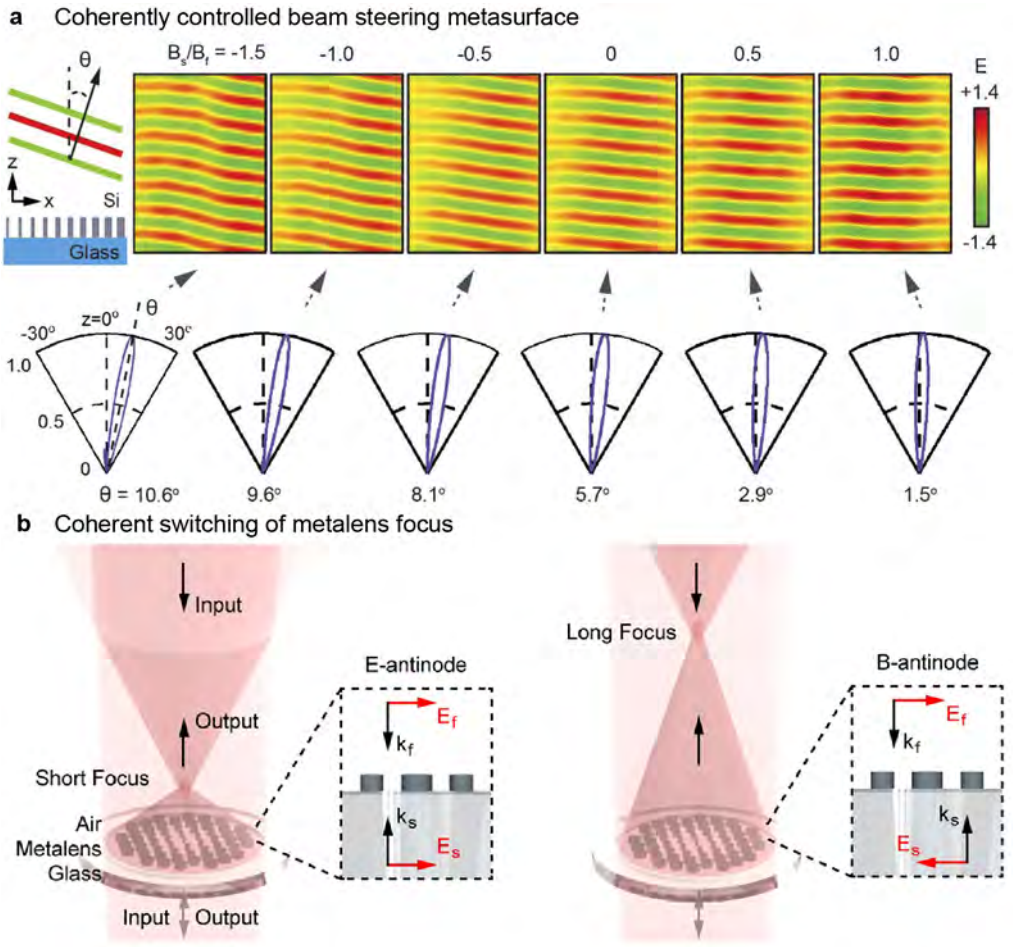

Fig. 2.17. Applications of coherent controlling. (a) Schematic diagrams of a metalens array consisting of Si nanopillars on a glass substrate illuminated by two coherent, counter-propagating waves (not indicated). The electric field distribution of the output light from the metalens array is shown under six different coherent conditions. (b) Illustration of a metalens under two coherent light waves. Inset demonstrates the coherent conditions with polarization direction (red arrows) and propagation directions of two incident waves (black arrows) specified. The figures are reproduced (a) from [190]; (b) from [201].

In summary, this section has analyzed the advantages of imaging (e.g. tunable focusing) and trapping (e.g. holographic multiple trapping) in the far field by employing a two-dimensional planar metamaterial surface. Metasurface with a sub-wavelength thickness allows for a high degree of control, which shows tunability via wavelength, polarization, and coherent modulation. These benefits provide an opportunity to utilize metasurface lenses in a microfluidic system to achieve, portability and minimization.

2.6 Multi-functional metasurface lens

Metasurfaces provide a high level of control over light propagation by applying localized, space-variable phase modulation to an incident electromagnetic field. Nevertheless, it also

faces challenges (for example, suppressing spherical, coma and chromatic aberration in metalenses) that are difficult to overcome. One of the solutions is interleaving multiple distinct optical elements on a singlet metasurface, known as interleaved metalens or segmented metalens, with different elements corresponding to distinct functions within a single shared aperture. Such metasurface lenses can achieve multiple functions within a shared surface area. For instance, Lin *et al*. have demonstrated multi-tasking interleaved Si-based metalens to achieve focusing light of different wavelengths on the same focal plane, as shown in **Fig. 2.18 a** [205]. The metalens array is divided into approximately 100 pieces, with the segments spread over the metalens' shared area. There are three sub-metalenses that can focus light into three focal points (see **Fig. 2.18 b**) along the longitudinal axis when illuminated with wavelengths at 480, 550, and 620 nm, respectively [205]. All these three wavelengths of light can be observed at a pre-set focal plane. Multi-wavelength imaging systems and hologram imaging may both benefit from such interleaved metalenses [205–208]. In 2017, Chen *et al*. showed segmented metalens for pixel-level focusing and routing. The researchers designed metasurfaces consisting of GaN-based nanofin arrays that could operate on-axial and off-axial, focusing independently at three incident wavelengths at 430, 530, and 633 nm [209]. The three metasurfaces are interleaved into a singlet metalens, as shown in **Fig. 2.18 c**. **Fig. 2.18 d** illustrates how the three wavelengths of light are focused in four independent directions while routing each color onto the same focal plane for full-color routers [209].

Another solution is to use laminated metamaterial surfaces, namely cascaded metasurfaces. In accordance with conventional optical systems design principles, the image lenses consist of two components: a focusing lens and a correcting lens placed in front to suppress coma and astigmatism. A cascaded metalens with two co-axial metasurface layers, known as metalens doublet, can mimic this optical system with a meticulously designed double-layer metasurface. In 2016, Arbabi *et al*. designed a doublet metalens (see **Fig. 2.19**) with a wide-angle aberration correction [210]. The doublet metalens has a low f-number (i.e., focus length/ diameter of the effective aperture) of 0.9 while achieving a field of view larger than 60°. As shown in **Fig. 2.19 a**, each metasurface layer is comprised of amorphous silicon nanopillars with a 600 nm height on a fused silica substrate [210]. The metasurface doublet lens comprises two metasurfaces on two sides of a silica substrate with a 1 mm thickness. Depending on the incidence angle, the focusing efficiency of this metalens doublet varies from 45% to 70%. In addition, the researchers compared the performance of the metalens doublet and a single focusing metalens (see **Fig. 2.19 b**) [210]. It could be found that the modulation transfer function (MTF) of the metalens singlet considerably deviates from the diffraction limit under a slightly oblique incidence (i.e., 2.5°). However, the spatial resolution of the metalens doublet stays close to the diffraction limit under a large angle illumination (i.e., 20°). Similarly, one year later, Groever *et al*. fabricated a metalens doublet in the visible region, which developed functions of diffraction-limited monochromatic imaging at a wavelength of 532 nm [211]. In their research, the metalens doublet comprises focusing and aperture metalens, and the two metasurface lenses are patterned on two sides of a 500 μm glass substrate. Each patterned metasurface consists of geometric phase modulated TiO_2 nanofins, as shown in **Fig. 2.19 c**. The metalens doublet can function

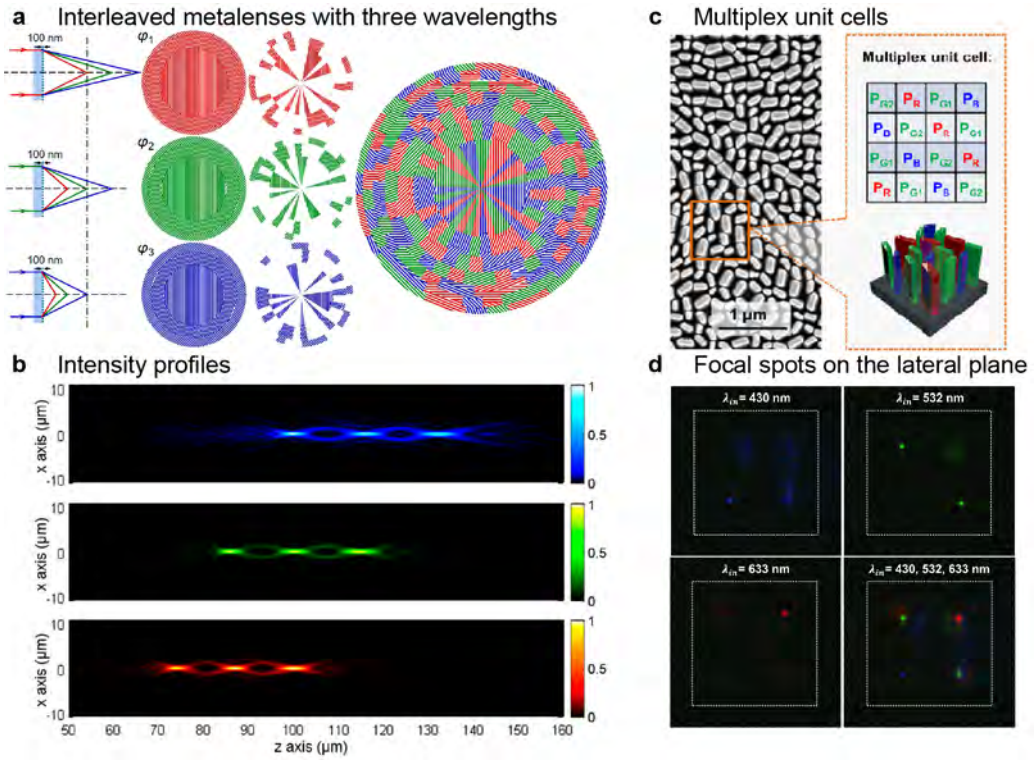

Fig. 2.18. Perspective views and focal spots of interleaved metalenses. (a) Illustration of three metalenses designed to focus light of different wavelengths at the same focal plane. (b) On the transmission side of the interleaved metalens, field intensity distribution along the propagation plane under the illumination of 480, 550, and 620 nm wavelengths, respectively. (c) Schematic diagram of multiplex unit cell composed of nanofins functioning under three wavelengths. (d) Imaging of focal spots on the same plane. When the interleaved metalens is illuminated with various wavelengths, the focus moves laterally in the focal plane. Four focal spots appear on the focal plane when three wavelengths are present. The figures are reproduced (a, b) from [205]; (c, d) from [209].

under LCP and RCP illumination and has a field of view of 50°. Ray diagrams (see **Fig. 2.19 d**) show the principle of aberration correction, which exhibit the aberration of utilizing a hyperbolic metalens only, a hyperbolic metalens with an aperture metalens, and a correction of hyperbolic metalens with an aperture metalens, respectively [211]. By combining the two metasurfaces, the metalens doublet can perfectly exhibit diffraction-limited imaging at an incident angle of up to 25° [211].

As a work that inspired my work in Chapter 5, Arbabi *et al.* presented a unique design of cascade metalens that acts as a retroreflector, as shown in **Fig. 2.20 a** [212]. It consists of an upper transmitted metasurface (i.e. metasurface *I*) and a bottom reflected metasurface (i.e. metasurface *II*). In this design, the incident wave passes through metasurface *I*, reflects on metasurface *II*, and is modulated again by metasurface *I*. Each unit-cell (see **Fig. 2.20 a**) of the metalens doublet consists of an amorphous cylindrical nanopillar on a silica substrate, following hexagonal lattice distribution. An additional gold layer exists on the unit cell of the bottom metasurface. In **Fig. 2.20 b**, metasurface *I* focuses the incident plane wave onto metasurface *II*, which imposes momentum corrections on the reflected light to return the light

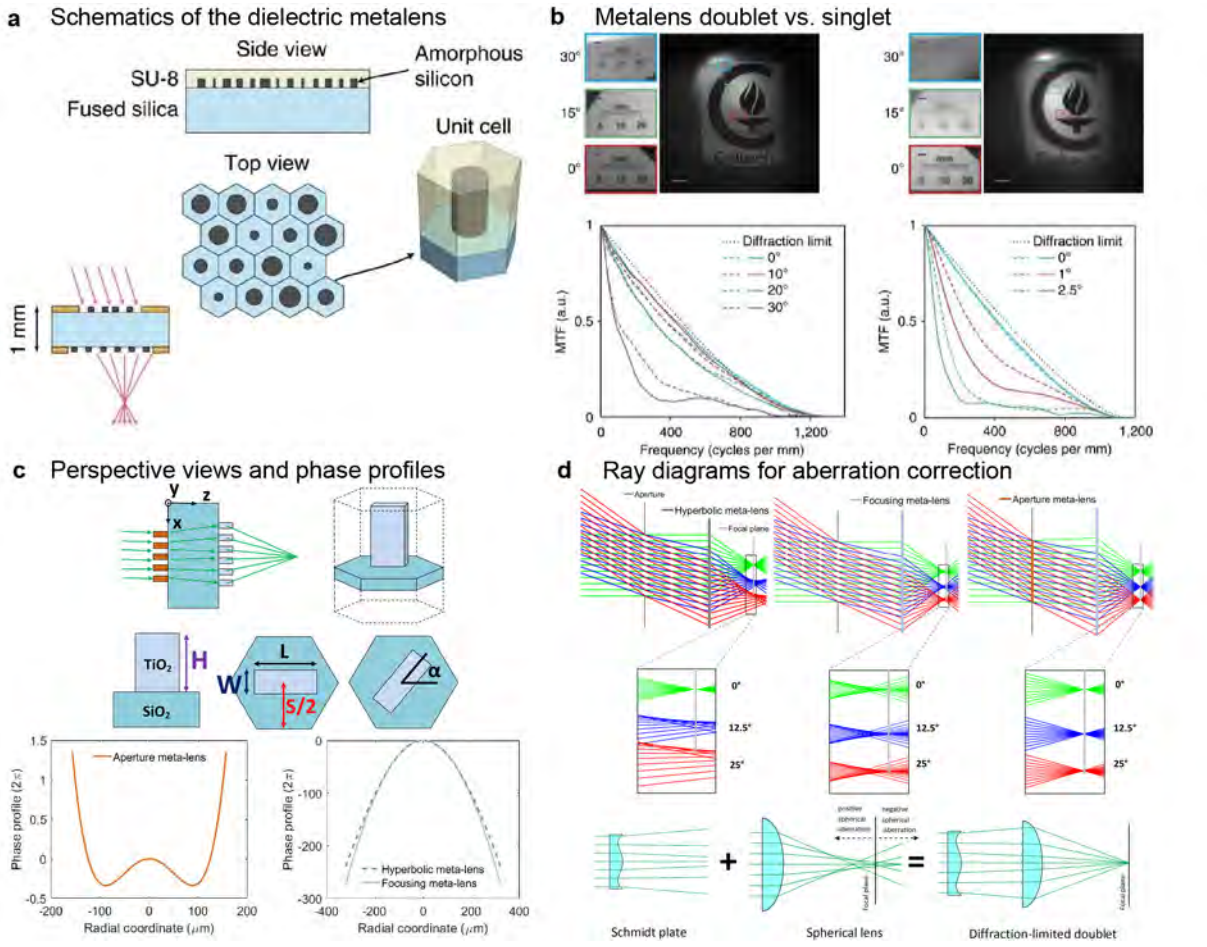

Fig. 2.19. Metalens doublet for coma and astigmatism correction. (a) Schematic diagrams of metalens doublet and its unit cell. Each unit cell consists of an amorphous silicon nanopillar allocated in a hexagonal lattice. (b) Imaging with the metalens doublet and singlet under three oblique incidents. The modulation transfer function (MTF) of the metalens doublet and singlet, respectively. Solid curves represent the MTF in the tangential plane, and dash curves depict the sagittal plane. (c) The schematic and geometric diagram of the metalens doublet consisting of TiO_2 nanofins in a hexagonal lattice on two sides of a SiO_2 substrate. Phase profiles of the aperture metasurface and focusing metasurface with the comparison of the hyperbolic metasurface. (d) Ray diagrams of a hyperbolic metasurface only, a focusing metasurface only, and a focusing metasurface with a combined aperture metasurface, respectively. Oblique illumination with a different angle is demonstrated by green, blue, and red lines, respectively. Regarding spherical aberration correction, the functioning of the metalens doublet is identical to that of a Schmidt plate paired with a spherical lens. The figures are reproduced (a, b) from [210]; (c, d) from [211].

to its original path. This retroreflector metalens doublet reflects light in the direction it comes from with an incident efficiency of 78% and achieves a 60° half-power field of view [212].

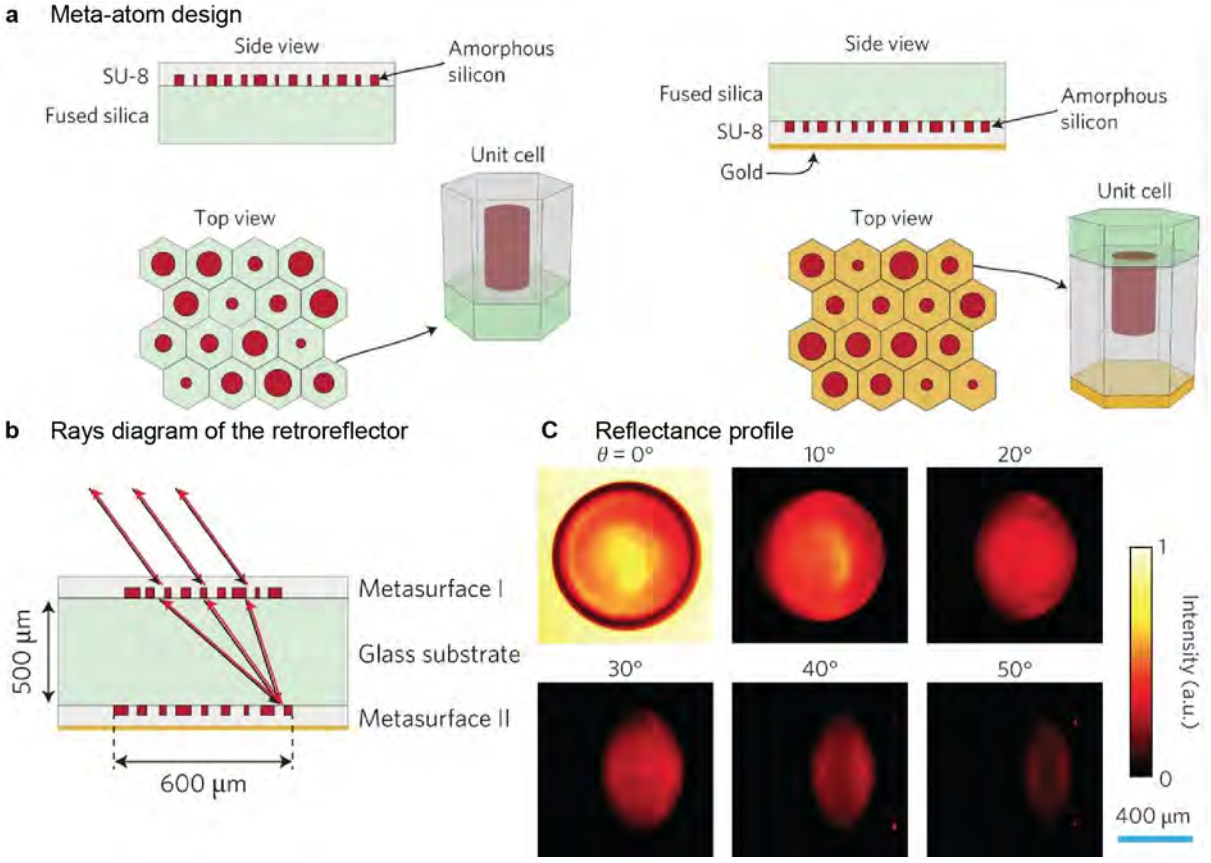

Fig. 2.20. Schematic of a planar metasurface retroreflector. Illustration of of the transmissive metasurface, metasurface *I*, and the reflective metasurface, metasurface *II*. They are comprised of amorphous silicon nanopillars allocated in a hexagonal lattice. A gold layer is employed on the reflective metasurface. (b) Rays diagram of the retroreflector metasurface under oblique incidence, in which black arrows represent incident waves, and red arrows represent output waves. A 500-µm thick glass substrate separates the two metasurface layers. (c) Field distribution of the reflectance profile of the retroreflector under 6 different incident angles. The figures are reproduced (a-c) from [212].

In summary, multifunctional metamaterial surface provides a higher degree of freedom to design a metalens. Desired correction of wavefront to incident wave can be achieved by utilizing complex, multiplexed metasurface geometries, whether cascaded or interleaved. As compared with conventional singlet metasurface, a novel metasurface doublet can realize wide-angle, achromatic imaging while capable of complex wavefront control, which has applications in optical free-space communication, dynamic optical tags, color filters, and holography.

2.7 Conclusions to Chapter 2

In this chapter, I have introduce the principle of optofluidics systems, which can be categorized as optics-to-fluidics and fluidics-to-optics interaction. I have also discussed the applications of

optofluidics in lasing, waveguiding, and optical modulation. By utilizing microfluidic control in photonics systems, a high degree of freedom for imaging, detection, and manipulation of small objects can be achieved. Moreover, the compatibility of fluidic and photonic devices makes optical and photonic devices useful in optofluidics.

In addition, I have discussed optical tweezers, which apply optical gradient force and radiation pressure to trap sub-wavelength scale objects. As compared to conventional optical tweezers, plasmon-based optical tweezers demonstrate significant advantages in near-field particle manipulation at the deep sub-wavelength scales. Via structured metallic film, e.g. disks, antennas, and apertures, plasmonic optical tweezers can generate an enhanced evanescent field for trapping, routing, and sorting. In contrast, far-field manipulation is possible to achieve multiple foci in free space, which exhibits a prospect for the development of far-field manipulation, i.e., holographic imaging. Furthermore, I have introduced metamaterial surface. Metalenses with a high numerical aperture can establish a strong gradient force at the focus for trapping. The focus can be modulated using different methods (e.g. coherent control). Multifunctional metasurface is discussed which can impose wavefront modulation on the propagation wave to achieve efficient focusing and complex tasks.

Chapter 3

Nanoparticle trapping and routing on plasmonic nanorails in a microfluidic channel

Plasmonic nanostructures hold great promise for enabling advanced optical manipulation of nanoparticles in microfluidic channels, resulting from the generation of strong and controllable light focal points at the nanoscale. However, a primary challenge in the current integration of plasmonics and microfluidics is transporting trapped nanoparticles along designated routes. By using numerical simulation, a plasmonic nanoparticle router demonstrates its capability of trapping and routing a nanoparticle in a microfluidic channel with a continuous fluidic flow. The nanoparticle router contains a series of gold nanostrips on top of a continuous gold film. The nanostrips support both localized and propagating surface plasmons under light illumination, which underpins the trapping and routing functionalities. The nanoparticle guiding at a Y-branch junction is enabled by a small change of 50 nm in the wavelength of incident light. Most results in this chapter are presented in the journal publication: S. Yin, F. He, N. G. Green, and X. Fang, "Nanoparticle trapping and routing on plasmonic nanorails in a microfluidic channel," Opt Express 28 (2), 1357-1368 (2020).

3.1 Introduction to Chapter 3

Introducing nanophotonic components into microfluidic channels to achieve novel nanoparticle manipulation is an active, current research area [165]. As compared to traditional optical tweezers, which rely on the use of microscope objectives with a high numerical aperture, nanophotonics-based approaches have many advantages for optofluidic applications in aspects including device miniaturization and detection throughout [213]. These benefits result from the near-field focusing made possible by utilizing nanophotonic components, which

is most often accomplished without concentrating the incident light beam. Lens-free near-field focusing overcomes the diffraction limit imposed on far-field focusing, which establishes nanoscale focal spots of enhanced field intensity. This characteristic is advantageous for various applications, in particular biological applications requiring effective nanoparticle trapping at relatively low laser intensity [214, 215].

Recently, near-field particle manipulation has been demonstrated in a wide range of various nanophotonic devices that generate evanescent optical fields, which include waveguides [216–218], microring resonators [219], whispering gallery mode resonators [220], photonic crystals [221–223], all-dielectric nanoantennas [224] and plasmonic resonators [225–227]. The employment of surface plasmons, a hybridized oscillation of free electrons and light at the surface of a metal, has recently received considerable interest from the research community. Surface plasmons, including localized surface plasmons, have two key characteristics: strong light focusing capability (light focusing down to volumes of less than 1 nm^3 has been confirmed with low loss [228]) and their precise tunability, which can be achieved by manipulating various properties of the incident light (e.g. the wavelength, the polarization, the orbital angular momentum [229], and the relative phase and polarization of multiple coherent beams [230, 231]). While surface plasmons have been widely investigated for application outside of optofluidics, exploiting them for microfluidics is relatively recent, which has led to the emergence of a new research field, so-called plasmonfluidics [225–227].

Plasmonic trapping, i.e. trapping of deep sub-wavelength particles in plasmonic near-field excited by incident light, has been demonstrated using well-designed metallic nanostructures [131, 134, 152, 232–235]. A key remaining challenge in plasmonics-microfluidics integration is to transport a trapped nanoparticle in a fluidic flow-through microfluidic channel. A number of different approaches have been explored to achieve this higher level of plasmonic nanoparticle manipulation, which rely on continuously changing the location of plasmon-based focal spots by adjusting the properties (e.g. the wavelength, the polarization, and the wavefront) of the incident light [161, 162, 236–240]. As the particle traces the trajectory of the activated focal spots, it moves in the microchannel while remaining trapped and under a controlled situation. Such plasmonic optical tweezers depend only on the plasmonic-induced optical force (i.e. gradient force) for the nanoparticle transport, which often leads to limited efficiency in nanoparticle delivery. Combining the plasmonic force with other forces can increase the efficiency, however requires precise control over multiple fields (e.g. electromagnetic, electric and thermal fields) simultaneously at the nanoscale [241, 242].

This chapter presents the concept that nanoparticle transport can be achieved by employing the plasmonic force to guide and route nanoparticles along the predefined paths in a continuous-flow microchannel. The method preserves the simplicity of all-optical nanoparticle trapping and manipulation while motivating nanoparticle delivery's effectiveness by using fluidic flow. Numerical simulation is used to exhibit a structure through which a nanoparticle can travel along either one of two predefined paths, with the path selection enabled by a

small shift of 50 nm in the incident wavelength. As most lab-on-a-chip devices require continuous flow microchannels, this plasmon-guided nanoparticle transport mechanism has the potential for various applications involving bio-sensing, nanoparticle drug delivery, single-molecule biophysics, and nano-assembly [1, 20, 134, 135].

3.2 Structure and functionality of the plasmonic nanoparticle router

A perspective view of the plasmonic nanoparticle router is shown in **Fig. 3.1**. The plasmonic router comprises several sets of gold nanorails and gratings on a gold film at the bottom of a microfluidic channel. Each set of nanorails is a pair of identical strips separated by a constant gap, while each set of grating has seven similar, evenly spaced strips. Except for the Y-branch junction, where the Entrance Route splits into Route 1 and Route 2, all the strips are along the y direction. At the junction, both gratings follow the associated route in their planar curvature, keeping the grating-rail distance constant. This distance is the only difference between the dimensions of the two routes, and it is a critical parameter in producing controllable nanoparticle routing.

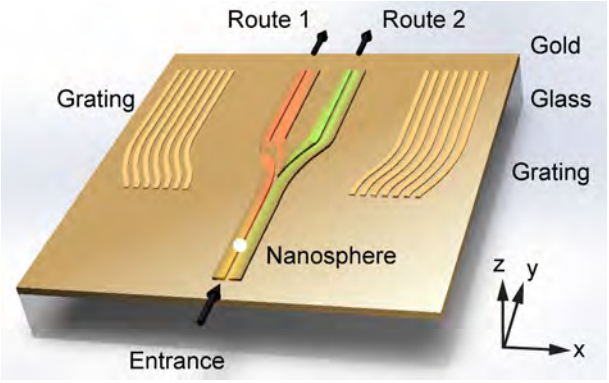

Fig. 3.1. Schematic diagram of the plasmonic nanoparticle router. The router is a nanostructured, continuous gold thin film on top of a glass substrate. The entrance to the router consists of a pair of nanorails, which then diverges into two routes (Route 1 and Route 2) via a Y-branch junction. Two gratings, each consisting of seven nanostrips, are aligned with the outer boundaries of Route 1 and Route 2. The whole router is at the bottom of a microfluidic channel, and it is illuminated by a collimated beam of light at normal incidence from above (along the -z direction). A nanoparticle (the white sphere), which moves relatively slowly along the y direction with the fluidic above the router, will be confined to the vicinity of the nanorails due to the plasmonic near-field (highlighted in red and green). The interaction is that the particle will follow either Route 1 or Route 2, depending on the incident wavelength.

It is necessary to have a functional, multiplexing router for continuous-flow microchannels in order to confine a nanoparticle in a preset route, with the nanoparticle being forced forward by the flow of the liquid that is around it, while also providing for a selection from several routes. The wavelength-controlled router that is provided here satisfies both of these conditions. The routes are realized using the plasmonic focusing described in this chapter, and a slight shift in wavelength is utilized to choose the route. The plasmonic system is optimized to operate at two near-infrared wavelengths (i.e. 1224 nm and 1274 nm), selected based on the

availability of laser sources for future research [243] and the low absorption of water used as the carrier fluid. In the absence of illumination, the nanoparticle in the microfluidic channel follows the laminar flow rather than the two output routes. It will pass over the plasmonic sorter as if it was not there. With the incident light switched on, the trapped particle can be guided and manipulated along a designed trajectory (i.e., from the Entrance to Route 1, or from the Entrance to Route 2).

In order to determine the performance of the plasmonic router consisting of novel metallic structures for dielectric nanoparticle trapping and routing, the electromagnetic properties, i.e. plasmon-induced near-field enhancement was simulated by using a 3D-finite-element solver (COMSOL Multiphysics). The permittivity of gold [244] is $-69.9 + 5.9i$ and $-76.4 + 6.2i$ at 1224 nm and 1274 nm, respectively. The liquid defined in the microfluidic channel is pure water with a refractive index of 1.33 at both wavelengths. The whole plasmonic structures are established on a silicon dioxide substrate. As the incident light cannot penetrate the gold film, the optical properties of the substrate do not affect the numerical simulation. The planar gold film above the glass substrate has a thickness of 300 nm as a buffer layer that separates the structured plasmonic geometries and the substrate. Moreover, the relatively thick gold film enables quick heat dissipation, suppressing thermal convection influences for trapping. This is due to the high thermal conductivity of gold (317 $\mathrm{W/K \cdot m}$) as compared to silicon dioxide ($\sim 1\ \mathrm{W/K \cdot m}$) [132]. The nanostructures can also be fabricated on silicon substrates. However, gold does not adhere very well to silicon. Therefore, an adhesion layer [245] (e.g. chromium or titanium) is required as an adhesive layer between the silicon and gold thin layers.

The performance of the plasmonic router is evaluated using polycarbonate (PC) nano-scale spheres with a diameter of 220 nm and a refractive index of 1.58 under both incident wavelengths. The incident light is defined as a plane wave illuminating the router from above at a normal incident, with both linear and circular polarization investigated. The exhibited near-field electric field distributions in Sections 3.3 - 3.5 are simulated without the nanospheres. This is because the particle-water interface will affect the distribution of the near field, complicating the characterization of near-field enhancement. After performing the enhancement analysis without any particle, the nanosphere is put back into the microchannel. Optical force is then calculated by integrating the Maxwell stress tensor (MST) at the surface of the nanosphere. The electric field distributions surrounding the nanospheres are obtained and shown in Appendix A. At each position, the trapping potential is the line integral of the calculated optical force along a straight line, starting at a point where there is no near-field enhancement that can be seen. In the numerical simulation, the beginning positions correspond to the center of the nanosphere being 300 nm above the top of the nanorails. This is due to the fact that the observable near-field enhancement (i.e. the evanescent field) is mostly confined within 200 nm above the top of nanorails. The cross sections of the Entrance route, Route 1 and Route 2 are simulated in a two-dimensional model, perpendicular to the direction of fluidic flow (y direction as shown in **Fig. 3.1**) for a better analysis of the routing system far from the Y-branched

junction. Subsequently, the full three-dimensional Y-branched junction is simulated for visualizing wavelength dependence and the detailed analysis of the performance of the router. The numerical calculation can provide a rough estimate of the maximum velocity of the nanoparticles allowed for maintaining effective guiding, and this is discussed in detail in Section 3.5.

3.3 Nanoparticle trapping at the Entrance Route

Fig. 3.2 shows, the geometric design of the Entrance route and its optical response under the two wavelengths are exhibit, respectively. **Fig. 3.2 a** illustrates the cross sectional structure of the Entrance nanorails in the xz plane, which consist of a pair of identical gold nanostrips with dimensions of 440 nm in width, 110 nm in height, and separated by a 150 nm gap. The whole gold structure is on a 300-nm-thick gold thin film. **Figs. 3.2 b** and **c** demonstrate the numerically simulated near-field distribution of electric field intensity with the incident wavelength at 1224 nm and 1274 nm, respectively. For the Entrance route, only x-polarized incident light is considered, since y-polarized incident light can not induce any visualized near-field enhancement at the two wavelengths. It is due to the fact that, the nanorails at the Entrance being much longer than the incident wavelengths in the y direction and cannot excite localized surface plasmon resonances to generate enhanced near-field. Both figures show considerable field enhancement, known as hot spots, between the two nanorails that resemble a pair of plasmonic tweezers. A dielectric nanospheres suspended in aqueous solution above the nanorails will be trapped between the two nanorails. The similarity between the two figures suggests that the trapping performance at these two wavelengths is comparable.

Simultaneously, **Figs. 3.2 d** and **e** show the optical potential energy and the optical force (F_x) on a PC nanosphere with a diameter of 220 nm along the x axis following the dashed line from one side of the nanorails, across the optical trapping region, to the other side. The center of the gap between the two nanorails ($x = 0$) is the stable position for both incident wavelengths, in which the potential energy is lowest, and no horizontal force exists ($F_x = 0$) at this position. The depth of the trap, as calculated by the difference between the lowest position at $x = 0$ and the highest position $x = \pm 325$ nm, is $6.51\,\mathrm{k_B \cdot T/(mW \cdot \mu m^{-2})}$ and $7.66\,\mathrm{k_B \cdot T/(mW \cdot \mu m^{-2})}$) for 1224 nm and 1274 nm illumination, respectively. Here, k_B is the Boltzmann constant, and T is 297.15 K. Besides, **Fig. 3.2 d** exhibits two shallow potential wells at $x \approx \pm 600$ nm, which correspond to the near-field enhancement at the outer edges of the nanorails in **Figs. 3.2 b** and **c**. Both the potential and the force curves (**Figs. 3.2 d** and **e**, as well as in several other following figures) show small fluctuations, which can be attributed to numerical error. In this research, the trapped nanosphere is assumed to maintain at a height of 10 nm above the nanorails top, based on several previous research [118, 161]. It is a reasonable value, considering that forces such as: heat convection, wall-induced force, and light-induced gradient force, can all affect the particle's position.

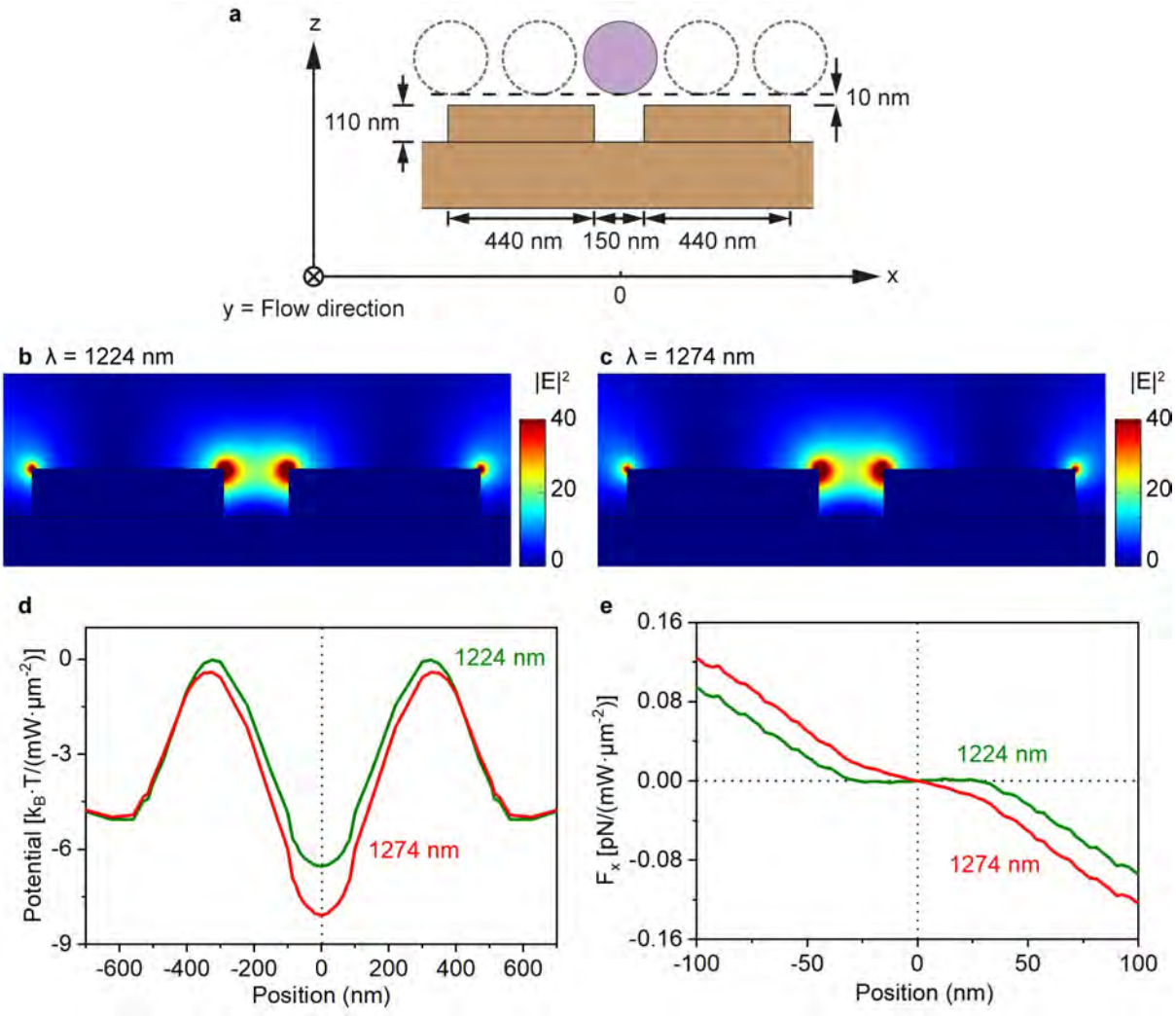

Fig. 3.2. Nanoparticle trapping characteristics of the entrance nanorails. (a) Schematic of the cross section of the Entrance Route, consisting of two gold nanorails on a thick gold file and a nanoparticle suspended in water above the nanorails. The incident light is polarized along the x axis, i.e. orthogonal to the nanorails. The bottom of the nanoparticles is 10 nm above the top of the nanorails, as indicated by the dashed circles. The solid, purple circle indicates the stable position. (b) An enhancement factor of the electric field density at 1224 nm as normalized against the incident field, with the upper limit of the color scale set at 40 for visualization. (c) Corresponding distribution at 1274 nm using the same color scale. (d) Dependence of trapping potential on the x position of the nanoparticle under the illumination of light at 1224 nm (green line) or 1274 nm (red line). (e) Corresponding optical force along the x axis, F_x, at these two wavelengths.

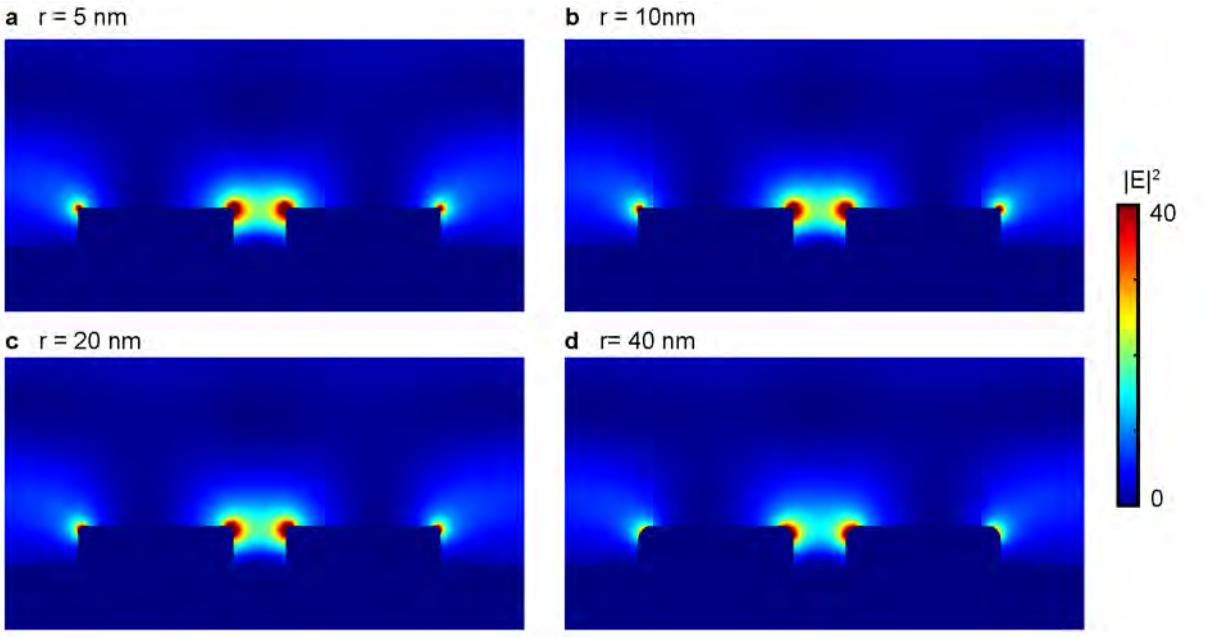

Fig. 3.3. Field enhancement for nanorails with rounded edge. Enhancement factors of the electric field density normalized against the incident field, with (a) 5 nm, (b) 10 nm, (c) 20 nm, and 40 nm radius of rounded edges, respectively. The color scale set at 40 for visualization. The wavelength is 1224 nm.

It is worth noting that an ideal sharp edge is impossible to achieve in standard nanofabrication (e.g. evaporating and lift-off). In **Fig. 3.3**, two nanorails with rounded edges demonstrate the influence of rounded edge, where the top rectangular edges are arcs of radius r. Under the illumination of 1224 nm, there is no significant difference in the enhanced near-field distribution as compared with the field shown in **Fig. 3.2 b**, when the arcs' radii are 5, 10, and 20 nm. When the radius is increased to 40 nm, the near-field distribution changes noticeably, but it still meets the design requirement (i.e. a symmetric localized field enhancement appears in the middle of two nanorails). Nevertheless, although the sharpness of the edge has relatively small influence on the near-field distribution, it can affect the near-field enhancement magnitude of the nanorails, resulting in a lower device efficiency in experiment.

3.4 Nanoparticle trapping at Route 1 and Route 2

The previous section has confirmed that this design can trap nanoparticles between the two nanorails. The next step is to select one of the two paths for the nanoparticles, while maintaining a stable trap. The simulation result in **Fig. 3.4** demonstrates that of similarity between the two wavelengths of interest depicted in **Fig. 3.2** changes, when a grating is established on the side of the nanorails. The grating structure is comprised of seven gold nanostrips with a periodicity, a width, and a height of 400 nm, 200 nm, and 70 nm, respectively, while the grating-rail distance is a free parameter. Since plasmonic trapping significantly relies on near-field enhancement, the distribution of the trapping potential power corresponds to the distribution

of the electric field, and this effect can be analyzed by evaluating the electric field at the center point (see **Fig. 3.4 a**) between the two nanorails, as shown in **Fig. 3.4 b**. At both wavelengths, the enhancement factor oscillates with the grating-rail distance. Here, the enhancement factor is calculated by comparing the electric field at the test point in **Fig. 3.4**, against the field at the same point with the grating removed. This oscillation is caused by the interference between the localized surface plasmons generated by the nanorails and the propagating surface plasmon polaritons (SPPs) created by the grating. The grating acts as a plasmonic antenna, which can convert incident light into surface plasmons that propagate over the grating-rail distance to the central test point. The interference at the test point changes by adjusting the grating-rail distance. The interference between localized and propagating surface plasmons has been investigated in the context of extraordinary optical transmission, primarily in a slit-groove geometry [153]. This work provides a similar rail-grating setup intended to utilize the near-field enhancement. Following previous research [153, 154], the height of the grating is adjusted to optimize device performance. To trap particles, the grating height should be lower than the height of the nanorails to ensure that the maximum field enhancement appears at the nanorails.

The contrast between the two working wavelengths is critical to the functionality of the plasmonic router. Although both wavelengths exhibit an oscillatory dependency on the grating-rail distance, the oscillation is distinct in both phase and amplitude. This is due to the fact that there are several sources contributing to the oscillation, involving the dispersion of both types of surface plasmons. **Fig. 3.4 b** shows the ratio of the field enhancement that is used to emphasize the contrast between these two wavelengths. Over the investigated range of grating-rail distance, the ratio oscillates between 1.47 and 0.70, which underpins the routing functionality.

Due to the influence of the additional grating, Route 1 and Route 2 can operate at different wavelengths. Route 1 is optimized to well-operate at 1274 nm wavelength. The grating-rail distance is consequently chosen to be 2736 nm (see **Fig. 3.5 a**). **Figs. 3.5 b-c** demonstrates that the field enhancement is more significant at 1274 nm than at 1224 nm across the whole gap between the two nanorails, which is in accordance with those results based on an analysis of the electric field at the single test point. The potential energy in **Fig. 3.5 f** shows that the bottom of the potential well at 1274 nm is deeper than twice of that at 1224 nm. With a comparison to the results on the nanorails without the flanked grating, the trapping depth decreases by $\approx 35\%$ to 4.25 $k_B \cdot T/(mW \cdot \mu m^{-2})$ at 1224 nm and increases by $\sim 22\%$ to 9.35 $k_B \cdot T/(mW \cdot \mu m^{-2})$ at 1274 nm. This result correlates with the constructive and destructive interference shown in **Fig. 3.4**. In addition, as a result of the grating structure, the stable point $F_x = 0$, which was previously located in the middle of the two nanorails, shifts to the side of the grating with a deviation of approximately 50 nm from the central points ($x = 0$) (see **Fig. 3.5 g**).

By exploiting a variable grating-rail distance, the trapping strength of nanoparticles between the two wavelengths can be reversed. In **Fig. 3.6**, the grating-rail distance is changed to 2468 nm. This is a condition for Route 2 under the 1224 nm illumination. As shown in **Fig. 3.4**, this value of grating-rail distance generates constructive and destructive interference

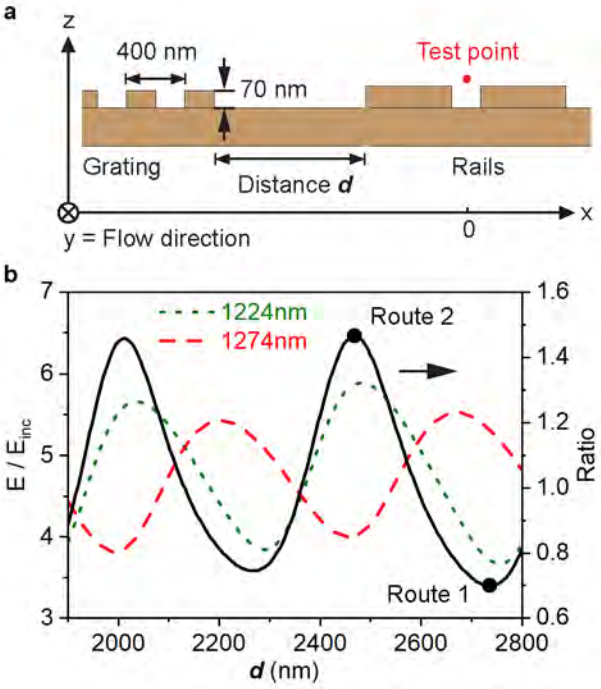

Fig. 3.4. Route 1 **and Route** 2 **adopt a side grating to affect the nanoparticle trapping.** (a) Schematic diagram of the pair of nanorails and the side gratings. The grating consists of seven nanostrips that are slightly smaller in height than the rails. (b) At both wavelengths of 1224 nm (green dotted line) and 1274 nm (red dash line), the electric field at the test point (in the middle between the two rails and 10 nm above their tops) oscillates with d, the distance between the nanorail and the gratings. The field is normalized against the incident light, which is x-polarized. The ratio of the normalized electric field at these two wavelengths is drawn as the black line, on which the values of the distance d in Routes 1 and 2 are specified using the two black dots.

at the center of the two nanorails at wavelengths of 1224 nm and 1274 nm, respectively. The constructive interference at 1224 nm leads to a significant local field enhancement between the two nanorails and an increased potential energy of 10.57 $k_B \cdot T/(mW \cdot \mu m^{-2})$, as shown in **Figs. 3.6 b**, **d**, and **f**. In contrast, the near-field enhancement decrease considerably under the illumination of 1274 nm (see **Figs. 3.6 c** and **e**). The trapping depth is 5.55 $k_B \cdot T/(mW \cdot \mu m^{-2})$, roughly half of the depth at the condition of 1224 nm. Furthermore, due to the breaking of mirror symmetry, the stable position deviates to $x \approx 60$ nm from the center of the two nanorails, as shown in **Fig. 3.6 g**. The entire nanorail with the flanked grating as shown in **Figs. 3.7** covers an area of 70 μm^2. Therefore, the laser power required to achieve the above trapping potential is 70 mW.

It is worth to pointing out that, this work utilizes a dielectric, non-resonant particle to numerically demonstrate trapping. As the particle has little influence on the plasmonic field shown in **Figs. 3.2**, **3.5** and **3.6**, the optical force can be directly predicted from the plasmonic field. To support this view, the nanosphere's electric field distribution is depicted in Appendix A.

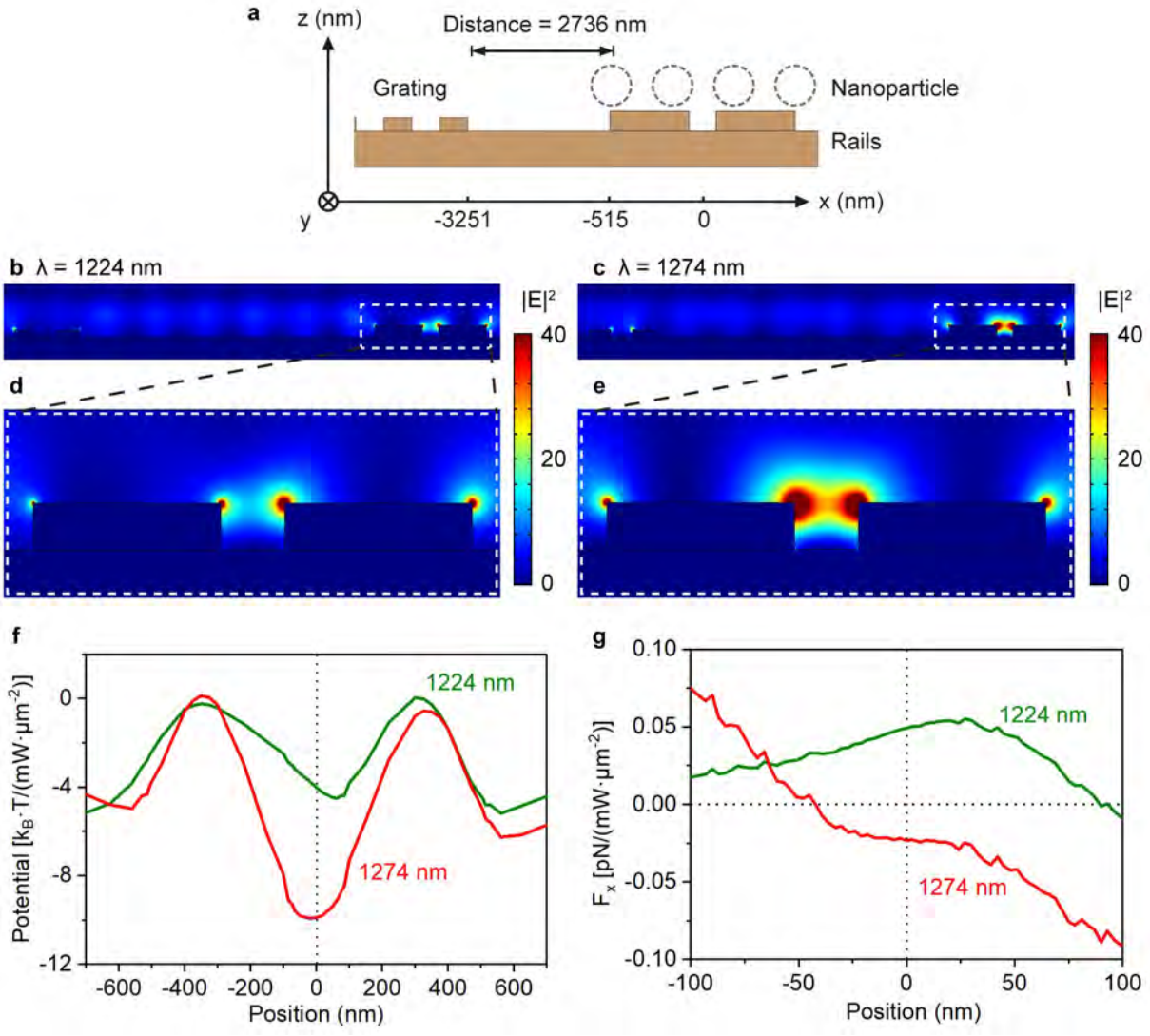

Fig. 3.5. Schematic diagram and trapping characteristics of Route 1. (a) Schematic diagram of the nanostructure. The rail-to-grating distance d is 2736 nm. (b) An enhancement factor of the electric field density at 1224 nm as normalized against the incident field. The upper limit of the color scale is set to 40 for visualization. The incident light is polarized along the x axis. (c) Corresponding distributions at 1274 nm. (d) A zoom-in view of panel b. (e) A zoom-in view of panel c. (f) Dependence of trapping potential energy on the central position of the nanoparticle. (g) Corresponding force F_x.

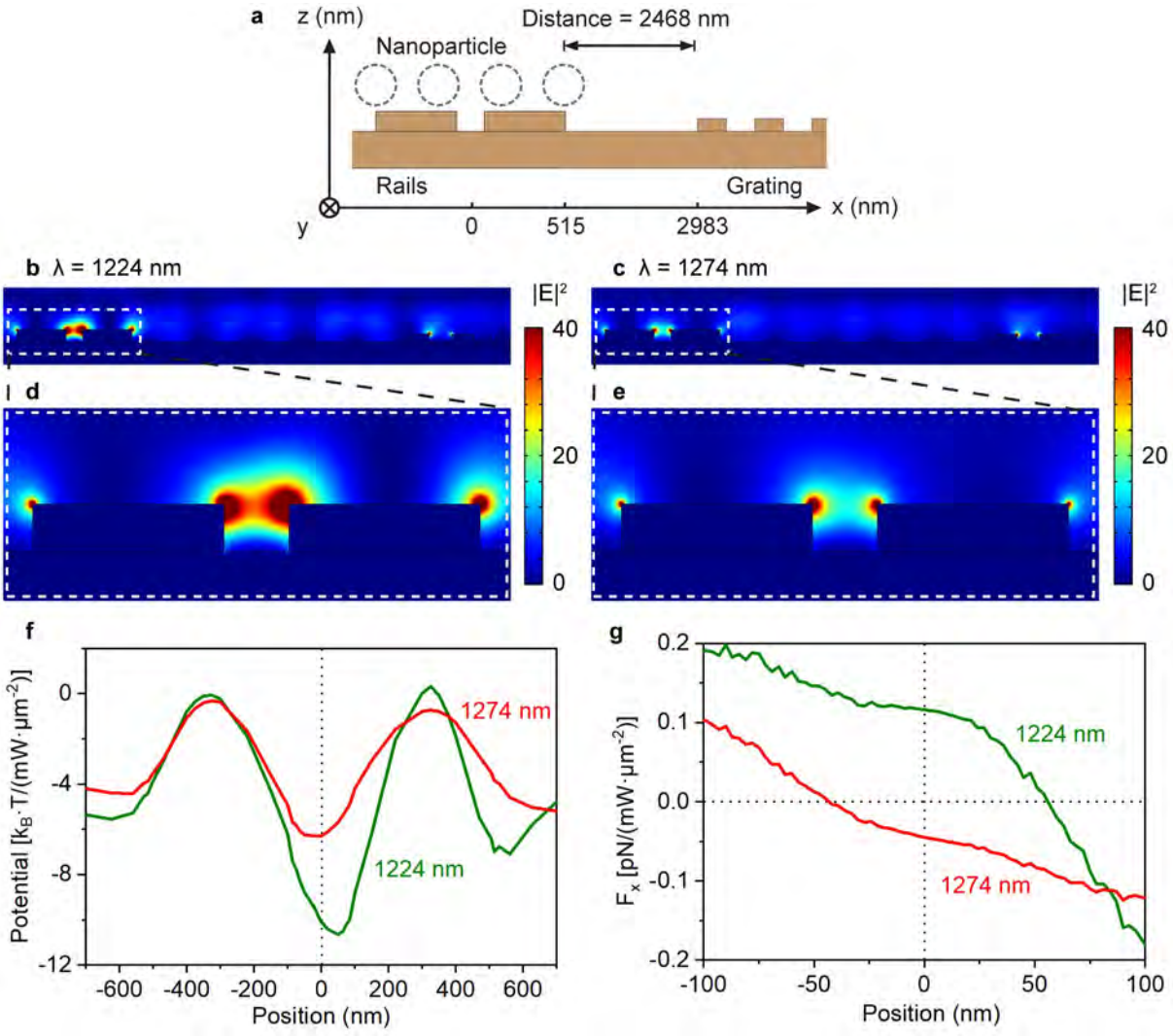

Fig. 3.6. Schematic diagram and trapping characteristics of Route 2. The route has a rail-grating distance d of 2468 nm. The panels (b–g) are plotted following the same specifications as **Fig. 3.5**.

3.5 Nanoparticle routing at the Y-branch junction

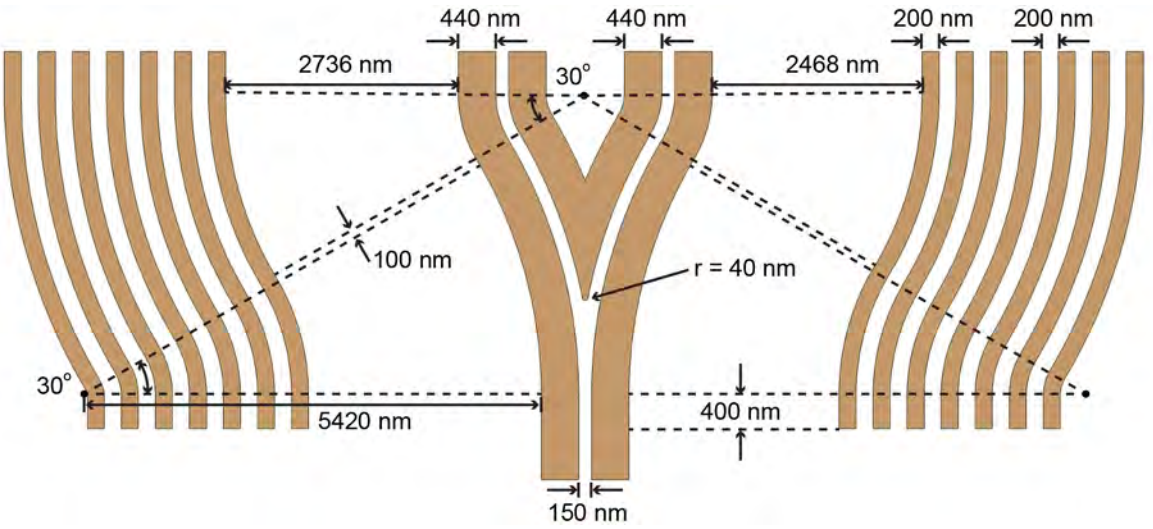

Fig. 3.7. Planar dimensions of the gold nanostrips at the Y-branch junction. The gold strips are on top of a plain gold thin film and consist of both curved and straight segments. The whole set of nanorails, including the Entrance Route, Route 1, and Route 2, possess mirror symmetry concerning its central axis. The tip of the Y-junction has a radius of 40 nm. The two side gratings have a route-dependent rail-grating distance, which is 2736 nm for Route 1 and 2468 nm for Route 2.

In Sections 3.3 and 3.4, all the plasmonic nanorails and the grating are treated as infinitely long in the two-dimensional simulation, The wavelength sensitivity in the optical force can approximate locations on the plasmonic router that are not close to the Y-junction. It is necessary to provide similar wavelength sensitivity at the Y-junction, so that the nanoparticle can be guided in the proper direction, that is, Route 1 at 1274 nm and Route 2 at 1224 nm. In order to achieve this functionality, it is possible to combine the nanorails and the grating by utilizing flanked grating on both sides of the nanorails, as shown in **Fig. 3.7**. As compared to straight segments (i.e. Entrance, Route 1 and Route 2), the Y-junction has a more complex geometry. Two gratings start at the line of -1.5 μm from the tip of the Y-junction as $(x, y) = (0, 0)$, which overlaps with the bottom boundary of the **Figs. 3.8 a** and **c**. More details of the whole plasmonic router design are exhibited in **Fig. 3.7**. Considering nanofabrication capabilities of future experiments, the tip of the Y-junction is set to be a 40-nm-radius semi-circle. In this Y-junction design, the deflection angle of the junction is designed to be 30°. The polarization of the incident light is changed from linear polarization for the straight nanostrips to circular polarization, owing to the planar curvature of the nanorails and gratings at the Y-junction.

The evanescent field distribution of the electric field intensity at the xy-plane 10 nm above the top of the nanorails, with the incident light at 1274 nm, is shown in **Fig. 3.8 a**. Similar to the simulation results shown in **Figs. 3.2**, **3.5**, and **3.6** for straight nanorails, strong localized surface plasmonic resonance (LSPR) is observed at the edges of the nanorails, especially at the inner edges of the rails. The curve of strong field enhancement traces the curvature of the Y-junction. Simultaneously, differences in the field distribution between the two arms of the

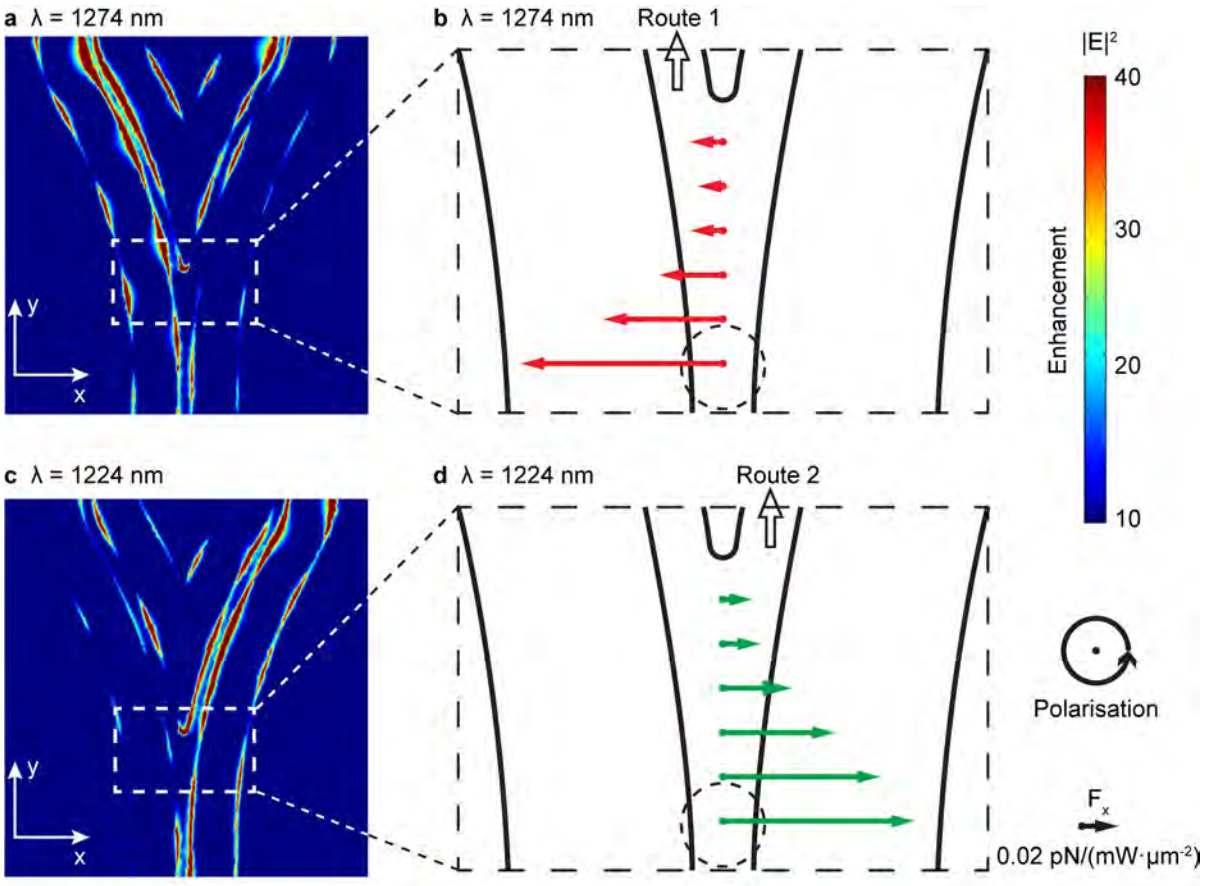

Fig. 3.8. Routing of the nanoparticle at the Y-branch junction. (a) Enhancement factor of electric field density at the xy plane is 10 nm above the top surface of the nanorails. The electric field is normalized against the field of incident light. The upper and lower limit of the color scale is set at 40 and 10, respectively, for visualization. The incident light is circularly polarized, and the wavelength $\lambda = 1274$ nm. The start line of the two side gratings overlaps with the bottom edge of the figure. (b) Optical force along the x axis, F_x, with the nanoparticle (the black circle) at six evenly spaced, representative locations along the center of the Y-branch junction. The scale is 0.02 $\mathrm{pN}/(\mathrm{mW}\cdot\mu\mathrm{m}^{-2})$. (c, d) Corresponding field distribution and force F_x at 1224 nm, The largest force at the six simulated locations is 0.11 $\mathrm{pN}/(\mathrm{mW}\cdot\mu\mathrm{m}^{-2})$ at both wavelengths.

Y-junction can be observed as well. The left arm is brighter than the right arm under the 1274 nm illumination. Strong contrast can be observed near the tip of the Y-junction, where the end of the Entrance route and divergence of the two arms begin. This contrast between the two arms indicates that the left arm traps the nanoparticle at 1274 nm more effectively. The same tendency can be seen in the force maps (see **Fig. 3.8 b**). A trapped nanosphere can travel along the center of the Entrance route and bias toward the left side when close to the junction, until being guided to the left arm (i.e. Route 1) by the asymmetric plasmonic near-field. In contrast, **Figs. 3.8 b** and **d** show the other condition, that is, the near-field enhancement on the right arm (i.e. Route 2) of the Y-junction is stronger than the left arm under the illumination at 1224 nm wavelength. A nanoparticle allocated at the same location can experience an optical force that guides it to the right arm.

The modification to circular polarization was made to emphasize the impact of surface plasmons on nanoparticle capture. In fact, neither localized nor propagating surface plasmons can be excited by a y-polarized incoming wave at these wavelengths for straight nanostrips. The trapping potential and force, which have the normalized units of $k_BT/(mW \cdot \mu m^{-2})$ and $pN/(mW \cdot \mu m^{-2})$, fall by 50% when the incident light polarization is adjusted to circulation polarization. As stable trapping needs a minimum potential depth (the recommendation value ranges [120, 146] between 1 k_BT and 10 k_BT, depending on the time-frame of the trapping), circularly polarized light is less power efficient for straight nanorails. It is worth noting, however that the contrast in the trapping efficiency at the two wavelengths does not change and the whole nanoparticle pathway is still functional under the illumination of circularly polarized light. In Appendix A, I list the key equations used to calculate the Maxwell stress tensor, based on which the optical force and potential are derived.

To ensure that a particle will be correctly guided to the desired outlet, the speed of the particle has to be below a threshold value. This maximum speed can be numerically calculated by using the Stokes' law as shown in Eq. 3.1

$$F_d = 6\pi\mu_{water} r v \tag{3.1}$$

where F_d is the fractional force (i.e. the force of viscosity on a nanoparticle moving through a viscous fluid), μ is the dynamic viscosity of water (i.e. $\sim 1\ mPa \cdot s$), r is the radius of the nanoparticle (i.e. 110 nm), and v is the flow velocity relative to the nanoparticle.

By substituting the force on the nanoparticle when it enters the Y-junction (i.e. the lowest of the six position simulated in **Fig. 3.8**) into Eq. 3.1, the terminal velocity is calculated to be 53.1 $\mu m/s$ under an illumination with a unit power of 1 $mW/\mu m^2$. In this case, the viscosity force is the same as the optical gradient force, which is 0.11 pN. The nanoparticle weighs 6.72×10^{-21} kg, giving a gravity force of 6.59×10^{-20} N, which is much smaller than the optical force. The velocity that the nanoparticle can reach under the optical force as calculated by using Newton's second law ($v = 1.5$ m/s) is far greater than the terminal velocity calculated by using Eq. 3.1. Therefore, only the terminal velocity is considered.

Assuming that when a nanoparticle enters any branch, it is located in the middle of the two nanostrips, which is considered to be effectively guided. That is, for a particle to move 900 nm in the y direction (i.e. distance of the Entrance to the tip of Y-junction), it has to move 75 nm in the x direction (i.e. semi-width of the gap between two nanorails). The time it takes to move along the x axis is 1.41 ms, from which the maximum velocity in the y direction can be calculated as 0.64 mm/s.

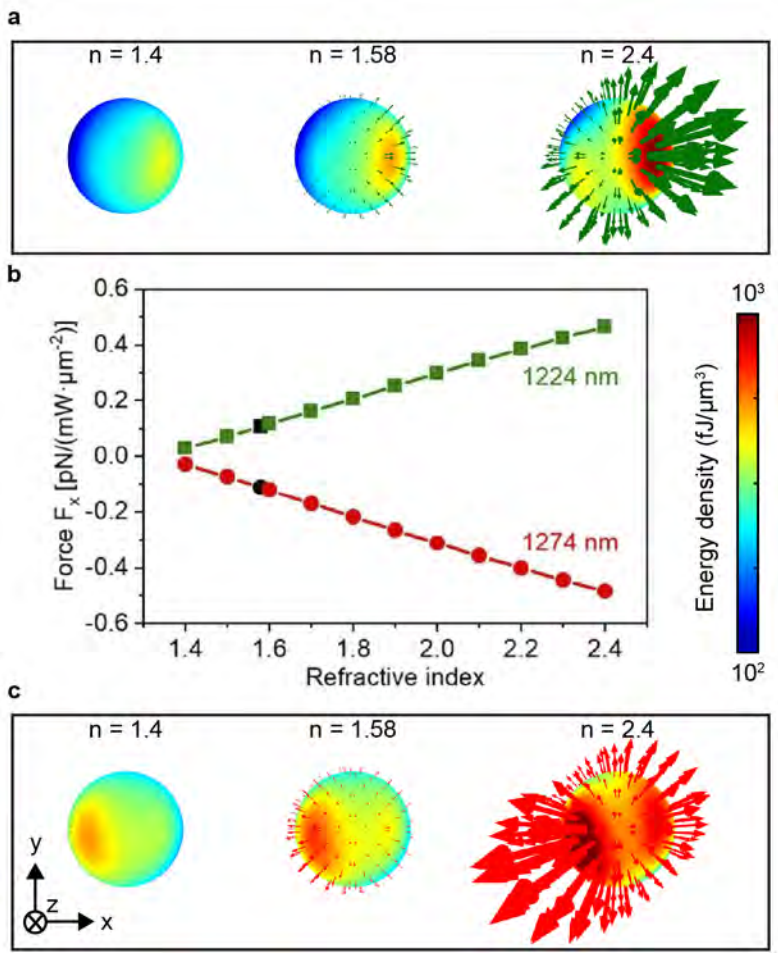

Fig. 3.9. Dependence of the optical force F_x on the refractive index of the nanoparticle. (b) The nanoparticle is at the lowest of the six positions simulated in **Fig. 3.8**. The sign of the force indicates the direction, and a positive force directs the nanoparticle along the $+x$ direction (i.e. to Route 2). The two black symbols correspond to a refractive index of 1.58 which is used in the previous sections. The (a) top and (c) bottom panels demonstrate the time-average energy density on the bottom surface of the nanoparticle with a refractive index at 1.4, 1.58, and 2.4, (a) is for 1224 nm and (b) is for 1274 nm. The red and green arrows represent the Maxwell stress tensor.

3.6 The dependence on the refractive index of the optical force

Finally, the light force on a nanosphere with different refractive indices at the Y-junction is analyzed. The simulation condition is the same as in **Fig. 3.8**. The energy density on the outer surface of the nanosphere is calculated using the near fields in **Figs. 3.8 a** and **3.8 c**, respectively. To analyze the influence of the refractive index contrast, nanospheres with a refractive index (n_{sphere}) ranging from 1.4 to 2.4 are used. Their refractive index is always greater than that of the media ($n_{medium} = 1.33$). At both wavelengths, the force scales linearly with the refractive index contrast between the nanoparticle and the liquid, and the sensitivity is $\sim 0.45\,\mathrm{pN}/(\mathrm{mW}\cdot\mu\mathrm{m}^{-2})$ per unit change of the refractive index. As the contrast between n_{sphere} and n_{medium} diminishes, so does the optical force exerted on the nanosphere. When the refractive index of

the nanosphere reaches 2.4, the force is about four times of that on the nanosphere simulated in previous sections, which has a refractive index of 1.58. It can be deduced that when the size of the sphere is close to the incident wavelength, a larger refractive index contrast gives a greater trapping stiffness.

3.7 Conclusions to Chapter 3

In conclusion, a plasmonic nanoparticle router/switch activated by the wavelength of incoming light has been analyzed using numerical modeling. The router is comprised of a sequence of gold nanostrips on a thin coating of gold. It can enable trapping, directing, and routing of nanoparticles in a continuous-flow microfluidic channel illuminated by unfocused light at normal incidence. With a 50 nm shift in the input light's wavelength, a nanoparticle may be directed towards either one of the two specific paths. These functions are accomplished by utilizing the interference between localized and propagating surface plasmons produced on gold nanostrips.

The concept is straightforward and has the potential to allow the integration of a cascaded, multi-route nanoparticle transport network with lab-on-a-chip devices. Simply by adjusting the size of the plasmonic nanostructures, it can operate at a variety of wavelengths throughout a large spectrum. Combining plasmonic force with the continuous liquid flow to produce controlled nanoparticle transport is a defining characteristic of the nanoparticle router. Compared to pure plasmonic manipulation, this strategy might increase the efficiency of manipulating nanoparticles. In addition, it meets increasing needs in advanced plasmonic nanoparticle manipulation that moves from controlling the location to controlling the motion of a nanoparticle. With the capacity to both trap and transport nanoparticles, this novel control approach opens up new possibilities for plasmonic nanoparticle manipulation, which may be beneficial for a variety of on-chip optofluidic applications.

Chapter 4

Coherently tunable metalens tweezers for optofluidic particle routing

In the previous chapter, I have numerical demonstrated plasmonic trapping and guiding of a nano-scale dielectric particle on a structured plasmonic surface, which is a *near-field* phenomenon. Introducing metalens in microfluidics research provides the new capability of using nanophotonic devices for *far-field* optical manipulation. In this chapter, I demonstrate, via numerical simulation, the first tunable metalens-based optical tweezers that function under dual-beam illumination. The structured surface is a dielectric metasurface comprising Si nanopillars on a PDMS-covered glass substrate. The phase profile of the metalens can be modulated by controlling the relative strength and phase of two coherent incident light beams. As a result, the microchannel is sensitive to changes in light illumination conditions. This produces a controllable and reconfigurable path for particle transport. Particle routing in a Y-branch junction, for both nano- and micro-particles, is evaluated as an example functionality for the tunable metalens tweezers. This chapter shows that tunable far-field particle manipulation can be achieved by utilizing near-field nano-engineering and coherent control, opening a new approach for the integration of nanophotonics and microfluidics. Most results in this chapter are presented in the journal publication: S. Yin, F. He, W. Kubo, Q. Wang, J. Frame, N. G. Green, and X. Fang, "Coherently tuneable metalens tweezers for optofluidic particle routing," Opt Express 28 (26), 38949-38959 (2020).

4.1 Introduction to Chapter 4

Nanophotonic devices provide an unprecedented level of control over light waves via engineering light-matter interactions at the nanoscale. The integration of such nanophotonic devices with microfluidic systems enables advanced particle manipulation beyond the scope of conventional optical tweezers for trapping, guiding, rotating, and propelling [165, 213]. This promise has motivated researchers to investigate a wide variety of various nanophotonic

devices involving waveguides [246], microring [247], whispering gallery mode resonators [220, 248], photonic crystals [223], all-dielectric nanoantennas [224], and plasmonic resonators [8, 235]. All of these previous approaches, including the research exhibited in the previous chapter, achieve particle manipulation by exploiting electromagnetic near-field effects. Indeed, nanophotonics in the context of microfluidic applications is widely considered equivalent to "near-field photonics" [214]. By comparison, utilizing metasurface-based optical trapping [110, 194, 249, 250] develops a new research direction, i.e. nanophotonic particle manipulation in optical far-field. A metalens is a proposed-designed metamaterial surface, known as a two-dimensional metamaterial surface, that retailors the output light wavefront for functionality characteristics, mostly focuses light in the far-field like a conventional glass lens, but achieves the required light bending with a subwavelength thickness [251]. Metalens, in the context of optofluidics, creates the nanoscale light shaping capabilities provided by the nanophotonic device while retaining the far-field particle manipulation capabilities of traditional optical tweezers (i.e. optical tweezers that rely on the use of microscope objectives with a high numerical aperture). Besides, all-dielectric metalens is supported by the aqueous properties (higher refractive index than air) to establish a higher numerical aperture. This combination offers unique opportunities for advanced particle manipulation in lab-on-a-chip systems, which mutually improve photonics and microfluidics.

In this chapter, I present the first study of tunable, metalens-based optical tweezers that function under dual-beam illumination. As opposed to the most common configuration of optical tweezers, where a single incident light beam is utilized, dual-beam illumination employs two counter-propagating light beams. The combined optical force provided by two incident beams has been exploited to trap macro-sized particles [252], stretch biological cells [253, 254], translate trapped particles along the beam axis [217, 236, 255], and even control their orientation in an optical trap [256]. Further exploration of the coherence between the two beams has enabled more advanced control, such as particle translation with nanometer accuracy [218] and transferring optical angular momentum to trapped particles [257, 258]. In these previous research, two counter-propagating light beams interact with the trapped particle directly. In contrast, this chapter demonstrates a fundamentally different use of two incident beams, that is, controlling the electromagnetic response of ultra-thin metalens. Two counter-propagating incident light beams with the same wavelength and controlled phase and power contrast, known as coherent control, provide a continuously tunable illumination condition. The coherent interaction between two incident beams and the metalens enables control over the phase profile of the metalens, which results in a steerable focus and consequently translation of trapped particles. The designed metalens shown in this chapter is the first research that introduces coherent control of metasurfaces, a research area that has recently emerged from the development of tunable metamaterials [259], into the realm of microfluidics.

4.2 System design: metalens particle router

As a proof-of-principle demonstration, this chapter analyses a tunable metalens-based particle router that can route fluid-borne particles in a Y-branch junction on demand, a functionality that resembles tunable optical tweezers (see **Fig. 4.1**). The photonic component of the tunable metalens tweezers is an array of silicon nanopillars supported by a glass substrate, as shown in **Figs. 4.1 a** and **b**. The unit cell (i.e. the smallest periodic unit of the metalens) is a row of 25 silicon nanopillars along the x axis (see **Fig. 4.1 c**), and the whole array is created by replicating this unit cell along the y direction at a periodicity of 900 nm. For all the nanopillars, also named meta-atoms, the center-to-center distance is 900 nm, the height of 500 nm, and the cross section is elliptical. The width of the elliptical cross section is defined in the x direction, while the length of the elliptical cross section is defined in the y axis. As shown in **Fig. 4.1 c** and listed in **Table 4.1**, both the shape and dimensions of the cross section vary with the x position of the nanopillar, which is a key design feature of the tunable metalens.

The tunable metalens is covered by a layer of polydimethylsiloxane (PDMS) and located beneath a microfluidic channel as the fluidic component, as shown in **Fig. 4.1 b**. The microchannel has a width of 22.5 μm (in the x direction, matched to that of the metalens) and a base 130 μm above the metalens arrays (in the z direction, defined from the middle height of the nanopillars). Water inside the microchannel moves slowly forward in the $+y$ direction along the entrance section and predictably divided into two branches, with the left and right half of the fluid moving towards Exit 1 and 2, respectively. Dielectric particles of interest, which are injected into the entrance section, pass above the metalens towards the branch point of the Y-junction. The tunable metalens tweezers are designed to optically trap particles of interest in a controlled position in the xz cross sectional plane while leaving them free to move in the y direction. Particles trapped in the left and right half of the entrance section are guided towards Exit 1 and 2, respectively, via a laminar flow enabling the intended functionality of all-optical particle routing.

Laminar flow occurs when the flow rate is extremely low, and the fluid moves in layers without mixing. This phenomenon is quantified by using the ratio of inertial force and viscous force, which is the Reynolds number. When the Reynolds number is low, viscous forces have a large impact on the flow field than inertial force, while the flow velocity disturbances in the flow field will be suppressed owing to viscous force. The fluid flow is thus stable and laminar. For the most common case where the flow is through a pipe, the Reynolds number (Re) is defined as

$$Re = \frac{\rho v D_H}{\mu} \tag{4.1}$$

Here, ρ is the density of the fluid, v is the average speed of the fluid, D_H is the hydraulic diameter of the pipe, and μ is the dynamic viscosity of the fluid. Typically, a Reynolds number $Re < 2100$ corresponds to a laminar flow [260]. In this work, the fluid in the microfluidic

channel is assumed to be laminar flow, which only provides the function of transferring the particle forward in the y direction.

Table 4.1. Cross sectional dimensions of the 25 constituent nanopillars in nanometers. All the nanopillars have an elliptical cross section with the principal axes along x and y.

No.	x axis	y axis	No.	x axis	y axis	No.	x axis	y axis
1	120	250	10,11	170	170	17,18	380	235
2,3	130	350	12	350	253	19,20	380	230
4,5	130	310	13	380	245	21,22	380	220
6,7	140	270	14	380	242	23,24	380	210
8,9	160	190	15,16	380	240	25	400	130

The particle trapping and routing are achieved by employing coherent control in my work. In the context of metamaterial and metasurface modulation, coherent control utilizes two coherent, counter-propagating light beams with controllable relative phase and intensity as illumination [259]. A crucial feature of coherent control is the creation of local electromagnetic field configurations that are inaccessible to conventional plane waves [231]. The most typical configurations are the E-antinode (electric field antinode or magnetic field node) and the B-antinode (electric field node or magnetic field antinode), where the local magnetic and electric field is always zero (i.e. a wave node), respectively. As compared with conventional single-beam illumination with finite magnitudes of electric and magnetic fields, these different field configurations can induce varying electromagnetic responses in a metasurface [198, 230]. In this case, the dual-beam illumination is employed to generate a tunable focus, with the E-antinode focus and the B-antinode focus guiding suspended particles towards different exits.

The light focusing and particle manipulation properties of the tunable metalens are numerical simulated by using a commercial finite element solver (COMSOL Multiphysics). For all illumination conditions utilized in this chapter, the incident waves are linearly polarized along the x axis. The incident wavelength employed in the metalens is 1550 nm, a telecommunications wavelength also frequently used in optofluidic experiments due to the low absorption of water at that wavelength [10]. At that wavelength, the refractive indices of water, glass, PDMS and silicon is set at 1.33 (n_{water}), 1.50 (n_{Glass}), 1.40 (n_{PDMS}), and 3.48 (n_{Si}), respectively [261, 262]. The metalens array is considered to be infinite long in the y direction, approximating an entrance channel far away from the two exit branches. Following my previous research [8, 10] that is discussed in Chapter 3, all the illumination conditions are determined using the incident magnetic field at the middle height of the metalens, in which B_{Glass} and B_{PDMS} are for the incident light from the glass side (bottom side) and the PDMS side (top side), respectively. Under the E-antinode illumination condition, the field ratio $B_{Glass}/B_{PDMS} = -n_{Glass}/n_{PDMS}$ is equal to $-1.50/1.40$ (the negative sign implied that the two fields are π out of phase), while the B-antinode condition corresponded to $B_{Glass}/B_{PDMS} = 1$ (the two fields are in phase). Two polystyrene spheres (refractive index = 1.56) [263], a nanosphere with a diameter of 100 nm and a microsphere with a diameter of 1 μm, are employed to determine typical particle response

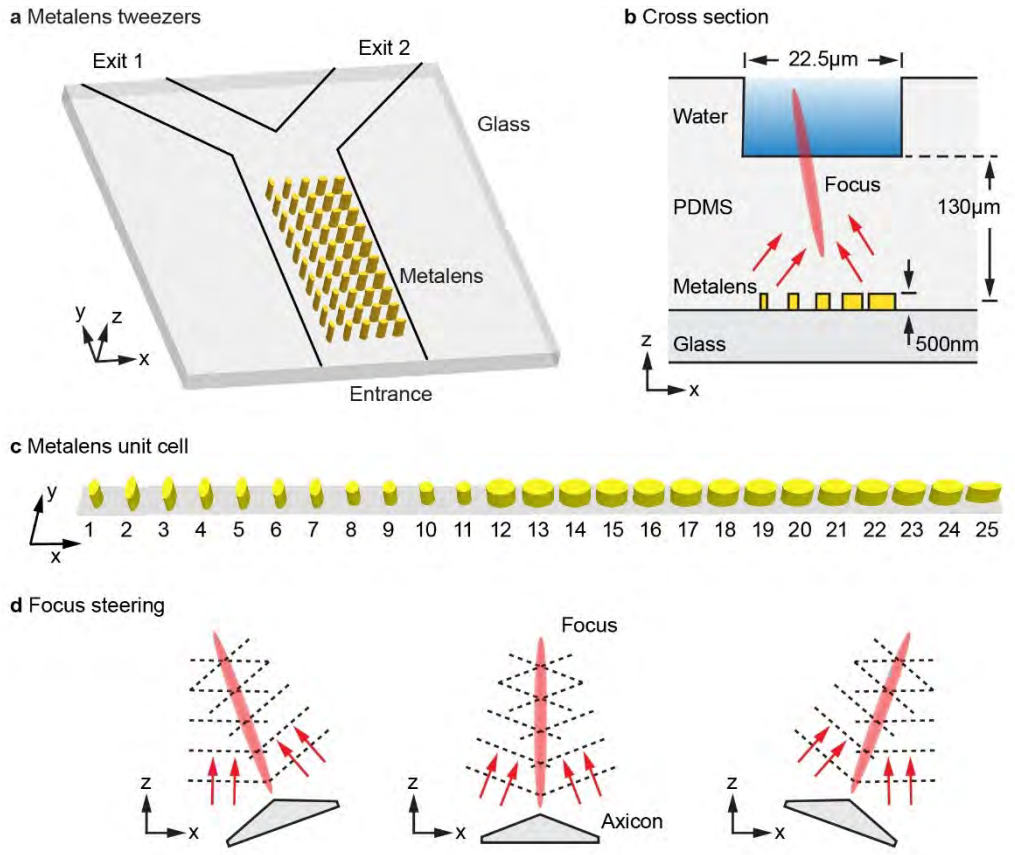

Fig. 4.1. Schematic diagram of tunable metalens tweezers and the application as an optofluidic particle router. (a) Schematic of the metalens, which is an array of Si nanopillars (in yellow color) on top of a glass substrate. The array has 25 nanopillars (only five are depicted here due to space constraints) in each row along the x axis, and rows are identical along the y axis. The metalens lies beneath a microfluidic channel defined by a layer of PDMS (not depicted). The boundaries of the microchannel have the shape of a Y-branch junction, consisting of one entrance and two exits. The intended functionality of the metalens tweezers is to define the x position of suspended particles in the entrance section, enabling routing towards either of the two exits. (b) Cross section of the device through the entrance channel. Under the illumination of two coherent, x-polarized, counter-propagating light beams at normal incidence (not depicted), constructive interference of light scattered by the nanopillars (red arrows) forms a focus inside the microchannel and the intermediate PDMS layer. The xz cross section of the focus approximates a Bessel beam. Several dimensions are annotated, and the device is not drawn to scale. (c) Schematic of a single unit cell of the metalens, which consists of a row of 25 nanopillars. The figure is drawn to scale. (d) By using the technique of coherent control, the focus can be steered in the xz plane. The shape and the steering of the focus suggest that the tunable metalens behaves like a conventional cylindrical axicon lens that rotates in the xz plane.

to the illumination. Initially, the optical force is derived by integrating the Maxwell stress tensor at the surface of the particles utilizing the electromagnetic field simulation. As detailed in Section 4.7, the trapping potential was then calculated by integrating the force along a straight line. Furthermore, a Lorentz force formula based on the momentum of a dipole is used to figure out the optical potential on the nanosphere of the metalens tweezers which can be found in Section 4.8.

4.3 Formula derivation: Standing wave at PDMS/Glass interface

In this section, the coherent illumination at the PDMS/Glass interface is considered. Two coherent, counter-propagating waves, one from the PDMS side along the $-z$ direction and the other from the glass substrate side along the $+z$ direction, illuminate the interface at normal incidence. The two waves have the same wavelength and are collinearly polarized. To create a standing wave at the PDMS/Glass interface, the relative phase and amplitude of the incident fields should be controlled at the interface. Here, the analysis begins with the Fresnel equations [264], which dictate the transmitted and reflected fields of an incident wave at an interface. I begin the derivation by defining the components of the light field propagating in the two mediums (i.e. glass and PDMS). E^i_{Glass}, E^t_{Glass}, and E^r_{Glass} represent the incident, transmitted, and reflected electric fields at the interface from the glass substrate, respectively, while B^i_{Glass}, B^t_{Glass}, and B^r_{Glass} represent the corresponding magnetic field components. Similarly, the respective field component of a light wave from the PDMS side can be defined in the same way, i.e. E^i_{PDMS}, E^t_{PDMS}, E^r_{PDMS}, B^i_{PDMS}, B^t_{PDMS}, and B^r_{PDMS}. The equations below can be obtained directly for the fields in the PDMS:

$$\begin{cases} E^i_{PDMS} = E_0 e^{i(kr-wt)} \\ E^r_{PMDS} = r_{12} E_0 e^{i(kr-wt)} \\ E^t_{PDMS} = t_{12} E_0 e^{i(kr-wt)} \end{cases} \tag{4.2}$$

$$\begin{cases} B^i_{PDMS} = \frac{n_{PDMS}}{c} E_0 e^{i(kr-wt)} \\ B^r_{PDMS} = -r_{12} \frac{n_{PDMS}}{c} E_0 e^{i(kr-wt)} \\ B^t_{PDMS} = t_{12} \frac{n_{PDMS}}{c} E_0 e^{i(kr-wt)} \end{cases} \tag{4.3}$$

where E_0 is the amplitude of the incident field, i is the imaginary unit, k is the wave vector, r is the position vector, w is the angular frequency, and t is time. r_{12} is the reflective coefficient from the glass back to PDMS, and t_{12} is the transmission coefficient from PDMS to glass. n_{PDMS}, n_{Glass} are the refractive indices of the PDMS layer and glass substrate, respectively.

Based on the Maxwell equations that guide the behavior of electromagnetic fields, the tangential components of the electric and magnetic fields are continuous on both sides of the interface between the two mediums. Hence, the tangential electric/magnetic field components

at the interface can be described by

$$E^i_{PDMS} + E^r_{PDMS} = E^t_{PDMS} \tag{4.4}$$

$$B^i_{PDMS} + B^r_{PDMS} = B^t_{PDMS} \tag{4.5}$$

By substituting Eq. 4.2 and Eq. 4.3 into Eq. 4.4 and Eq. 4.5, respectively, the continuous electric field and magnetic field at the interface are obtained

$$1 + r_{12} = t_{12} \tag{4.6}$$

$$n_1 + r_{12}n_1 = t_{12}n_2 \tag{4.7}$$

which are easily solved for r_{12} and t_{12}, yielding

$$r_{12} = \frac{n_{PDMS} - n_{Glass}}{n_{PDMS} + n_{Glass}} \tag{4.8}$$

$$t_{12} = \frac{2n_{PDMS}}{n_{PDMS} + n_{Glass}} \tag{4.9}$$

Hence, the transmitted and reflected waves in the PDMS layer can be described by

$$E^r_{PDMS} = r_{12}E^i_{PDMS} = \frac{n_{PDMS} - n_{Glass}}{n_{PDMS} + n_{Glass}} E^i_{PDMS} \tag{4.10}$$

$$E^t_{PDMS} = t_{12}E^i_{PDMS} = \frac{2n_{PDMS}}{n_{PDMS} + n_{Glass}} E^i_{PDMS} \tag{4.11}$$

The same approach can apply to the analysis of the magnetic field at the interface from the PDMS side, which can be described by

$$B^r_{PDMS} = \frac{n_{PDMS} - n_{Glass}}{n_{PDMS} + n_{Glass}} B^i_{PDMS} \tag{4.12}$$

$$B^t_{PDMS} = \frac{2n_{PDMS}}{n_{PDMS} + n_{Glass}} B^i_{PDMS} \tag{4.13}$$

Similar to the waves in the PDMS side, the reflective and transmission coefficients of the waves in the glass substrate are derived to be:

$$E^r_{Glass} = \frac{n_{Glass} - n_{PDMS}}{n_{PDMS} + n_{Glass}} E^i_{Glass} \tag{4.14}$$

$$E^t_{Glass} = \frac{2n_{Glass}}{n_{PDMS} + n_{Glass}} E^i_{Glass} \tag{4.15}$$

$$B^r_{Glass} = \frac{n_{Glass} - n_{PDMS}}{n_{PDMS} + n_{Glass}} B^i_{Glass} \tag{4.16}$$

$$B^t_{Glass} = \frac{2n_{Glass}}{n_{PDMS} + n_{Glass}} B^i_{Glass} \tag{4.17}$$

By combination Eqs. 4.10 -4.13 and Eqs. 4.14 -4.17, the total electric amplitude and magnetic amplitude at the PDMS/Glass interface, are described by

$$E^i_{PDMS} + E^r_{PDMS} + E^t_{Glass} = E^i_{Glass} + E^r_{Glass} + E^t_{PDMS} \tag{4.18}$$

$$B^i_{PDMS} + B^r_{PDMS} + B^t_{Glass} = B^i_{Glass} + B^r_{Glass} + B^t_{PDMS} \tag{4.19}$$

By substituting reflective and transmission coefficients into Eq. 4.18, the total instantaneous electric field E is obtained as

$$E = \frac{2n_{PDMS}}{n_{PDMS} + n_{Glass}} E^i_{PDMS} + \frac{2n_{Glass}}{n_{PDMS} + n_{Glass}} E^i_{Glass} \tag{4.20}$$

Similar, by substituting reflective and transmission coefficients into Eq. 4.19, the total instantaneous magnetic field B is obtained

$$B = \frac{2n_{Glass}}{n_{PDMS} + n_{Glass}} B^i_{PDMS} + \frac{2n_{PDMS}}{n_{PDMS} + n_{Glass}} B^i_{Glass} \tag{4.21}$$

From Eqs. 4.20 and 4.21, it is straightforward to determine the unique solutions required to satisfy the E-antinode (or magnetic field node) and the B-antinode (or electric field node) conditions. Hence, the relative magnetic field amplitude B_{Glass}/B_{PDMS} at the E-antinode is given by

$$B_{Glass}/B_{PDMS} = -n_{Glass}/n_{PDMS} \tag{4.22}$$

Meanwhile, the relative magnetic field amplitude at the B-antinode is obtain as

$$B_{Glass} = B_{PDMS} \tag{4.23}$$

In addition, the relative incident power can also be derived [265], which is expressed as

$$I = \frac{cn\epsilon_0}{2}|E|^2 \tag{4.24}$$

where n is the refractive index of the medium, c is the speed of light in vacuum, and ϵ_0 is the vacuum permittivity. E is the complex amplitude of the electric field. The net power P through a closed surface A is described by

$$P = \int I \cdot dA \tag{4.25}$$

By substituting the two media of interest at the interface, the relative incident power can be obtained as

$$\frac{P_{Glass}}{P_{PDMS}} = \frac{n_{Glass}|E_{Glass}|^2}{n_{PDMS}|E_{PDMS}|^2} = \frac{n_{PDMS}|B_{Glass}|^2}{n_{Glass}|B_{PDMS}|^2} \tag{4.26}$$

where E and B are the electric and magnetic amplitudes in the corresponding medium, respectively. The value is 1.07 for the E-antinode condition and 0.93 for the B-antinode condition, these values were utilized in the subsequent simulations.

4.4 Meta-atom design: Optical response of nanopillar arrays

The metasurface lens forms a focal point as a result of the constructive interference of light scattered by the nanopillars, a process in which the phase of the scattered light is critical. **Fig. 4.2** uses cylindrical nanopillars, where the cross section is a circle, to demonstrate coherent control over the output phase. To simplify the phase extraction [178, 266], a uniform array of same-sized nanopillars is simulated for this initial study. The nanopillars are periodic along both the x- and y-axes. Both the glass substrate and the PDMS layer are treated as infinitely thick. The microfluidic channel is not considered at this stage, which is a good approximation due to the similarity between water and PDMS in their refractive indices, 1.33 for water and 1.40 for PDMS. The spacing of the nanopillars is set to be the same value of 900 nm as in the metalens surface (see **Fig. 4.2 a**). The array is illuminated by light at normal incidence, either from both the PDMS and the glass side or from only the PDMS side. The array scatters incident light both upwards (into the PDMS layer) and downwards (into the glass substrate), whereas only the former is analyzed here due to its relevance to particle manipulation. The radius of the nanopillar, shown in **Fig. 4.2 a**, changes from 100 nm to 400 nm with a 10 nm step (**Fig. 4.2 b**).

The output scattering phase dispersion is modifiable with coherent illumination. In comparison to the single-beam illumination, the slope of the phase dispersion at the E-antinode condition is steeper within the radius range between 200 nm and 300 nm. In contrast, the phase dispersion at the B-antinode condition is pronounced in the $150 - 200$ nm and $350 - 400$ nm regions. This difference underpins the rotaion of the V-shaped phase profile, which is shown later in the chapter.

I further calculated elliptical nanopillars, which can provide a better phase match to the target wavefront as compared with circular nanopillars. In **Fig. 4.3**, nanopillars with 961 different cross sections are simulated, with the dimensions along the x and y axis adjusted independently from each other from 100 to 400 nm at a step of 10 nm. Both the amplitude and phase maps exhibit variant optical response of the nanopillar array. The phase curves in **Fig. 4.2 b** can now be considered as special situations that correspond to the diagonal of the phase maps in **Fig. 4.3**. By adjusting the length of the nanopillar, elliptic nanopillars show more abundant variant in phase. When compared to the single-beam illumination condition, the phase variation/coverage at the E-antinode condition is smaller when the nanopillar semi-width is less than 160 nm, but bigger when the nanopillar semi-width is more than 350 nm. In contrast, under the illumination condition of the B-antinode, the change demonstrates an opposing tendency. In **Fig. 4.2 c**, a pair of counter-propagating, coherent light beams are employed to demonstrate the coherent control of two beams from different materials [198]. The two beams with the same wavelength and polarization condition have different phase and amplitude. At the air/substrate interface, only an electric field or magnetic field exists in the E- or B-antinode condition, respectively. In the coherently tunable metalens tweezers, the two beams superimpose at the plane, which is located at the middle height of the silicon nanopillars [9, 190, 201].

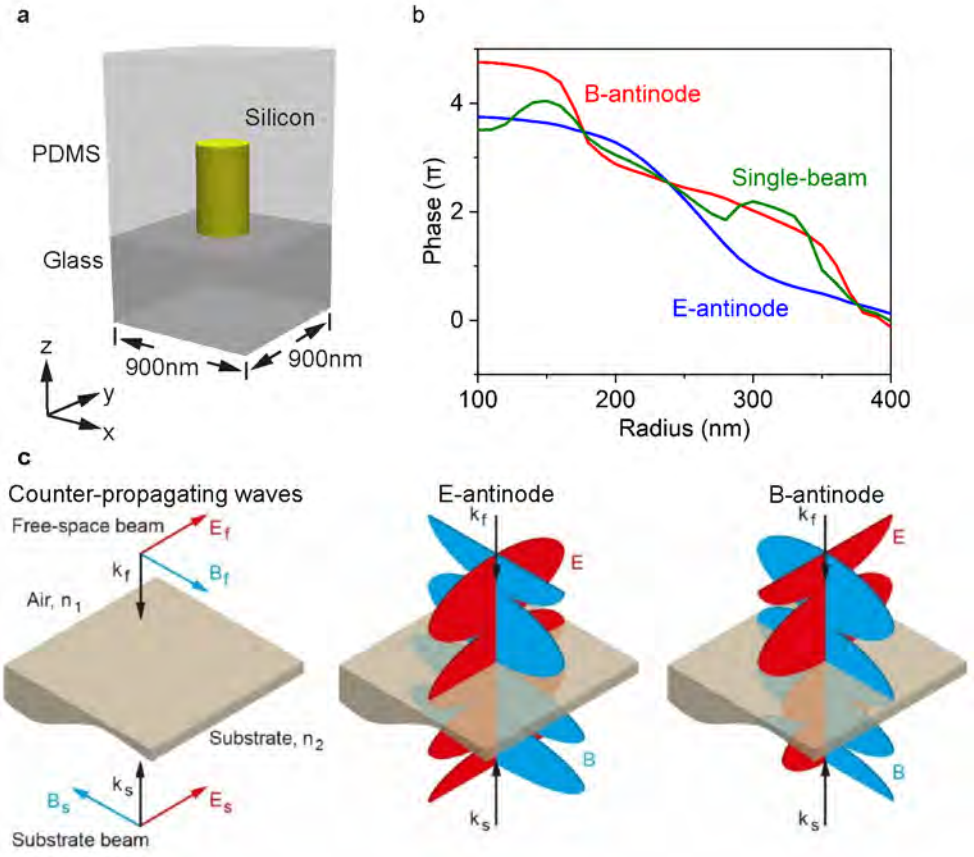

Fig. 4.2. Phase response in the output light of a cylindrical nanopillar. (a) A schematic diagram of a nanopillar has a cylindrical cross section. To determine the phase, a uniform array of the nanopillar with a periodicity of 900 nm in both the x and y directions is simulated. The incident light propagates along the $\pm z$ directions. The height of the cylindrical nanopillar is 500 nm. (b) Phase shifts of a varying nanopillar, which radius changes from 100 nm to 400 nm, under three illumination conditions of interest, i.e. the E-antinode (blue), single-beam (olive), and the B-antinode (red), respectively. (c) Coherent illumination of a substrate surface plane using two counter-propagating light beams. Electric and magnetic field distributions for standing waves in which the surface of the substrate is at the E-antinode (middle subpanel) and the B-antinode (right subpanel). Panel (c) is reproduced from [198].

Fig. 4.4 employs a specific nanopillar, nanopillar #1 (with a semi-width of 120 nm and semi-length of 250 nm) in **Fig. 4.1 c** and **Table 4.1**, as an example to demonstrate coherent control over the output phase. As discussed above the nanopillars form a bi-periodic array for phase extraction (see **Fig. 4.4 a**). The array is illuminated by light from both the PDMS and the glass sides (**Figs. 4.4 c** and **e**) or from the PDMS side only (**Fig. 4.4 d**). All the field maps show a plane wave propagating along the $+z$ direction, as only the zeroth-order diffraction is allowed for an effective wavelength (1107 nm in the PDMS) larger than the periodicity (900 nm). The output wave maintains the x polarization of the incident wave, as polarization rotation is forbidden by the planar symmetry.

As demonstrated previously [190], two coherent, counter-propagating light waves illuminating an interface at the normal incident can form a standing wave, even if the media on the two sides of the interface have different refractive indices. If the interface is at the E-antinode

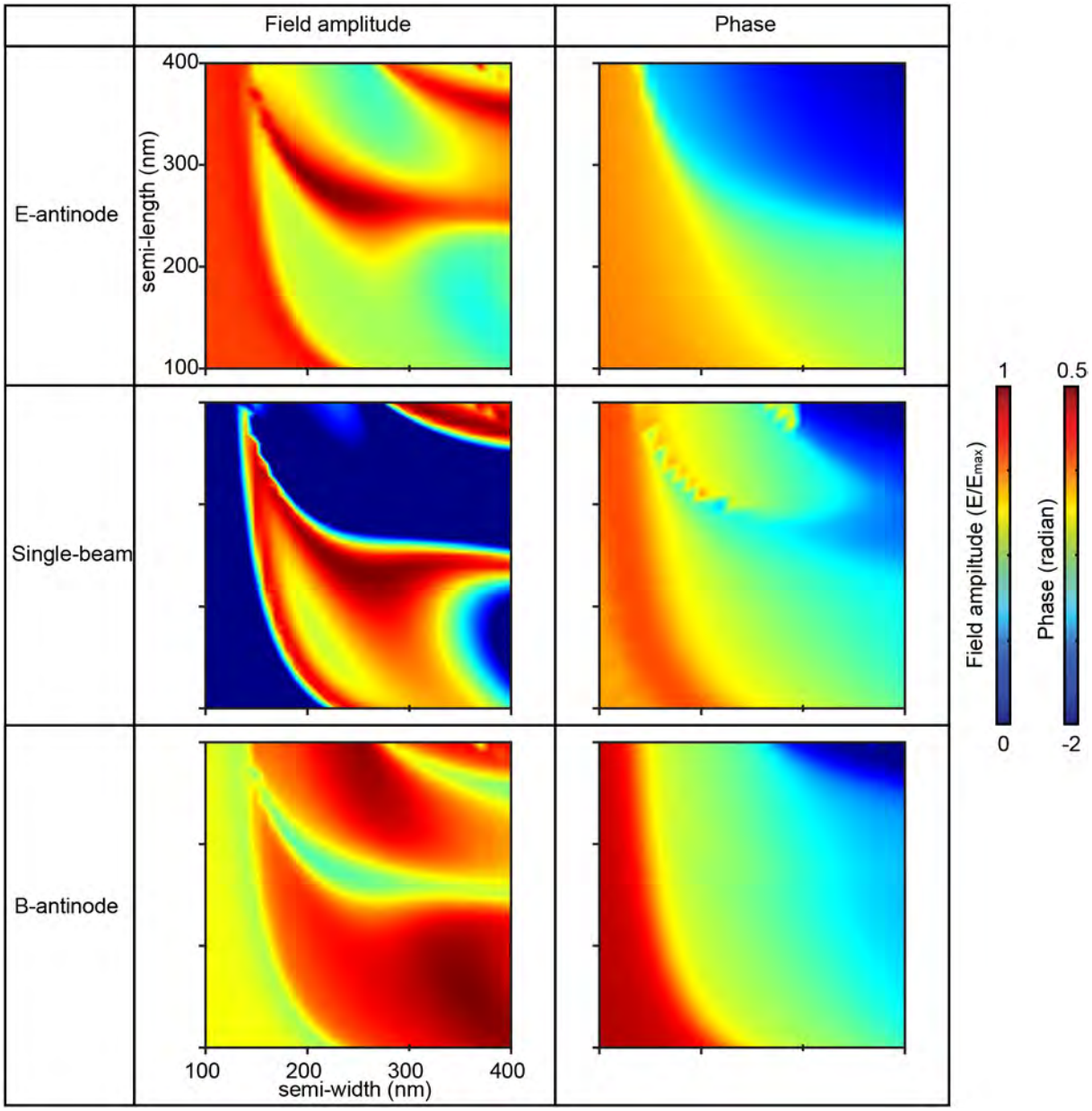

Fig. 4.3. The simulated output field amplitude and phase of elliptical nanopillars with varying dimensions at the designed wavelength of 1550 **nm under three illuminate conditions, the E-antinode, single-beam, and the B-antinode.** The nanopillar has an elliptical cross section with a semi-width (along the x axis) and a semi-length (along the y axis) varying from 100 nm to 400 nm.The phase map in the left column shows the modulated phase of output light, which is extracted 2 μm above the arrays of nanopillar. All three maps of field amplitude in the right column are normalized against the maximum value in each individual map.

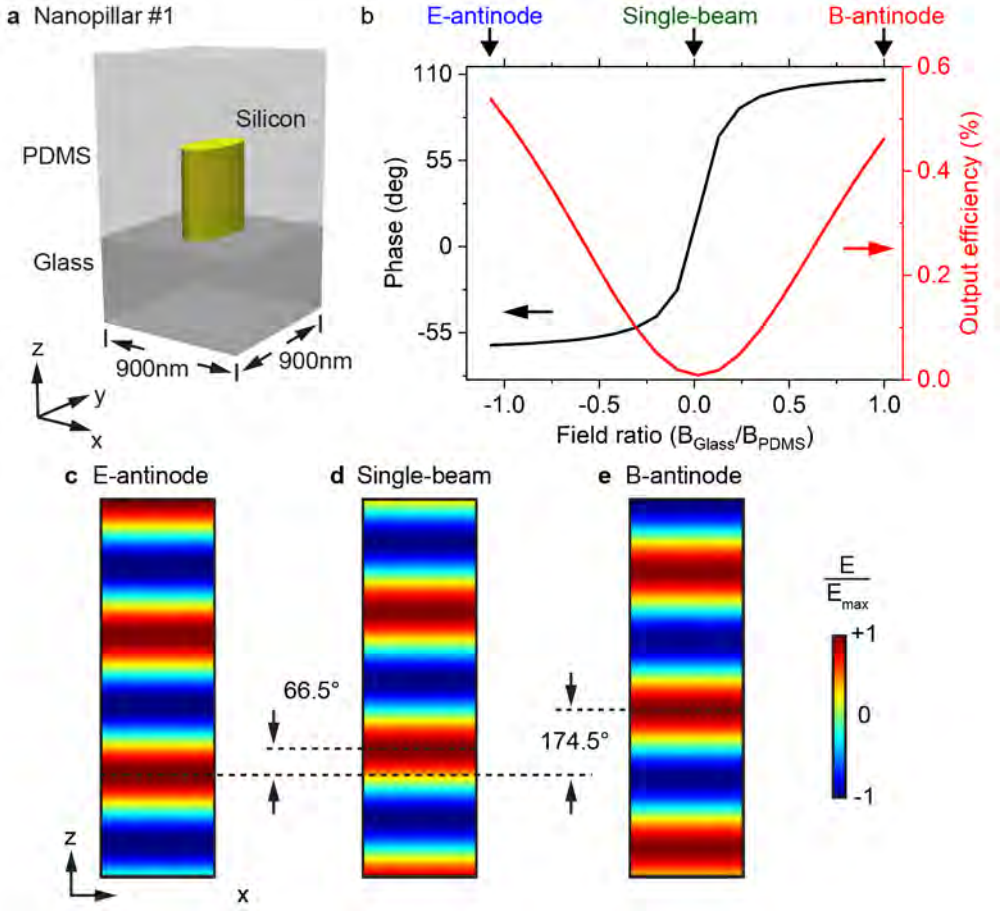

Fig. 4.4. Phase and strength of the output light from an example nanopillar. (a) Illustration of the nanopillar, which has an elliptical cross section with a semi-width of 120 nm and a semi-length of 250 nm. An array with a periodicity of 900 nm in both the x- and y-axes is used to extract the phase. The z axis is the propagation axis for the incident waves. (b) Optical response on the example nanopillar with a varying field ratio, B_{Glass}/B_{PDMS}, from $-1.5/1.4$ (E-antinode condition) to 1 (B-antinode condition) as discussed in Section 4.2, which demonstrates phase shift (black line) and output efficiency (red line). The output efficiency is normalized against the total input power from both PDMS and glass sides. (c-e) Output electric field inside the PDMS, with the array (c) at the E-antinode of a standing wave formed by two incident light beams, (d) under the illumination of a single beam from the PDMS sides, and (e) at the B-antinode of a standing wave. All three maps exhibit the same area of 900 nm $\times$ 3 μm in the xz plane (2 μm to 5 μm above the array of nanopillars). The field is normalized against the maximum value in each individual map.

(equivalently the B-node) of the standing wave (i.e. the illumination condition of **Fig. 4.4 c**), the local electromagnetic field is purely electric. In contrast, if the interface is at the B-antinode (equivalently the E-node, the illumination condition of **Fig. 4.4 e**), the local field is purely magnetic. A gradual transition from the E-antinode to the B-antinode can be achieved by maintaining one incident wave unchanged, while adjusting the phase and strength of the other incident wave. In this work, the incident light from the PDMS side is selected as the invariant wave, and **Fig. 4.4 c** corresponds to a specific case in the gradual transition where the other wave (i.e. the wave from the glass substrate side) is switched off.

To obtain tunable metalens tweezers, the variation of scattering properties between the

limiting cases of the E-antinode and the B-antinode is considered. **Fig. 4.4 b** demonstrates the phase shift and scattering efficiency of the example nanopillar with the gradual transition of illumination condition. The tuning range is represented by the magnetic field ratio of the incident waves from the glass side (B_{Glass}) and the PDMS side (B_{PDMS}). The sign of B_{Glass}/B_{PDMS} indicates the relative phase of the two incident waves, while the amplitude represents their relative strength. A phase tuning range from -65° to 109.5° is observed for the nanopillar, with an approximately parabolic variation of output efficiency of 55% (at the E-antinode) and 47% (at the B-antinode), as shown in **Fig. 4.4 b**.

Figs. 4.4 c-e highlight the change in phase of the output light at the three specific illumination conditions. The difference is 66.5° between the E-antinode and the single-beam, and it can reach 174.5°, almost a total phase reverse of π, between the E-antinode and the B-antinode. The simulated phase shift is only about half of the ideal maximum shift (i.e. 2π). This limits the dimensions of the metalens tweezers in the x direction. The phase shift clearly reveals that the optical properties of the Si nanopillar can be modulated through coherent control. Such modulation originates from the fact that the nanopillar possesses multiple Mie resonances at this wavelength, where the electric dipole and magnetic dipole resonances are selectively dominant under the E-antinode and the B-antinode conditions, respectively (see next section for near-field analysis). Due to the fact that various resonances impart different phase shifts in light scattering, the nanopillar shows a scattering phase that is exclusively controlled by incident light.

A light-focusing metalens requires its constituent units (in this case, the nanopillars) to exhibit a tailored phase profile across the whole metalens, and a tunable metalens further requires this phase profile to be modified in a designated fashion. In this work, both requirements are satisfied by adjusting the cross section of the nanopillars across the metalens. Suitable nanopillars are identified based on the phase shift (as the dominant factor) and the strength (as the secondary factor) in light scattering. As a result, the 25 nanopillars in a metalens unit cell adopt 15 different cross sections (see **Table 4.1**). Reducing the dimension step from 10 nm to an even smaller value will increase the number of nanopillars available for selection, albeit also increasing the difficulty for the nanofabrication of the device.

4.5 Meta-atom characteristics: near-field tuning by coherent control

Previous sections have analyzed electromagnetic responses at the far field (i.e. about two wavelengths away from the middle height of the nanopillar array) under the E-antinode, the single-beam, and the B-antinode illumination conditions. Near-field properties can provide complementary information for metalens design, and they are analyzed in this section. **Fig. 4.5** demonstrates the electric and magnetic field distribution at the middle xy plane of the nanopillar under three illumination conditions. The simulation result indicates that the illumination condition changes the near-field, particularly its magnitude. As shown in **Fig. 4.5**, the electric

field magnitude at the E-antinode condition decreases when changing to the single-beam condition, and the B-antinode condition. In comparison, the magnetic field is the strongest at the B-antinode.

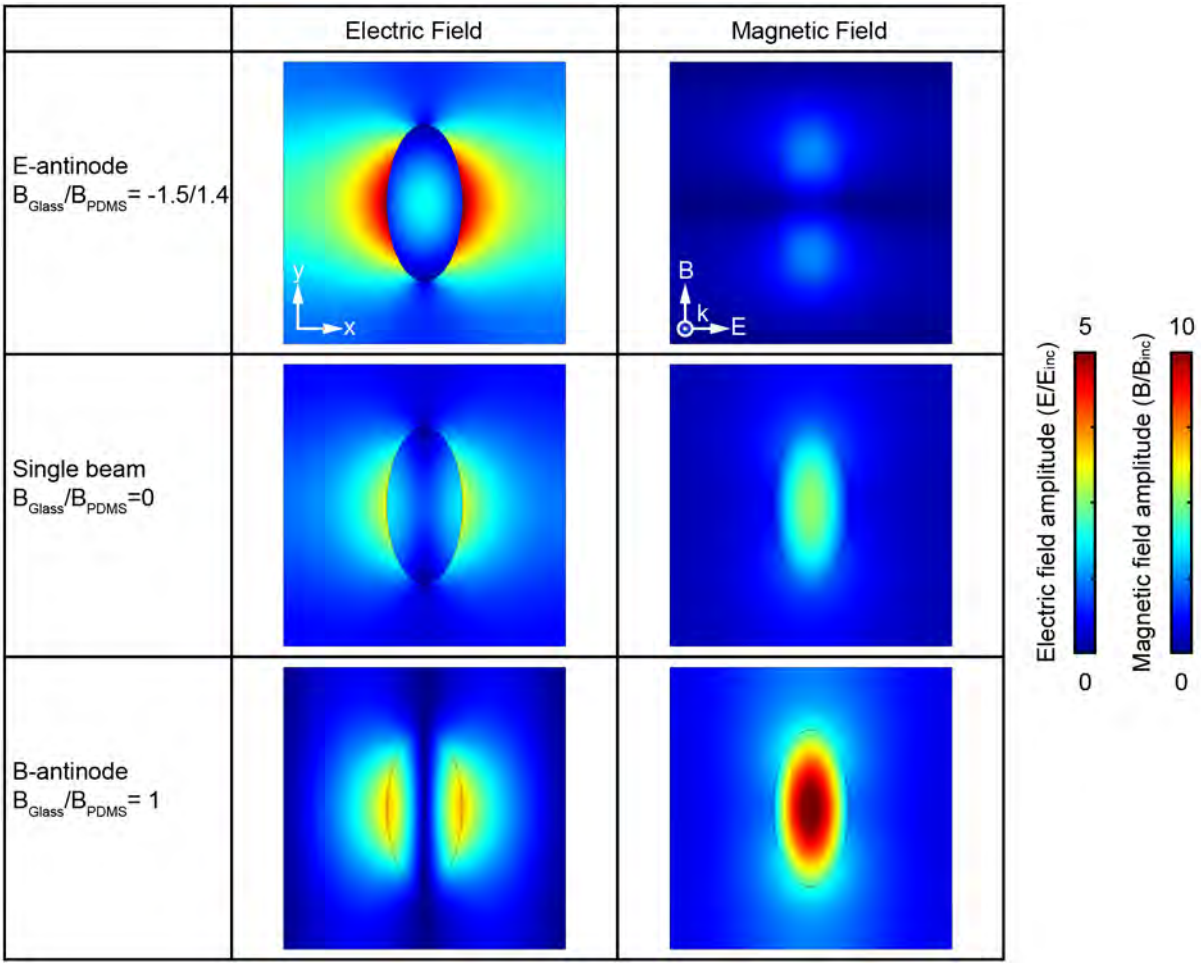

Fig. 4.5. Electric and magnetic field distributions of the nanopillar #1 (see Fig. 4.4 a) under three different illumination conditions. The field distributions are extracted at the middle *xy* plane of the example nanopillar. The directions of the incident electric and magnetic fields are depicted in the top right panel. The incident wavelength is 1550 nm. All six fields are normalized against the incident light from the PDMS side, which is invariant with illumination conditions.

Fig. 4.6 depicts the electric and magnetic field distributions in the same *xz* plane, the cross section at the center of the nanopillar together with the displacement current. At each illumination condition, the black arrows indicate the local direction and strength of the displacement current, while it should be noticed that the field strength is not normalized across panels. Both the electric field and the current clearly depend on the illumination condition, supporting the interpretation in previous sections that the optical response of the nanopillars depends on the illumination condition. As shown in **Fig. 4.6 a**, at the E-antinode condition, the displacement current is almost straight in the center along the *x* axis. In contrast, at the B-antinode condition (see **Fig. 4.6 b**), a circulating displacement current is observed, which correlates with the magnetic field distribution shown in **Figs. 4.5** and **4.7**.

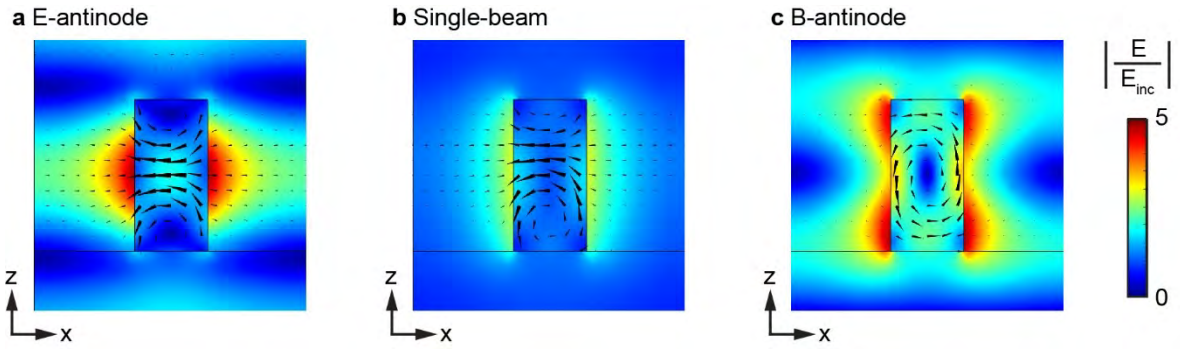

Fig. 4.6. The electric field distribution (color maps) and the displacement current (arrows) for nanopillar #1 under three different illumination conditions. The field distributions are extracted at the middle xz plane of the example nanopillar. The electric field of all the maps is normalized against the same value, that is, the electric field of the incident light from the PDMS side. Meanwhile, the displacement current is not normalized across the three maps.

Elliptical nanopillars have an additional variable that can be adjusted when compared to cylindrical nanopillars (i.e. different values of the width and length along the x- and y axis). According to the phase diagram shown in **Fig. 4.3**, the width-to-length aspect ratio has a substantial impact on the optical response under all illumination conditions of interest. Based on this observation, nanopillar #1 (see **Fig. 4.7**), which has the smallest width-to-length aspect ratio (120/250), and nanopillar #25 (see **Fig. 4.8**), which has the largest width-to-length aspect ratio (400/130) are chosen as examples for analysis. All of the electric and magnetic field distributions are normalized against the respective field of the incident light from the PDMS side, which is invariant with the illumination condition. It is worth highlighting that, no obvious near-field cross-talk can be observed in the simulation, even in nanopillar #25 that has a small pillar-to-pillar gap of 200 nm. In both nanopillars, a strong dependence on illumination condition is observed.

Near-field crosstalk has been investigated in subwavelength-periodically patterned thin-film structures [267]. Two adjacent polarized structures can show near field coupling once the two structures are too close to each other [268]. This coupling will reduce efficiency and generate wavefront distortion in metasurfaces [269]. In **Figs. 4.7** and **4.8**, the localized field concentrates on the sidewalls of the nanopillar array rather than on the boundaries of the meta-atoms (i.e. panel edges). This feature indicates that the cross talking is very weak. Based on this observation, these nanopillars can be used to assemble the metalens tweezers with the designed Bessel-beam wavefront.

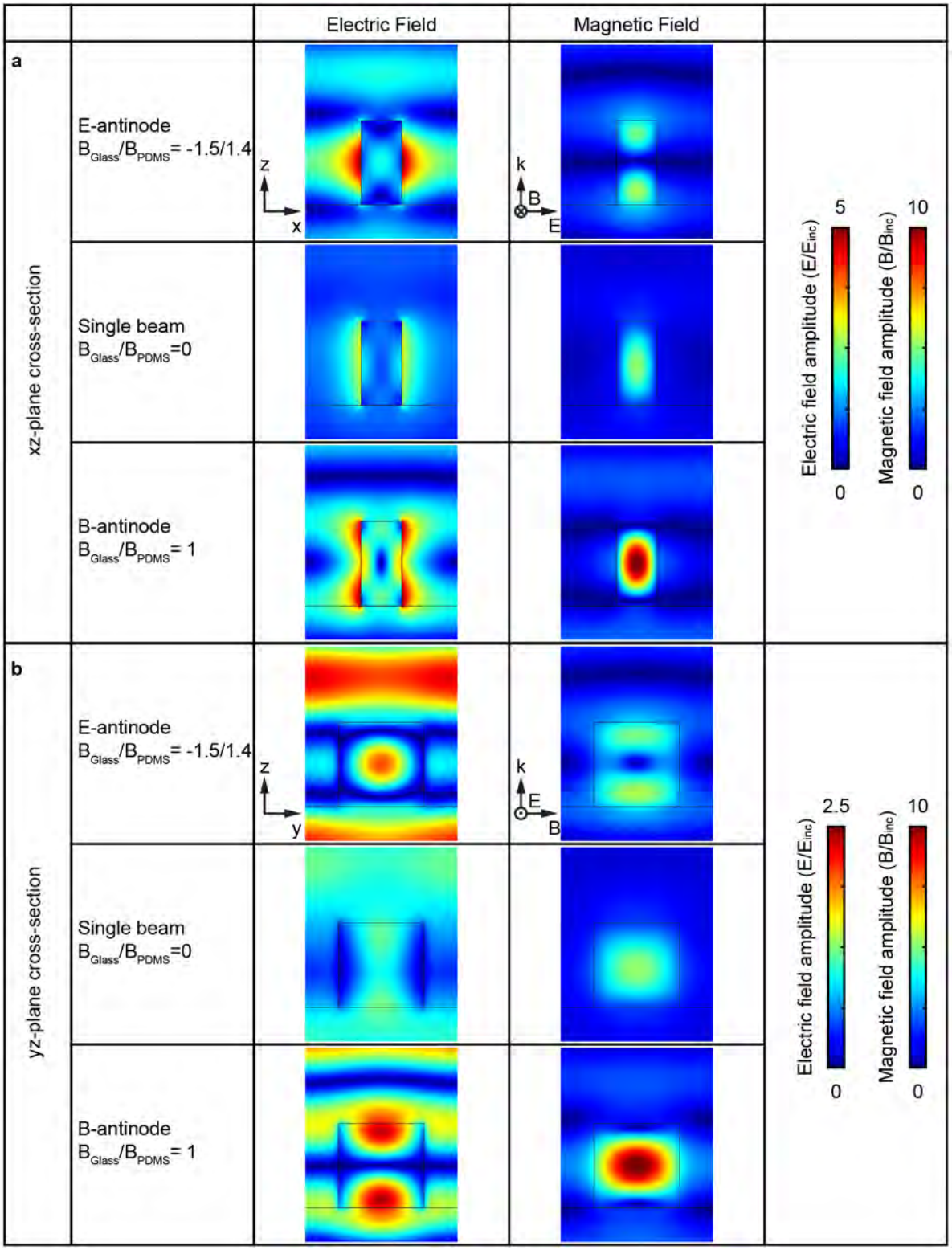

Fig. 4.7. Electric and magnetic field of nanopillar #1 (semi-width is 120 nm and semi-length is 250 nm) under different illumination conditions of interest at the wavelength of 1550 nm. The field distributions are extracted at the middle (a) xz and (b) yz plane of the nanopillar. The directions of the incident electric and magnetic fields are specified in the top right panel of **Figs. 4.7 a** and **b**, respectively. The two type fields are normalized against the respective field of the incident light from the PDMS side, which is invariant with illumination condition.

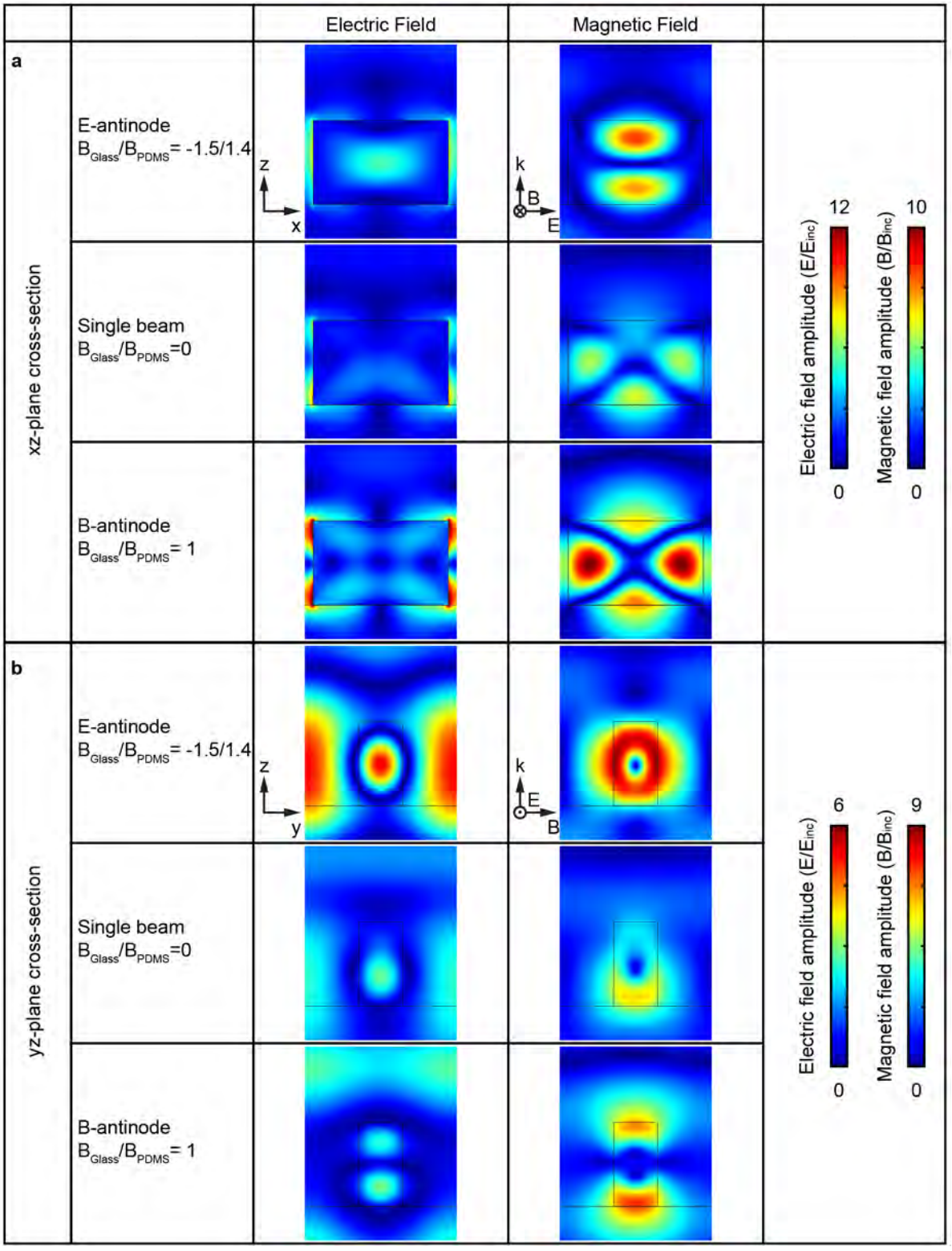

Fig. 4.8. Electric and magnetic field of the nanopillar #25 **(semi-width is** 400 **nm and semi-length is** 130 **nm) under different illumination conditions of interest at the wavelength of** 1550 **nm.** The field distributions are extracted at the middle (a) xz and (b) yz plane of the nanopillar. The directions of the incident electric and magnetic fields are specified in the top right panel of **Figs. 4.8 a** and **b**, respectively. The two type fields are normalized against the respective field of the incident light from the PDMS side, which is invariant with illumination condition.

4.6 All nanopillars used in the metalens

Figs. 4.9 a-c show the output electric field of all the 25 nanopillars under three illumination conditions. In each figure, the 25 nanopillars are allocated in the order that they appear in the metalens unit cell. **Figs. 4.4 c-e**, which are extracted amplitude shifts for nanopillar #1, match with the first panel in **Figs. 4.9 a-c**. These results are obtained from uniform arrays of same-sized nanopillars, which provide a useful initial step in designing the function of the metalens [190, 270]. All the 75 panels, i.e. 25 pillars under 3 different illumination conditions, of **Figs. 4.9 a-c** demonstrate a plane wave propagating upwards away from the nanopillars. The vertical phase shift of the wave among these panels demonstrates that the phase of output scattering light depends on both the geometry (dimension and size) of the nanopillar and the illumination condition. For visualization, all 75 panels are normalized against the maximum value of the respective field amplitude in the corresponding panels.

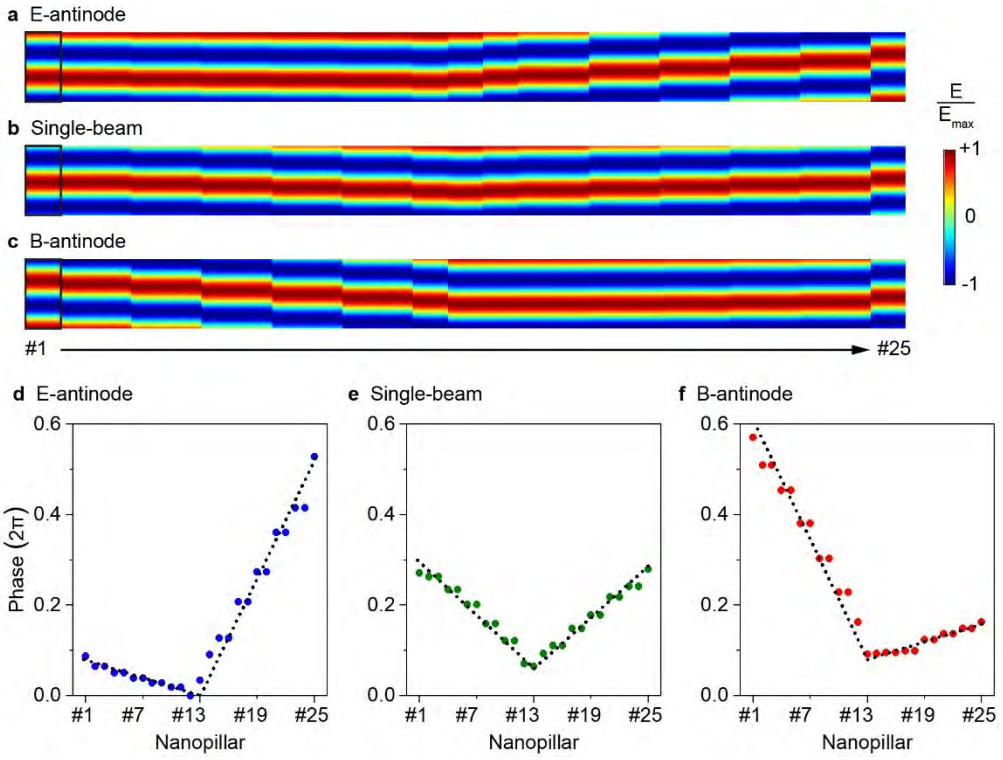

Fig. 4.9. Field distribution and phase shift of output field from uniform arrays of nanopillar #1 to #25. (a-c) Output electric field for different illuminations of interest. The panels are arranged as the nanopillar allocates in the metalens super-cell. Each single panel (dimension highlighted for the first panel in each row with a black box) corresponds to the same area of $900\,nm \times 1.8$ μm in the xz plane. The field is normalized against the maximum value in the respective panel. (d-f) Values of phase (dots) extracted from corresponding field maps, with the dashed lines as a guide for the eye.

Figs. 4.9 d, **e**, and **f** show the phase obtained from **Figs. 4.9 a**, **b**, and **c**, respectively. The phase is extracted at the same height above the 25 nanopillars, i.e. two wavelengths incidence. In each figure, the phase variant across the 25 nanopillars has roughly a V shape, with two straight lines intersecting at the center (i.e. at nanopillar #13). As the illumination condition

changes from the E-antinode (**Fig. 4.9 d**) to the B-antinode (**Fig. 4.9 f**), the V shape wavefront rotates in the clockwise direction. This rotation results from the different illumination-induced phase shifts among the nanopillars with two features: the outer nanopillars (i.e. those closest to #1 and #25) have larger shifts than the inner nanopillars (i.e. those closest to #13) and the nanopillars on the left and on the right shift in opposite directions.

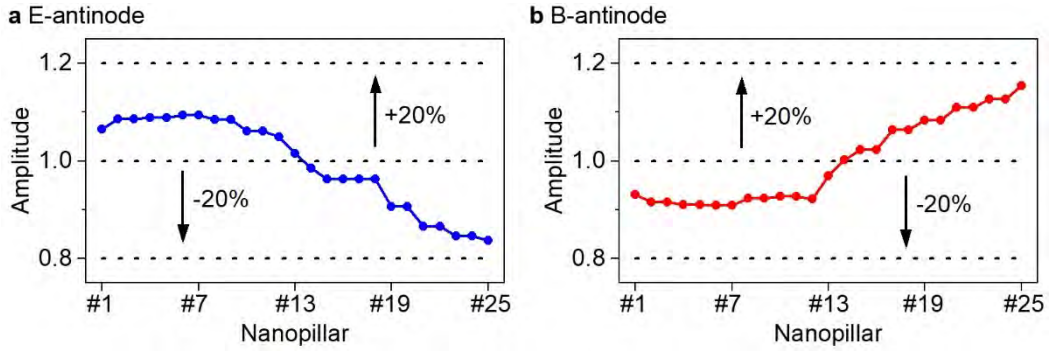

Fig. 4.10. The output electric field amplitude from all 25 nanopillars in the metalens supercell, obtained using the same methods for Figs. 4.4 and 4.9. Only the E-antinode and B-antinode conditions are analyzed. All the values are normalized to the electric field of the incident light from the PDMS side, which is constant for all cases.

As mentioned previously, the other key factor of nanopillar selection is the output strength of the scattering light from the nanopillar towards the PDMS side. Output amplitudes of the scattering light from the 25 nanopillars under the E-antinode and the B-antinode condition are analyzed in **Fig. 4.10**. All 50 output strengths are extracted from the same xy plane above the 25 nanopillars under the two illumination conditions. The results here show that the Si metalens slightly deviates (within $\pm 20\%$ of unit value) from the perfect metalens, which would require all the nanopillars to have a constant output magnitude under either illumination condition.

4.7 Tuneable metalens: Coherently controlled light focusing and particle routing

As long as the near-field coupling between adjacent nanopillars is sufficiently weak and all the nanopillars have similar scattering strength (see **Fig. 4.7** for details) [270], the light shaping performance of the metalens can be reasonably predicted based on the results in **Fig. 4.9**. This prediction is confirmed in **Fig. 4.11**, which shows the output of the metalens tweezers illustrated in **Fig. 4.1**. To better characterize the modulation in the output, in addition to the three illumination conditions discussed above, that is, the E-antinode, the single-beam, and the B-antinode conditions, **Fig. 4.11** also includes two intermediate conditions. All five conditions can be easily specified by the field ratio B_{Glass}/B_{PDMS}, which is $-1.5/1.4$, $(1/2) \times (-1.5/1.4)$, 0, $1/2$, and 1 for **Figs. 4.11 a**, **b**, **c**, **d**, and **e**, respectively (note that $1.5/1.4$ comes from n_{Glass}/n_{PDMS} as discussed previously). All the conditions can be achieved by keeping the input beam from the PDMS side unchanged, while controlling the strength and phase of the beam from the glass

side. Note that, the same as **Figs. 4.4** and **4.9**, the field distribution shown here is purely the output field and contains no input field. Different from those two previous figures, the PDMS layer above the nanopillars is no longer treated as infinitely thick due to the inclusion of the microchannel in the simulation.

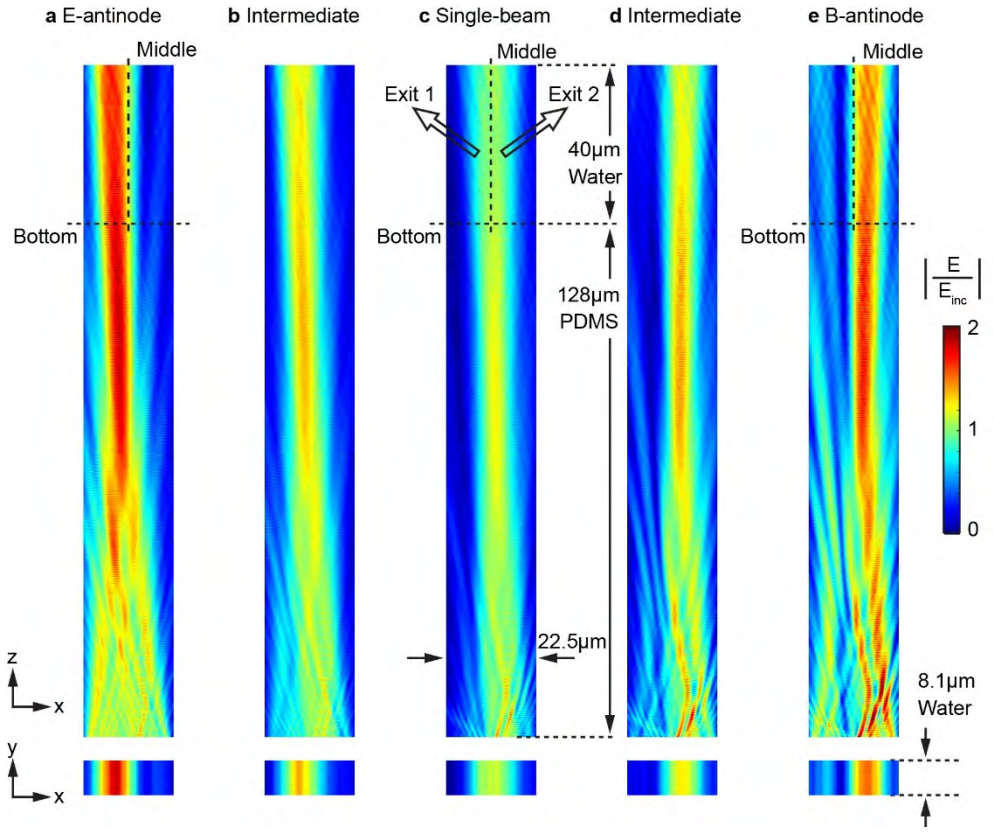

Fig. 4.11. Light focusing and steering situation of the metalens under five different coherent conditions, with the field ratio B_{Glass}/B_{PDMS} equals (a) $-1.5/1.4$, (b) $-1.5/2.8$, (c) 0, (d) 0.5 and (e) 1. The field in all the maps is normalized to the electric field of the incident light from the PDMS side, which is constant for all cases.

The top row of **Fig. 4.11** demonstrates the output field distribution in the xz plane (i.e. the cross section of the microchannel). Each map is 22.5 μm in width (the width of the metalens) and 168 μm in height (from 40 μm above the microchannel base to $\sim$ 2 μm above the metalens). A long, narrow focus flanked by weak sidebands is observed. The focus is steered continuously, moving across the middle line of the microchannel from **Fig. 4.11 a** to **Fig. 4.11 e**. The angle between the central axis of the focus and the z axis is $-1.37°$ and $1.36°$ in **Figs. 4.11 a** and **e**, respectively, representing a steering angle of approximately 2.7°. The conversion efficiency, which is defined as the energy ratio of the main focus lobe and the total input, is 16.4% and 10.4% for the E-antinode focus and the B-antinode focus, respectively.

The elongated focus and its sidebands in the xz plane (see **Fig. 4.11**), together with the V-shaped phase profile (see **Fig. 4.9**), resemble a Bessel-beam focus as shown in **Fig. 4.12**. Bessel beams are produced traditionally employing a glass axicon lens and, more recently, utilizing a variety of metasurface lenses (hence the terminology of axicon metalens and meta-axicon)

[271–273]. They possess unique properties such as no-diffracting (i.e. capable of maintaining its transversal intensity profile in propagation) and self-healing (i.e. capable of recovering its original beam profile even if it is obstructed by a finite-sized object), which are ideal for high-throughput particle manipulation [274, 275]. The results in **Figs. 4.9** and **4.11** demonstrate that the metalens functions like a steerable, cylindrical (referring to the invariant focus shape along the y direction) glass axicon lens that can be used as variable-position optical traps and tweezers.

Fig. 4.12 demonstrates the output field profile extracted from the numerical simulation, matched with the conventional Bessel function of

$$J_0(x) = \frac{2}{\pi}\int_0^{\pi} \cos(x \cdot \sin\theta - n \cdot \theta)d\theta \tag{4.27}$$

where x is the coordinates orthogonal to the optical axis, and n is the integer order. In this case, only the first kind of Bessel beam is considered with zeroth integer order; hence Eq. 4.27 can be simplified to

$$J_0(x) = \frac{2}{\pi}\int_0^{\pi} \cos(x \cdot \sin\theta)d\theta \tag{4.28}$$

By mutiplying, the Bessel function with a field amplitude A_0, the intensity profile of a Bessel beam is obtained as

$$I = |A_0|^2 J_0^2 \tag{4.29}$$

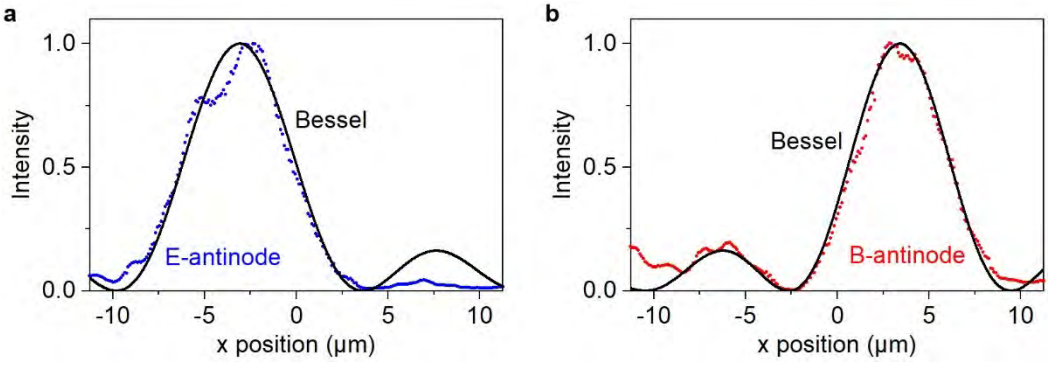

Fig. 4.12. Comparing the focus to an ideal Bessel beam. Output light intensity at a height of 10 μm above the microchannel base, overlaid with a zeroth-order Bessel function of the first kind for (a) the E-antinode focus and (b) the B-antinode focus. The center of the Bessel function is at (a) $x = -3.1\,\mu$m and (b) $x = 3.4\,\mu$m. Deviation from the ideal Bessel beam is attributed to the imperfect phase profile (see **Fig. 4.9**) and the output strength variation among the nanopillars (see **Fig. 4.10**).

Based on the output field in **Fig. 4.11**, trapping potential is calculated for two exampled polystyrene (PS) particles, a microsphere with a diameter of 1 μm (see **Fig. 4.13 a**) and a nanosphere with a diameter of 100 nm (see **Fig. 4.13 b**), in the microchannel. In the calculation, both particles are swept from the left to the right boundary of the microchannel at a height of 10 μm above the channel base. The trapping potential along this straight line is then calculated with respect to the starting point. As seen in **Fig. 4.13**, for both particles, the bottom of the potential well appears in the left half of the channel (at $x \approx -2.5$ μm) for the E-antinode

focus, while it moves to the right half (at $x \approx 2.5$ μm) for the B-antinode focus. This horizontal shift of the potential well clearly shows that coherent control enables particle routing. The depth of the potential well is roughly 100 and 0.1 $k_B \cdot T/(mW \cdot \mu m^{-2})$ for the microsphere and nanosphere, respectively, where k_B is the Boltzmann constant, and T is 297.15 K. It scales with the particle volume, as commonly observed in conventional optical traps (e.g. those generated by focusing a single input beam using a microscope objective). As the trapping strength is sensitive to particle size, the routing functionality demonstrated here may be adopted for size-based sorting in the future, potentially by judicially balancing the optical trapping with microfluidic forces.

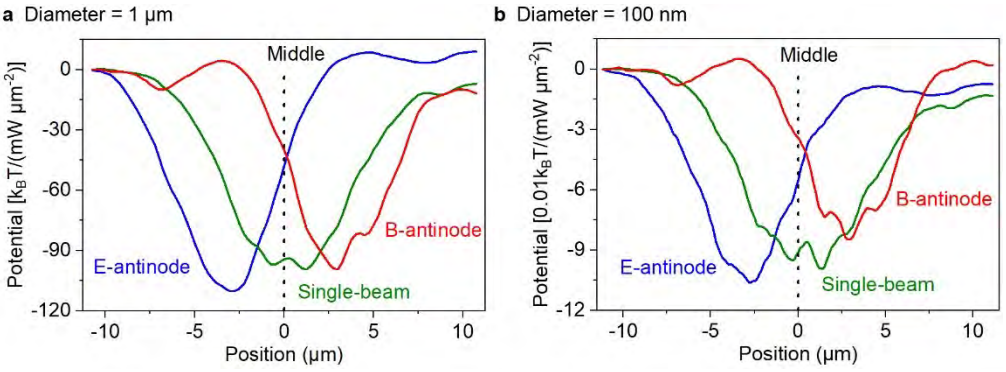

Fig. 4.13. Potential energy for trapping a single particle in the microchannel under three different illumination conditions. The particle diameter is (a) 1 μm and (b) 100 nm. In both cases, the center of the particle is fixed at 10 μm above the microchannel base. The vertical dashed lines indicate the middle of the microchannel. The potential is normalized against the total incident power, and it is set as zero at the left end of all curves.

In **Table 4.2**, three relevant forces on the particles are utilized to estimate the trajectories of the particles under the illumination conditions. The radiation pressure (i.e. the scattering force) pushes the particle along the $+z$ direction as calculated by using Eq. 4.36. The radiation pressures are strong enough to overcome gravities under all these three illuminations. The mean viscous force, which is equal to the average optically induced gradient force, is the average Stoke's drag, as the particles move across the viscous flow. As discussed in Chapter 3, when the particle weight is much smaller than the optical gradient force, only the effect of the viscosity force on the terminal velocity is considered. Based on the potential wells shown in **Fig. 4.13**, effective guiding requires manipulating the particles 2.5 μm horizontally (i.e. x axis). By using Eq. 3.1, the terminal velocities of the micro- and nano-sphere are calculated to be 2.38 μm/s and 33.23 nm/s, respectively. The time requirements to travel across 2.5 μm are 1.05 s and 75 s, respectively. Assuming that the length of the guiding channel is 1 cm, the maximum water velocities that can be used for the particle sorting are 9.52 and 0.13 mm/s, respectively.

Table 4.2. Relevant forces on the micro- and nano-particle in the microchannel under the E-antinode, the B-antinode, and the single beam conditions. All the values are force in the unit of $\mathrm{N/mW \cdot \mu m^{-2}}$**.**

Diameter	Gravity	Radiation pressure			Mean viscosity force		
		E	B	S	E	B	S
1 μm	5.1e-18	1.7e-14	1.5e-14	1.7e-14	2.4e-14	2.0e-14	1.9e-14
100 nm	5.1e-21	1.6e-16	1.5e-16	1.7e-16	2.2e-17	1.9e-17	2.0e-17

4.8 Optical force on Rayleigh and Mie particles

In this section, more details on the optical force analysis are discussed. Both the microsphere and nanosphere are simulated at 10 μm above the microfluidic base and located in 5 different locations along the x axis. By referring to the potential map (see **Fig. 4.13**), these locations are selected at $x = -6$ μm, -3 μm, 0, 3 μm, and 6 μm, respectively (**Figs. 4.14** and **4.15**). Where -3 μm and 3 μm are approximately the stable trapping position under the E-antinode and the B-antinode illumination condition, while the maximum trapping depth at the single-beam illumination is approximately at the middle of the microchannel (i.e. $x = 0$). For visualization, each sphere is segmented into 50 equivalent pieces, with respective optical forces analyzed on each of them as shown by using the arrows. All optical forces are calculated by using the Maxwell stress tensor (see Eq. A.25, in Appendix A), which is extracted from COMSOL numerical simulation.

Fig. 4.14 shows force maps (shown by arrows) and power outflow (in the color map) on the surface of the trapped microsphere at the five different locations. The microsphere has a refractive index of 1.46 and a diameter of 1 μm. Three illumination conditions are considered, which are the E-antinode (left column), the single beam (middle column), and the B-antinode (right column). At the E-antinode, the force is the strongest when the microsphere is located at $x = -3$ μm, while the arrow distribution is almost symmetric with respect to the z axis. A similar feature is observed in the power outflow on the sphere with $x = -3$ μm showing the strongest response. When $x = -6$ μm and 0 the field distribution on the left hemisphere is different from that on the right hemisphere, and the arrows have an asymmetric size distribution as well. The arrows on the right half are slightly smaller than that on the left half when the microsphere is located at $x = -6$ μm. In contrast, when the microsphere is located at $x = 0$, the arrows on the left are larger. At the other two positions (i.e. $x = 3$ and 6 μm), the distribution of optical force and energy outflow on the sphere is hard to observe and can be ignored. Such force and power distribution support the result in **Figs. 4.11 a**, **4.12 a**, and **4.13 a**, which show the output field distribution, the light intensity distribution, and the potential distribution, respectively.

Similar responses are observed at the B-antinode condition. The left-half arrows are relatively smaller or larger than the right-half arrows when the microsphere is located at $x = 0$ or 6 μm, respectively. The optical force is hard to observe, when the of the microsphere is at

$x = -6$ μm and $x = -3$ μm; The relatively larger arrows on the microsphere at $x = -6$ μm correspond to the flanked sideband of the focus (see **Fig. 4.11 e**). The focus has a larger x span in the single-beam condition (**Fig. 4.11**). Arrows (i.e. optical force) of considerable size can still be observed on the microsphere far from the focus, that is, at $x = \pm 6$ μm, at the single-beam condition. The optical force is approximately balanced when the microsphere is in the middle of the channel. Meanwhile, the light force on the right hemisphere is stronger for the microsphere positioned in the left half of the channel (i.e. $x = -6$ and -3 μm) and vice versa.

As regard to the power density, it is always more pronounced on the upper edge of the microsphere than on the lower in all panels. This phenomenon originates from Mie scattering [276], which occurs if the size of the particle is similar to the wavelength of incident light. In this case, the microsphere with a diameter of 1 μm is close to the wavelength of the wavelength in water, which is 1.165 μm. The scattering intensity of the Mie scattering is greater in the forward direction (in this case, $+z$ direction) than in the reverse direction ($-z$ direction); that is, most of the incident light is scattered along the direction of propagation [277]. Based on the trajectory of a particle in an inhomogeneous electromagnetic field analyzed in Chapter 3, the particle tends to move towards positions where the electromagnetic field is the strongest. Due to this property, in order to trap Mie objects via strong gradient forces that overcome scattered field forces, 3-dimensional tweezers based on optical trapping should have a large numerical aperture.

In comparison to the Mie-sized sphere (i.e. the microsphere) in **Fig. 4.14**, the nanosphere shows distinct power and force distributions under all three illumination conditions, as shown in **Fig. 4.15**. The most obvious difference is that overall power outflow distribution is mostly uniform, except for the region around the equator. The equator region shows relatively low power outflow as compared to the other regions. While the equator region is perpendicular to the propagation direction of the scattering waves (see **Fig. 4.11**). In the 25 panels in **Fig. 4.15**, the largest arrow at the E-antinode, the single-beam, and the B-antinode appears with the nanosphere located at $x = -3$ μm, 0, and 3 μm, respectively. These positions correspond to the side wall of trapping potential wells (see **Fig. 4.13 b**). In addition, the optical force does not show any obvious difference between the left semi-sphere and the right semi-sphere of the nanosphere in all the maps. This indicates that trapping potential (see **Fig. 4.13 b**) is small. Due to the shallow potential well, these tunable metalens tweezers may require stronger incident power and an extended metalens array (in the y direction) to achieve trapping and routing of a nanosphere as compared with a microsphere.

Numerical calculation can be employed to predict the movement of an ultra-small particle allocated in an inhomogeneous electromagnetic field. When the particle's radius is much smaller than the incidence wavelength ($\leq \lambda/20$), it is a Rayleigh particle. In this case, the nanosphere with a radius of 50 nm is approximately $\lambda/24$, which satisfies the definition of a Rayleigh particle. This nanosphere can be simplified to an electric dipole, which follows the principle of Rayleigh scattering, namely Rayleigh approximation or Dipole approximation [278, 279]. As for an electric dipole, under the influence of an external photoelectric field (i.e.

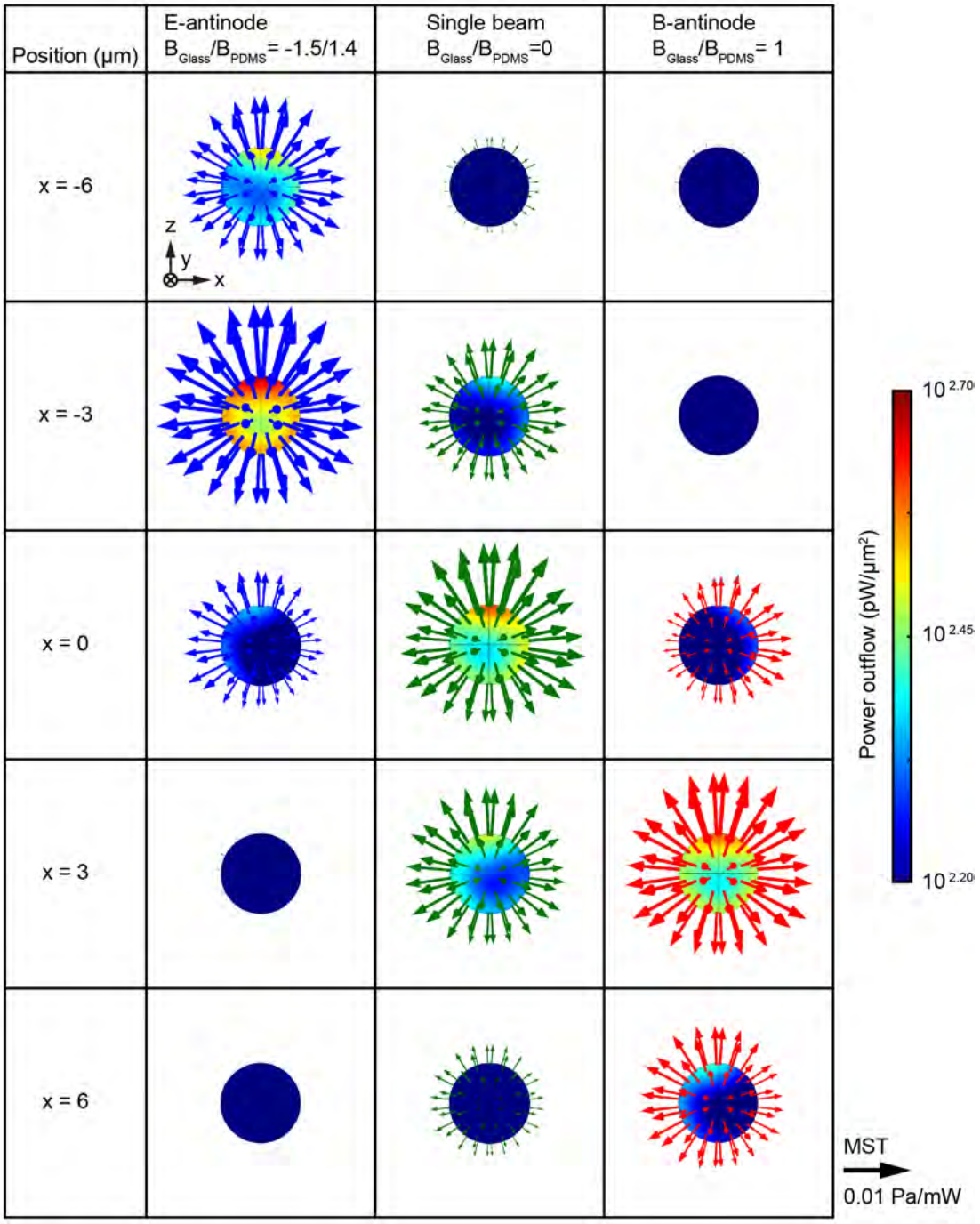

Fig. 4.14. Force maps for trapped particle with a diameter of 1 μm **under three different illumination conditions.** The power outflows (color map) and the Maxwell stress tensors (arrows) on the outer surface of the particle. The axes are specified in the top left panel. The power outflows show in the common logarithm. The color bar demonstrates the common logarithmic energy outflow, with the limit of the color scale set at $10^{2.2}$ to $10^{2.7}$ for visualization. Corresponding segmented optical force, i.e. Maxwell stress tensor (MST), with the micro-particle at five evenly spaced, representative locations along the horizontal direction, 10 μm above the microfluidic base (same condition as **Fig. 4.13 a**). Arrow maps represent the optical force on the corresponding segment of the micro-particle under three illumination conditions of interest. The scale is 0.01 Pa/mW.

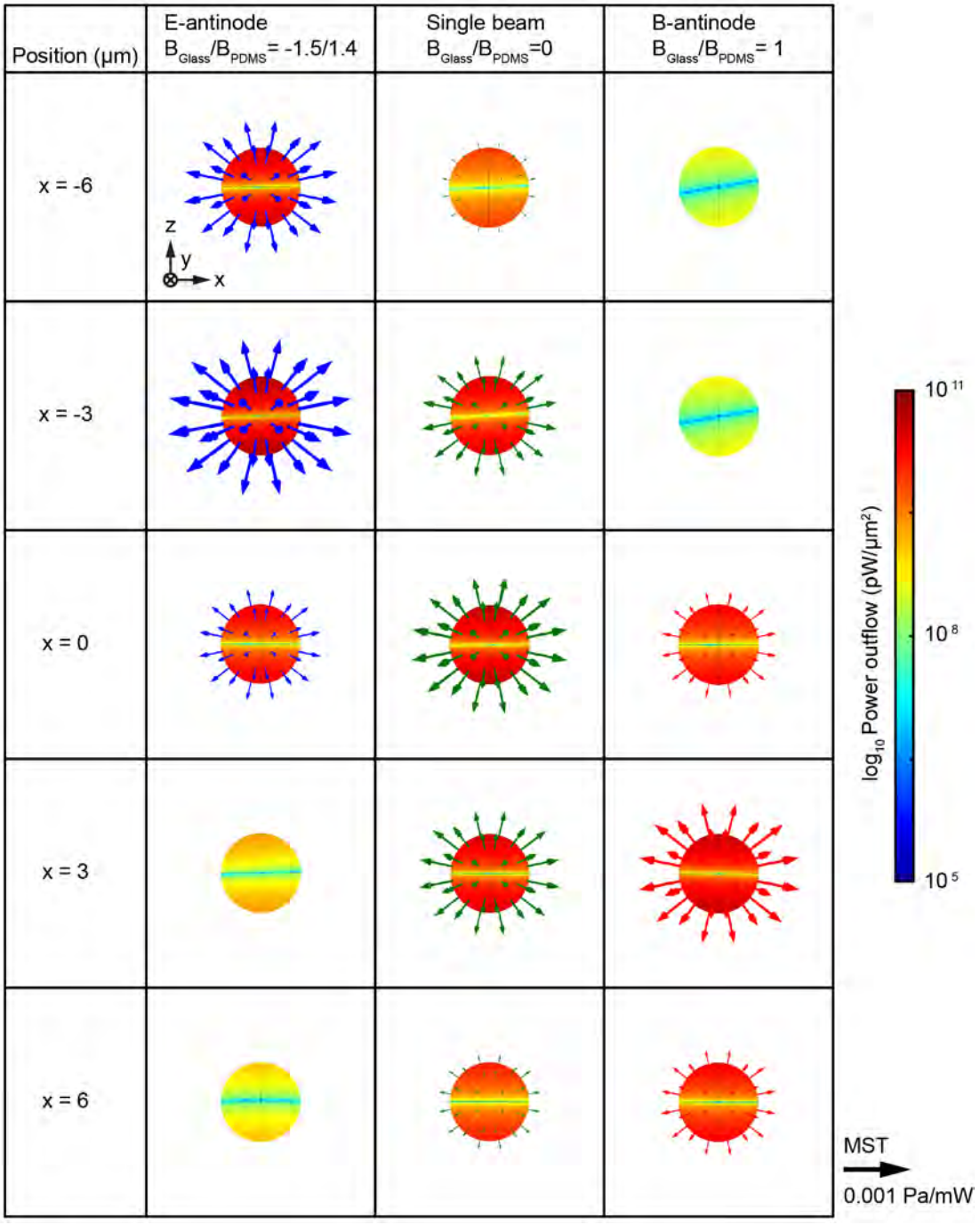

Fig. 4.15. Force maps for a trapped particle with a diameter of 100 **nm under three different illumination conditions.** All the panels are plotted following the same specifications as **Fig. 4.14**. The color scale is set from 10^5 to 10^{11} for visualization. The scale of the arrow is 0.001 Pa/mW.

electromagnetic field), a neutral dielectric sphere can be polarized into an oscillating electric dipole consisting of an electric dipole, a system comprised of two-point charges with equal value and different signs. As compared to the wavelength, the particle is so small that the electric field of the incident field across it is uniform. In the instantaneous electric field $E(r,t)$, the particle acts like a simple point dipole located at its center. At this condition, the dipole moment is obtained as

$$p(r,t) = 4\pi\epsilon_{medium}\alpha^3\left(\frac{\epsilon_{particle}-\epsilon_{medium}}{\epsilon_{particle}+2\epsilon_{medium}}\right)E(r,t) \tag{4.30}$$

$$p(r,t) = 4\pi n_2^2\epsilon_0\alpha^3\left(\frac{m^2-1}{m^2+2}\right)E(r,t) \tag{4.31}$$

where $\epsilon_{particle}$, ϵ_{medium} are the permittivity of the particle and the medium, respectively, while α is the radius of the particle. ϵ_0 is the vacuum permittivity. $m = n_{particle}/n_{medium}$ is the relative refractive index of the particle.

As regard to the radiation pressure force on the Rayleigh particle, one of the force is called a "scattering force" [280]. As the electric field oscillates in time in a harmonic situation, the induced point dipole moves in time with it. The particle then acts as an oscillating electric dipole that radiates secondary waves in all directions (corresponding to the arrows shown in **Fig. 4.15**). The scattering force occurring on the particle due to momentum conservation is described as

$$F_{scat}(r) = \frac{\sigma_{scat}\langle S(r,t)\rangle_T}{c/n_{medium}} \tag{4.32}$$

$$F_{scat}(r) = \frac{\sigma_{scat}n_{medium}\hat{z}I(r)}{c} \tag{4.33}$$

where c is the speed of light in vacuum, and $I(r)$ is the field intensity of the incident beam. The time-averaged Poynting vector $\langle S(r,t)\rangle_T$ and the cross section for the radian pressure of the particle σ_{scat} [280] are given by

$$\langle S(r,t)\rangle_T \equiv I(r) = \frac{1}{2}Re[E(r)\times H^*(r)] \tag{4.34}$$

$$\langle S(r,t)\rangle_T = \hat{z}\frac{n_{medium}\epsilon_0 c}{2}|E(r)|^2 = \hat{z}I(r) \tag{4.35}$$

$$\sigma_{scat} = \frac{8}{3}\pi(k\alpha)^4\alpha^2\left(\frac{m^2-1}{m^2+2}\right)^2 \tag{4.36}$$

where $k = 2\pi/\lambda$ is the wave vector. Eq. 4.36 can be derived to

$$\sigma_{scat} = \frac{128\pi^5\alpha^6}{3\lambda^4}\left(\frac{m^2-1}{m^2+2}\right)^2 \tag{4.37}$$

By substituting Eq. 4.37 into Eq. 4.33, the time-averaged scattering force is given by

$$F_{scat}(r) = \frac{128\pi^5\alpha^6}{3\lambda^4}\left(\frac{m^2-1}{m^2+2}\right)^2\frac{n_{medium}\hat{z}I(r)}{c} \tag{4.38}$$

Another component of trapping force is a gradient force [281], due to the Lorentz force acting on the Rayleigh particle by in an inhomogeneous electromagnetic field. By employing the electric dipole moment of Eq. 4.31 as an electrostatics analog of the electromagnetic field, a gradient force is obtained as

$$F_{grad}(r,t) = [p(r,t)\cdot\nabla]E(r,t) \tag{4.39}$$

$$F_{grad}(r,t) = 4\pi n_{medium}^2\epsilon_0\alpha^3(\frac{m^2-1}{m^2+2})\frac{1}{2}\nabla E^2(r,t) \tag{4.40}$$

By substituting Eq. A.16 and Eq. 4.40 into Eq. 4.39, the time-averaged gradient force is given by

$$F_{grad}(r) = \left\langle F_{grad}(r,t)\right\rangle_T \tag{4.41}$$

$$F_{grad}(r) = 4\pi n_{medium}^2\epsilon_0\alpha^3(\frac{m^2-1}{m^2+2})\frac{1}{2}\nabla\left\langle E^2(r,t)\right\rangle_T \tag{4.42}$$

$$F_{grad}(r) = \pi n_{medium}^2\epsilon_0\alpha^3(\frac{m^2-1}{m^2+2})\nabla E^2(r,t) \tag{4.43}$$

$$F_{grad}(r) = \frac{2\pi n_{medium}\alpha^3}{c}(\frac{m^2-1}{m^2+2})\nabla I(r) \tag{4.44}$$

By combining the scattering force (Eq. 4.38) and the gradient force (Eq. 4.44), the total force on the nanosphere, can be calculated. Because the scattering field propagates along the $+z$ axis, the trapping force of interest is a horizontal force in the x axis. The propagating wave is further approximated as a plane wave. Consequently, only the gradient force applied on the nanosphere by the narrow focusing beam is considered in the numerical calculation. Based on the field intensity in **Fig. 4.12**, optical force on the nanosphere under the E-antinode and B-antinode are calculated by employing Eq. 4.44. By integrating the calculated gradient force along the $+x$ direction, the trapping potential is obtained. In **Fig. 4.16**, the simulated potential of the nanosphere under the E-antinode and the B-antinode conditions are reproduced from **Fig. 4.13** as a reference. I notice that, the calculated potential needs to be divided by a factor of 1.4 to make the two maximum depths [i.e. calculated curves (dash lines) and simulated curves (straight lines)] roughly identical. After this correction, the numerical and the analytical results show good match.

The differences between the numerically simulated and the analytically calculated results may be due to the omission of scattering force in the calculation. Nevertheless, the profile of the analytical trapping potential is sufficiently accurate to predict the trapping location (i.e. maximum trapping depth). As shown in **Fig. 4.16**, the trapping location of the nanosphere under the E-antinode and the B-antinode conditions is $x = -2.80$ μm and $x = 2.90$ μm, respectively. In contrast, the calculated maximum trapping depth appears at $x = -2.95$ μm and $x = 3.1$ μm under the corresponding illumination conditions. Utilizing the Rayleigh approximation, one can quickly calculate the trapping position and trapping potential for a Rayleigh sphere in an electromagnetic field. Since the scattering field is symmetric around the optical axis, it

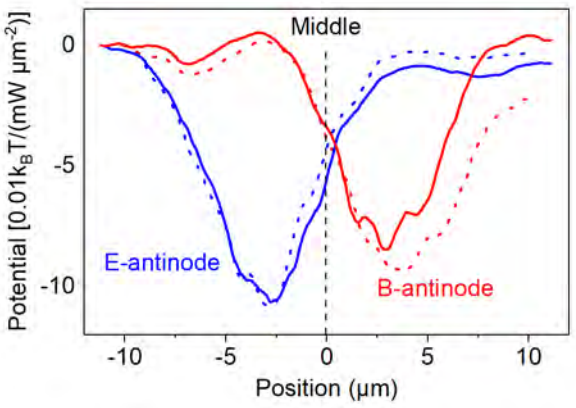

Fig. 4.16. Comparison of numerically simulated and analytically calculated potential energy. Potential energy for trapping a Rayleigh size particle in the microchannel under the E-antinode (blue) and the B-antinode (red) illumination conditions. The particle is 100 nm in diameter, and the position is plotted following the same specifications as **Fig. 4.13 b**. Straight lines represent numerical simulation, and dot lines represent analytical calculation.

is possible to get a more accurate result when the focusing beam moves along the optical axis, which is perpendicular to the focusing lens.

4.9 Conclusion of Chapter 4

To conclude, I have proposed and numerically evaluated a coherently controlled metalens that functions as tunable optical tweezers. Being an array of Si nano-pillars with a subwavelength thickness, the metalens focuses incident light into a thin sheet, which is similar to a cylindrical, axicon lens made of glass. The phase profile of the metalens can be coherently controlled, where the two counter-propagating incident light beams are adjusted in their relative phase and strength. This results in continuous steering of the focus across the microfluidic channel, enabling the routing of both nano- and micro-sized particles in a Y-branch junction. Through modulating the response of the metalens, the coherent illumination enables controllable transverse (i.e. normal to the beam axis) particle steering, which has not been achieved in traditional dual-beam optical traps. I also built a tunable metalens tweezers using a hyperbolic phase profile for comparison, see Appendix B for details.

Simultaneously, the optical force and power outflow on the microsphere and nanosphere are analyzed. Differences between Mie particles (the microspheres) and Rayleigh particles (the nanospheres) in a homogeneous electromagnetic field are discussed. The Rayleigh approximation is used to simplify the optical force calculation for a particle with dimensions in the Rayleigh regime.

Metalens, as well as the broader concept of the metasurface, enables novel light manipulation through nano-engineering. This capability that holds great promise for novel particle manipulation in next-generation optofluidics and lab-on-a-chip systems. Although it no

longer provides sub-wavelength focusing as seen in other nanophotonic platforms, metalens enables a very high level of flexibility in shaping the light field, as the far field distribution (here a steerable Bessel-beam focus) no longer has to trace the geometric shape (here an array of nano-pillars with fixed shape and dimensions) of the nanostructures. This work opens a new avenue for exploring the integration of nanophotonics and microfluidics by demonstrating particle routing based on coherently tunable metalens tweezers.

Chapter 5

Self-sorting metalens-doublet tweezers

Tuneable manipulation of dielectric spheres in a microfluidic channel in the near-field and far-field has been numerically demonstrated in the previous two chapters. These approaches realize micro- and nano-scale particle trapping and manipulation by using a structured surface beneath a continuous flow. However, these systems require external modulation mechanisms that are not autonomous. Here, I report a novel self-tracing sorter that can automatically guide target fluorescent spheres to an appointed microfluidic channel without a judge-and-control mechanism. The particle sorter is a metalens-doublet that consists of two layers of amorphous silicon nanopillars on both sides of a silicon dioxide layer. The metalens array can automatically trace fluorescent beads with a fluorescent wavelength of 680 nm. Adding an optical reflection layer enables the fluorescent sphere to be sorted and guided in an *X*-branch microchannel.

5.1 Introduction to Chapter 5

Metasurface lens is a two-dimensional array of subwavelength artificial structures. It can efficiently modulate the amplitude, phase, propagation mode, and polarization of electromagnetic waves while possessing the properties of low loss, ultrathin thickness, and easy integration. It is also possible to modulate the dispersion of electromagnetic waves within a certain spectral region. Therefore, metalens show advantages over conventional diffractive lenses in many applications are anticipated to critical for the future generation's miniaturized, efficient, and adaptable optical imaging systems, for instance, broadband achromatic [282], imaging beyond the diffraction limit [283, 284], multifocal [285, 286], phase gradient imaging [287], chiral imaging [288], tomography [289], and tunable steering systems [9, 201]. All of these previous approaches achieve light bending by utilizing a thin layer of well-designed metamaterial surface, known as metalens singlet. In contrast, a multi-layered cascaded metalens has been employed recently to remedy the insufficiency of the metalens singlet. In the context of optics correction,

such cascaded metalens, metalens doublet or metalens triplet, realize wide broadband achromatic correction [290, 291], large angle coma correction [210], astigmatism correction [210] and aberration correction [211]. With the advancement of metalens research, a number of specialized imaging functionalities have been achieved, owing to single-phase modulation evolving into a combination of multi-modulation approaches. In addition, continuous optical focusing control becomes possible, and the integration of multiple functions has also been accomplished [292–294].

In this chapter, I demonstrate a metalens doublet as a refocusing metalens for automatic trapping, guiding, and sorting of fluorescent beads. This innovative retroreflector (i.e. planar retro-reflective metalens [212]) design enables the automated tracking of point light sources. Conventional fluorescent bead sorting, namely Fluorescence-Activated Cell Sorting (FACS), requires bulk equipment with a detector, controller, and electrodes to generate instantaneous electric field for sorting [295]. Because of its various drawbacks (e.g. large footprint and high cost), a significant amount of research has been devoted to developing its microfluidic counterpart, μFACS. In contrast, optical tweezers, i.e. utilizing optical and photonic structures to establish a strong electromagnetic field for confining tiny objects in the field, have been applied in medical, biomedical, and biochemical research. By utilizing near-field tweezers (plasmonic tweezers) [8] and far-field tweezers (photonic tweezers) [9], various manipulation of the particle can be achieved with an integrated microfluidic system, which is known as optofluidics [10]. This technique provides a series of potential applications , for instance, Optical cell stretcher [296], dual-beam laser traps [256], and fiber-based optical tweezers [297]. These previous researches use fiber to confine the propagating wave into the microchannel, which restricts the integrated level. The metalens doublet design shown in this chapter exhibits self-tracking functions that can be used to realize continuous manipulation of waterborne fluorescent beads. The interaction between the metalens doublet and the fluorescence radiation can automatically trap and sort fluorescent beads based on radiation wavelength. The design in this chapter is the first research that introduces the self-tracking of metalens doublet embedded in microfluidics. As compared to FACS and μFACS, because the embedded metalens doublet eliminates the need for any additional sorting mechanism, the technique can be referred to as FEACS (Fluorescence-Enabled Automatic Cell Sorting) to highlight its self-sorting capability.

5.2 System design: self-tracing metalens doublet sorter

This section shows the schematic of a self-tracking, metalens-doublet-based fluorescent bead sorter that sorts waterborne fluorescent beads in an X-shape microfluidic channel. The whole system acts as self-feedback optical tweezers. The photonic component of the metalens-doublet-sorter is an array of metalens unit cells (i.e. the minimum periodic structure in the array), which comprises of silicon nanopillars supported on both sides of a glass layer with a thickness of 20 μm (see **Fig. 5.1 a**). Each unit cell of the metalens array consists of two metalenses, i.e. metalens A and B, as shown in **Fig. 5.1 a**. A SU-8 photoresist layer protects the

metalens B, and a gold layer as a mirror is developed on the bottom of the SU-8 layer (more details is **Fig. 5.3 a,d**). Each unit cell has approximately 15.6 μm width (on the x axis) and 15 μm length (on the y axis), with a periodic of 16 μm in both the x- and y-axes.

The metalens-doublet sorter is located beneath a microfluidic channel (see **Fig. 5.1 a**). The microspheres are carried by fluidic flow along the $+y$ direction. The fluid contains three different spheres (i.e. red fluorescent beads with an emission wavelength of 680 nm, blue fluorescent beads with an emission wavelength of 430 nm, and non-fluorescent beads). As **Fig. 5.1 b** illustrates, the microfluidic channel consists of two inlets and two outlets (i.e. a symmetric structure). The fluidic flows, which are classified as the buffer flow and the sample flow, are controlled separately to generating a velocity difference. Two flows are highlighted by a different color in **Fig. 5.1 b** for visualization, and both velocities are adjusted to satisfy the requirement of laminar flow, referring to Eq. 4.1. By speeding up the flow velocity of the buffer flow, a water "barrier" is established to realize that the sample flow can be restricted to the inlet-1-to-outlet-1 path rather than leaking to outlet 2 [298]. In this design, the buffer flow velocity is set to be twice that of the sample flow to create the water barrier [299]. The metalens-doublet-array is allocated along the path of inlet-1-to-outlet-2 while athwart the two fluidic flows.

The metalens-doublet sorter is essentially a planar retro-reflector, similar to a cat's-eye mirror; this function, based on Arbabi's research [212], cannot be achieved by using a single-layer gradient metasurface. For conventional retro-reflectors, it is difficult to achieve on-chip integration due to their bulky, spherical profile. Therefore, the double-layer coaxial metalens array is selected in this design to achieve the sorting function in a microfluidic channel. In addition, the fluorescent sphere is employed as the target particle in this design. Once light illuminates the fluorescent sphere, its energy induces electrons to jump from the ground state to a higher state. The excited state is unstable, and the electrons will return to the ground state, which causes energy to be released in the form of photons. In order to excite the fluorescent sphere, continuous illumination is required from the side of the microfluidic channel.

All microspheres (i.e. the red fluorescent beads, the blue fluorescent beads, and the non-fluorescent beads) enter the microchannel from inlet 1, namely the sample port, and are transported by the continuous fluidic flow along the channel. Without the photonic components, all microspheres will follow the fluid and outflow the microchannel from outlet 1 (the waste port). The metalens-doublet-sorter can refocus the fluorescence radiation from the red fluorescent beads (i.e. target microspheres) back on them (see **Fig. 5.1 a**). As discussed in the previous chapters, the converging light beam can trap the microsphere at its focus. According to the gradient force on the red fluorescent bead, the target microsphere could stride over the water barrier and drift along the metalens array into the buffer flow, resulting in the target microsphere reaching outlet 2 (namely the collect port). Residual microspheres, i.e. the blue fluorescent beads and the non-fluorescent beads, would remain in the sample flow and outflow the microchannel via the waste port, as shown in **Fig. 5.1 b**.

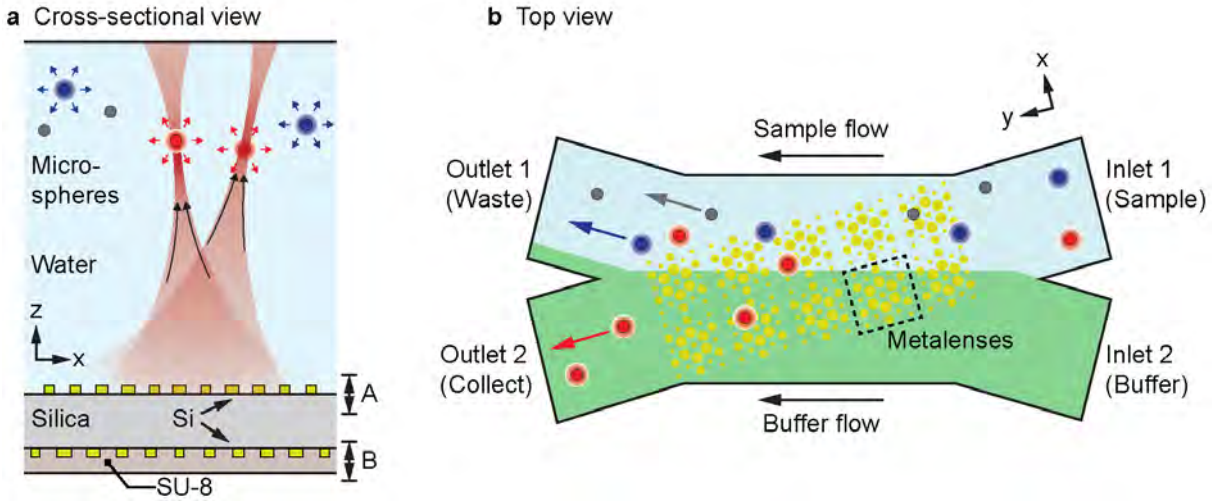

Fig. 5.1. Schematic diagram of self-feedback metalens doublet and the application of optofluidic particle sorting. (a) Schematic of the metalens doublets, which are arrays of Si nanopillars (in yellow) on the opposite sides of a silica substrate. The metalens doublet is positioned under a microfluidic channel that contains different fluorescent particles (red and green) and non-fluorescent particles. These two layers focus the light radiated by the target particle back onto the source. A and B represent the metalens *A* component and the metalens *B* component (see **Fig. 5.5** for details) in the metalens doublet, respectively. (b) The metalenses with a tilted angle (from inlet 1 to outlet 2) beneath the *X*-shape microfluidic channel. All particles are injected into this micro-channel from inlet 1. The target particles (in red color) can be transported to outlet 2 via their interaction with the metalenses.

The fluorescence radiation, light focusing, and optical force of the metalens doublets sorter are numerically simulated by using a commercial finite element solver (COMSOL Multiphysics) and a Finite-Difference Time-Domain (FDTD) solver (Lumerical). For all illumination conditions utilized in this chapter, the incident wave is polarized along the x axis. The target wavelength of the metalens doublet is 680 nm (i.e. the red fluorescent bead). At this wavelength, the refractive indices of water, *SU*-8, glass, gold and amorphous silicon is set at 1.3306 (n_{water}), 1.5839 (n_{su8}), 1.4558 (n_{glass}), $0.1773 + 3.8844i$ (n_{gold}), and $3.6941 + 0.0167i$ (n_{Si}) [244, 300–302]. Based on my previous research shown in the Chapter 3 and Chapter 4, the fluorescent light is approximated using an electric dipole, referring to the radiation of a tiny fluorescent bead [303]. The polarization of the electric dipole is set in the x direction. All microspheres are polystyrene beads with a refractive index of 1.5841 (n_{ps}) [304] and a diameter of 1 μm. Optical force on the microsphere is derived by integrating the Maxwell stress tensor at the surface. As shown in the Section 5.10, the trapping potential is calculated by integrating the optical force along a straight line.

5.3 Ray tracing method: Ray transfer matrix analysis

In this section, ray transfer matrix analysis is used to predict light ray propagation in the system. **Fig. 5.2** show two ray diagrams that represent the possible optical paths of the metalens

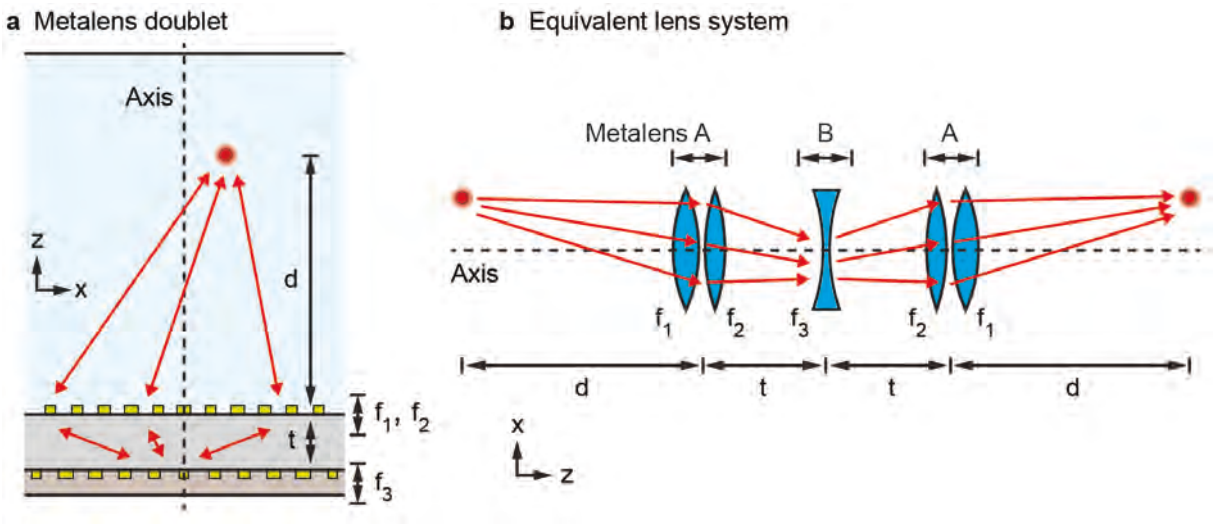

Fig. 5.2. Schematic illustration of the metalens doublet and its equivalent glass lenses for focusing analysis. (a) A single microsphere is positioned at a distance of d above Metalens A, which is separated from Metalens B by a spacer layer with a thickness of t. The phase profile of Metalens A contains two terms of f_1 and f_2, while that of Metalens B contains a single term of f_3. The arrowed lines indicate that the fluorescent light radiated by the microsphere is focused by the metalens doublet back onto the microsphere. (b) The equivalent lens system consists of a set of five lenses in the sequence of f_1, f_2, f_3, f_2, and f_1. Each pair of lenses f_1 and f_2 is in close proximity, and its distance to lens f_3 is t. The lens system focuses light radiated by the source microsphere on an image microsphere. The re-focusing functionality is achieved if the whole system, including the five lenses and the two microspheres, possesses a left-right mirror symmetry.

doublet. Divergent rays (i.e. a spherical wave from a fluorescent bead) propagate to metalens A and are focused onto metalens B. The reflected rays from metalens B focus back on the fluorescent bead via metalens A (see **Fig. 5.2 a**). For visualization, an equivalent lens system is shown in **Fig. 5.2 b** to clarify the operation principle of this metalens doublet. Metalens A consists of two components. Both are spherical convex lenses, and they have different focal distances of f_1 and f_2. In the equivalent lens system (see **Fig. 5.2**) and phase gradient selection (see **Fig. 5.9**), metalens A is split into two lenses, one to modulate the fluorescent sphere scatters light and the other to focus it. Such equivalence simplifies the design of wavefronts. By contrast, metalens B as a concave lens has a single hyperbolic component with a focal distance of f_3. Metalens A and B, as a pair of co-axial lenses, are separated by a glass layer with a thickness t, which is equal to f_2 and f_3 (i.e. $t = f_2 = f_3$). Initially, the position of the target microsphere is at $z = f_1$ and $x = 0$ (on the optical axis).

In the ray matrix analysis, an optical system can be characterized using a 2×2 matrix of

$$M = \begin{bmatrix} m_{11} & m_{12} \\ m_{21} & m_{22} \end{bmatrix} \tag{5.1}$$

which links the input and output light as below

$$\begin{bmatrix} r_{out} \\ r'_{out} \end{bmatrix} = M \begin{bmatrix} r_{in} \\ r'_{in} \end{bmatrix} \tag{5.2}$$

Here, r_{in} and r'_{in} are the position (with respect to the optical axis) and the slope (the tangent function of the angle formed by the ray and the optical axis) for the incident light. r_{out} and r'_{out} are the corresponding parameters of the output light.

As an example, for an optical system that contains only a single lens, the corresponding ray matrix M is

$$M = \begin{bmatrix} 1 & 0 \\ -\frac{1}{f} & 1 \end{bmatrix} \tag{5.3}$$

where f is the focal length of the lens. It is positive for a convergent lens and negative for a divergent lens. Meanwhile, for two lenses placed in close vicinity, the matrix M is

$$M = \begin{bmatrix} 1 & 0 \\ -\frac{f_1+f_2}{f_1 f_2} & 1 \end{bmatrix} \tag{5.4}$$

where f_1 and f_2 are the focal lengths of the two lenses. By comparing with the equation above, we can see that these two lenses are equivalent to a single lens with a focal length of $f_1 f_2/(f_1 + f_2)$.

For a generic configuration where a lens f_a, a lens f_b and a lens f_a are spaced evenly and in sequence along the optical axis, the matrix M is expressed as

$$M = \begin{bmatrix} 1 & 0 \\ -\frac{1}{f_a} & 1 \end{bmatrix} \begin{bmatrix} 1 & t \\ 0 & 1 \end{bmatrix} \begin{bmatrix} 1 & 0 \\ -\frac{1}{f_b} & 1 \end{bmatrix} \begin{bmatrix} 1 & t \\ 0 & 1 \end{bmatrix} \begin{bmatrix} 1 & 0 \\ -\frac{1}{f_a} & 1 \end{bmatrix} \tag{5.5}$$

where t is the distance between adjacent lenses. The components of the matrix are

$$m_{11} = \frac{f_a f_b - (f_a + 2f_b)t = t^2}{f_a f_b} \tag{5.6}$$

$$m_{12} = t(2 - \frac{t}{f_b}) \tag{5.7}$$

$$m_{21} = -\frac{(f_a - t)(f_a + 2f_b - t)}{f_a^2 f_b} \tag{5.8}$$

$$m_{22} = m_{11} \tag{5.9}$$

Under the condition of $f_a = -f_b = t$, the matrix can be simplified as

$$M = \begin{bmatrix} 1 & 3t \\ 0 & -1 \end{bmatrix} \tag{5.10}$$

which results in the retro-reflection of plane waves.

The matrix M of the particle-tracing metalens proposed in this work, which is depicted in **Fig. 5.2**, also takes the form of Eq. 5.5, where

$$f_a = \frac{f_1 f_2}{f_1 + f_2} \tag{5.11}$$

$$f_b = f_3 \tag{5.12}$$

$$f_2 = -f_3 = t \tag{5.13}$$

It can be simplified to

$$M_{tr} = \begin{bmatrix} -1 - \frac{3t}{f_1} & 3t \\ \frac{1}{f_1}(2 + \frac{3t}{f_1}) & -1 - \frac{3t}{f_1} \end{bmatrix} \tag{5.14}$$

A series of conclusions can be derived from this equation, depending on the distance d between the particle and the first lens f_1, as well as whether the particle is on the optical axis.

5.3.1 Focusing for a particle that is on-axis and $d = f_1$

In this case, the vector of any input light ray can be expressed as

$$\begin{bmatrix} r_{in} \\ r'_{in} \end{bmatrix} = \begin{bmatrix} r'_{in} d \\ r'_{in} \end{bmatrix} \tag{5.15}$$

The vector of the output light rays is consequently

$$\begin{bmatrix} r_{out} \\ r'_{out} \end{bmatrix} = M_{tr} \begin{bmatrix} r'_{in} d \\ r'_{in} \end{bmatrix} = \begin{bmatrix} -r'_{in} d \\ r'_{in} \end{bmatrix} = \begin{bmatrix} r'_{in} f_1 \\ r'_{in} \end{bmatrix} \tag{5.16}$$

This result indicates that the output light is focused on the optical axis at a distance of f_1 from the output lens. In the metalens doublet configuration, it is equivalent to focusing back on the light-emitting particle. It is worth noting that $r_{out}/r'_{out} = r_{in}/r'_{in}$, with the negative sign indicating that for any input light ray, its corresponding output light ray is on the opposite side of the optical axis.

5.3.2 Focusing for a particle that is off-axis and $d = f_1$

In this situation, the particle deviates from the optical axis by a distance of $\Delta\rho$. The input light has

$$r'_{in} = \frac{r_{in} - \Delta\rho}{d} = \frac{r_i n - \Delta\rho}{f_1} \tag{5.17}$$

The vector of the output light lays is consequently

$$\begin{bmatrix} r_{out} \\ r'_{out} \end{bmatrix} = M_{tr} \begin{bmatrix} r'_{in} f_1 + \Delta\rho \\ r'_{in} \end{bmatrix} = \begin{bmatrix} -(r'_{in} f_1^2 + \Delta\rho(f_1 + 3t))/f_1 \\ (r'_{in} f_1^2 + \Delta\rho(2f_1 + 3t))/f_1^2 \end{bmatrix} \tag{5.18}$$

which leads to

$$-r_{rout} + \Delta\rho = r'_{out} f_1 \tag{5.19}$$

This result indicates a focus that is at a distance of f_1 from the output lens and is off-axis by $\Delta\rho$. In the metalens doublet configuration, it indicates that the focus is still on the particle.

5.3.3 Focusing for a particle that is on axis and $d \neq f_1$

We can assume that d deviates from f_1 by a distance of Δz, with

$$d = f_1 + \Delta z \tag{5.20}$$

The vector of any input light ray is now

$$\begin{bmatrix} r_{in} \\ r'_{in} \end{bmatrix} = \begin{bmatrix} r'_{in}(f_1 + \Delta z) \\ r'_{in} \end{bmatrix} \tag{5.21}$$

The vector of the output is consequently

$$\begin{bmatrix} r_{out} \\ r'_{out} \end{bmatrix} = M_{tr} \begin{bmatrix} r'_{in}(d + \Delta z) \\ r'_{in} \end{bmatrix} = \begin{bmatrix} -r'_{in}(f_1^2 + \Delta z(f_1 + 3t))/f_1 \\ r'_{in}(f_1^2 + \Delta z(2f_1 + 3t))/f_1^2 \end{bmatrix} \tag{5.22}$$

The deviation of the focal point from the particle is

$$-\frac{r_{out}}{r'_{out}} - f_1 = -\frac{\Delta z f_1^2}{f_1^2 + \Delta z(2f_1 + 3t)} \tag{5.23}$$

where the negative sign in front of the term r_{out}/r'_{out} is required to address the relative position of the output ray with respect to the input ray. For a small value of Δz, $f_1^2 + \Delta z(2f_1 + 3t) \approx f_1^2$, which leads to

$$-\frac{r_{out}}{r'_{out}} - f_1 \approx -\Delta z \tag{5.24}$$

In the metalens doublet, this result indicates a negative feedback force. For a light-emitting particle on the optical axis, a small vertical drift from the position of $d = f_1$ induces a drift in the focus, which is by the equal distance in the opposite direction. An optical gradient force is created due to the relative movement between the focus and the source, which can be used to restore the vertical position of the particle to $d = f_1$ in the microchannel.

Based on Eqs. 5.16, 5.19, and 5.24, the relative movement of the fluorescent sphere and the refocal point can be predicted. The focus can coincide with the target sphere when the sphere is located at the initial position. When the microsphere at a fixed height deviates from the optical axis, refocusing light will follow the trajectory of the microsphere. Meanwhile, the refocal point will move in the opposite direction once the microsphere moves along the optical axis ($\pm z$ direction).

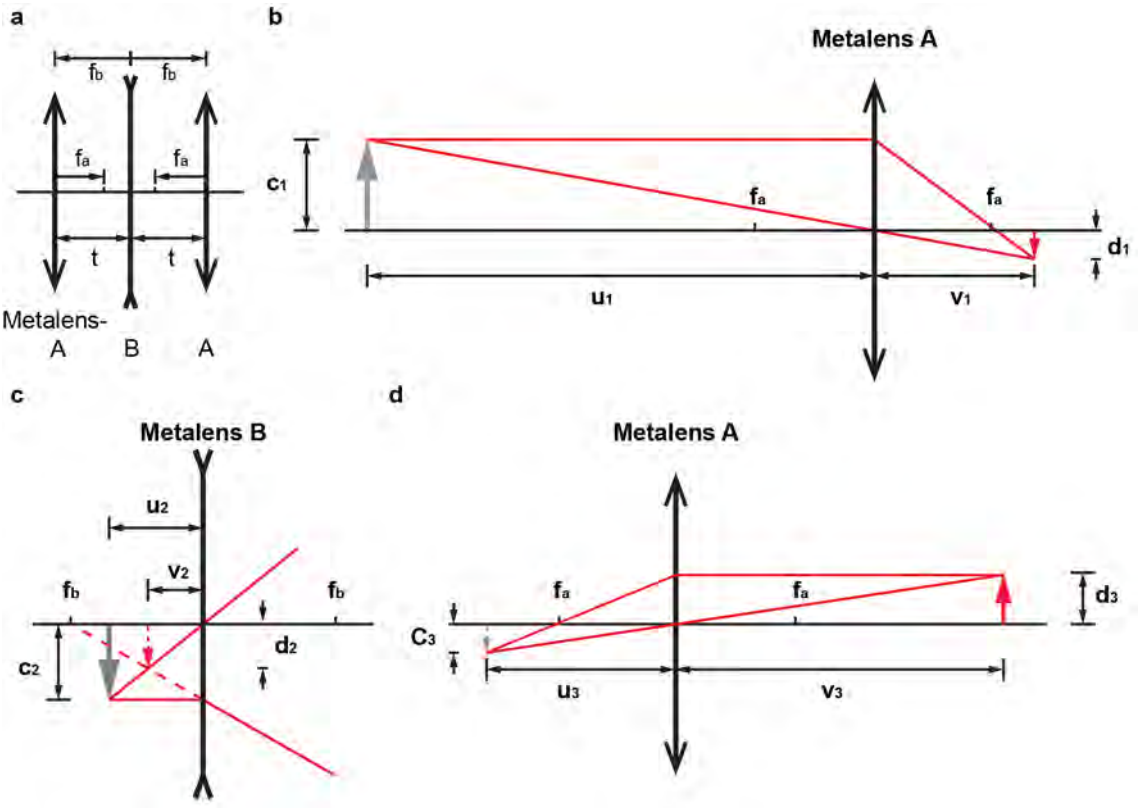

Fig. 5.3. Schematic view of the metalens doublet and its ray tracing utilizing a standard imaging system. (a) The equivalent lens system consists of a set of three lenses in a sequence of metalens A, B, and A, referring to **Fig. 5.2 b**. The distance between adjacent lenses is based on the focus of the metalens B (i.e. f_b), with $|f_a| < |f_b|$. metalens A is set as a convex lens, and metalens B is defined as a concave lens. (b) Imaging by the convex lens (i.e. metalens A), where the grey and red arrows represent the object and real image, respectively. (c) Imaging by the concave lens (i.e. metalens B), where the grey arrow and red dash arrow represent the object (i.e. real image from the metalens A) and the virtual image, respectively. (d) Imaging by the convex lens, where the object (grey dash arrow, virtual image from the metalens B) an the real image (red arrow) locate on the opposite sides of the lens.

5.4 Ray tracing method: Geometrical optics

An alternative, potentially more intuitive method to analyze the focus is to use the ray tracing in geometrical optics, which is discussed in this section. In this case, the cascaded metalens doublet is equivalent to a convex-concave-convex lens system, as shown in **Fig. 5.3 a**. The positions of the fluorescent sphere and focal points are represented by objects and real images with heights (see **Figs. 5.3 a** and **b**). To a divergent beam where there is no focus, a virtual image is utilized (see **Figs. 5.3 c** and **5.4**). A benefit of using this method is that, it can also describe a complex situation where the microsphere is neither on the optical axis nor at the initial height.

In this metalens doublet, the focal distance of the metalens is B f_b. The distance between metalens A and B is t. The focal length of metalens A contains two terms f_1 and f_2, which can

be described by

$$\frac{1}{f_a} = \frac{1}{f_1} + \frac{1}{f_2} \tag{5.25}$$

$$f_b = f_2 = t \tag{5.26}$$

5.4.1 The situation in Fig. 5.3 b

The distances can be found using the thin lens formula as

$$\frac{1}{v_1} = \frac{1}{f_a} - \frac{1}{u_1} \tag{5.27}$$

Based on the Euclidean geometry, the height of the object and that of the image have the same ratio as their corresponding distance to the lens, which can be described as

$$\frac{d_1}{c_1} = \frac{v_1}{u_1} \tag{5.28}$$

5.4.2 The situation in Fig. 5.3 c

The distances, derived using a thin concave lens are

$$\frac{1}{-v_2} = \frac{1}{-f_b} - \frac{1}{u_2} = \frac{1}{-f_b} - \frac{1}{t - v_1} \tag{5.29}$$

Based on the Euclidean geometry, the height of the corresponding virtual image is

$$d_2 = \frac{v_2}{u_2} c_2 \tag{5.30}$$

5.4.3 The situation in Fig. 5.3 d

The imaging distance (i.e. position of the focal point on the optical axis) is

$$\frac{1}{v_3} = \frac{1}{f_a} - \frac{1}{u_3} = \frac{1}{f_a} - \frac{1}{t + v_2} \tag{5.31}$$

Based on the Euclidean geometry, the height of the real image (i.e. deviation of the refocal point from the optical axis) can be described as

$$d_3 = \frac{v_3}{u_3} c_3 \tag{5.32}$$

The refocusing angle is obtained by utilizing d_3 and v_3 as

$$\theta_{out} = \arctan(\frac{d_3}{v_3}) \tag{5.33}$$

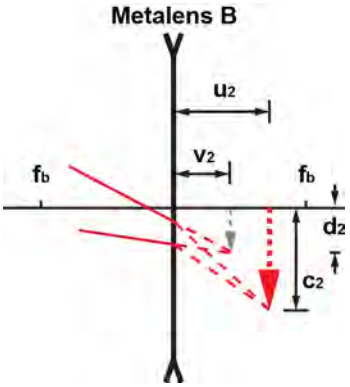

Fig. 5.4. Special incident condition of the concave lens, namely metalens B**.** The object (grey dash arrow) and the virtual image (red dash arrow) are on the same side of the lens.

The simplified calculations based on glass lenses and Euclidean geometry is possible to predict the refocusing status when the fluorescent bead is off-axial and not at target height.

When $u_1 \geq f_1$, the position of the focal point can be predicted and described by the focal length of metalens A f_a, the distance between two adjacent metalens t, the distance between the object and metalens A u_1, and deviation from the optical axis c_1, as shown below

$$d_3 = \frac{c_1 f_a^2 t}{a f_a^2 t + u_1 f_a^2 - 3 f_a t^2 - 4 u_1 f_a t + 3 u_1 t^2} \tag{5.34}$$

$$v_3 = -\frac{f_a t(3 f_a t + 2 f_a u_1 - 3 t u_1)}{2 f_a^2 t + u_1 f_a^2 - 3 f_a t - 4 u_a f_a t + 3 u_1 t^2} \tag{5.35}$$

5.4.4 The situation in Fig. 5.4

When $u_1 < f_1$, a special condition should be considered, in which the real image from the metalens A will focus behind the metalens B, as shown in **Fig. 5.4**. Under this condition, both the object and virtual image appear on the same side of metalens B. In **Fig. 5.4**, the intersection points of the two rays focusing on the virtual image and metalens B are

$$I_1 = c_1 \frac{t}{u_1} \tag{5.36}$$

$$I_2 = c_1 \frac{f_b - f_a}{f_a} \tag{5.37}$$

Their corresponding output angles can be described as

$$O_1 = \arctan(\frac{c_1}{f_a}) + \arctan(\frac{c_1 t}{u_1 f_b}) \tag{5.38}$$

$$O_2 = \arctan(\frac{c_1(f_b - f_a)}{f_a} + \arctan(\frac{c_1(f_b - f_a)}{f_b f_a} \tag{5.39}$$

As the two rays meet at one point, the position of the point can be obtained by using Eqs. 5.36-5.39. And since the angle is relatively small, $\tan(x/y)$ can be simplified to (x/y). Hence,

$$-v_2 \approx (\frac{c_1(f_b - f_a)}{f_a} - \frac{c_1 t}{u_1})/(\frac{c_1}{f_a} - \frac{c_1}{u_1}) \tag{5.40}$$

$$-d_2 \approx O_1 v_2 - c_1 \frac{t}{u_1} \tag{5.41}$$

Based on the Euclidean geometry and the convex thin lens formula, the position of the output focal point can be described as

$$d_3 = \frac{c_1 t(u_1 - f_a t)(f_a - t)}{f_a^2 t - 2f_a t^2 + f_a^2 u_1 + t^2 u_1 + t^3 u_1 - 2f_a t^2 u_1 + f_a^2 t u_1 - 2f_a t u_1} \tag{5.42}$$

$$v_3 = -\frac{f_a t(2f_a t + 2f_a u_1 - t u_1 - t^2 u_1 + f_a t u_1}{f_a^2 t - 2f_a t^2 + f_a^2 u_1 + t^2 u_1 + t^3 u_1 - 2f_a t^2 u_1 + f_a^2 t u_1 + 2f_a t u_1} \tag{5.43}$$

To summarize, the geometrical optics approach described in this section can reproduce the results in the previous section. Furthermore, it can predict the focus if the particle is off-axis and not at the target height. This result is used in Section 5.8.

5.5 Optical response of the meta-atom

The focal point of the metasurface lens is created by using a continuous phase gradient, which results from the interference of light scattered by well-designed nanopillars. Therefore, it is crucial to tailor the phase and amplitude of the scattered light for each meta-atoms in the metalens. To simplify the analysis, an uniform array of same-sized nanopillars is utilized to extract the phase, a method that is also used in the previous two chapters [178, 266]. The nanopillars are set on a fused silicon dioxide layer under a water layer. Both the silicon dioxide and the water layers are treated as infinite thick. **Fig. 5.5 a** shows the schematic of metalens A and B. They are both hexagonal arrays of amorphous silicon circular nanopillars with a subwavelength lattice constant (350 nm). The lattice constant is chosen as less than the propagation wavelength of 680 nm in the silicon dioxide (680 nm$/n_{SiO_2} = 467$ nm). This value ensures that only the zeroth order diffraction exists at normal incidence.

The height of the nanopillars H is chosen based on phase coverage. The maximal phase shift accumulates in a homogeneous film by $\phi_{max} = 2\pi n_{eff} H/\lambda$, where n_{eff} (i.e. n_{si} - n_{water}) is the relative refractive index of the film [185]. In order to reach a phase difference $\phi_{max} = 2\pi$, the thickness of the amorphous silicon should be larger than $0.32\,\lambda$, which is fixed at 470 nm in this design. With a fixed height, the scattered phase and amplitude can be modulated by varying the diameter of the circular nanopillar, i.e. varying the relative refractive index. **Fig. 5.5 b** shows the optical response of the nanopillars under plane-wave illumination, with the pillar diameter changing from 100 nm to 340 nm. All output phases and strengths are extracted

from a plane 2 μm beneath the nanopillar base. It shows a phase coverage over 4π, which provides flexibility in choosing nanopillars. Only nanopillars with a transmission efficiency greater than 64% are selected in metalens A to improve the overall output efficiency. The resulted phase profile of metalens A approximates that of a convex lens, i.e. the phase in the center of the lens is lower than that at the boundary, as shown in **Fig. 5.5 c**. A cross section view in **Fig. 5.5 c** shows the central region of metalens A, with the pillar dimensions and its phase variation shown side by side. Several samples of focusing planer metasurface are fabricated in the cleanroom, see Appendixes C,D,E for details.

The meta-atoms of metalens B have a similar geometric structure; however, a reflective concave lens, metallic material is utilized to improve reflection efficiency. In **Fig. 5.5 d**, a SU-8 layer of 2 μm thick is employed to protect the nanopillar array and support a gold layer as the reflective component. By considering the process in the actual fabrication, a layer of aluminum oxide with a refractive index of 1.7640 ($n_{alumina}$) is designed at the lower end of the nanopillar as a hard mask [212, 305]. Another commonly used hard mask material is chromium (Cr), which has a refractive index of $3.0713 + 3.3633i$ at the wavelength of interest (i.e. 680 nm) [306, 307]. In comparison, aluminum oxide exhibit more advantages in this design, owing to its low absorption. It is possible to maintain the silicon component's optical response, even without removing the alumina component in fabrication (referring to [185]).

In this simulation, a plane wave with the wavelength of interest illuminates the nanopillars from the silica side. All phases and strength are extracted from the xy plane 2 μm above the silica/Si-nanopillar interface. The meta-atoms of the reflective metalens B have a phase coverage of over 6π. They can provide a sufficient phase coverage even if the minimum reflection efficiency is defined at 60% (see **Fig. 5.5 e**). The resulted metalens B shows the output phase as a reflective concave lens, as shown in **Fig. 5.5 f**, where the margin phase is lower than the center phase.

Different from the metalens discussed in Chapter 4, the metalens doublet here functions under a traveling wave rather than a standing wave. **Figs. 5.6** and **5.7** demonstrate the electric field and magnetic field distributions of two example nanopillars in metalens A and B. The two nanopillars have a radius of 50 nm and 165 nm, which are the smallest and largest nanopillars that are used in metalens A and B. All planes are extracted at the middle xz plane and the xy middle plane of the nanopillar's silicon section. As shown in **Fig. 5.6 a**, most of the electric field is on the edge of the silicon nanopillar that has a radius of 50 nm. The maximum field is on two opposite sides of the nanopillar along the polarization direction (i.e. the x axis). In contrast, the maximum-sized nanopillar can confine an electromagnetic field in the silicon (see **Fig. 5.6 b**). There is no obvious cross-talk between adjacent nanopillars. At each nanopillar, the black arrows represent the direction of the local displacement current. In both **Figs. 5.6 a** and **b**, the displacement current forms approximately three loops in the nanopillars. The number of three is approximately the ratio of the nanopillar height (470 nm) and the wavelength in the silicon (680 nm/n_{Si} = 184 nm).

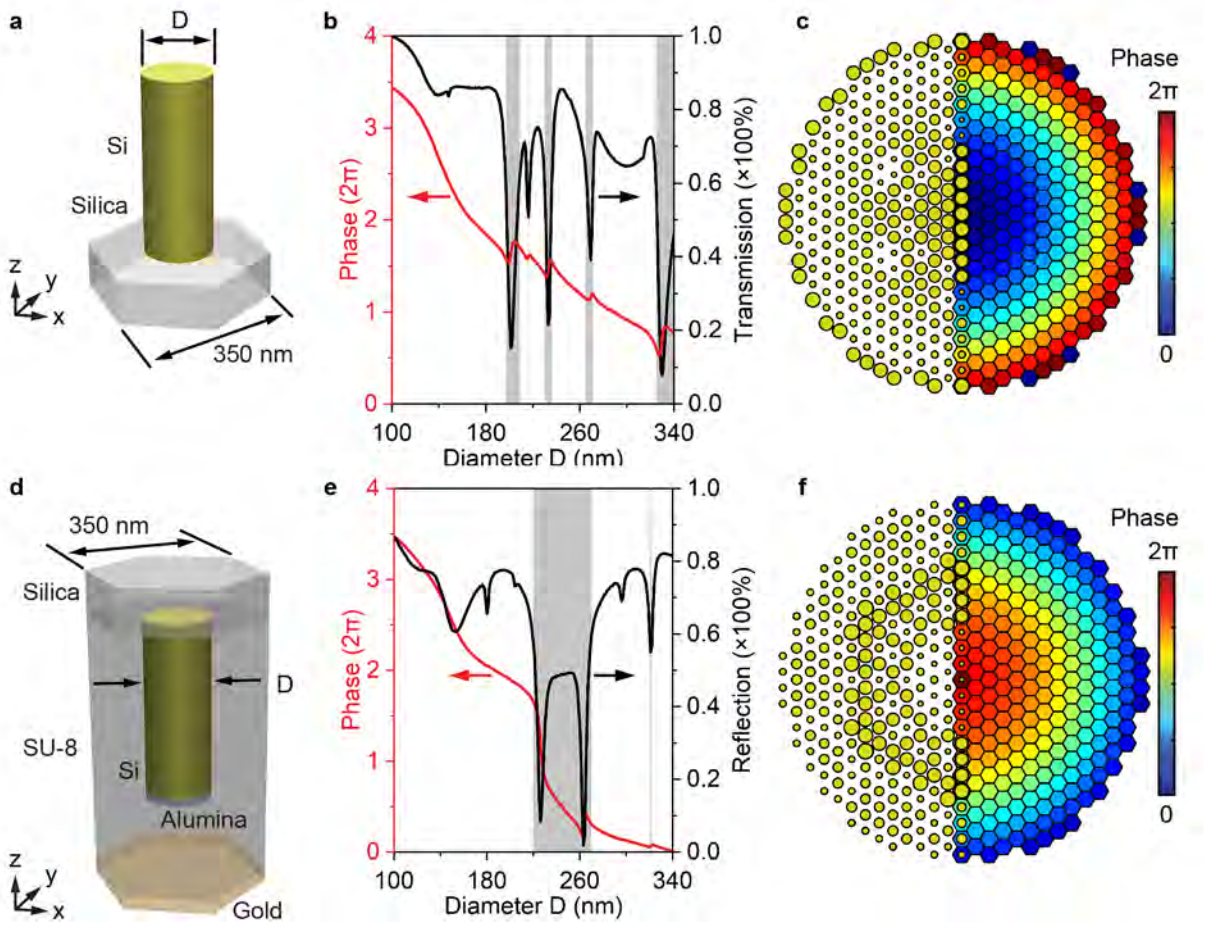

Fig. 5.5. Phase gradient and efficiency respond in the output light from a unit-cell where (a-c) for metalens layer-*A* and (d-f) for metalens layer-*B*. (a) Schematic of the nanopillar with 470 nm height, which has a cylindrical cross section. A uniform nanopillar array, with a hexagonal periodicity of 350 nm in each parallel boundary, is simulated to determine the phase. The incident light propagates along the –*z* direction. (b) Phase shift (the red curve) and transmission variation (the black curve) with variable diameters of nanopillars. Shadow area marks the nanopillars whose transmission efficiency is less than 64%, and those nanopillars are not considered in the integrated metalenses. (c) Schematic of metalens (within 4 μm from the axis), which demonstrates phase gradient (right-half) and the corresponding distribution of nanopillars (left-half). (d) The Si-nanopillar with alumina capping is surrounded by *SU*-8 and a layer of gold beneath the *SU*-8 layer. (e) Phase shift and reflection variation with a variable diameter of nanopillars and the reflection efficiency of nanopillars less than 60% are marked in shadow. (f) The panel is plotted following the same specifications as (c).

The phase extraction is conducted by using the numerical tool of COMSOL Multiphysics (version 5.4) on each single nanopillar. The extracted values are then used to assemble the metalens, the properties of which are then simulated by using another numerical tool of Lumerical. The change to Lumerical is because the latter is more suitable in the simulation of large devices. It is worth noting that, as an intrinsic feature of COMSOL, which treats the imaginary unit i as $-i$, the phase extracted from the nanopillars is always flipped in its sign. This feature does not affect the results of the Lumerical simulation, which fits with the theoretical predictions.

The electric field distributions show that the incident and the reflected wave from the gold side generate a standing wave in the nanopillar (**Fig. 5.7**). The standing wave is more pronounced in the smaller nanopillar. The magnetic hot-spots correspond to the centers of the circling electric displacement current. In addition, the electromagnetic field at the alumina/silicon interface is smooth and continuous, which confirms that the influence of the alumina cap on the silicon nanopillar is negligible. Furthermore, there is no obvious near-field crosstalk between adjacent nanopillars [308, 309]. A crosstalk-free metalens can produce a far field focusing (see **Figs. 5.10** and **5.13**) that matches the designed wavefront (see **Figs. 5.9** and **5.12**).

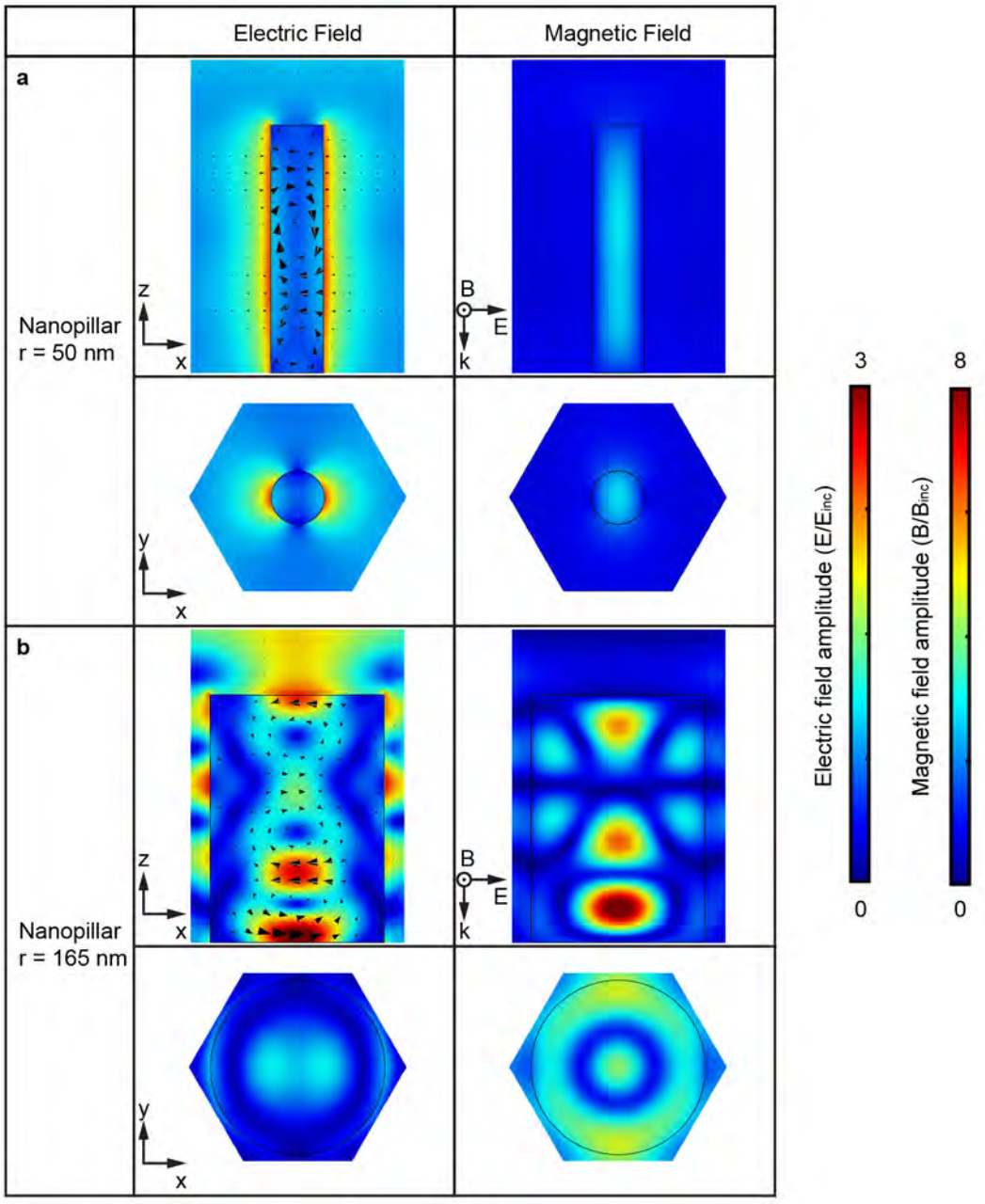

Fig. 5.6. Near field response in two example nanopillars of metalens A under illumination from above. The directions of the incident electric and magnetic fields are depicted in the corresponding top-right panel. The nanopillar, with a radius of (a) 50 nm and (b) 165 nm, shows electric, magnetic fields (color maps) and displacement current (black arrows). The field distributions are extracted at the middle xz- and xy plane of the example nanopillar, respectively. All fields are normalized against the respective field of the incident light, while the displacement current is shown without normalization across panels.

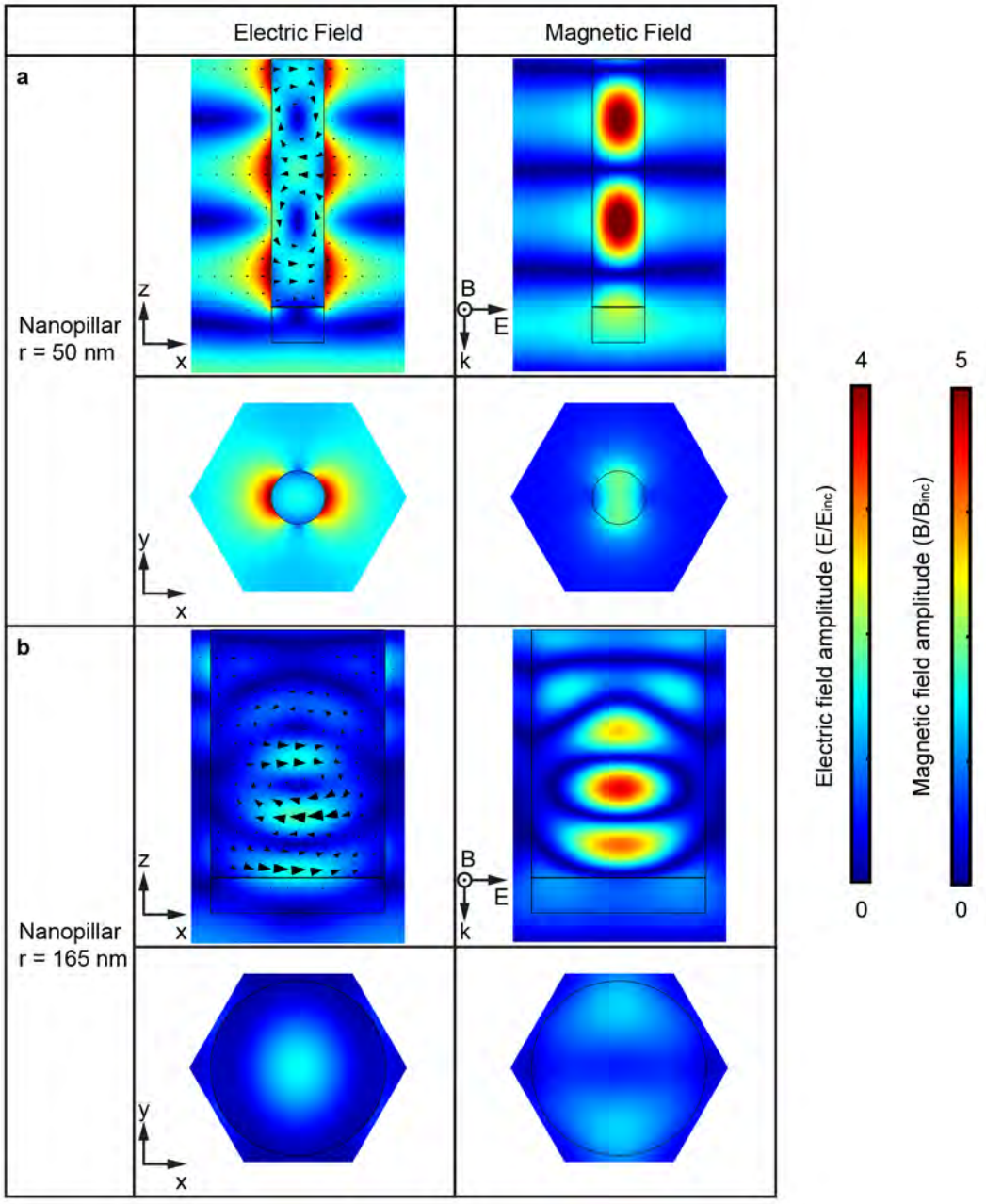

Fig. 5.7. Near field response in two example nanopillars with a radius of (a) 50 **nm and (b)** 165 **nm, which is comprised of Si and alumina sections, of metalens** B **under the illumination from above.** The electric and magnetic field distributions in the xy plane and the xz plane are extracted from the middle cross section of the Si section and the center xz plane, respectively. The panels are plotted following the same specifications as **Fig. 5.6**

5.6 The design of Metalens A and Metalens B

This section describes in detail the method used to select nanopillars with suitable output phase and strength. The FEM and the FDTD solver, namely COMSOL Multiphysics and Lumerical, are employed to simulate the meta-atoms and the metalenses. **Figs. 5.8** and **5.11** show the output phase maps of metalens A (in the transmission field) and B (in the reflective field), respectively. These results are obtained from uniform arrays of same-sized nanopillars, which is the standard initial process in designing metalenses [9]. **Figs. 5.8** and **5.9** depict the phase profile of the recherche metalens A. The overall phase distribution of metalens A, as shown in **Fig. 5.8**, has a concentric circular phase gradient. The phase gradient is wrapped into a range from 0 and 2π, while the center phase is fixed at 0 for visualization. Along both the x and y axes, the phase coverage of metalens A is over 6π, whereas the phase coverage reaches approximately 10π along the diagonal. The dimension of the metalens A is $\sim$ 15.6 µm in width (i.e. in the x axis) and $\sim$ 15 µm in length (i.e. in the y axis). The central area of **Fig. 5.8**, which is highlighted using the white dashed circle, has been shown previously in **Fig. 5.5 c**.

Fig. 5.9 a shows the dimensions of the nanopillars in metalens A and the corresponding phases along the y axis (referring to the black line in **Fig. 5.6**). The smallest and the largest nanopillars in metalens A are 100 nm and 320 nm in diameter, respectively. To obtain a better phase matching, the initial point in **Fig. 5.9 a**, i.e. the center nanopillar, has an output phase at 311°, obtained by employing a data optimization solver (i.e. MATLAB). In metalens A, the

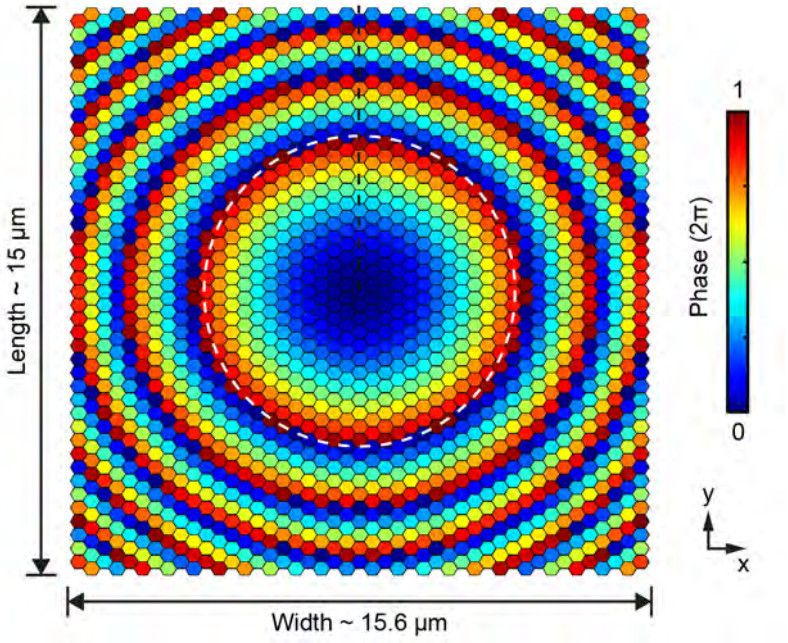

Fig. 5.8. Output phase of each meta-atom in metalens A. The color map in each hexagon represents the phase extracted from the corresponding meta-atom, 1 µm below the nanopillar base. All output phases remain in the range of 0 to 2π, while the central phase is set at 0 for visualization.

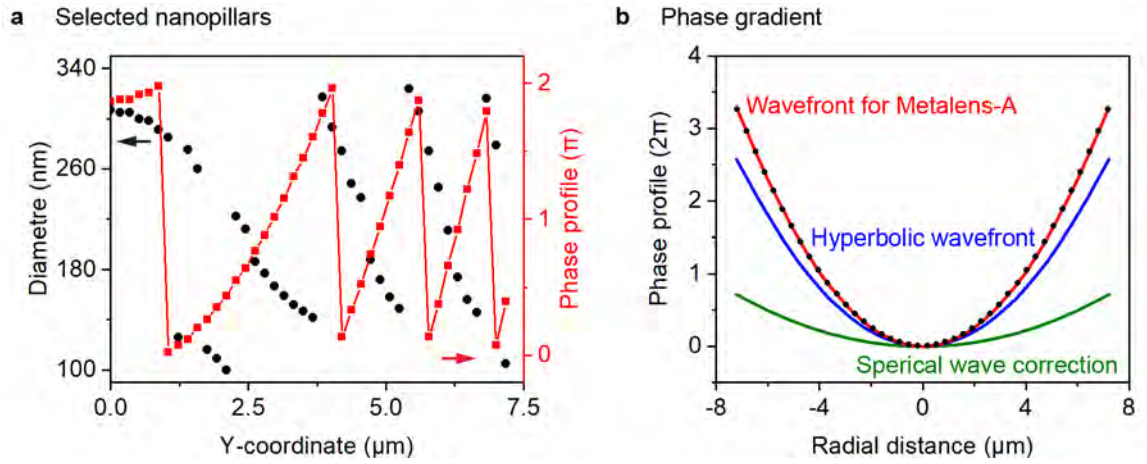

Fig. 5.9. A line of nanopillars along metalens A as an example. All dimension and phase data are extracted along the black dash line in **Fig. 5.6 a** correlation between the radius of nanopillars (black) and the corresponding output phase shift (red) is obtained. (b) The phase gradient of metalens A and its two components are depicted in the red, blue and green curves, respectively. The targets (lines) are matched to the extracted data (black dots).

phase profile is comprised of two hyperbolic components. The phase profile ϕ of a hyperbolic component can be expressed using the equation below

$$\phi = \frac{2\pi}{\lambda}(\sqrt{f^2 + r^2} - f) \tag{5.44}$$

where λ is the wavelength in the medium, f is the focal length, and r is the radial distance from the optical axis (while $r^2 = x^2 + y^2$). In metalens A, two components (see **Fig. 5.9 b**) are employed, to collect the spherical waves radiated by the fluorescent sphere of interest and converge them onto the silicon dioxide layer to metalens B. Accordingly, its phase profile is

$$\phi_A = \frac{2\pi}{\lambda_{water}}(\sqrt{f_{sphere}^2 + r^2} - f_{sphere}) + \frac{2\pi}{\lambda_{silica}}(\sqrt{f_t^2 + r^2} - f_t) \tag{5.45}$$

where λ_{water} is the wavelength in water (i.e. 680 nm$/n_{water}$), f_{sphere} is the distance between the initial position of the fluorescent sphere and the metalens A base (i.e. 67 μm), λ_{silica} is the wavelength in silicon dioxide (i.e. 680 nm$/n_{silica}$), and f_t is the spacing thickness between metalens A and B (i.e. 20 μm). Dimensions of all nanopillars are selected and positioned on a hexagonal lattice based on Eq. 5.45. In addition, the numerical aperture in the silicon dioxide layer is described by

$$NA = n\sin[\arctan(\frac{D}{2f})] \tag{5.46}$$

For the downward propagation wave (i.e. along -z direction), the numerical aperture of metalens A is approximately 0.53. But as the overall planar shape of the lens is a rectangle rather than a circle, the actual focusing (also the numerical aperture) is slightly different from a standard circular lens.

My previous results [9] indicate that the light-bending ability of the metalens can be accurately predicted as long as the near-field cross-talking between adjacent nanopillars is sufficiently weak and all the nanopillars have similar scattering intensity. **Fig. 5.10** confirms this prediction. It shows the metalens A output in the silicon dioxide layer. One red fluorescent bead with a radiation wavelength of 680 μm is immersed in the water layer at the designed initial position (i.e. 67 μm above the nanopillar base and on the optical axis of this metalens). **Figs. 5.10 b-d** show the focus of this spherical input waves. The field map in **Fig. 5.10 b** is extracted from the xy plane 20 μm below the metalens A base. A circular focal spot with four flanked sidebands is obtained at the focal plane, in which the sidebands appear due to the rectangular shape of the unit cell. Two groups of field intensity at $y = 0$ and $x = 0$ are extracted to obtain the focusing intensity in the x and y direction, respectively. The full width at half maximum (FWHM) of the two extracted intensity profile is 598 nm (along the x axis) and 619 nm (along the y axis), respectively. This small difference is due to the difference in width ($\sim$ 15.6 μm) and the length ($\sim$ 15 μm) of metalens A. Simultaneously, the intensity profile gives a the spot size along the x axis as 1015 nm. The beam quality M^2 is obtained as

$$M^2 = \frac{2w_0\pi D}{4\lambda f} \tag{5.47}$$

where w_0 is the waist radius of the focusing beam, D is the diameter of the lens (employing the width of metalens A), and f is the focal length of the lens (i.e. the spacing distance between metalens A and B). In this case, the beam quality is equal to 1.3323. In addition, the depth of field (2.65 μm) measured in **Fig. 5.10 c** matches the calculated result (2.58 μm) by using Eq. 5.48

$$DOF = 2\frac{\pi w_0^2}{M^2\lambda} \tag{5.48}$$

In **Figs. 5.10 c** and **d**, the field maps are extracted in the xz plane that bisects the middle of metalens A. The field intensity profile shown in **Fig. 5.10 c** is extracted on the optical axis for observing the field intensity of the scattering field. The local field intensity (see **Fig. 5.10 d**) is extracted from the region enclosed by a white dash frame in **Fig. 5.10 c**. Light from the fluorescence sphere converges on the position of the top surface of metalens B as theoretically calculated, which fits with prediction.

The phase gradient of metalens B is a hyperbolic function (i.e. Eq. 5.44) with a negative sign, which can be described as

$$\phi_A = -\frac{2\pi}{\lambda_{silica}}(\sqrt{f_t^2 + r^2} - f_t) \tag{5.49}$$

As a concave mirror, the functionality of this metasurface is to generate a spherical wave under the illumination of a plane wave at normal incidence. **Fig. 5.11** shows the output phase of the nanopillars. The center phase (i.e. at the optical axis) is set as 2π for visualization. With a comparison of **Fig. 5.8**, the overall phase gradient of metalens B is smaller, and the total phase

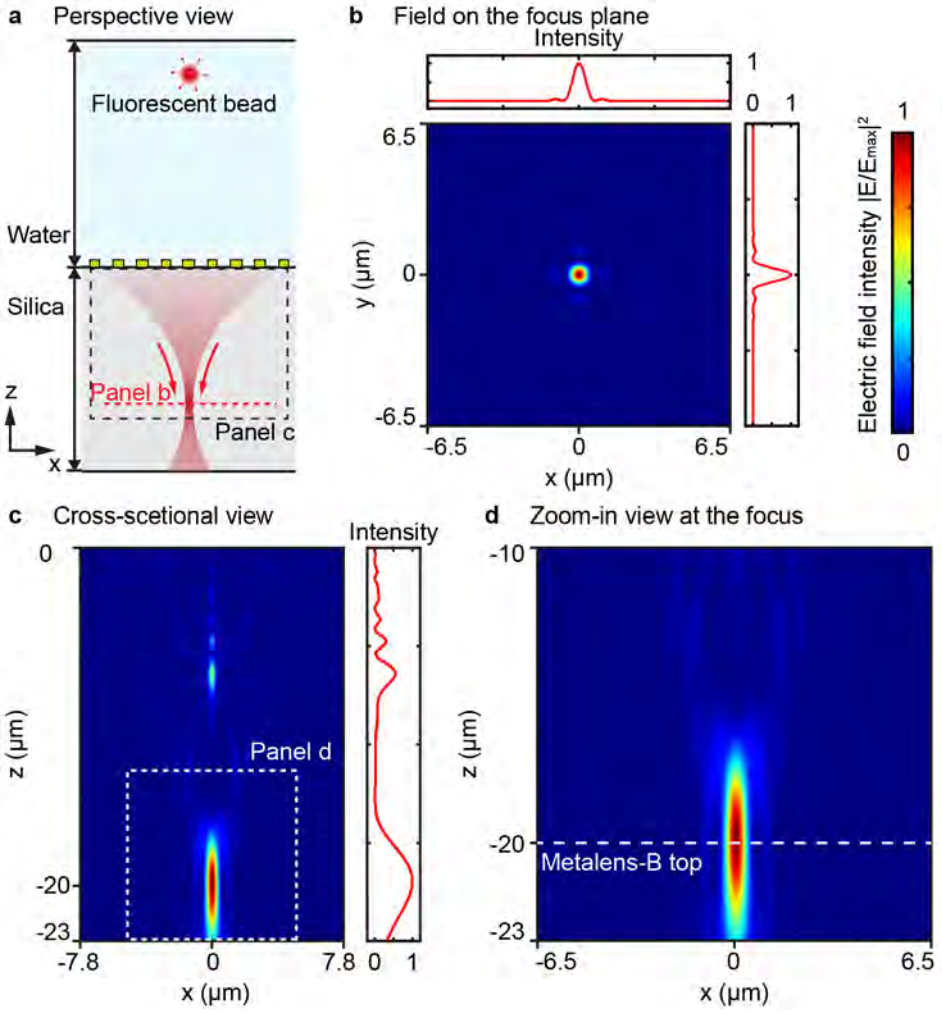

Fig. 5.10. Optical properties of metalens A with the fluorescent bead at the initial position (i.e. $z = 67$ μm, on-axis). (a) A schematic diagram of a focusing beam generates by metalens A with a light source of the red fluorescent bead (a red spot with arrows) in the xz plane. The yellow rectangles represent the metalens A nanopillars, while the red arrows show the propagation direction. (b) Field intensity at the focal plane, i.e. 20 μm below the metalens base, is extracted at the red dash line in panel a. Corresponding cross sectional field intensities at $x = 0$ and $y = 0$ are shown at the top and on the right. (c) Field distribution (color map) and corresponding extracted intensity (red curve) are extracted at the middle xz plane of metalens A. (d) Local field intensity at the focal point, corresponding to the white dash frame in panel c. The white ashed line indicates the position of the top of metalens B, which is not included in the simulation here. All fields and extracted lines are normalized against the maximum value of their respective fields.

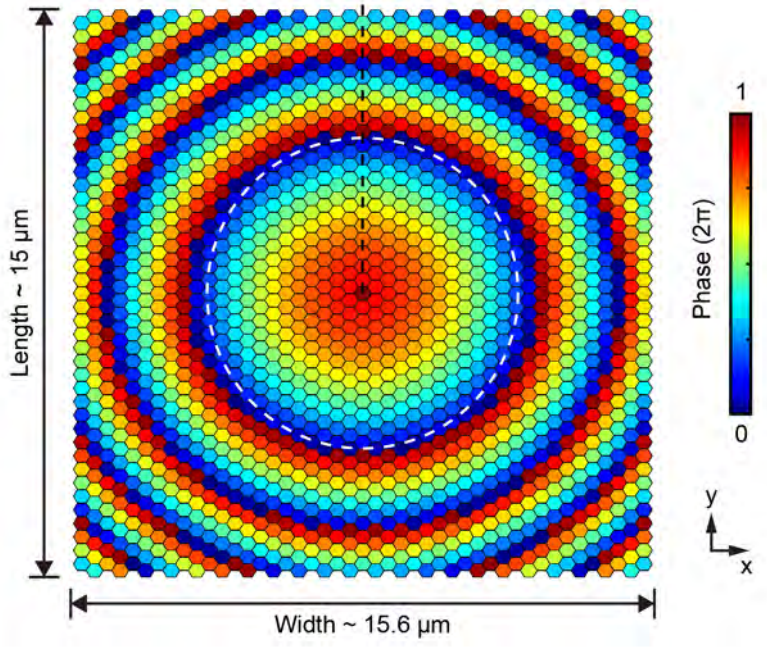

Fig. 5.11. Output phase of nanopillars in metalens *B*. The color map in each hexagon represents the phase extracted from the corresponding meta-atom, taken at 1 μm below the nanopillar base (i.e. the bottom of the alumina component). All output phases is in the range of 0 to 2π, while the central phase is set at 2π for visualization.

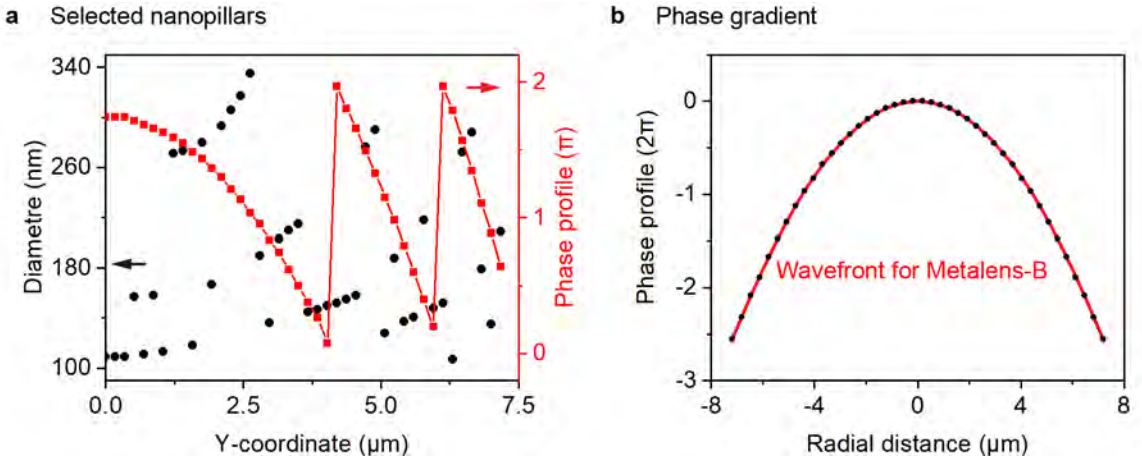

Fig. 5.12. Selected dimensions of the nanopillars are their corresponding phase in the metalens *B*. All dimension and phase data are extracted following the black dash line in **Fig. 5.9**. (a) The relationship between the radius of nanopillars (black) and the corresponding output phase shift (red) is obtained. (b) The phase gradient of the metalens *A* (red curve) is matched to the extracted data (black dots).

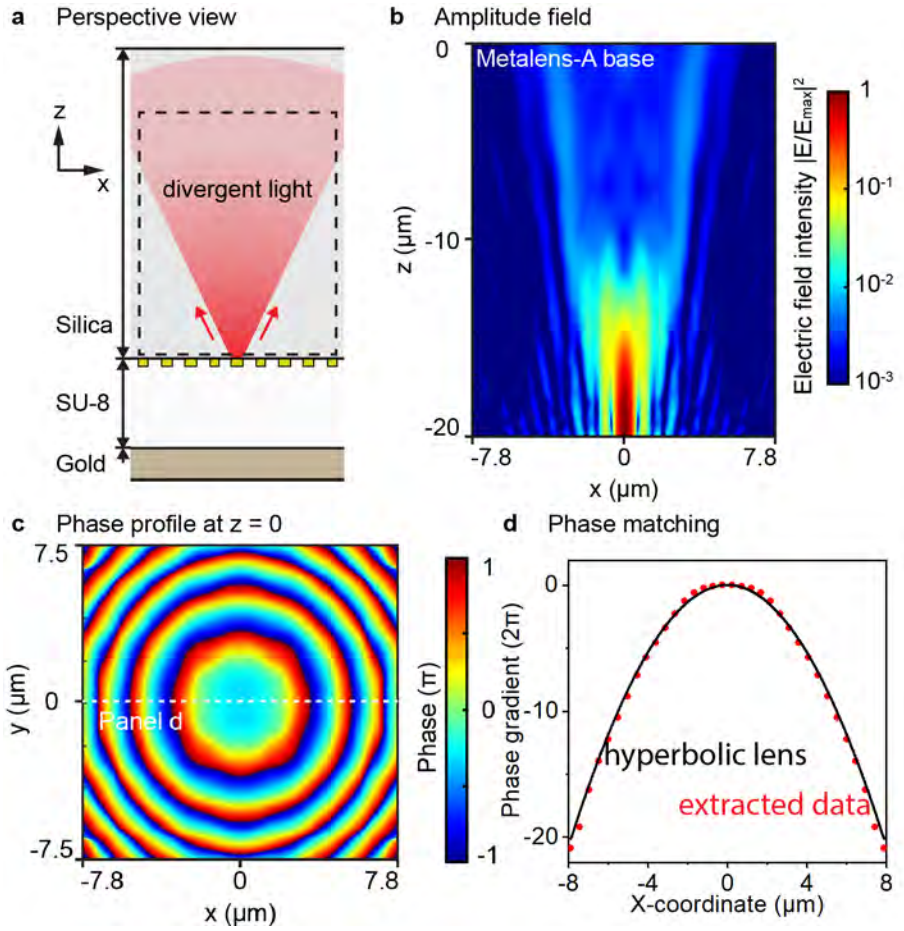

Fig. 5.13. Optical response of metalens B under the illumination of a focusing light from metalens A (not depicted in the figure). (a) Perspective view of metalens B which contains, nanopillars (yellow rectangles), Silica, SU-8 and gold layers in the xz plane. A reflected scattering field as a divergent field propagates along the $+z$ direction (red arrows). (b) Field distribution of the electric field intensity in the range from $z = 0$ (i.e. metalens A base) to $z = -20$ μm (i.e. metalens B top). (c) The phase map is extracted at the xy plain 20 μm above the metalens B top. (d) Phase matching situation shows the extracted data (red dots) from the white dash line (in panel c) with a theoretical hyperbolic line (black curve).

coverage about 8π along the diagonal. The base phase in metalens B (i.e. central position) is 330° , shown as in **Fig. 5.12 a**. In **Fig. 5.12 b**, it is shifted to 0 for better visualization.

With the output phase profile shown in **Figs. 5.11** and **Fig. 5.12 b**, the metalens B can produce a spherical wave output under the illumination shown in **Fig. 5.10**, i.e. a focus established at the silica/metalens-B interface. **Fig. 5.13** demonstrates the corresponding result, where the incident field is hidden in both the schematic diagram (see **Fig. 5.13 a**) and the field distribution (see **Figs. 5.13 b,c**). **Fig. 5.13 b** shows the field distribution of the output field intensity above metalens B interface. Note that metalens A is not considered at this stage; a thick silicon dioxide layer is used instead. In **Fig. 5.13 b**, a logarithmic field distribution is utilized to observe the field intensity of the scattering spherical wave, and the output scattering field diverges rapidly along the upwards direction (i.e. $+z$ direction). At this illumination condition, approximately 75% power can be reach the metalens-A/silica interface, that is, the xy plane with 20 μm above

the silica/metalens-B interface. That is, the net reflection efficiency of the metalens B is 75% (the power reflected back to the metalens A divided by the power transmitted from the metalens A). The extracted phase map at the interface, as shown in **Fig. 5.13 c**, shows concentric ring distribution. A phase profile is extracted along the white dash line in **Fig. 5.13 c**. The extracted data matches the hyperbolic lens wavefront (i.e. Eq. 5.49, where $f_t = 20$ μm), which also aligns with the prediction of ray tracing models.

5.7 Performance at oblique incidence

Before assembling the two metalenses, it is necessary to verify their optical response at oblique incidence. To produce oblique incidence, the target fluorescent sphere is set to horizontally deviate from the initial position. It is moved to an angle of 1°, 2°, 3°, 4°, 5°, 6°, and 6.81° [i.e. the maximum deviation angle, where the microsphere center is at the boundary of the metalens unit-cell in the x axis ($x = 8$ μm)] from the optical axis. The output of metalens A is calculated at each deviation angle (see **Fig. 5.14**). Each map is 2 μm in width (in the x axis) and 2 μm in length (in the y axis), while the center of the field map is fixed at the predicted position of the corresponding focal point. Here I utilize the formula of trigonometric functions and the Snell's law

$$x = t \arctan(\arcsin(\frac{n_{water}}{n_{silica}} \sin(\phi))) \tag{5.50}$$

where t (20 μm) is the distance between the metalens A base and the focal plane, and ϕ is mentioned deviation angle. The resultant focal point on the focal plane should be approximately at $x = -0.32, -0.64, -0.96, -1.28, -1.60, -1.92$, and -2.18 μm for **Figs. 5.14 a**, **b** ,**c**, **d**, **e**, **f**, and **g**, respectively. The quality of focus under the oblique incidence good with negligible coma aberration and astigmatism. The FWHM of the focus point increases slightly as the incidence angle increases, whereas the FWHM at the largest incident angle (i.e., 6.81°) increases by just 3.63%, to 619.7 nm, with respective to 598 nm under normal incidence (**Fig. 5.12 h**).

Extracting the field distribution of the focal plane (see **Fig. 5.14**) and setting it as the input for metalens B, the optical response of metalens B can be simulated. **Figs. 5.15 a-g** demonstrate the output field distribution in the middle xz plane of metalens B. Each map is 15.6 μm in width (the width of metalens B) and 20 μm in height (from 20 μm above the metalens B to the silica/metalens-B interface). The field diminishes rapidly with propagation along then $+z$ direction. The reflected field continues to steer anticlockwise as the deviation angle increases. It can be noticed that part of the electric field is lost at the boundary in **Figs. 5.15 b-g**, which is more obvious at larger angles (see **Figs. 5.15 e-g**). Resultant power efficiency decreases. The power efficiency of metalens B drops from 75% at normal incident to 59% at the oblique incident with the deviation angle at 6.81°, as shown in **Fig. 5.15 h**.

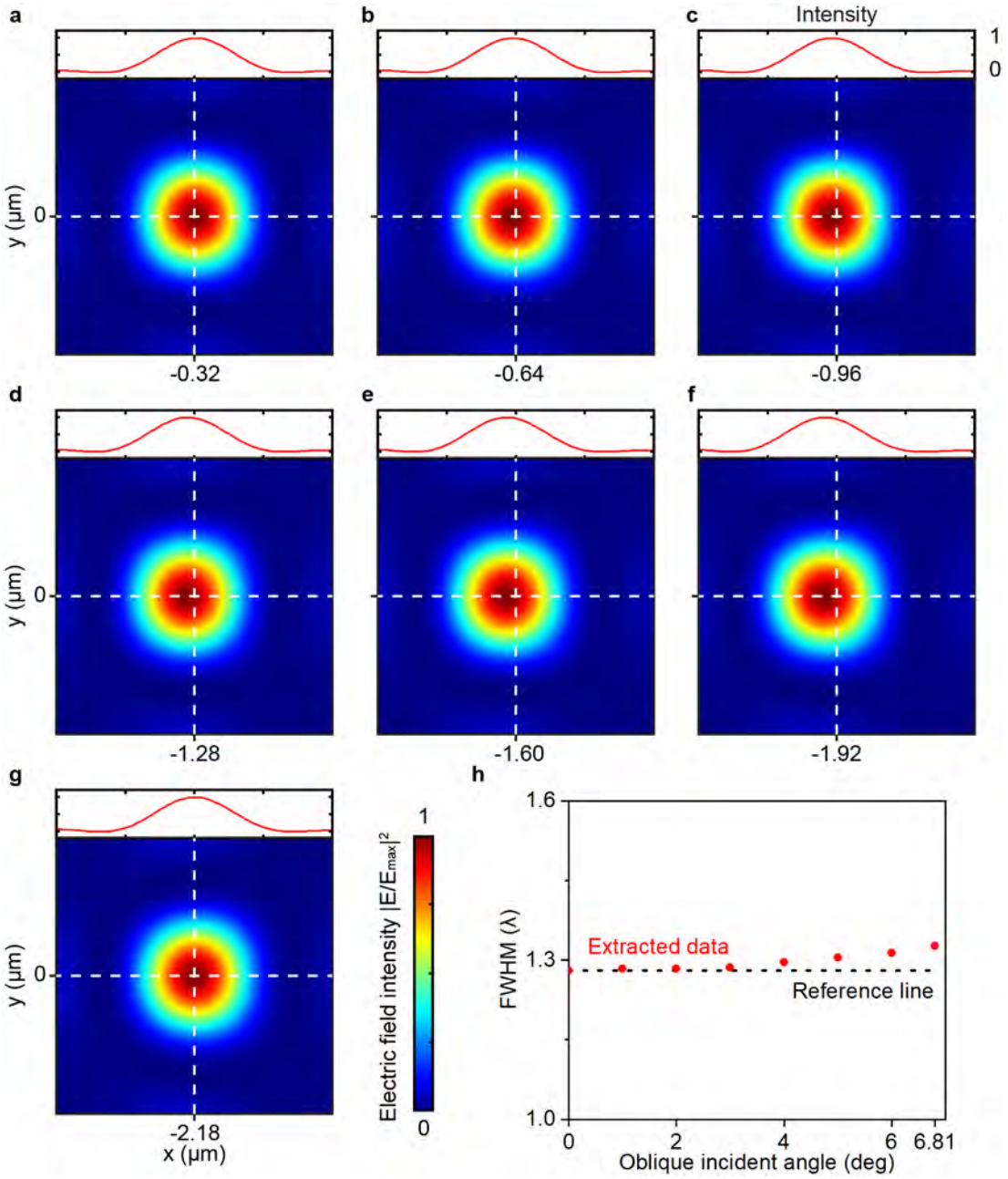

Fig. 5.14. Focus of metalens A under oblique incident. (a-g) The field distributions in the xy plane with reference lines (white dashed lines) that show where the foci are expected to be under oblique lighting at angles of (a) 1°, (b) 2°, (c) 3°, (d) 4°, (e) 5°, (f) 6°, and (g) 6.81°, respectively. The extracted intensity profile shown on the top of each panel depicts the field intensity at $y = 0$ for visualization. (h) Corresponding full width at half maximum (FWHM) at oblique incidence (red dots), as compared with the FWHM with the normal incidence (black dash line and first red dot). All fields and extracted lines are normalized against the maximum value of the respective field.

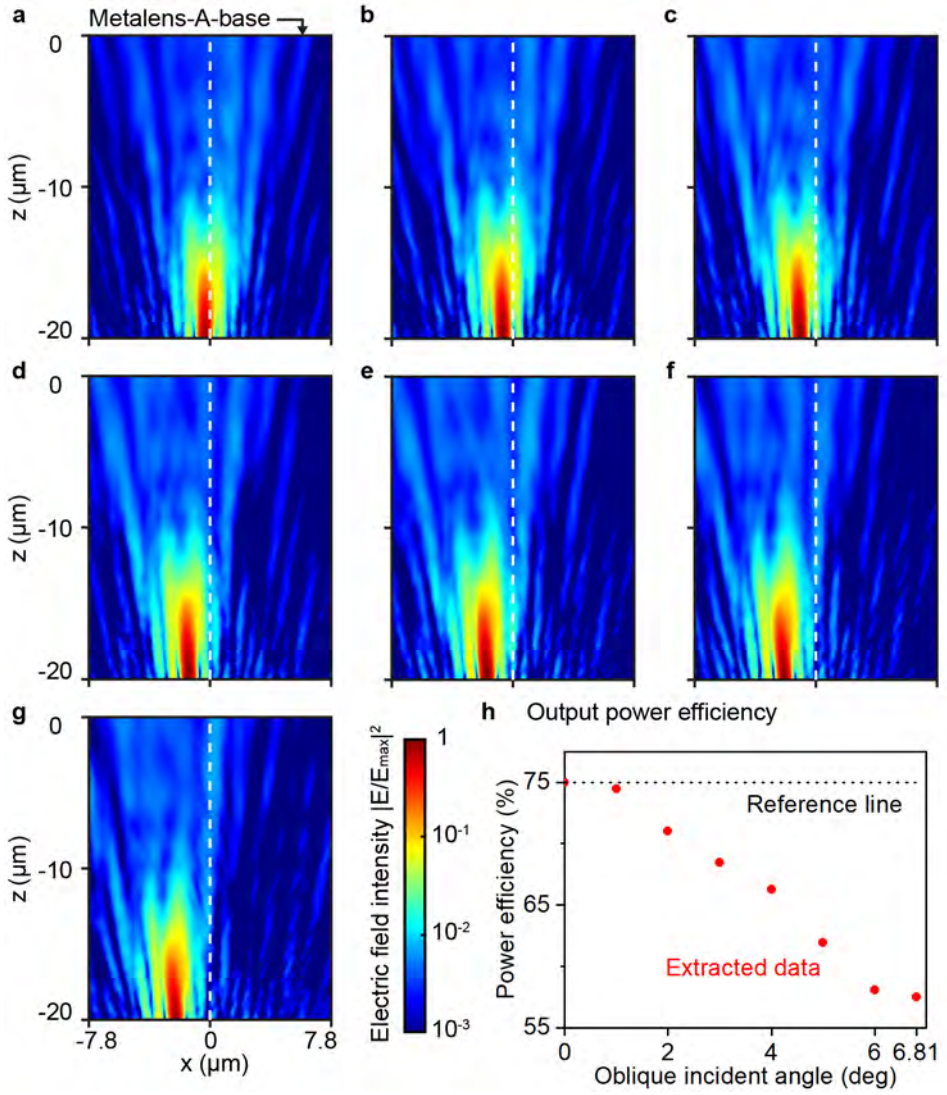

Fig. 5.15. Output of metalens B at oblique incidence. Field intensity extracted from the middle xy plane of the metalens under oblique illumination at angles of (a) 1°, (b) 2°, (c) 3°, (d) 4°, (e) 5°, (f) 6°, and (g) 6.81°, respectively. All field distributions are normalized against the maximum value in the respective field, and the color bar is set to logarithmic distribution for visualization. (h) Corresponding output power efficiency is the contrast of the output power (red dots) extracted from the monitored plane (at $z = 0$) and the incident power on the metalens B. The reference line represents the power efficient under normal incidence.

5.8 Metalens doublet: self-tracing of fluorescent beads

Combining metalens A and metalens B gives a metalens-doublet that is possible to reconvergent the output wave from a target fluorescent sphere back onto it. The two layers of metasurface lens are separated by a 20-μm-thickness silicon dioxide layer (see **Fig. 5.16 a**), while the whole metalens-doublet is beneath an 80-μm-thick microchannel. The width and length of the microchannel are defined at this stage by referring to the periodicity of the metalens unit-cell, which is 16 μm. **Fig. 5.16** shows the output field of the metalens doublet under the illumination condition that the target fluorescent sphere at the initial position (i.e. $x = 0$,

$z = 67$ μm). **Fig. 5.16 b** illustrates the output field distribution in the xz plane that bisects the metalens doublet. The area is 15.6 μm in width (the width of the metalens-doublet) and 60 μm in height (from 80 μm to 20 μm above the metalens-A/silica interface). A long, narrow focus flanked by weak sidebands is observed. The focal point is located at $z = 66.71$ μm on the optical axis of the metalens-doublet. The intensity profile, the right column of **Fig. 5.16 b**, is extracted from the middle of the elongated focus, which also depicts the relative position of the re-focal point and the target sphere. More details (see **Figs. 5.16 c** and **d**) can be seen in the local field intensity in the xz- and xy plane, respectively, which is extracted based on the highlighted regions in **Fig. 5.16 b**. The refocusing beam's maximum field intensity coincides with the target microsphere. Under this condition, the numerical aperture of the metalens doublet is approximately 0.15, and the beam spot is 4.22 μm in diameter. By using Eq. 5.47, the beam quality is obtained at 1.51. Accordingly, the depth of field can be calculated using Eq. 5.48, and it is 36.27 μm.

In the following, I will discuss the three scenarios that have been analyzed using the ray tracing methods. Firstly, the target fluorescent bead deviates from the optical axis, but is fixed at the initial height. In the same approach as in the previous section, the deviation angle is employed as the parameter to characterize the deviation. As predicted using the ray matrix (i.e. Eq. 5.19) the refocused spot traces the fluorescent sphere. This phenomenon is observed in **Fig. 5.17**. In **Fig. 5.17 a**, the output field at an oblique incident of 2° is extracted at the middle xz plane of the microchannel. The area is 15 μm in width and 26 μm in height (from 79 μm to 53 μm above the metalens-A/silica interface). A slightly tilted focusing beam passes approximately through the center of the fluorescent sphere. The top panel depicts the intensity profile extracted at $z = 67$ μm (i.e. the focal point) and there is negligible positional difference of the focal spot and the microsphere.

Fig. 5.17 b shows the relative position of the predicted focus and simulated focal point under the illumination conditions of 0, 1°, 2°, 3°, 4°, 5°, 6°, and 6.81°, respectively. As the deviation angle along the x axis increases, the actual angle gradually deviates from the predicted line. Nevertheless, the error is only 0.31° for the maximum deviation angle (i.e. 6.81°). In addition to analyzing deviation from the x axis, the deviation along the xy axis is also considered (i.e. along the diagonal of the metalens-doublet unit-cell). The maximum deviation angle ϕ_{xy} of the microsphere is equal to 9.58° [$\arctan(\sqrt{8^2 + 8^2}/67)$]. To better characterize the change in the output field, in addition to ϕ_{xy}, three intermediate angles are included in **Fig. 5.17 b**, that is $(1/4) \times \phi_{xy}$, $(1/2) \times \phi_{xy}$, and $(3/4) \times \phi_{xy}$. Even at the maximum deviation angle in the xy direction, the angle at which the focus is generated differs from the prediction by only 3.44%. **Table 5.1** records more details of the output angle when the fluorescent bead moves from the center to the margin of the metalens-doublet unit cell, across the microchannel.

The second scenario analyzed using the ray tracing method is that, the target fluorescent bead deviates from the initial height and remains on the optical axis (i.e. move along the z axis). **Figs. 5.18 a** and **b** show two example output fields of the field intensity distribution in the microchannel, with the fluorescent sphere at 64 μm and 70 μm, respectively. Both field

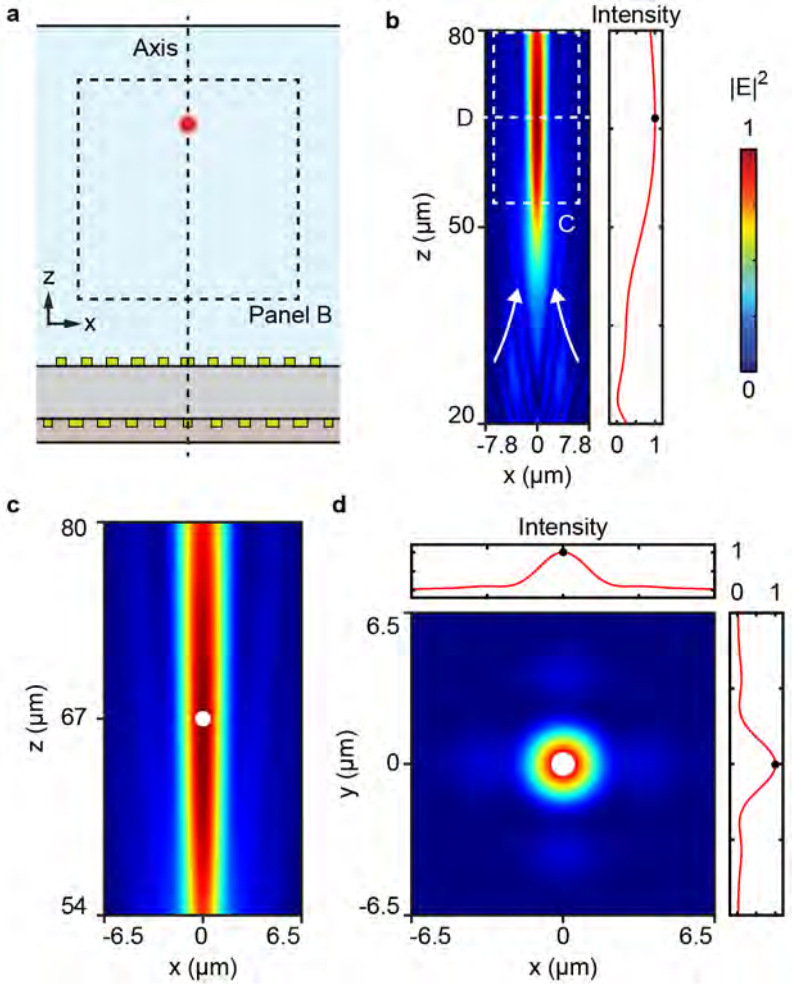

Fig. 5.16. Refocusing beam of the metalens doublet. The red fluorescent bead has a diameter of 1 μm and it is at its initial position. (a) Perspective view of the metalens doublt under the microfluidic channel in the xz plane, while the waterborne fluorescent bead on the optical axis of the metalens doublet at $z = 67$ μm. (b) An overall view of the refocusing beam in a range from $z = 20$ and $z = 80$ μm. Only the output fields is shown in the panel. The field propagates along $+z$ direction (white arrows). The extracted intensity on the right demonstrates the electric field intensity of the refocusing beam on the optical axis, and the location of the fluorescent bead is represented by the black dot. (c) The local field distribution (extracted from panel b, as the white dash frame shown) shows the narrow, long focusing with flanked sidebands at the focal point, together with the fluorescent bead (the white dot, to scale). (d) The field distribution of electric field intensity at the focus plane ($z = 67$ μm). The extracted red curves on the top and right sides depict the field intensity distributions at $y = 0$ and $x = 0$, respectively, with the black dots highlighting the relative location of the fluorescent bead (the white dot in the color map). All field and extracted curves are normalized against the maximum value of their respective field.

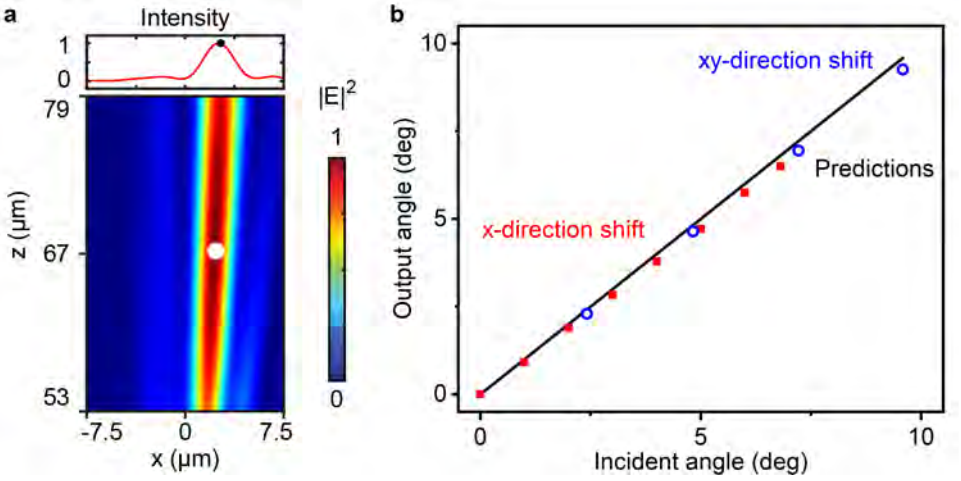

Fig. 5.17. Refocusing at oblique incidence, with the fluorescent bead off axis but at the original height ($z = 67$ μm). (a) An example condition. The illumination angle is 2°, i.e. the relative angle between the 1-μm-diameter fluorescent bead and the optical axis of the metalens doublet. The field intensity distribution (color map) shows an tilted output beam with flanked sidebands. The extracted data on the top depicts the field intensity distribution at $z = 67$ μm, with a black dot (position of the fluorescent bead). The field intensity is normalized to its maximum value. (b) A reference line (black) shows the focus drift when the fluorescent bead move in the x direction (red dots) and xy direction (blue dots).

maps show an area 13 μm in width and 26 μm in height (from the microchannel top to 54 μm above the metalens-A/silica interface). The relative movement between the fluorescent spheres and generated focus is extracted. The focus moves opposite to the microsphere. This trend of relative motion can be clearly observed in the field intensity profile extracted from the midline of the field map (i.e .where $x = 0$), shown in **Figs. 5.18 a** and **b**. The comparison between the predicted height based on Eq. 5.24 and the actual height of the focal point is shown in **Fig. 5.18 c**. In the case of the fluorescent microsphere at a height in the range of 64 μm and 70 μm (i.e. within ±3 μm of the initial height), the exciting focal length can match the predicted line. If the position exceeds this range, the resulting focal length deviates from the predicted line. In this simulation, the height of the microsphere was set to shift in the range of 57 μm to 77 μm (i.e. within ±10 μm of the initial height). When the microsphere is located at 57 μm, the predicted values show a maximum deviation of 3.47 μm (see **Table 5.2** for more details). Due to the long depth of field, 36.27 μm, of the output light in this design, the microsphere can still be covered by the elongated focus even if it is at the maximum deviation height.

Table 5.1. Deviation angles from analytical prediction and simulation. All the values are the angle (°) to the optical axis.

x direction						xy direction		
ϕ_{in}	$\phi_{predict}$	ϕ_{actual}	ϕ_{in}	$\phi_{predict}$	ϕ_{actual}	ϕ_{in}	$\phi_{predict}$	ϕ_{actual}
0	0	0	4	4	3.79	2.42	2.42	2.29
1	1	0.91	5	5	4.71	4.83	4.83	4.64
2	2	1.89	6	6	5.75	7.22	7.22	6.95
3	3	2.83	6.81	6.81	6.50	9.58	9.58	9.25

Table 5.2. Height of focus, from analytical prediction and simulation. All the values represent the distance (μm) from the metalens-*A*/silica interface.

H_{sphere}	$H_{predict}$	H_{actual}	H_{sphere}	$H_{predict}$	H_{actual}	H_{sphere}	$H_{predict}$	H_{actual}
57	77	73.53	65	69	68.75	70	64	64.41
60	74	72.26	67	67	66.71	72	62	63.44
62	72	71.01	68	66	65.94	75	59	60.82
64	70	69.99	69	65	64.97	77	57	58.63

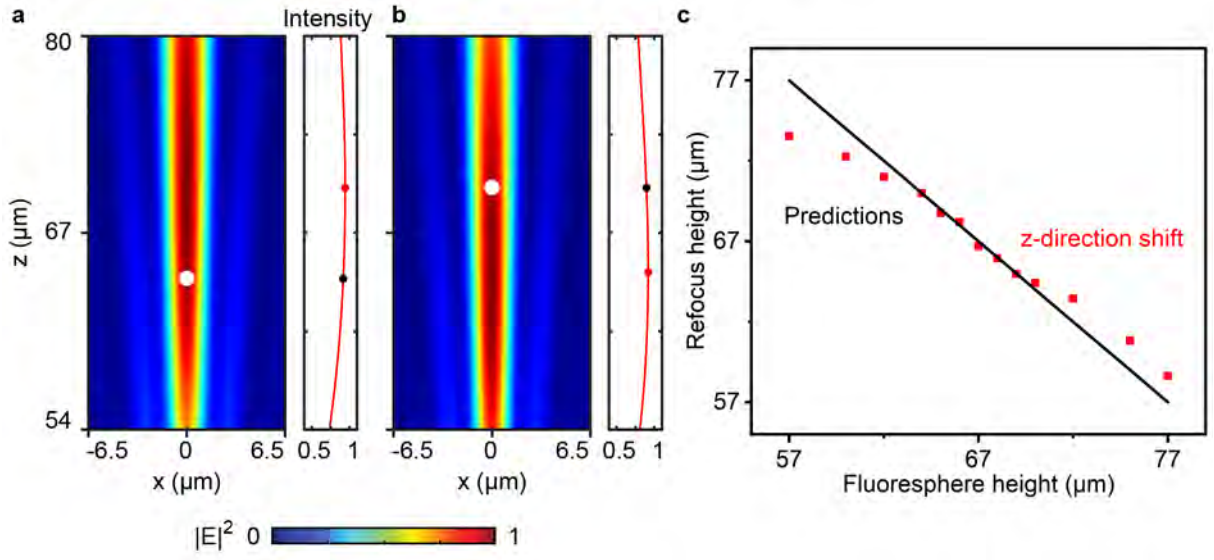

Fig. 5.18. Refocusing beam under the illumination conditions when the fluorescent bead at different heights on the optical axis. Field distribution of the local electric field intensity at the focal points when the fluorescent bead (white dot, to scale) is fixed at (a) 64 μm and (b) 70 μ m, respectively. (a,b) The extracted data on the right demonstrates the relative height of the refocus point (red dot) and the fluorescent bead (black dot), with the field intensity at $x = 0$, at corresponding conditions. Two fields and curves are normalized against the maximum value of the respective field. (c) Prediction line (black) and extracted height of the refocus points (red dots) show the variant trend when the fluorescent bead move along $\pm z$ directions on the optical axis of the metalens doublet.

The third and final scenario is that, the fluorescent sphere is neither on the optical axis nor at the initial height. **Fig. 5.19** shows two example output fields of the field intensity distribution in the middle xz plane of the metalens doublet. The fluorescent sphere is at $z = 57$ μm, with a 5° deviated angle in **Fig. 5.19 a**, and it is at $z = 77$ μm, with a 5° deviated angle in **Fig. 5.19 b**. Both field maps show an area that is 15 μm in width and 30 μm in height. In comparing the two conditions, the output angle is similar in these two cases. However, the height of the output focus is different. In **Fig. 5.19 a**, the position of the focus extracted from the field map is 69.15 μm on the z axis, and 6.042 μm on the x axis, i.e. the output angle is 4.99°. By utilizing Eqs. 5.42 and 5.43, the predicted focal point is located at $x = 6.49$ μm and $z = 69.68$ μm, i.e. predicted angle is 5.32°. In contrast, the focal point in **Fig. 5.19 b** is 4.53 μm on the x axis, and 57.79 μm on the z axis; that is, the output angle is 4.48°. By using Eqs. 5.34 and 5.35, the predicted focus should appear at $x = 4.70$ μm and $z = 59.95$ μm, i.e. predicted angle is 4.48°.

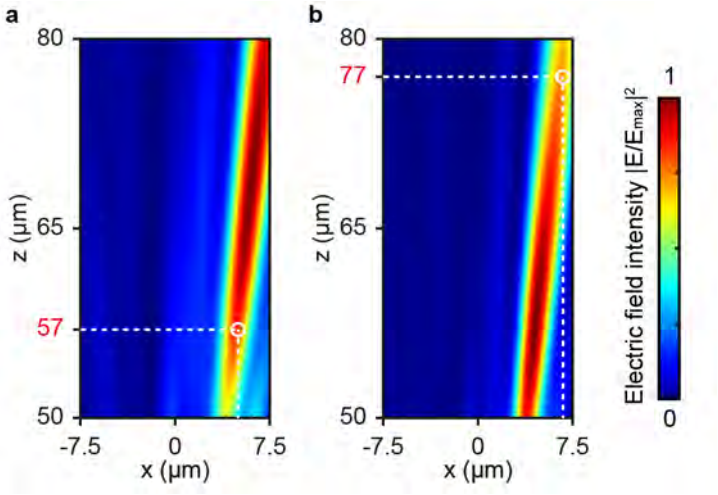

Fig. 5.19. Refocusing beam under the illumination condition that the fluorescent bead is not at the initial height and off axis. Two example conditions of the fluorescent bead with a 5° angle with the optical axis at the height of (a) 57 μm and (b) 77 μm, respectively. (a,b) Field intensity distribution in the xz plane demonstrates the refocusing beam's relative position (color map) and the fluorescent bead (white circle) with two reference lines for visualization. All fields are normalized against the maximum value of their field.

Here, the position and angle of the output focus can be predicted by the ray matrix and the geometric optics.

As mentioned before, a metalens with a hyperbolic phase profile has chromatic aberration. This means that it is unlikely to work at other wavelengths. As a comparison to the target fluorescent sphere, which has an emission wavelength of 680 nm, a blue fluorescent sphere with a 430-nm emission wavelength is employed as a control group(**Fig. 5.20**). Both field maps show an area 13 μm in width and 26 μm in height. The height of the blue fluorescent sphere is set at $z = 67$ μm and 72 μm, respectively, on the optical axis of the metalens doublet. Although the output focus movement still follows the prediction, the focal point is always below the blue fluorescent sphere, at approximately $z = 58$ μm and $z = 57$ μm. In **Fig. 5.20 a**, the maximum field intensity is only 0.32% of the condition that utilizes the target fluorescent sphere at the same position. In addition, the total power efficiency of this condition is 0.02%. This value is extremly low when compared with the total power efficiency of the target microsphere, which is approximately 11%. The power converging on the target microsphere is 550 times that on the control microsphere. It is possible to achieve sorting based on different wavelengths owing to the huge differences in optical response. The self sorting performance of the metalens doublet will be discussed in Section 5.10 with an additional tilted mirror.

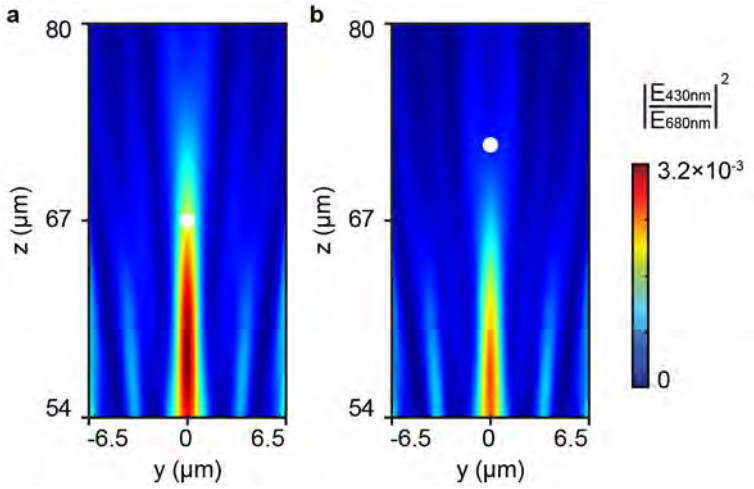

Fig. 5.20. The output field intensity with that of a non-target source with 430 nm wavelength at the height of (a) $z = 67$ **μm and (b)** $z = 72$ **μm, respectively.** Two example conditions of the fluorescent bead with 5° angle with the optical axis at the height of (a) 57 μm and (b) 77 μm, respectively. (a,b) Field intensity distribution in the xz plane demonstrates the refocusing beam's relative position (color map) and the fluorescent bead (white circle) with two reference lines for visualization. All fields are normalized against the maximum value of their field.

5.9 Metalens doublets in an array

If identical metalens doublets are organized into an array, I expect that relatively weak focusing light from adjacent metalens-doublet unit-cells can converge on the microsphere at the same time. In this section, two extreme examples must are considered: the microsphere moving in the middle of two adjacent metalens unit cells (see **Fig. 5.21**), and the microsphere moving to the center of four neighboring metalens unit cells (see **Fig. 5.22**).

In **Fig. 5.21**, two identical metalens doublets are utilized, with a microchannel of 32 μm in width (in the x axis) and 16 μm in length (in the y axis), to observe the output focusing light. The structured portion (i.e. nanopillars) of each unit-cell is 15.6 μm in width, and 15 μm in length, i.e. a nanopillar-free region of approximately 400 nm exists between the two unit cells. The red fluorescent bead is located in the middle of the gap, at the initial position (i.e. where $x = 0$, $y = 0$, and $z = 67$ μm). **Figs. 5.21 b** and **c** show the output field of the field intensity distribution in the middle xz- and yz plane. Both field maps show an area 13 μm in width (i.e. along the x axis, and y axis, respectively) and 26 μm in height. In **Fig. 5.21 a**, a narrow, elliptical focus with flanked sidebands is observed in the field map, while the relative numerical aperture in the x axis increases to 0.31. In comparison with **Fig. 5.16**, the depth of field in this condition is obviously short, and the beam waist is smaller. **Fig. 5.21 d** shows the focal spot in the xy plane of $z = 67$ μm. The elliptical focus coincides with the position of the microsphere. The weak sidebands are attributed to the scattering field of two rectangular outlines (i.e. the profile shape of the two unit-cells).

Fig. 5.22 demonstrates the configuration of four metalens doublets. There is a cross-shaped nanopillar-free region with a thickness of 400 nm and 1 μm in the x- and y axis, respectively.

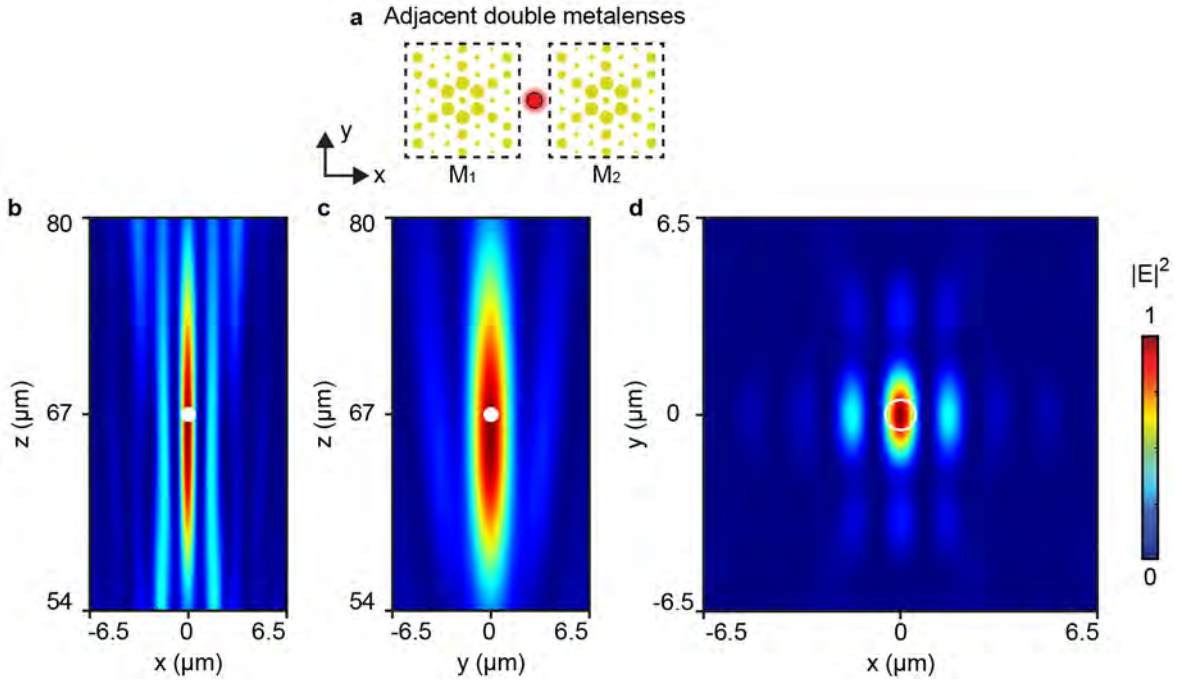

Fig. 5.21. Light focusing when the fluorescent bead moves at the middle of two adjacent metalens unit cells. (a) A perspective view shows the relative position of the fluorescent bead (red dot) and two metalens unit cells (M_1 and M_2). (b-d) The output field intensity of a source particle (white disk) in the center of two adjacent metalenses. Cross section views in (b) the xz plane, (c) the yz plane, and (d) the xy plane across the focus show the focal point with sidebands and the corresponding location of the source. All fields are normalized against the maximum electric field intensity.

The red fluorescent sphere locates in the center of this 2×2 unit-cell matrix, with the initial height (i.e. $z = 67$ μm). **Figs. 5.22 b** and **c** show the only output field of the field intensity distribution, with the position of the fluorescent bead, in the middle xz plane of the microfluidic channel and the xy plane with a height of $z = 67$ μm. The focus remains on the microsphere at this condition. **Figs. 5.21** and **5.22** indicate that placing identical metalens doublet into an array still provides the self-tracing functionality.

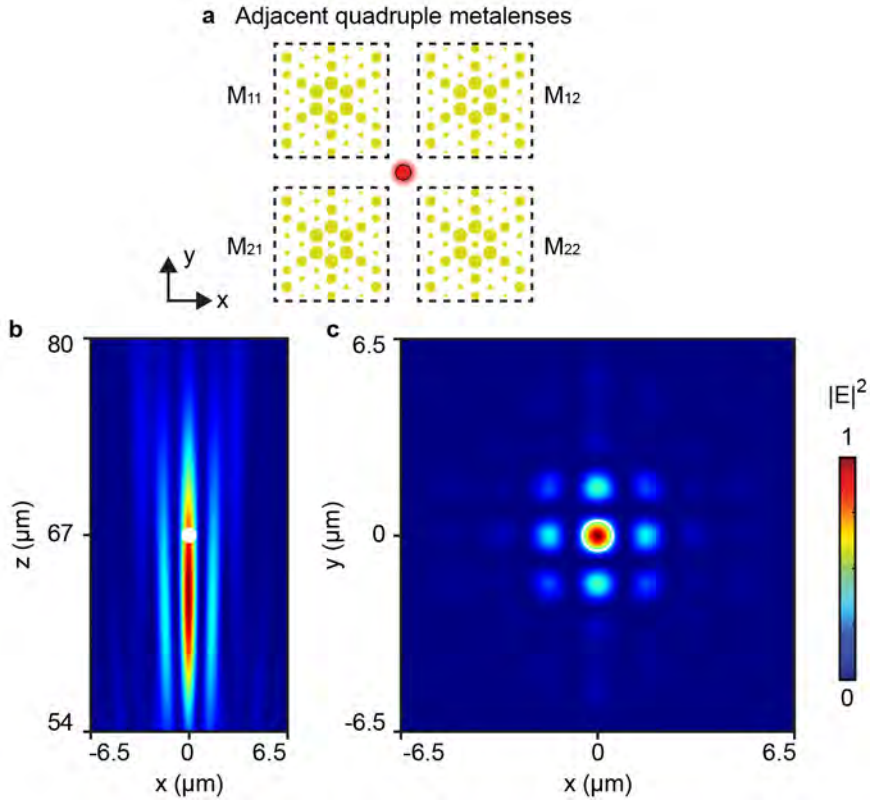

Fig. 5.22. Light focusing of four adjacent metalens unit cells. (a) Perspective view of the fluorescent bead (red dot) and 2×2 metalens unit cells (yellow disk metric), i.e. M_{11}, M_{12}, M_{21}, and M_{22}. (b,c) The output field intensity in the center of four adjacent metalenses. Cross section views in (b) the xz plane and (c) the xy plane across the focus show the converging field with sidebands and the corresponding location of the source. All fields are normalized against the maximum field intensity.

5.10 Modification for self-guiding

Previous sections have shown that the metalens-doublet array can achieve wavelength-specific self-tracing. However, the focus overlaps with the source microsphere. As I have analyzed in Chapter 3 and Chapter 4, the gradient force of optical tweezers is the smallest here [9]. To actively guide the microsphere, I add a typical optical component, a mirror that is comprised of a gold layer to the system. The mirror is tilted by 8°, as shown in **Fig. 5.23 a**. Due to the presence of the tilted mirror, the fluorescent sphere forms a image on the other side of the mirror, which constitutes another point source. The essence of this approach is that the tilted gold layer reflects the spherical waves onto the metalens-doublet array. To the metalens-doublet array, there are simultaneously two fluorescent spheres with the same radiation wavelength: the actual fluorescent sphere at the designated spot and the virtual fluorescent sphere placed slanting above the former. To simulate, the metalens-doublet unit-cell is placed beneath a microfluidic channel 16 μm wide, and 16 μm long, and a gold layer with a thickness of 100 nm is placed at an angle ($\phi = 8°$) with the x axis at the top of the microchannel, with the height of the middle position of the gold layer 75 μm above the metalens-A/silica interface.

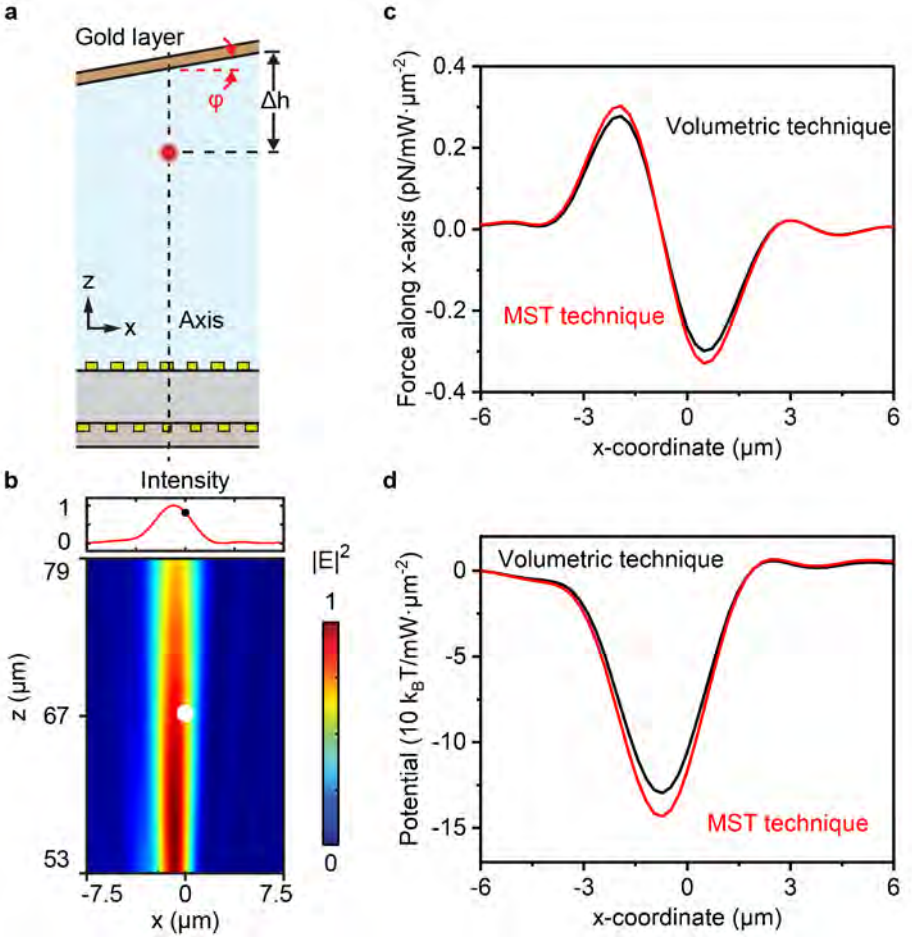

Fig. 5.23. Refocusing and trapping with a tilted gold layer. (a) Perspective view shows a gold layer on the top of the microfluidic channel with a tilted angle $\phi = 8°$, and 75 μm above the metalens A base. The fluorescent bead is fixed at the initial position, $\Delta h = 8$ μm. (b) Distribution of the electric field intensity under this condition. The extracted curve shown on the top depicts the relative position of the focus and the fluorescent bead at $z = 67$ μm. The field is normalized against the maximum field intensity. Corresponding (a) horizontal force map and (b) potential map under this condition.

Because the tilt angle of the gold layer is small, the focus remains as a single spot. Based on the prediction, the focal point should appear at the lower left of the sphere if the fluorescent sphere is at the initial position (i.e. $x = 0, y = 0, z = 67$ μm). This concept can be confirmed by the output field in the middle xz plane of the microchannel in **Fig. 5.23 b**. **Fig. 5.23 b** shows the output field map and an extracted field intensity profile at the height of $z = 67$ μm, demonstrating the relative position of the fluorescent sphere and the established focal spot. As compared with **Fig. 5.16 c**, the focus does not coincide perfectly with the fluorescent sphere. The resultant focusing bias and inhomogeneous field distribution generates a horizontal gradient force on the fluorescent microsphere. The optical force (see **Fig. 5.23 c**) is derived by integrating the Maxwell stress tensor at the surface of the microsphere utilizing the electromagnetic field simulation (see Eqs. A.24 and A.25). At this condition, the fluorescent microsphere with a diameter of 1 μm experiences an optical force on the x axis with a value of -0.24 pN/mW $\cdot$ μm^{-2}. The dynamic stable point (i.e. where $F_x = 0$) locates at $x = -753$ nm on the left of the fluorescent

bead. And the trapping potential is then calculated by integrating the force along a straight line (Eq. A.26), as shown in **Fig. 5.23 d**. The maximum trapping depth is shown at the stable point with a value of 143 $k_BT/mW \cdot \mu m^{-2}$. Both horizontal force and potential well indicate that the microsphere experiences a horizontal force towards the left.

It is worth pointing that, another method to calculate the force on a charged particle in an electromagnetic field. It is the volumetric technique that can be found in Lumerical FDTD software. The method can be derived from Eq. A.3 ($f = \rho E + J \times B$). In the frequency domain, the polarization P and current density J are described as

$$\mathbf{P}(\omega) = \int e^{i\omega t}\mathbf{P}(t)dt \tag{5.51}$$

$$\mathbf{J}(\omega) = -i\omega\mathbf{P}(\omega) \tag{5.52}$$

where, ω is the angular frequency, and t is time. By substituting Eqs. A.4 and 5.52 into Eq. A.3, the force per unit volume is obtained as

$$\mathbf{F}_v = \epsilon_0(\nabla \cdot \mathbf{E})\mathbf{E} - i\omega\mathbf{P} \times \mathbf{B} \tag{5.53}$$

$$\mathbf{F}_v = \epsilon_0(\nabla \cdot \mathbf{E})\mathbf{E} - i\omega(\epsilon - \epsilon_0)\mathbf{E} \times \mathbf{B} \tag{5.54}$$

If the background permittivity is not 1 rescaling the relative permittivity, gives

$$\mathbf{F}_v = \epsilon_b\epsilon_0(\nabla \cdot \mathbf{E})\mathbf{E} - i\omega\epsilon_0(\epsilon_r - \epsilon_b)\mathbf{E} \times \mathbf{B} \tag{5.55}$$

where ϵ_b is the background permittivity, and ϵ_r is the relative permittivity of the volume. With a comparison of the Maxwell stress tensor, the volumetric technique calculates the electromagnetic field in the whole volume, which is less sensitivity to numerical noise. The volumetric technique is better than the Maxwell stress tensor technique when used for calculating tiny objects or small index contrast. In this case, the size of the microsphere is larger than the incident wavelength. Therefore, both techniques are suitable to calculate the optical force. In **Figs. 5.23** and **5.24**, the contrast between the two techniques is less than $\pm 9.38\%$, and the overall profile is similar.

Fig. 5.24 demonstrates the performance of this self-guiding metalens-doublet sorter with the fluorescent sphere moving across the microchannel from the left to the right. The fluorescent sphere is fixed at a height of 67 μm with a deviation angle changing in a range from -6° and 6°. In **Fig. 5.24 b**, the horizontal force on the microsphere at the each deviation angle is calculated by using the Maxwell stress tensor. Without exception, the horizontal optical force performing at all the angles are all negative. It means that force always points to the left. When the microsphere is positioned at the left and right ends,the horizontal optical force is -0.01 pN and -0.09 pN, respectively. When the deviation angle is 0, the microsphere experiences the maximum force. **Fig. 5.24 c** illustrates the output field of the intensity distribution in the xy plane, extracted at $z = 67$ μm, with the microsphere represented by a white circle so that the

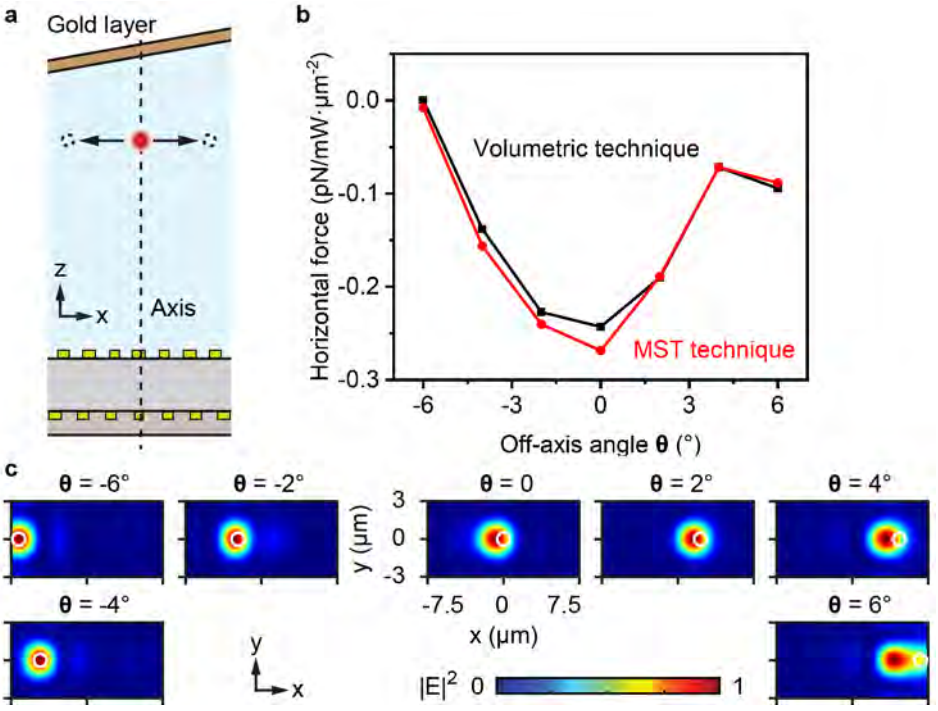

Fig. 5.24. Horizontal force on the fluorescent bead and the corresponding field intensity. (a) Perspective view of the position (arrows and dash circles). (b) Horizontal force on the fluorescent bead at different angles with the optical axis. (c) Seven field distributions of the field intensity with a reference circle representing the fluorescent bead. All fields are normalized against the maximum value of the respective field.

relative position of the focus and the sphere can be observed. All the areas are 15 μm in width and 6 μm in length. The focus is always on the left of the microsphere. Utilizing the output field at a deviation angle of 0 as a reference, the focal spot is gradually compressed along the x axis as the microsphere moves to the left and gradually elongated as it moves to the right (see **Fig. 5.24 c**). Based on this result, I expect that a waterborne fluorescent microsphere with the target wavelength can be trapped and guided along the $-x$ direction.

As discussed in Chapter 3 and Chapter 4, the terminal velocity of a particle moving across the fluid can be calculated by substituting the optical force into Eq. 3.1. The overall efficiency can be estimated by considering the efficiency of each step. The fluorescence efficiency of the scarlet fluorescent sphere can exceed 70% [310]. The radiation energy received by one metalens-doublet aperture is approximately 3.47%. The refocusing efficiency of the metalens-doublet is 11%. The refocusing energy accounts for 6.2‰ of the energy required to excite the fluorescent bead when only one metalens-doublet is utilized. Based on the values above, the laser power required for the particle sorting at a terminal velocity of 200 nm/s is 1 mW/μm^2, and the dependence of the two is linear. Based on the research of fluorescence decay [311], I estimate that the fluorescent bead can be sorted by the metalens-doublet array, with a 70 mW laser and a spot size of 10 μm^2 [312]. In numerical calculation, the trapped fluorescent bead can traverse half of one metalens-doublet (i.e. 8 μm) within its lifespan.

5.11 Conclusion to Chapter 5

In conclusion, I have designed and numerically simulated a metalens-doublet sorter capable of self-tracing and self-guiding at a designated wavelength. By utilizing two arrays of amorphous silicon nanopillars, the metalens doublet can focus the waves from a fluorescent sphere back onto it, similar to a retroreflector. A mirror is subsequently added to the model for realizing a horizontal optical force. With the mirror, the metalens doublet could perform automatic sorting and guiding of fluorescent spheres without any additional active control.

The focus can be analytically predicted using two models, the ray matrix model and the geometric optics model. Both models can can produce theoretical results that match with numerical simulation. The prediction can guide the design of multi-layered metasurface lenses (i.e. cascaded metalens). The minimum laser power required to achieve sorting (assumed to be moving from the center of the metalens-doublet to its edge) is 7 $mW/\mu m^2$, considering only the effect of a single unit of the metalens array.

As a novel multiplexing structure, metalens doublet can achieve advanced functionalities that are difficult to realize in conventional singlet metasurface lenses. I believe that introducing metalens doublet into microfluidic systems could lead to a range of novel devices.

Chapter 6

Conclusions and Outlook

Optofluidics, an emerging research realm that combines nanophotonics and microfluidics, has diverged into various research directions in recent years [10]. It has shown unique advantages in realizing different miniaturized, portable lab-on-a-chip systems. It can be used to modulate the properties of light via employing a fluid (i.e. on-chip dye-lasing, light router, and beam controller), and to detect and manipulate fluid and particles inside. Due to the excellent compatibility between photonic and fluidic devices, optofluidics devices are suitable for the medical, biological, and bio-chemistry realms.

Since the introduction of the concept of optical tweezers, numerous technologies have become compatible with optical tweezers technology, such as fluorescence excitation, Raman spectrometer, and optofluidics analysis. The essence of optical tweezers is to trap and manipulate an object by utilizing a gradient force in an inhomogeneous electromagnetic field. Nanophotonics structures can generate such inhomogeneous field for trapping and can be embedded in microfluidic chips, creating on-chip optical tweezers.

My research has aimed at producing tunable optical forces for particle trapping and routing by using photonic devices embedded in microfluidic systems. I have numerically demonstrated a plasmonic nanorail system that produces highly concentrated near fields. The distribution of the near field can be tuned by the incident wavelength, allowing for tunable particle routing along the rails. I have also numerically demonstrated a metalens that focuses light in the far field. The focus can be swept across a microfluidic channel by controlling the relative phase and intensity of two coherent incident beams. This tunability allows for particle routing in the far field. As the third piece of my PhD work, I have designed a cascaded metalens that can focus fluorescent light from a particle back to itself. This design could be used to sort particles automatically based on fluorescence color.

Beside using the numerical simulation tools, I have also explored several analytical methods to analyze the optical force. Chapter 3 and Chapter 4 have analyzed optical force on the Rayleigh particle and the Mie particle, which is calculated by using the dipole momentum

technique and the Maxwell stress tensor technique. In Chapter 5, the volumetric technique is employed to analyze a charged sphere. Moreover, by using the ray matrix and the geometric optics, I can predict the output rays of the cascaded metalenses and simplify the wavefront design.

Based on the current simulation results, the efficiency of fluorescence self-sorting by metalens array is still quite limited. In further steps, I will try to improve the net working efficiency of the metalens-doublet, and the correction at a large angle incident, so that a larger metalens array can be used. This method (FEACS) has the potential to enable passive optical sorting without the use of an additional detecting system.

Direct use of such optical sorters in cell manipulation may be difficult due to the similar refractive indices between cells and the liquid environment. In addition to fluorescence modification for providing sorting conditions, optical sorters can be employed to sort proteins (common refractive index: $1.33 - 1.6$) or isolate viruses (e.g. refractive index of the flu virus is 1.48) from mixed cells. Due to the non-contact nature of optical tweezers, they can trap, manipulate, or sort without damaging the cell and molecule, which has a broad application prospect in the field of biomedicine and biology.

Due to time constraint and disruptions caused by the covid pandemic, experimental verification for the third piece of work was planned but not completed. Preliminary results can be found in the appendix. I foresee that in some of the devices that I have fabricated, optical force-induced self-organization of particles can be observed in the near future. Once the cascaded metalens is fabricated, the existing measurement system should allow us see the predicted phenomenon of fluorescence-based self sorting.

Appendix A

Optical force on a nanoparticle

Evanescent field can interact with a dielectric nanosphere, and its contribution to plasmonic trapping can be numerically calculated. Chapter 3 has analyzed enhanced near-field distribution on the plasmonic nanorails at the Entrance route, Route 1, Route 2 and the Y-junction. Although the plasmon-induced potential and horizontal force exerted on the nanosphere are shown in **Figs. 3.2 -3.8**, electromagnetic fields on the nanosphere have not been discussed in the chapter. **Fig. A.1** shows the enhanced near-field distribution on the outer, bottom surface of the trapped nanosphere. The nanosphere is located 10 nm above the top of the nanorails and at the center of the gap. The bottom view demonstrates the concentration of the electric field at the water/nanoparticle interface. Similar to the distribution of the evanescent field surrounding the nanorails, a symmetric field is observed on the nanosphere when it is at the Entrance route. Meanwhile, asymmetric field distribution appears on the nanosphere at Route 1 and Route 2, which matches with **Figs. 3.5** and**3.6**.

I have used the Maxwell stress tensor to compute the optical force acting on nanospheres and microspheres in previous chapters. Here, I lay out the key equations and used the nanosphere to demonstrate how to do the calculation. Initially, the nanosphere is considered to be a closed surface and is divided into a number of interfaces. The electromagnetic force on each interface is calculated independently, and the resultant force on the entire nanosphere is then determined using spherical integration. The derivation is as follows.

Energy is a scalar, and the energy flow density is a vector. In terms of the divergence of the tensor, the flow density of a momentum component in a certain direction is

$$(\nabla \cdot \overleftrightarrow{\mathrm{T}})_j = \sum_i \frac{\partial}{\partial x_i} T_{ji} \tag{A.1}$$

where the indices i and j refer to the coordinates x, y, and z. The electromagnetic field further satisfies the conservation of momentum. In a closed space, this implies that the sum of the

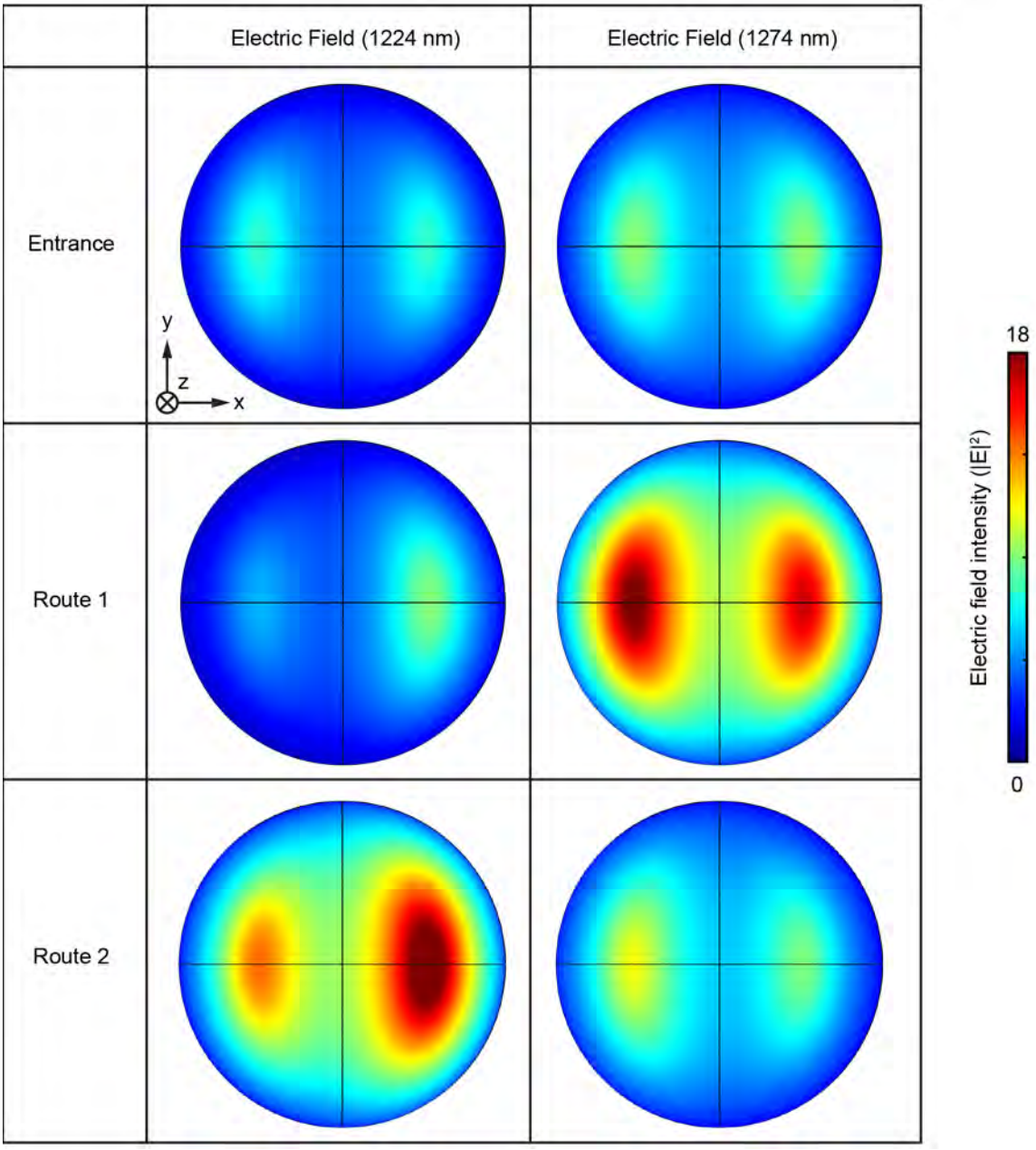

Fig. A.1. Electric field intensity on the lower hemisphere of a nanoparticle at two wavelengths. The nanosphere is positioned at on Entrance, Route 1 and Route 2, and its bottom is 10 nm above the nanorails. All field distributions are normalized against the field intensity of the corresponding incident beam. The upper limit of the color scale is set at 18 for visualization.

conversion rate, the increase rate and the outflow rate is zero. This condition gives

$$\mathbf{f} + \nabla \cdot \overleftrightarrow{\mathrm{T}} + \mu_0 \epsilon_0 \frac{\partial \mathbf{S}}{\partial t} = 0 \tag{A.2}$$

where the first term is the Lorentz force per unit volume affected by a charge distribution, the second term is the rate at which the total momentum of a volume (the momentum of the charge plus the momentum of the electromagnetic field) increases, and the third term is the rate of the energy flowing through the interface **S**. Here, we start from the generalized Lorentz force to calculate the force density of an electric charge

$$\mathbf{f} = \rho(\mathbf{E} + v \times \mathbf{B}) = \rho\mathbf{E} + \mathbf{J} \times \mathbf{B} \tag{A.3}$$

where **E** is the electric field, v is the average drift velocity of charged particles, and **B** is the magnetic field. The two terms of Eq. A.3 should relate to an electromagnetic field, and they cannot contain the terms of electric charge. Hence, the charge density ρ and current density **J** will be replaced with terms of the electromagnetic field by utilizing Maxwell's equations as shown in Eqs. A.4 and A.5

$$\nabla \cdot \mathbf{E} = \frac{\rho}{\epsilon_0} \tag{A.4}$$

$$\nabla \times \mathbf{B} = \mu_0 \mathbf{J} + \mu_0 \epsilon_0 \frac{\partial \mathbf{E}}{\partial t} \tag{A.5}$$

The Lorentz force is then expressed as

$$\mathbf{f} = \epsilon_0 (\nabla \cdot \mathbf{E}) \cdot \mathbf{E} + \frac{1}{\mu_0} (\nabla \times \mathbf{B} - \mu_0 \epsilon_0 \frac{\partial \mathbf{E}}{\partial t}) \times \mathbf{B} \tag{A.6}$$

$$\mathbf{f} = \epsilon_0 (\nabla \cdot \mathbf{E}) \cdot \mathbf{E} + \frac{1}{\mu_0} (\nabla \times \mathbf{B}) \times \mathbf{B} - \epsilon_0 \frac{\partial \mathbf{E}}{\partial t} \times \mathbf{B} \tag{A.7}$$

We also have

$$\frac{\partial \mathbf{E}}{\partial t} \times \mathbf{B} = \frac{\partial}{\partial t} (\mathbf{E} \times \mathbf{B}) - \mathbf{E} \times \frac{\partial \mathbf{B}}{\partial t} \tag{A.8}$$

$$\nabla \times \mathbf{E} = -\frac{\partial \mathbf{B}}{\partial t} \tag{A.9}$$

Based on Eq. A.9, Eq. A.8 can be derived to

$$\frac{\partial \mathbf{E}}{\partial t} \times \mathbf{B} = \frac{\partial}{\partial t} (\mathbf{E} \times \mathbf{B}) - (\nabla \times \mathbf{E}) \times \mathbf{E} \tag{A.10}$$

Substituting Eq. A.10 in Eq. A.7 to gives

$$\mathbf{f} = \epsilon_0 (\nabla \cdot \mathbf{E}) \cdot \mathbf{E} + \frac{1}{\mu_0} (\nabla \times \mathbf{B}) \times \mathbf{B} + \epsilon_0 (\nabla \times \mathbf{E}) \times \mathbf{E} - \epsilon_0 \frac{\partial}{\partial t} (\mathbf{E} \times \mathbf{B}) \tag{A.11}$$

In Eq. A.11, the rightmost term involves the Poynting vector as below

$$\mathbf{S} = \frac{1}{\mu_0}\mathbf{E} \times \mathbf{B} \tag{A.12}$$

We also have Gauss's law for magnetism, which is shown below

$$\nabla \cdot \mathbf{B} = 0 \tag{A.13}$$

In order to make the formula of the electromagnetic field more symmetric, a term based on Eq. A.13 can be added to Eq. A.11, which leads to

$$\mathbf{f} = \epsilon_0[(\nabla \cdot \mathbf{E}) \cdot \mathbf{E} + (\nabla \times \mathbf{E}) \times \mathbf{E}] + \frac{1}{\mu_0}[(\nabla \cdot \mathbf{B}) \cdot \mathbf{B} + (\nabla \times \mathbf{B}) \times \mathbf{B}] - \epsilon_0\mu_0\frac{\partial \mathbf{S}}{\partial t} \tag{A.14}$$

In general, wherever there are two consecutive cross products, we should try to turn them into dot products. Based on the relevant formula of the Del operation (the Nabla operation), of which

$$\nabla(\mathbf{A} \cdot \mathbf{B}) = \mathbf{A} \times (\nabla \times \mathbf{B}) + \mathbf{B} \times (\nabla \times \mathbf{A}) + (\mathbf{A} \cdot \nabla)\mathbf{B} + (\mathbf{B} \cdot \nabla)\mathbf{A} \tag{A.15}$$

if $\mathbf{A} = \mathbf{B} = \mathbf{E}$, we obtain

$$\nabla(\mathbf{E}^2) = 2\mathbf{E} \times (\nabla \times \mathbf{E}) + 2(\mathbf{E} \cdot \nabla)\mathbf{E} \tag{A.16}$$

$$\mathbf{E} \times (\nabla \times \mathbf{E}) = (\mathbf{E} \cdot \nabla)\mathbf{E} - \frac{1}{2}\nabla(\mathbf{E}^2) \tag{A.17}$$

Similar, the magnetic field can be derived as

$$\mathbf{B} \times (\nabla \times \mathbf{B}) = (\mathbf{B} \cdot \nabla)\mathbf{B} - \frac{1}{2}\nabla(\mathbf{B}^2) \tag{A.18}$$

Consequently, the formula for the force density of an electric charge can be written as

$$\mathbf{f} = \epsilon_0[(\nabla \cdot \mathbf{E}) \cdot \mathbf{E} + (\mathbf{E} \cdot \nabla)\mathbf{E} - \frac{1}{2}\nabla(\mathbf{E}^2)] + \frac{1}{\mu_0}[(\nabla \cdot \mathbf{B}) \cdot \mathbf{B} + (\mathbf{B} \cdot \nabla)\mathbf{B} - \frac{1}{2}\nabla(\mathbf{B}^2)] - \epsilon_0\mu_0\frac{\partial \mathbf{S}}{\partial t} \tag{A.19}$$

As compared with Eq. A.2, it can be found that, if no energy flow in and out of the interface, the divergence of momentum flow density tensor can be expressed as

$$\nabla \cdot T = -\epsilon_0[(\nabla \cdot \mathbf{E}) \cdot \mathbf{E} + (\mathbf{E} \cdot \nabla)\mathbf{E} - \frac{1}{2}\nabla(\mathbf{E}^2)] - \frac{1}{\mu_0}[(\nabla \cdot \mathbf{B}) \cdot \mathbf{B} + (\mathbf{B} \cdot \nabla)\mathbf{B} - \frac{1}{2}\nabla(\mathbf{B}^2)] \tag{A.20}$$

Hence, the momentum flow density tensor $\overleftrightarrow{\mathrm{T}}$ (a third-order matrix) can be obtained by comparing the coefficients from the divergence calculation formula of the second-order tensor (Eq. A.20). Now I rewrite the right-hand side of the Eq. A.20 in the summation notation. The following derivation employs the Kronecker delta and defines any vector with a subscript to

denote the n^{th} component, for instance

$$A_j = \begin{cases} A_x\,(j=1) \\ A_y\,(j=2) \\ A_z\,(j=3) \end{cases} \quad x_j = \begin{cases} x\,(j=1) \\ y\,(j=2) \\ z\,(j=3) \end{cases} \tag{A.21}$$

Accordingly, the momentum flow density tensor is obtained as

$$(\nabla \cdot T)j = -\epsilon_0(\sum_i \frac{\partial E_i}{\partial x_i}E_j + \sum_i E_i\frac{\partial E_j}{\partial x_i} - \frac{1}{2}\sum_i \frac{\partial \mathbf{E}^2}{\partial x_i}\delta_{ij}) - \frac{1}{\mu_0}(\sum_i \frac{\partial B_i}{\partial x_i}B_j + \sum_i B_i\frac{\partial B_j}{\partial x_i} - \frac{1}{2}\sum_i \frac{\partial \mathbf{B}^2}{\partial x_i}\delta_{ij})$$

$$(\nabla \cdot T)j = -\epsilon_0\sum_i(\frac{\partial E_i}{\partial x_i}E_j + E_i\frac{\partial E_j}{\partial x_i} - \frac{1}{2}\frac{\partial \mathbf{E}^2}{\partial x_i}\delta_{ij}) - \frac{1}{\mu_0}\sum_i(\frac{\partial B_i}{\partial x_i}B_j + B_i\frac{\partial B_j}{\partial x_i} - \frac{1}{2}\frac{\partial \mathbf{B}^2}{\partial x_i}\delta_{ij})$$

$$(\nabla \cdot T)j = -\epsilon_0\sum_i[\frac{\partial}{\partial x_i}(E_iE_j) - \frac{1}{2}\frac{\partial \mathbf{E}^2}{\partial x_i}\delta_{ij}] - \frac{1}{\mu_0}\sum_i[\frac{\partial B_i}{\partial x_i}(B_iB_j) - \frac{1}{2}\frac{\partial \mathbf{B}^2}{\partial x_i}\delta_{ij}]$$

$$(\nabla \cdot T)j = -\epsilon_0\sum_i\frac{\partial}{\partial x_i}(E_iE_j - \frac{1}{2}\mathbf{E}^2\delta_{ij}) - \frac{1}{\mu_0}\sum_i\frac{\partial B_i}{\partial x_i}(B_iB_j - \frac{1}{2}\mathbf{B}^2\delta_{ij})$$

$$(\nabla \cdot T)j = \epsilon_0\sum_i\frac{\partial}{\partial x_i}(\frac{1}{2}\mathbf{E}^2\delta_{ij} - E_iE_j) + \frac{1}{\mu_0}\sum_i\frac{\partial B_i}{\partial x_i}(\frac{1}{2}\mathbf{B}^2\delta_{ij} - B_iB_j) \tag{A.22}$$

And by the definition of tensor divergence

$$(\nabla \cdot T)_j = \sum_i \frac{\partial}{\partial x_i}T_{ij} \tag{A.23}$$

The momentum flow density tensor or Maxwell stress tensor is obtained as

$$T_{ij} = \epsilon_0(\frac{1}{2}\mathbf{E}^2\delta_{ij} - E_iE_j) + \frac{1}{\mu_0}(\frac{1}{2}\mathbf{B}^2\delta_{ij} - B_iBj) \tag{A.24}$$

For a harmonic electromagnetic field, the time-averaged electromagnetic force F on a dielectric particle in a vacuum is given by

$$F = \oint_s \overleftrightarrow{\mathrm{T}}\,\hat{n}dS \tag{A.25}$$

where $\hat{n}$ is the unit volume, and **S** represents a closed surface. In addition, the potential energy P shown in **Figs. 3.2**, **3.5**, and **3.6** can be calculated by applying a line integral of the time-averaged electromagnetic force along the trajectory of the nanosphere, in which the equation is shown as below

$$P = \int Fdl \tag{A.26}$$

Based on these equations, optical force distribution can be simulated by utilizing the Maxwell stress tensor the finite element analysis engine, COMSOL Multiphysics. Here I use **Fig. A.2** as an example result of this kind of calculation. Both the component forces (based on Eq. A.24, shown as in the insets of **Fig. A.2**) and the resultant force (based on Eq. A.25) are shown. Discussions related to the total force can be found in Chapter 3.

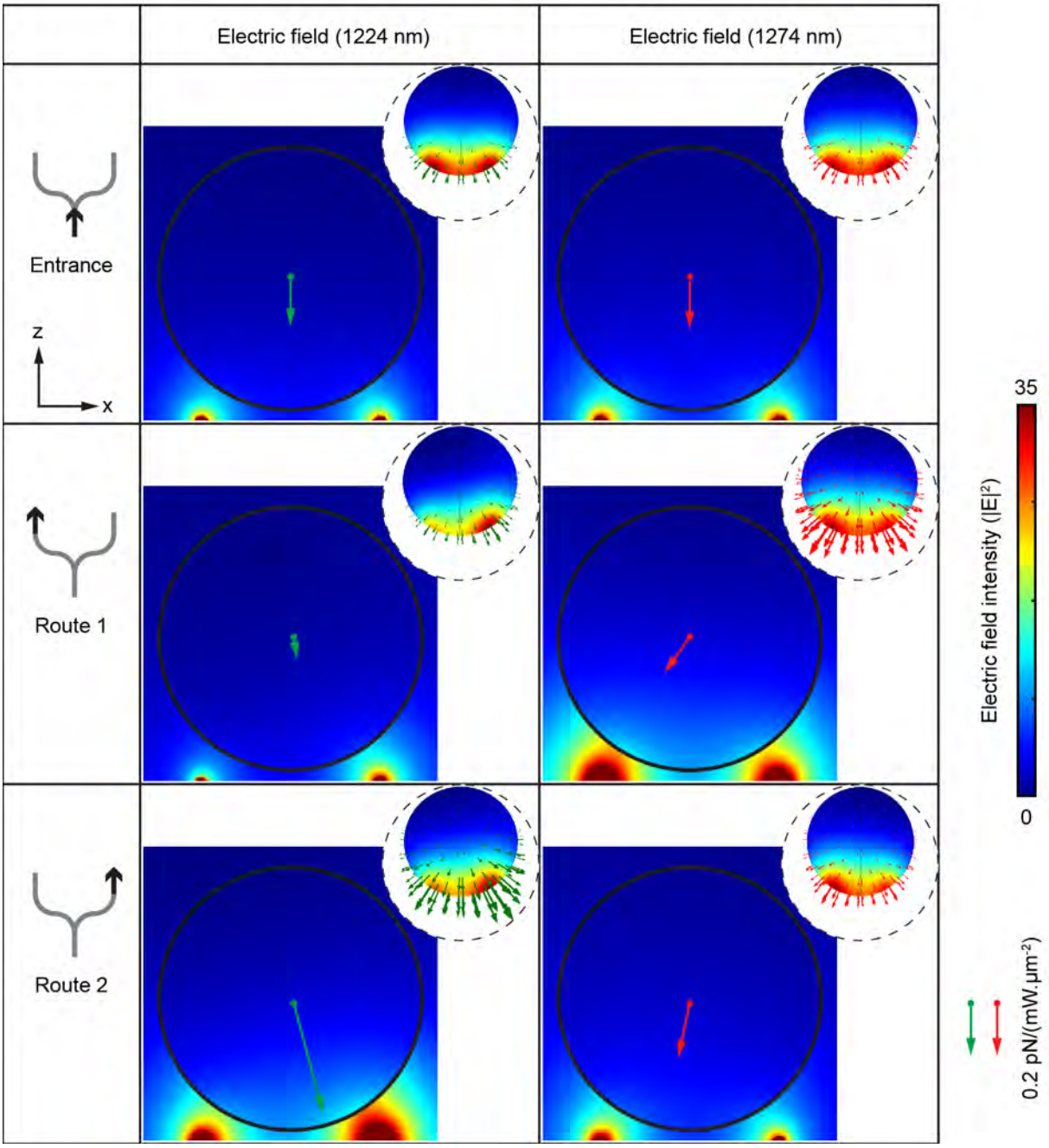

Fig. A.2. Electric field intensity of trapping field, with the nanoparticle (the black circle) at the middle of the nanorails gap under the illumination at 1224 **nm and** 1274 **nm.** These maps represent an area 240 nm $\times$ 240 nm in size, with the bottom edge at the top of the nanorails. The bottom of the nanoparticle is 10 nm above the top surface of the nanorails. All field distributions are normalized against the field intensity of the corresponding incident light. The upper limit of the color scale is set at 35 for visualization. Optical forces shown in green and red arrows indicate the total force. The scale is 0.2 $\mathrm{pN}/(\mathrm{mW}\cdot\mu\mathrm{m}^{-2})$. Inset: the distribution of power flow density and the Maxwell stress tensor on segmented interfaces (green and red arrows).

Appendix B

An alternative design of the tunable metalens tweezers

It is possible to build coherently controlled tunable metalens tweezers using a hyperbolic phase profile, as an alternative to the V-shape profile reported in Chapter 4. The cross section dimensions of the hyperbolic lens (Gaussian lens) are shown in **Table B.1**. Beforing deciding on choosing the Bessel metalens in the published journal paper (see **Figs. 4.11** and **4.13**), hyperbolic metalens tweezers were evaluated to analyze the focus status and trapping abilities. The design (see **Fig. 4.11**) is quite similar to the Bessel metalens. The width of the unit cell along the x-axis is 22.5 μm, also as the width of the microchannel before the junction. A 130-μm-thick PDMS layer covers the metalens structure under the microfluidic channel. The diameter of the lens is 22.5 μm, and its focus distance of 130 μm. The numerical aperture equation is expressed as

$$NA = n \cdot \sin\theta = n \cdot \sin[\arctan(\frac{D}{2f})] \tag{B.1}$$

where θ is the maximal half-angle of the light's cone, n is the refractive index of the medium, D is the diameter of the lens, and f is the focal distance. When this angle is small enough, the equation can be simplified to

$$NA \approx n\frac{D}{2f} \tag{B.2}$$

The numerical aperture of this metalens is approximately 0.12; it is a weak focusing lens with a full width at half maximum larger than 5 μm. The output focusing distribution of this metalens is shown in **Fig. B.1** under five illumination conditions mentioned previously, i.e. the E-antinode, the single-beam, the B-antinode, and two intermediate conditions. As compared with the field distribution in **Fig. 4.11**, the focus is shorter and the sidebands are weaker. Nevertheless, this beam is also possible to steer a particle across the middle of the microchannel continuously. In **Figs. B.1 a** and **e**, the angle between the central axis of the focus and the z-axis are -1.44° and 1.1°, respectively, indicating a steering angle of roughly 2.5°.

Table B.1. Cross-sectional dimensions of the 25 constituent nanopillars in nanometers. All the nanopillars have an elliptical cross section with the principal axes along x and y.

No.	x axis	y axis	No.	x axis	y axis	No.	x axis	y axis
1	100	320	8,9	160	220	21,22	360	230
2	130	270	10-13	200	130	23	360	220
3	140	260	14-16	400	240	24	360	200
4,5	140	290	17,18	380	240	25	400	130
6,7	150	250	19,20	360	240			

The trapping potential of a microsphere and a nanosphere is also analyzed in **Figs. B.1 f** and **g**. In the calculation, both particles are moved from the left side of the microchannel to the right side at 10 μm above the bottom of the channel, the same as in **Fig. 4.13**. When compared to Bessel metalens tweezers, the maximum potential depth of the 100-nm-diameter nanosphere is roughly the same, at 0.1 $k_B \cdot T/(mW \cdot \mu m^{-2})$. In contrast, the depth of the potential well is decreased by $\sim$ 40%, to approximately 60 $k_B \cdot T/(mW \cdot \mu m^{-2})$ for the microsphere with a 1-μm-diameter under all three illumination conditions. Accordingly, it can be concluded that for the two low-NA lenses of the very similar dimensions, the lens with an axicon profile (the Bessel lens) produces stronger trapping potential in the horizontal direction (i.e., perpendicular to the propagating direction) than the hyperbolic lens (a Gaussian lens) [274].

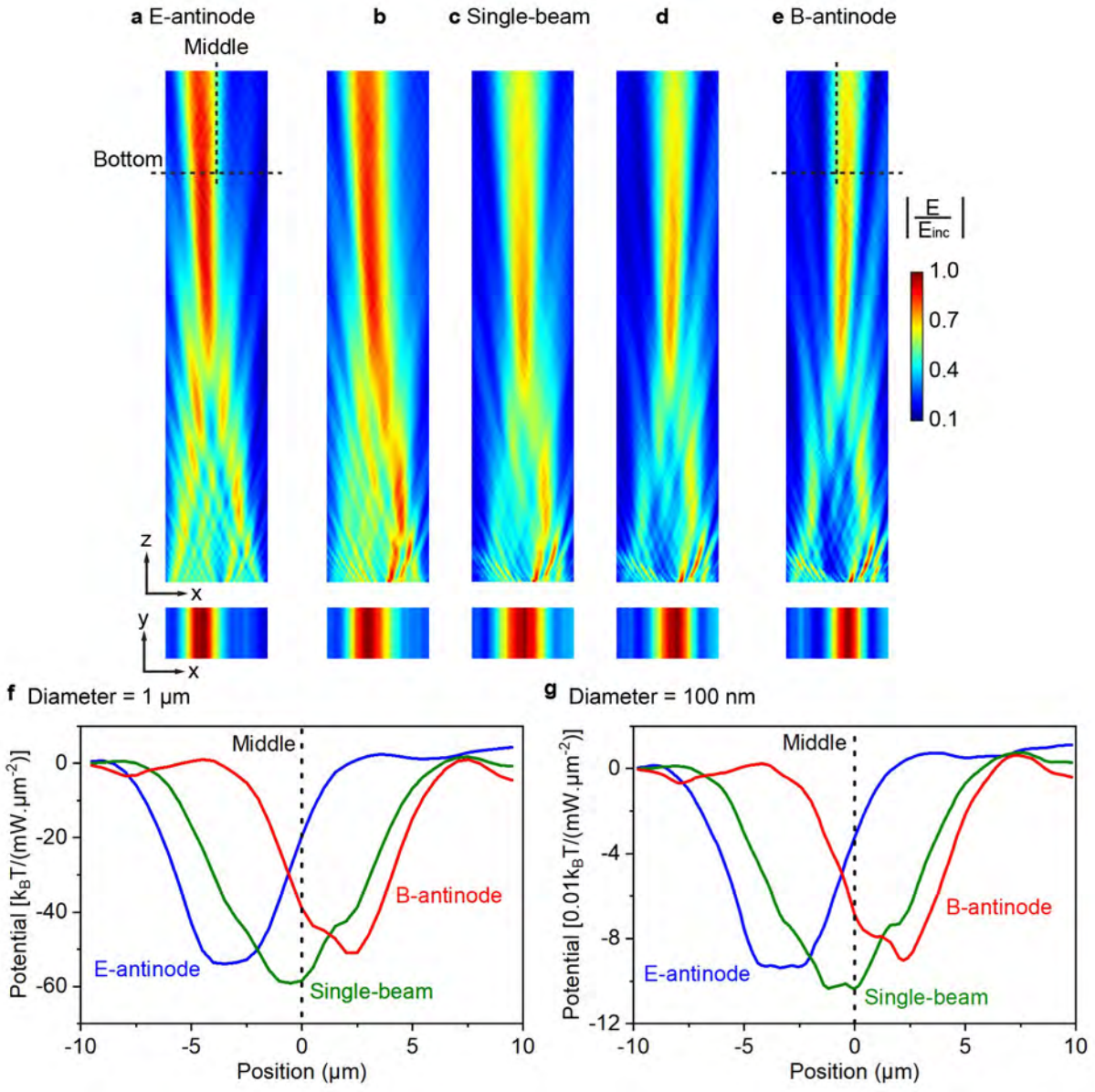

Fig. B.1. Light focusing and steering of the hyperbolic metalens under (a-e) five different illumination conditions, and the panels are plotted following the same specifications as Fig. 4.13. (f,g) Potential energy for particle trapping in the microfluidic channel under the three main illumination conditions. The particle diameter is (f) 1 μm and (g) 100 nm.

Appendix C

Fresnel zone plate: a flat metallic lens

Nanofabrication was also a part of my PhD plan. Unfortunately, due to the Covid-19 pandemic, the fabrication process originally scheduled to begin in March 2020 had to be postponed to November 2021. In order to simplify the fabrication, a Fresnel zone plate (FZP) was designed. This structure consists of a series of co-axial opaque rings to obstruct incident waves. The opaque zones on the FZP will cause light to diffract, and the diffracted light can produce a focus via constructive interference.

I fabricated a FZP on an aluminum thin film. The fabrication process is shown in **Fig. C.1**: (a) spin coating a 300-nm-thickness layer of ZEP-520A (i.e. a positive e-beam resist) on top of a silicon substrate and writing the pattern using e-beam lithography; (b) developing for 100 s in ZED-N50 and 2×45 s IPA to generate patterns in the resist layer; (c) e-beam evaporating a 50-nm-thickness aluminum film on top; (d) removing the resist and the adherent Al on the top of the resist by using NMP solution.

The FZP with a diameter of 4 mm (see **Fig. C.2 a**) is designed to operate under the telecom wavelength of 1550 nm. The aim is to generate a focus 5 mm above the plate. To get constructive interference at the focus, the patterns written by e-beam lithography should follow the equation

$$r_n = \sqrt{n\lambda f + \frac{1}{4}n^2\lambda^2} \tag{C.1}$$

where r_n is the radius where zones switch from opaque to transparent, n is an integer, λ is the incident wavelength, and f is the focal distance. By substituting the parameters required in this FZP design, the value of r_1 can be obtained as 88.034 μm, which is the same as the measured value shown in **Fig. C.2 c**. **Fig. C.2 d** shows the outermost ring with a width of 2.32 μm. In the microscopy images, the relative bright patterns (see **Fig. C.2**) can represent the aluminum, the residual regions represent the silicon substrate. As of the writing of this thesis, the focus of the FZP has not been characterized as Si metalenses discussed in later sections have been prioritized in experiment. More discussions can be found at the end of Appendix D.

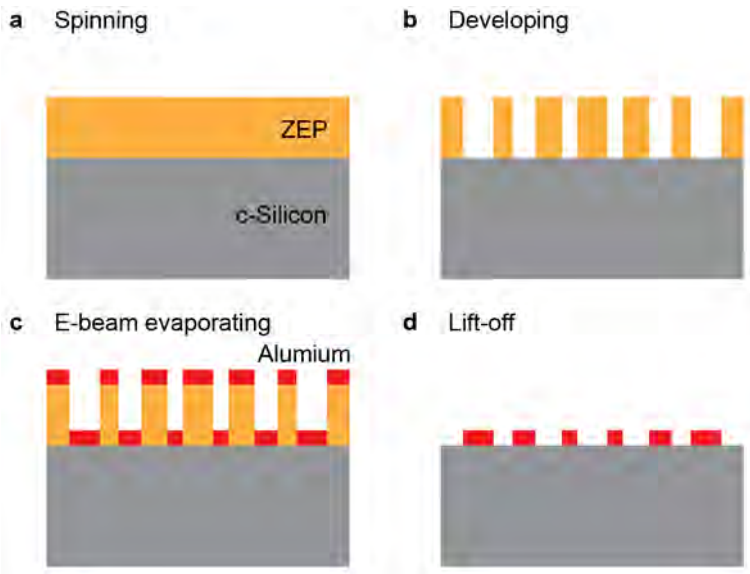

Fig. C.1. Flow chart of the fabrication process of Al patterns. (a) spin-coating, (b) e-beam lithograph and developing, (c) metallic patterns depositing by e-beam evaporating, and (d) removing the resist.

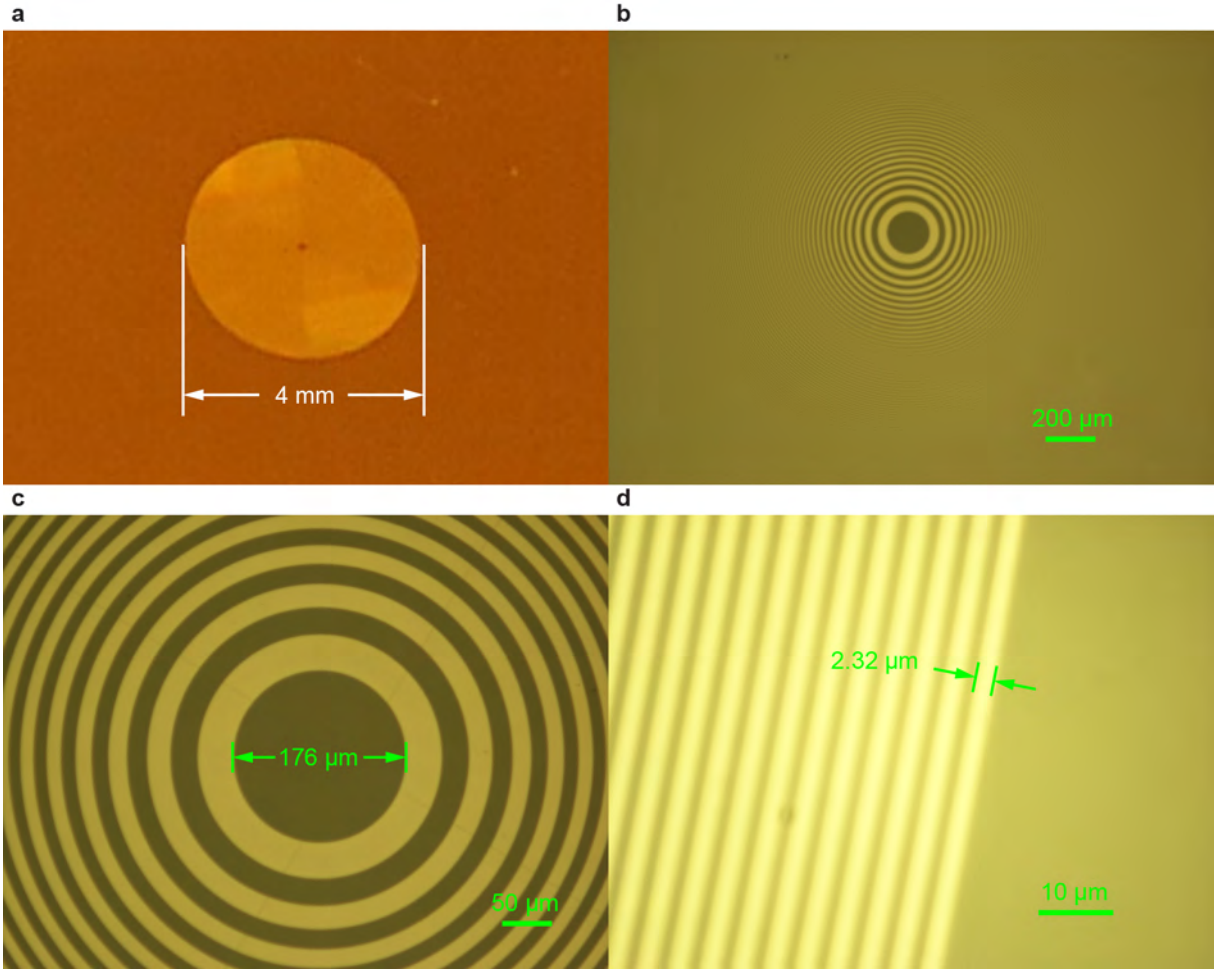

Fig. C.2. Images of the aluminum Fresnel zone plate (FZP) under a microscopy. The image under (a) a camera and a microscopy with an amplification factor of (b) ×5, (c) ×20, and (d) ×150. Panels (b,c) are at the center region of the FZP and (d) is at the edge of the FZP.

Appendix D

Silicon-base metamaterial lenses

As compared with the FZP, a metalens consisting of sub-wavelength pillars can achieve a higher degree of control over light propagation. In both Chapter 3 and Chapter 4, the metalenses use nanostructured silicon. A fabrication procedure for such silicon nanostructure is (see **Fig. D.1**): (a) spin-coating a 300-nm-thickness ZEP resist and writing patterns by utilizing e-beam lithography; (b) developing by using ZED-N50 and IPA solution; (c) depositing a chromium hard mask on top of the sample; (d) removing the residual resist by lift-off; (e) transferring the pattern from the Cr islands to the silicon substrate beneath by using inductively coupled plasma (ICP) etching, (f) removing the residual Cr on the top of the Si nanopillars by a Cr etching solution.

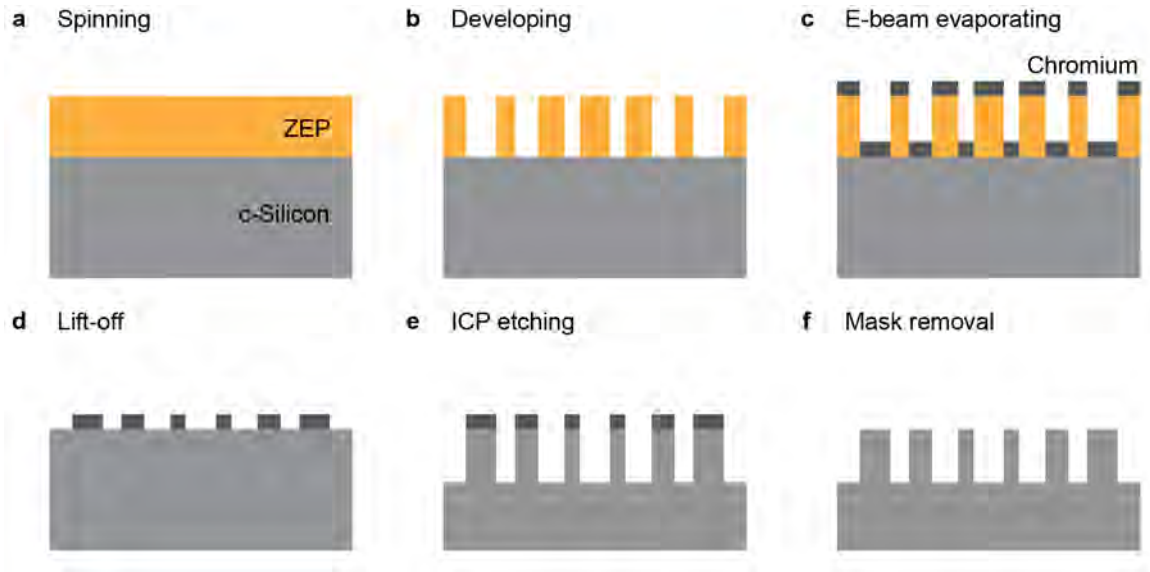

Fig. D.1. Flow chart of the fabrication process of c-Silicon nanopillars. This silicon-based process includes (a) spin-coating, (b) e-beam lithograph and developing, (c) hard mask depositing by e-beam evaporating, (d) resist lift-off, (e) inductively coupled plasma (ICP) etching, and (f) hard mask removal.

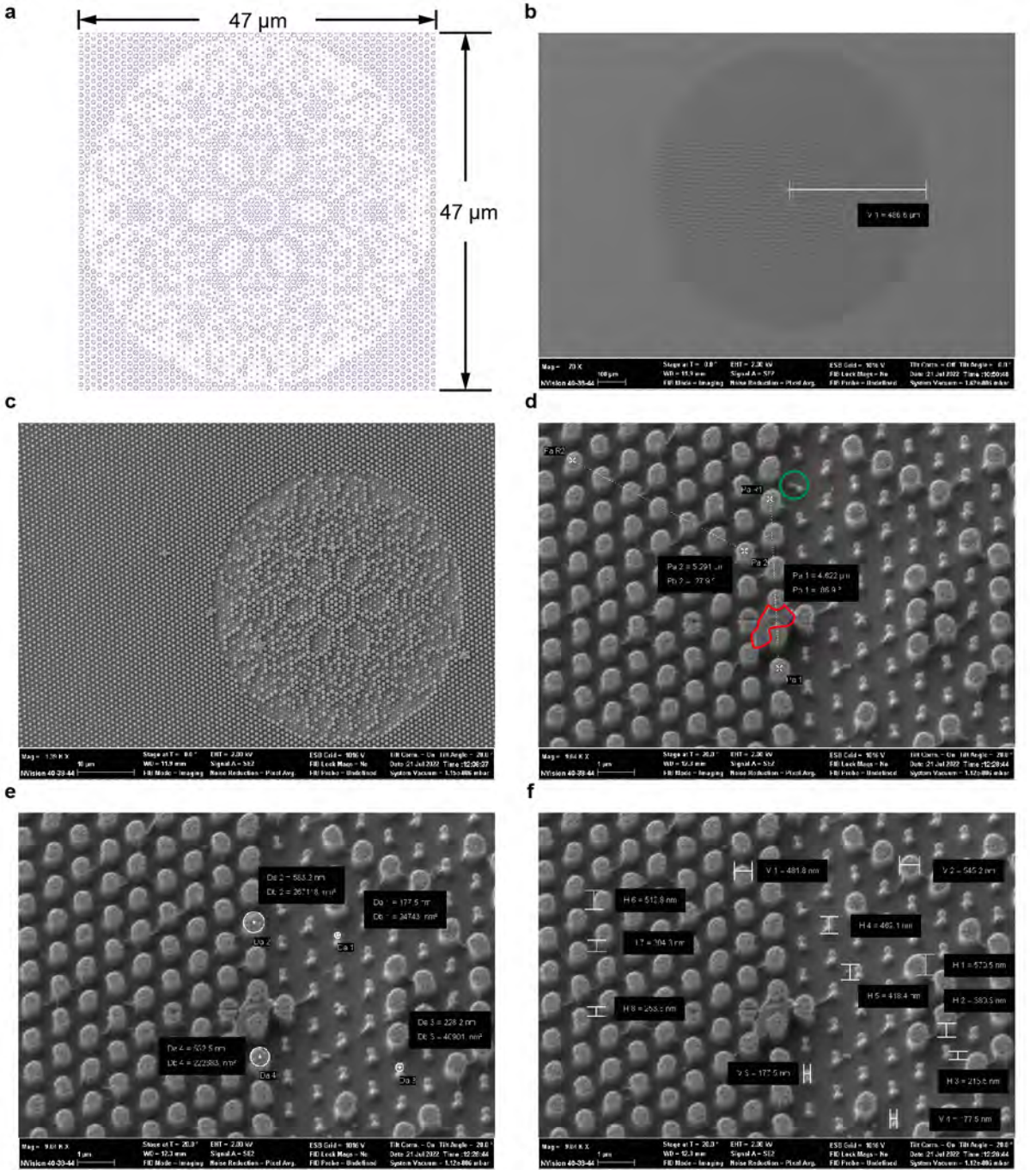

Fig. D.2. GDSii and SEM images of designed silicon metalens. (a) The central area of the designed GDSii file shows as a reference. (b-f) SEM images are labeled with (b) the radius of the metalens, (d) periodicity of the meta-atom in the metalens, (e) the diameters of the nanopillars with different scales, and (f) the height of the nanopillars. Panel (c) is the central area of the metalens and contains no label.

All nano-scale circles are drawn using the L-edit tanner controlled by a self-designed database. **Fig. D.2 a** shows central region a width of 47 μm and a length of 47 μm, where blue patterns are e-beam-written patterns. **Figs. D.2 b-f** illustrate one of the fabricated samples under a scanning electron microscope (SEM). The SEM image shows that the radius of the Si metalens is 486.6 μm (see **Fig. D.2 b**), which is less than the radius of design (i.e. 500 μm) due to the measuring error. **Fig. D.2 c** shows the distribution map of the nanopillar in the region corresponding to **Fig. D.2 a**. The center-to-center distances are measured along different directions, and measurement accuracy was increased by measuring the distance between multiple nanopillars. In **Fig. D.2 d**, the distance measured by 4 nanopillars apart is 4.622 μm, and the distance measured by 5 nanopillars apart is 5.291 μm. That gives a measured periodicity of the hexagonal lattice at 903 nm on average, which is closed to the target parameter of 910 nm. Although the largest pattern (583.2-nm-diameter measured vs. 567-nm-diameter designed) and the smallest pattern (177.5-nm-diameter measured vs. 212-nm-diameter designed) show deviation (see **Fig. D.2 e**), it is still expected to be within the allowed error range of the optical metalens. In **Fig. D.2 f**, the thickness of the nanopillar is measured by tilting the sample at 20 °. The measured result is in a range from 254 nm to 304 nm, giving a height between 695 nm and 835 nm after angle correction. The depth of ICP etching was also measured using a profiler for a higher accuracy. The value is from 798 nm to 811 nm, close to the target thickness of 800 nm. However, in **Fig. D.2 d**, a nano-pillar is destroyed (highlighted in green) in the nanofabrication, and an unexpected connection (highlighted in red) appeared. These two non-ideal phenomena are most likely caused by the failure to completely remove the residual resist in the lift-off process (referring to **Fig. D.2 d**), owing to the small dimension of the pattern.

In the process of conventional metalens rendering, the L-edit tanner is difficult to obtain non-nanopillar regions through the Boolean operation due to excessive structure. Therefore, by improving the drawing procedure, it is possible to avoid problems related to using a metallic hard mask. It is possible to utilize ZEP resist as a mask during ICP etching because the etching rate ratio of the ZEP/Si is approximately 0.3 when employing SF_6 and C_4F_8 as etching gases. Accordingly, the fabrication process of the Si-based metalens can be simplified as shown in **Fig. D.3**: (a) spin-coating ZEP resist and executing e-beam lithography; (b) developing; (c) etching by ICP and removing the residual resist.

Fig. D.3. The second flow chart of the fabrication process of c-Silicon nanopillars. This silicon-based process includes (a) spin-coating, (b) e-beam lithograph and developing, and (c) ICP etching and resist removal.

The improved pattern design is shown in **Fig. D.4 a**, which is an 8 μm × 8 μm square in the central area. After developing, the blue shaded area of resist will disappear, whereas the white area of resist will protect the Si beneath during the ICP etching process. **Figs. D.4 b-f** are SEM images of one fabricated sample after removing the resist mask. Continuously changing co-axial circles can be observed in **Fig. D.4**. Zoom in SEM images (see **Figs. D.4 c,d**) show the area of **Fig. D.4 a**. The center-to-center distance (i.e. $5421/6 = 903.5$ nm) well matches the designed lattice constant (i.e. 910 nm). Meanwhile, the diameter of the central nanopillar (625.1 nm as measured) is close to the designed value of 635 nm. **Fig. D.4 e** shows distinct hexagonal edges and periodically arranged nanopillars. With 20° tilted angle, the surface of the silicon substrate after etching is observed, which is still uniform (see **Fig. D.4 f**). After angle correction (i.e. $measured\,result/\tan 20^\circ$), the height of the nanopillars after etching is in a range from 815 nm to 834 nm, which is closed to the measured etching thickness on a silicon-on-insulator (SOI) dummy chip (i.e. 807 nm).

However, the silicon wafer is a single-side polished wafer, i.e. having a rough backside, which will induce unpredictable and intense scattering. Consequently, samples fabricated and demonstrated in Appendix C and Appendix D have not been characterized in their optical properties.

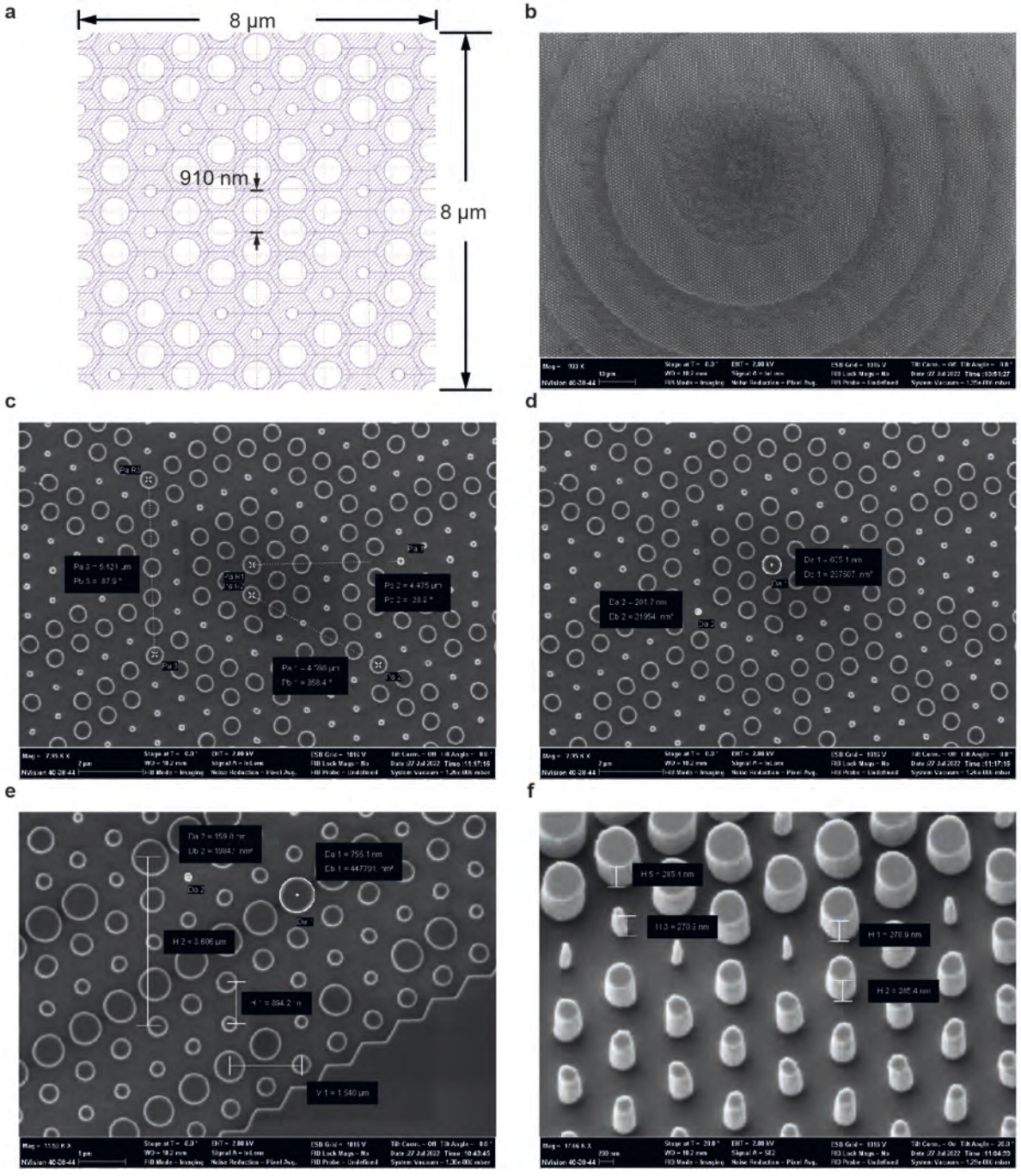

Fig. D.4. GDSii and SEM images of a silicon metalens using the revised algorithm. (a) The central area of the created GDSii file as a reference. (b-f) SEM images are labeled with (c,e) the periodicity of the meta-atom in the metalens, (d) the diameters of the minimum and maximum nanopillar, and (f) the height of the nanopillars. Panel (b) shows a relatively large are and is not labeled.

Appendix E

Cylindrical and spherical optical tweezers

To avoid additional scattering and further to improve power efficiency, a fused silica wafer ($n_{SiO_2} \approx 1.5$) is employed to replace the silicon wafer ($n_{Si} \approx 3.5$). The fused silica wafer is polished on both sides. The procedures of amorphous-silicon (a-Si) fabrication are (see **Fig. E.1**, which is referred to the optimized silicon fabrication in **Fig. D.3**): (a) depositing a uniform a-Si layer on a fused silica wafer by utilizing Plasma Enhanced Chemical Vapor Deposition (PECVD); (b) spin-coating 300-nm-thickness ZEP resist and an e-spacer layer on the top of the a-Si layer; (c) developing by using ZED and IPA solutions; (d) etching by ICP to transfer the patterns from the resist to the a-Si layer; (e) removing the residual resist in NMP solution and cleaning the surface by plasma asher.

In this case, the a-Si metalens keeps the design of hexagonal lattices. The lattice constant is 500 nm, while the height of the a-Si nanopillar is set at 400 nm to achieve a 2π phase coverage. It is essential to ensure the adhesion of the a-Si/fused silica interface, as the a-Si layer can easily peel off. Consequently, a thin film of silicon oxide was deposited by PECVD to guarantee a non-crystalline surface before depositing the functional a-Si layer. At $350^{\circ}C$, $N_2O/N_2/SiH_4$ gases are used to deposit SiO_2 at a rate of 1.15 nm/s. Then the a-Si was deposited at $250^{\circ}C$ utilizing SiH_4/H_2 gases at a deposition rate of 0.26 nm/s, which required 25 min 38 s to achieve the target thickness.

Prior to spin-coating the ZEP resist, it is crucial to measure the thickness of the deposited a-Si layer. Typically, samples are measured with an ellipsometer, and parametric fits are used to derive the thickness. The thickness distribution of the SiO_2 layer throughout the whole 2-inch wafer was acquired utilizing the scanning function of the ellipsometer and is shown in **Fig. E.2**. It shows poor center-to-edge uniformity (see **Fig. E.2 a**), probably because of temperature of the whole wafer in the chamber was not uniform. The fitting curves in **Fig. E.2 b** reveal the correspondence between the optical characteristics of the employed material model and the

optical properties of the actual deposited material, from which the actual thickness is derived. The parameters used for fitting are extracted from the center of the 2-inch wafer.

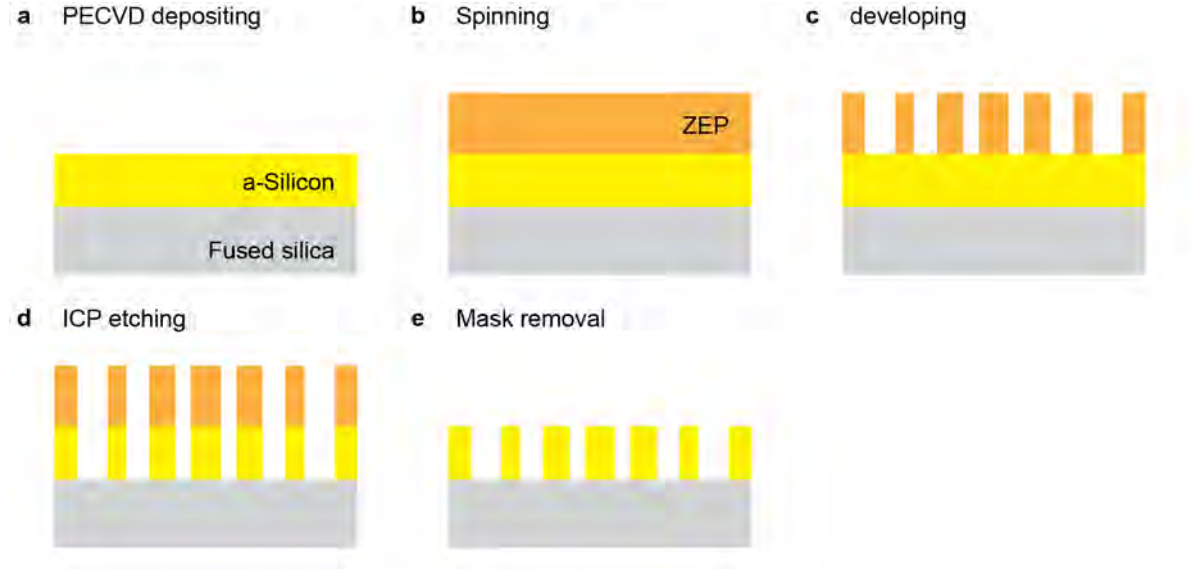

Fig. E.1. Flow chart of the fabrication process of a-Silicon nanopillars. This conventional silicon-based process including (a) PECVD depositing, (b) spin-coating, (c) e-beam lithograph and developing, (d) ICP etching, and (e) removing the residual resist.

From the fitting, we can see that minimum thickness is 401.06 $\pm$ 1.14 nm (extracted from the center), the maximum thickness is 412.34 $\pm$ 1.19 nm (extracted at the bottom edge), and the average thickness is 405.97 $\pm$ 0.726 nm with a mean square error (MSE) of 10.355. The diameter of the metalens, in this case is, 1.2 μm. Therefore the surface thickness may be deemed uniform over a short range, even though the thickness is not uniform over a long range.

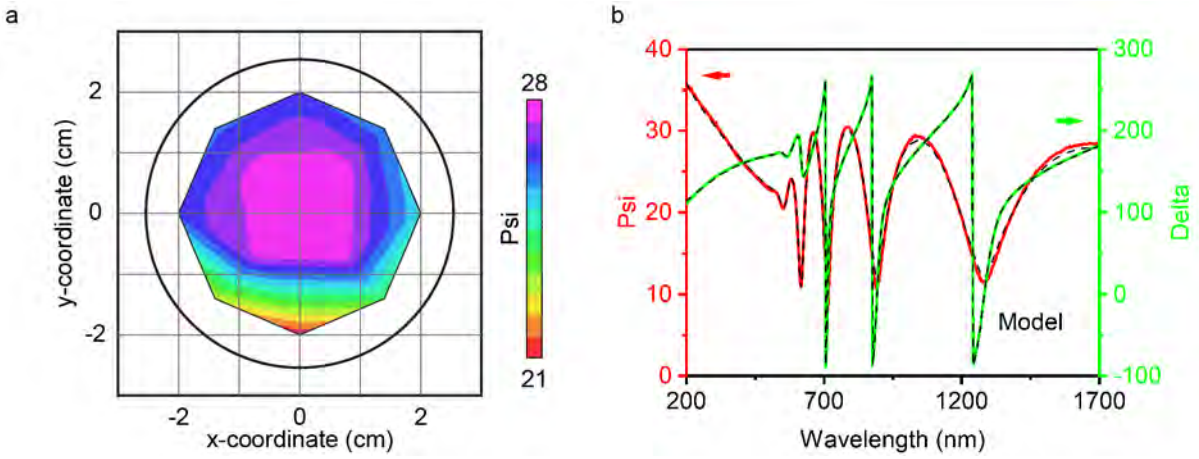

Fig. E.2. Uniformity of an amorphous silica film deposited using PECVD. (a) Distribution of the amplitude ratio *Psi* refers to the corresponding relative thickness of the amorphous-silicon on the silica substrate. The black circle represents the scale of the silica wafer as a guide for the eye. (b) The amplitude ratio *Psi* and phase change *Delta* demonstrate the similarity between the measured data (red and green curves) and the fitted data (black dashes).

In this design, a metalens has 4 strips of focusing field rising gradually in the direction of the radiation axis, generating a cross-focus. Due to the variable height of its focus plane, it can

produce holographic images. This metalens is aimed to operate under an incident wavelength of 680 nm. Its operating wavelength is visible, so that the focusing can be observed under an optical microscope. As shown in **Fig. E.3**, 4 shining arms appear on the metalens, extending outward from the center. To check whether the nanopillars are intact, the center and edge regions of the cross metalens are observed using the microscopy's maximum magnification (i.e. $\times$150), shown in **Figs. E.3 c,d**.

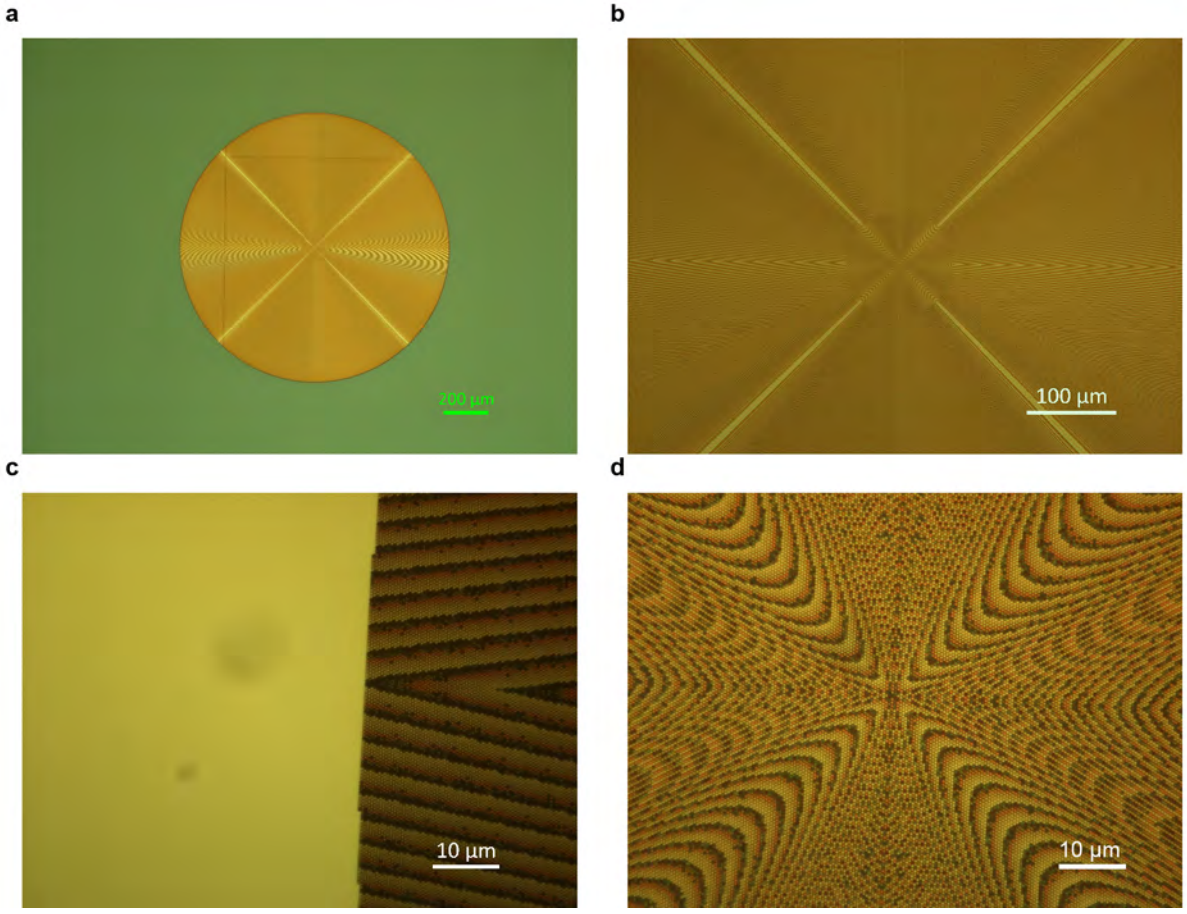

Fig. E.3. Microscopy images of the cross metalens. Amplification factors are (a) $\times$5 for observing overall structure, (b) $\times$20 in the central area, and (c,d) $\times$150 for observing nanopillars, respectively.

Simultaneously, SEM images are utilized to check the distribution of nanopillars (see **Fig. E.4**). An overall view of the whole metalens is shown in **Figs. E.4 a**, **b** and **c** show details in the center and at the edge of the metalens, respectively. The periodicity (i.e. shortest center-to-center, see **Fig. E.4 d**) is approximately 487 nm, which closely matches the designed value of 500 nm. As compared with a silicon substrate, the fused silica substrate quickly accumulates charges in the SEM. During observation, the image jitter is more obvious than that of the silicon substrate, and the profile of the nanopillar appears as a polygon after freezing the image. **Fig. E.4 e** shows the diameter of the largest nanopillar (343.3 nm measured vs.390 nm designed) and the smallest nanopillar (93.62 nm vs. 150 nm), in which all patterns have shrunk for is about 50 nm as compared to the design pattern. Utilizing other lenses for future observation may improve the precision of the measured data.

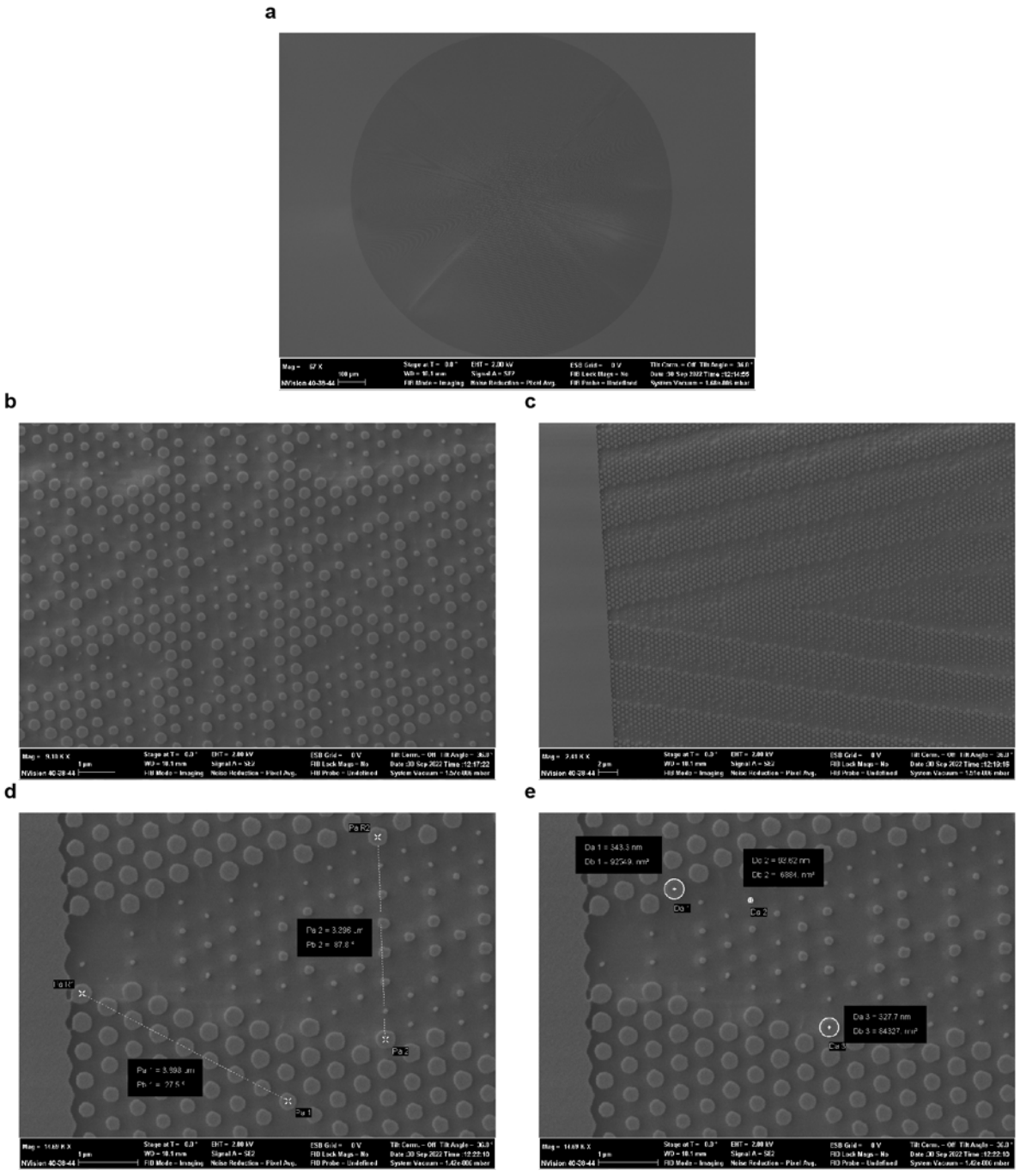

Fig. E.4. SEM images of the metalens. The images show (a) the overall view of the cross metalens and the nanopillar distribution, (b) in the center, and (c) at the edge of the cross metalens. The images are labeled (d) center-to-center distances for measuring periodicity and (e) diameters of the smallest and largest nanopillars in the cross metalens.

Our collaborator Dr. Bruce Ou provided an optical measurement system to examine the imaging of the metalens under laser excitation. In this measurement set up (see **Fig. E.5 a**), a fiber laser with a wavelength of 642 nm is employed to excite the designed metalens from the backside. One of the samples is located on a Piezo stage that can be raised and lowered. The camera is selected with a magnification factor of $\times 10$, so the monitor can only observe the center region of the metalens with a window of 960 μm in width and 540 μm in length. **Fig. E.5 b** illustrates two imaging conditions: the metalens at 5 μm and 50 μm below the objective plane. Under these two conditions, the focal points are located at para-central and submarginal positions on four focusing strings, respectively. By stacking 51 images, a holographic image shows the whole focus pattern (see **Fig. E.5 c**). The angle between the focusing string and the metalens plane is approximately 7.47°, which is equivalent to a ratio of the focal length to the radius of 0.13 ($f/r = 0.13$). This metalens is aimed to operate in a water environment ($n_{water} = 1.33$). However, the measurement system set up in the air ($n = 1$) results in the observation focus being lower than the design focus length. Even through, the observed focal length still conforms to the design ($f/r = 0.17$) after refractive index correction by numerical calculation ($0.13 \times 1.33 \approx 0.17$). The field intensity on one arm is significantly stronger than the other three arms. This phenomenon may be due to the influence of the stress generated by dicing the sample. **Fig. E.5 d** demonstrates field intensity maps at different heights (i.e. 5 μm and 50 μm referring to **Fig. E.5 b**) above the cross metalens, which can be more intuitive to observe the intensity distribution on the corresponding focal planes. Moreover, the extracted field intensity distribution is consistent with the design.

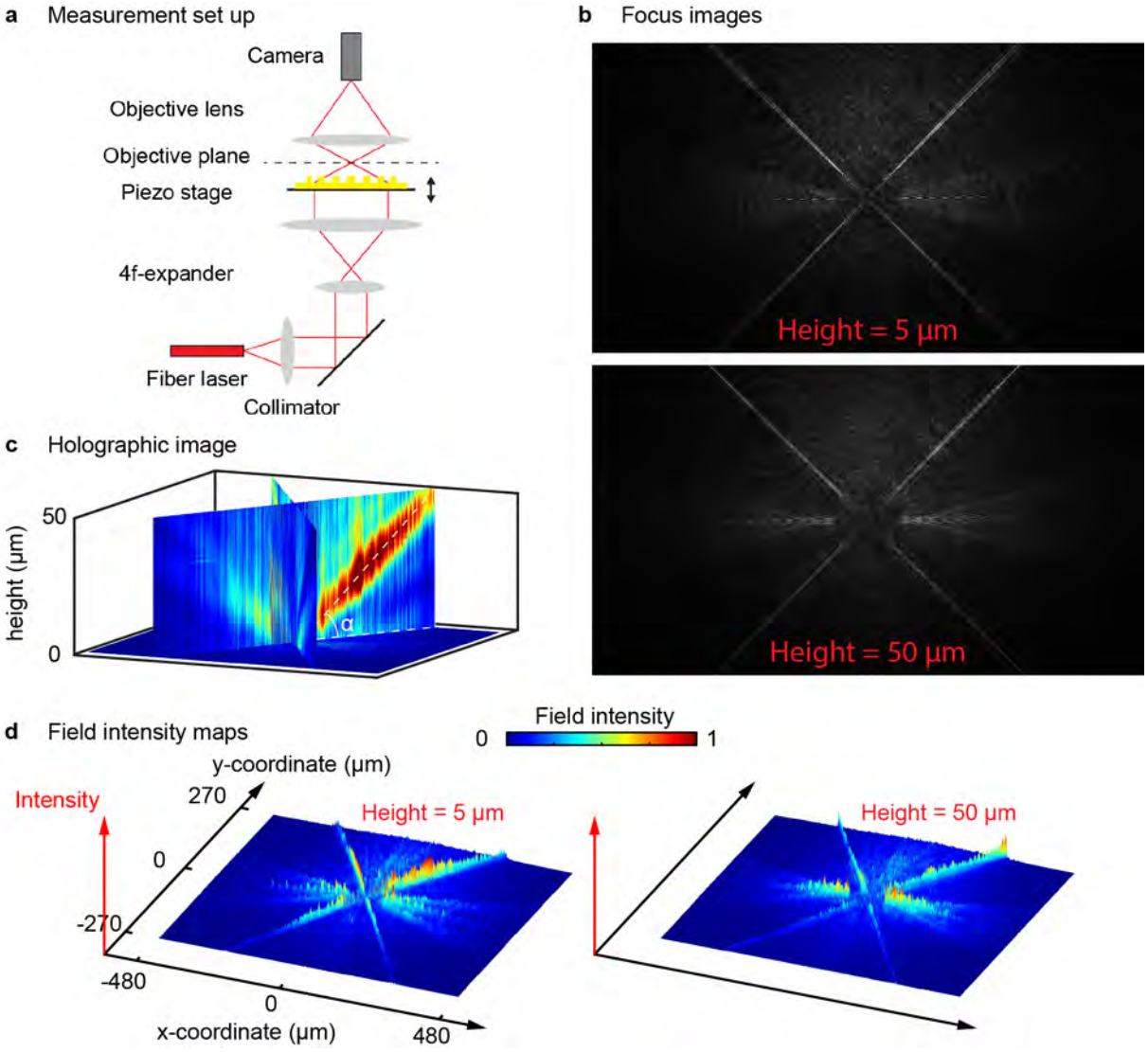

Fig. E.5. Experimental results of the cross metalens. (a) Perspective view of the measurement set up shows an optical system consisting of a laser source with a wavelength of 642 nm, a collimator, a 4f expander, a tunable Piezo stage, a $\times 10$ objective lens, and a camera for observation. Optical rays are illustrated in red lines. (b) Extracted focusing images at different objective planes with a height of 5 μm and 50 μm, respectively. (c) A stacking image shows a holographic focus in three dimensions. (d) Observed field intensity maps show a 4-arm cross focus at different heights. All color maps are normalized against the maximum value in each individual figure.

Another sample, a high numerical aperture metalens, is shown in **Fig. E.6**. This design is a spherical metalens with a diameter of 600 μm. It is expected to generate a focus at a height of 150 μm. The output phase gradient of the spherical metalens is derived from Eq. 5.44. This metalens aims to operate under the wavelength of 680 nm. Based on Eq. B.1, the numerical aperture of the metalens is approximately 0.97 in air. The central region of the metalens is observed using the maximum magnification of the microscope (i.e. $\times$ 150), as shown in **Fig. E.6 b**.

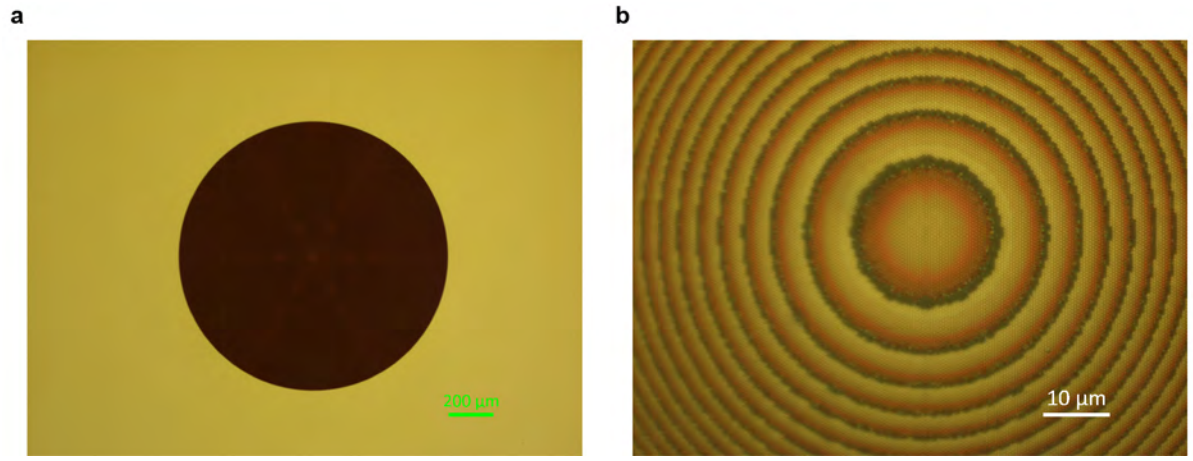

Fig. E.6. Microscopy images of the metalens. Amplification factors are (a) $\times$5 for observing overall structure and (b) $\times$150 in the central area.

Based on the previous experimental set up (see **Fig. E.5**), a $\times$ 400 objective lens replaces the $\times$ 10 objective lens. And the 4f expander is removed. In this case, a camera with a magnification factor of $\times$ 400 is available. With this camera, the observation window is 24 μm in width and 14 μm in length. **Fig. E.7** shows the whole focusing pattern by stacking 201 images. As the holder of the sample is not perfectly horizontal, the focus has slightly shifted away from the theoretical position (see **Fig. E.7 b**). The deviation angle α is 0.24° in both x and y directions. It should be noted that, the optical axis of the spherical lens is not at the same position as the center of the image. **Fig. E.7c** illustrates the imaging condition that the metalens is at 157 μm below the objective plane. A field intensity map shows the corresponding field distribution (**Fig. E.7d**).

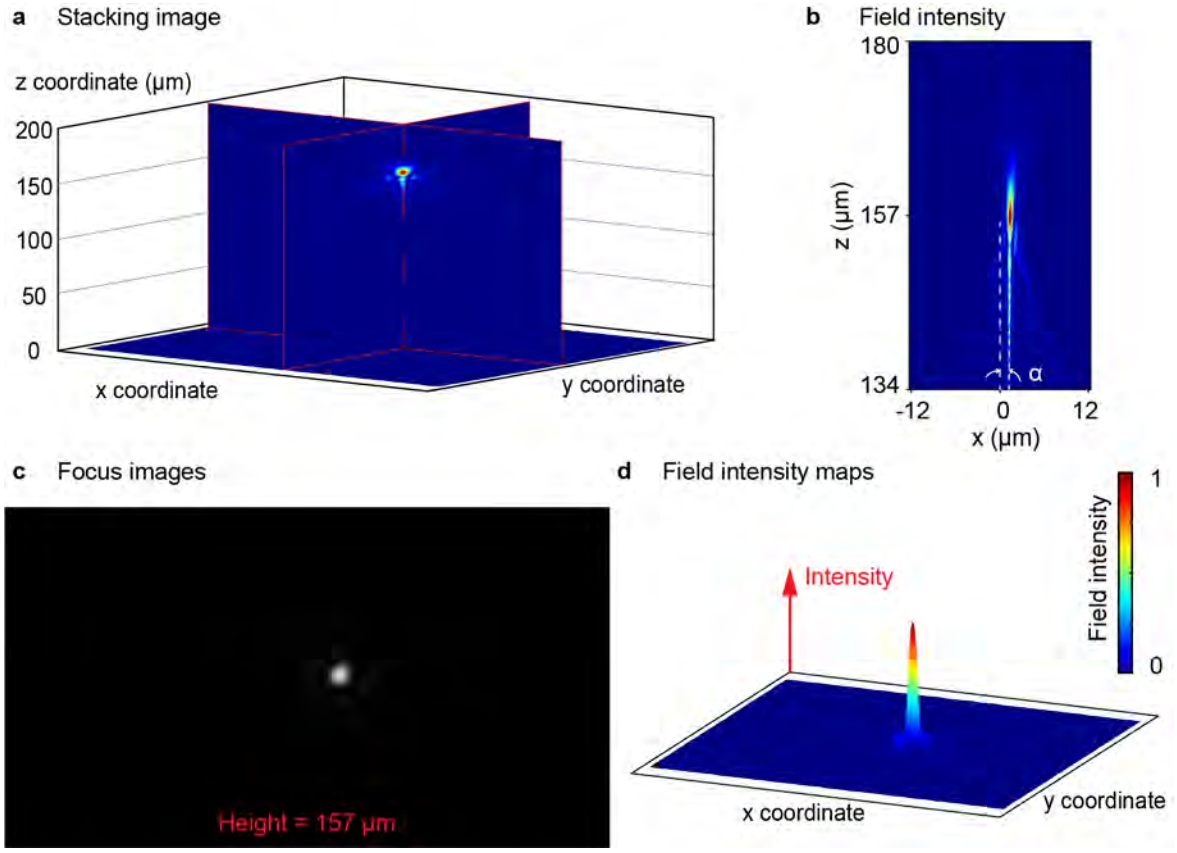

Fig. E.7. Experimental results of the spherical metalens. (a) A stacking image shows a focus in three dimensions. (b) A field distribution of electric field intensity shows focusing characteristics in the xz plane. (c) Extracted focusing images at different objective planes with a height of 157 μm. (d) Observed field intensity map shows the focus. All color maps are normalized against the maximum value in each individual figure.

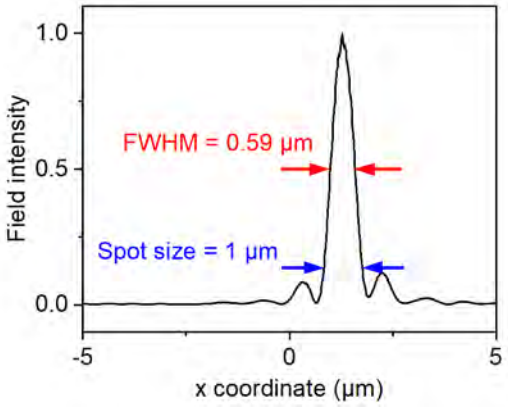

Fig. E.8. Field intensity was extracted at the focal spot. The curve is normalized against the maximum value of the field intensity.

In **Fig. E.8**, the field intensity at the focal spot is extracted along the x direction. For visualization, the data is selected between $x = -5$ μm and $x = 5$ μm. In the experimental result, the FWHM and the spot size of the focus is measured at 0.59 μm and 1 μm, respectively. By compared with the corresponding theoretical results (0.13 μm and 0.22 μm), the increase may be due to three factors. First, the spherical metalens is designed to operate at 680 nm. Under the incident light of 642 nm, high-order diffraction may occur on the output field. Second, the objective lens is selected to observe with a numerical aperture of 0.9, so the resolution of the observed image may be worse than the actual focus. Third, the metalens design is for operating at normal incident. Oblique incident may affect spherical aberration and comatic aberration, which can affect the resolution of the metalens. As a consequence, the focal spot could become larger and longer. A potential solution here is to use an aplanatic model rather than the hyperbolic model to achieve optical correction.

References

[1] Itia A. Favre-Bulle, Alexander B. Stilgoe, Ethan K. Scott, and Halina Rubinsztein-Dunlop. Optical trapping in vivo: theory, practice, and applications. *Nanophotonics*, 8(6):1023–1040, 2019.

[2] Holger Schmidt and Aaron R. Hawkins. The photonic integration of non-solid media using optofluidics. *Nature Photonics*, 5(10):598–604, 2011.

[3] C. Monat, P. Domachuk, and B. J. Eggleton. Integrated optofluidics a new river of light. *Nat Photonics*, 1(2):106–114, 2007.

[4] N. T. Huang, H. L. Zhang, M. T. Chung, J. H. Seo, and K. Kurabayashi. Recent advancements in optofluidics-based single-cell analysis: optical on-chip cellular manipulation, treatment, and property detection. *Lab Chip*, 14(7):1230–45, 2014.

[5] K. H. Lee, S. B. Kim, K. S. Lee, and H. J. Sung. Enhancement by optical force of separation in pinched flow fractionation. *Lab Chip*, 11(2):354–7, 2011.

[6] X. Heng, D. Erickson, L. R. Baugh, Z. Yaqoob, P. W. Sternberg, D. Psaltis, and C. Yang. Optofluidic microscopy–a method for implementing a high resolution optical microscope on a chip. *Lab Chip*, 6(10):1274–6, 2006.

[7] A. Keloth, O. Anderson, D. Risbridger, and L. Paterson. Single cell isolation using optical tweezers. *Micromachines (Basel)*, 9(9):434, 2018.

[8] S. Yin, F. He, N. Green, and X. Fang. Nanoparticle trapping and routing on plasmonic nanorails in a microfluidic channel. *Opt Express*, 28(2):1357–1368, 2020.

[9] S. Yin, F. He, W. Kubo, Q. Wang, J. Frame, N. G. Green, and X. Fang. Coherently tunable metalens tweezers for optofluidic particle routing. *Opt Express*, 28(26):38949–38959, 2020.

[10] Paolo Minzioni, Roberto Osellame, Cinzia Sada, Shen Zhao, FG Omenetto, Kristinn B Gylfason, Tommy Haraldsson, Yibo Zhang, Aydogan Ozcan, Adam Wax, et al. Roadmap for optofluidics. *Journal of Optics*, 19(9):093003, 2017.

[11] H. Zhang and Y. Sun. Optofluidic droplet dye laser generated by microfluidic nozzles. *Opt Express*, 26(9):11284–11291, 2018.

[12] Tingting Zhang, Zhuonan Jia, Zhenghua Li, Shuangquan Hua, Jingdong Chen, Wenjie Wang, and Shaoding Liu. Generation of optofluidic laser in stable fiber fabry–pérot microcavities. *Optics Communications*, 475:126234, 2020.

[13] X. Zhao, Y. Chen, Z. Guo, Y. Zhou, J. Guo, Z. Liu, X. Zhang, L. Xiao, Y. Fei, and X. Wu. Tunable optofluidic microbubble lens. *Opt Express*, 30(5):8317–8329, 2022.

[14] Hanyang Huang and Yi Zhao. Optofluidic lenses for 2d and 3d imaging. *Journal of Micromechanics and Microengineering*, 29(7):073001, 2019.

[15] M. Dao, C. T. Lim, and S. Suresh. Mechanics of the human red blood cell deformed by optical tweezers. *Journal of the Mechanics and Physics of Solids*, 51(11-12):2259–2280, 2003.

[16] M. D. Newton, B. J. Taylor, R. P. C. Driessen, L. Roos, N. Cvetesic, S. Allyjaun, B. Lenhard, M. E. Cuomo, and D. S. Rueda. Dna stretching induces cas9 off-target activity. *Nat Struct Mol Biol*, 26(3):185–192, 2019.

[17] D. Psaltis, S. R. Quake, and C. Yang. Developing optofluidic technology through the fusion of microfluidics and optics. *Nature*, 442(7101):381–6, 2006.

[18] M. Hammerich, C. Schutt, C. Stahler, P. Lentes, F. Rohricht, R. Hoppner, and R. Herges. Heterodiazocines: Synthesis and photochromic properties, trans to cis switching within the bio-optical window. *J Am Chem Soc*, 138(40):13111–13114, 2016.

[19] H. G. Jin, W. Zhong, S. Yin, X. Zhang, Y. H. Zhao, Y. Wang, L. Yuan, and X. B. Zhang. Lesson from nature: Biomimetic self-assembling phthalocyanines for high-efficient photothermal therapy within the biological transparent window. *ACS Appl Mater Interfaces*, 11(4):3800–3808, 2019.

[20] C. J. Bustamante, Y. R. Chemla, S. Liu, and M. D. Wang. Optical tweezers in single-molecule biophysics. *Nat Rev Methods Primers*, 1(1):25, 2021.

[21] Zhenyu Li, Zhaoyu Zhang, Axel Scherer, and Demetri Psaltis. Mechanically tunable optofluidic distributed feedback dye laser. *Opt Express*, 14(22):6, 2006.

[22] Wuzhou Song and Demetri Psaltis. Pneumatically tunable optofluidic dye laser. *Applied Physics Letters*, 96(8):081101, 2010.

[23] T. Sano, J. Black, S. Mitchell, H. Zhang, and H. Schmidt. Pneumatically tunable optofluidic dfb dye laser using corrugated sidewalls. *Opt Lett*, 45(21):5978–5981, 2020.

[24] Avraham Bakal, Christoph Vannahme, Anders Kristensen, and Uriel Levy. Tunable on chip optofluidic laser. *Applied Physics Letters*, 107(21):211105, 2015.

[25] C. Gong, Y. Gong, X. Zhao, Y. Luo, Q. Chen, X. Tan, Y. Wu, X. Fan, G. D. Peng, and Y. J. Rao. Distributed fibre optofluidic laser for chip-scale arrayed biochemical sensing. *Lab Chip*, 18(18):2741–2748, 2018.

[26] H. Zhang, P. Palit, Y. Liu, S. Vaziri, and Y. Sun. Reconfigurable integrated optofluidic droplet laser arrays. *ACS Appl Mater Interfaces*, 12(24):26936–26942, 2020.

[27] Z. Feng and L. Bai. Advances of optofluidic microcavities for microlasers and biosensors. *Micromachines (Basel)*, 9(3):122, 2018.

[28] D. Y. Li, H. Zhang, Z. Li, L. W. Zhou, M. D. Zhang, X. Y. Pu, Y. Z. Sun, H. Liu, and Y. X. Zhang. High sensitivity ph sensing by using a ring resonator laser integrated into a microfluidic chip. *Opt Express*, 30(3):4106–4116, 2022.

[29] Tingting Zhang, Chunhua Zhou, Wenjie Wang, and Jingdong Chen. Generation of low-threshold optofluidic lasers in a stable fabry-pérot microcavity. *Optics Laser Technology*, 91:108–111, 2017.

[30] Mohammad Hazhir Mozaffari and Ali Farmani. On-chip single-mode optofluidic microresonator dye laser sensor. *IEEE Sensors Journal*, 20(7):3556–3563, 2020.

[31] Jie Yu, Yange Liu, Mingming Luo, Zhi Wang, Guang Yang, Hongwei Zhang, and Xiaohui Zhang. Single longitudinal mode optofluidic microring laser based on a hollow-core microstructured optical fiber. *IEEE Photonics Journal*, 9(5):1–10, 2017.

[32] Jie Yu, Xiaoming Zhao, Bohan Liu, Hu Liang, Huimin Shi, Xiaoqi Liu, Zhi Wang, and Yange Liu. Reduction in lasing threshold of hollow-core microstructured optical fiber optofluidic laser based on fluorescence resonant energy transfer. *Optical Fiber Technology*, 58:102281, 2020.

[33] W. Lee, D. B. Kim, M. H. Song, and D. K. Yoon. Optofluidic ring resonator laser with an edible liquid laser gain medium. *Opt Express*, 25(13):14043–14048, 2017.

[34] Y. Ozbakir, A. Jonas, A. Kiraz, and C. Erkey. A new type of microphotoreactor with integrated optofluidic waveguide based on solid-air nanoporous aerogels. *R Soc Open Sci*, 5(11):180802, 2018.

[35] Shengxi Jiao, Xinzhi Li, Xiaolei Ren, Hanrui Yang, and Shibo Xu. Research on three-core photonic crystal fiber plasmonic sensor based on surface plasmon resonance with three v-groove microfluidic channel. *Optical Review*, 29(2):80–90, 2022.

[36] Antonio d'Alessandro and Rita Asquini. Light propagation in confined nematic liquid crystals and device applications. *Applied Sciences*, 11(18):8713, 2021.

[37] Farzeena Chalikkara, Pradip Singha, and Subramanyan Namboodiri Varanakkottu. Dual functional optofluidic platform based on light-actuated air plug. *Sensors and Actuators A: Physical*, 285:659–665, 2019.

[38] M. Rahman, M. A. Stott, M. Harrington, Y. Li, M. J. N. Sampad, L. Lancaster, T. D. Yuzvinsky, H. F. Noller, A. R. Hawkins, and H. Schmidt. On demand delivery and analysis of single molecules on a programmable nanopore-optofluidic device. *Nat Commun*, 10(1):3712, 2019.

[39] T. Wall, J. McMurray, G. Meena, V. Ganjalizadeh, H. Schmidt, and A. R. Hawkins. Optofluidic lab-on-a-chip fluorescence sensor using integrated buried arrow (barrow) waveguides. *Micromachines (Basel)*, 8(8):252, 2017.

[40] M.N. Amin, M. Hamblin, G.G. Meena, A.R. Hawkins, and H. Schmidt. Free space excitation in optofluidic devices for single particle detection. *2019 IEEE Photonics Conference (IPC)*, pages 1–2, 2019.

[41] A. Bertucci, A. Manicardi, A. Candiani, S. Giannetti, A. Cucinotta, G. Spoto, M. Konstantaki, S. Pissadakis, S. Selleri, and R. Corradini. Detection of unamplified genomic dna by a pna-based microstructured optical fiber (mof) bragg-grating optofluidic system. *Biosens Bioelectron*, 63:248–254, 2015.

[42] Sa'ad Hassan, Maryam Khodami, R. Niall Tait, and Pierre Berini. Fabrication of long-range surface plasmon-polariton bragg gratings with microfluidic channels in cytop claddings. *Microelectronic Engineering*, 135:38–44, 2015.

[43] Zhe Yu, Ruisheng Liang, Pixin Chen, Qiaodong Huang, Tingting Huang, and Xingkai Xu. Integrated tunable optofluidics optical filter based on mim side-coupled-cavity waveguide. *Plasmonics*, 7(4):603–607, 2012.

[44] K. Mishra, C. Murade, B. Carreel, I. Roghair, J. M. Oh, G. Manukyan, D. van den Ende, and F. Mugele. Optofluidic lens with tunable focal length and asphericity. *Sci Rep*, 4(1):6378, 2014.

[45] Rong-Ying Yuan, Lin Luo, Jin-Hui Wang, Lei Li, and Qiong-Hua Wang. 1×2 optofluidic switch for optical beam routing and variable power distribution. *IEEE Photonics Technology Letters*, 30(18):1629–1632, 2018.

[46] W. Song and D. Psaltis. Pneumatically tunable optofluidic 2 x 2 switch for reconfigurable optical circuit. *Lab Chip*, 11(14):2397–402, 2011.

[47] Q. H. Wang, L. Xiao, C. Liu, and L. Li. Optofluidic variable optical path modulator. *Sci Rep*, 9(1):7082, 2019.

[48] C. Liu, D. Wang, and Q. H. Wang. A multidirectional beam steering reflector actuated by hydraulic control. *Sci Rep*, 9(1):5086, 2019.

[49] P. Escudero, J. Yeste, C. Pascual-Izarra, R. Villa, and M. Alvarez. Color tunable pressure sensors based on polymer nanostructured membranes for optofluidic applications. *Sci Rep*, 9(1):3259, 2019.

[50] H. L. Liu, Y. Shi, L. Liang, L. Li, S. S. Guo, L. Yin, and Y. Yang. A liquid thermal gradient refractive index lens and using it to trap single living cell in flowing environments. *Lab Chip*, 17(7):1280–1286, 2017.

[51] José Francisco Algorri, Dimitrios C. Zografopoulos, Virginia Urruchi, and José Manuel Sánchez-Pena. Recent advances in adaptive liquid crystal lenses. *Crystals*, 9(5):272, 2019.

[52] S. Zhu, Y. Liu, L. Shi, X. Xu, S. Yuan, N. Liu, and X. Zhang. Tunable polarization beam splitter based on optofluidic ring resonator. *Opt Express*, 24(15):17511–21, 2016.

[53] P. Xu, J. Wan, S. Zhang, Y. Duan, B. Chen, and S. Zhang. 2 x 2 optofluidic switch chip with an air shutter. *Appl Opt*, 58(17):4637–4641, 2019.

[54] J. Tang, X. Cao, G. Qiu, A. deMello, and J. Wang. Optical-switch-enabled microfluidics for sensitive multichannel colorimetric analysis. *Anal Chem*, 93(17):6784–6791, 2021.

[55] J. Chen, Z. Kang, G. Wang, J. F. Loo, S. K. Kong, and H. P. Ho. Optofluidic guiding, valving, switching and mixing based on plasmonic heating in a random gold nanoisland substrate. *Lab Chip*, 15(11):2504–12, 2015.

[56] P. Muller, D. Kopp, A. Llobera, and H. Zappe. Optofluidic router based on tunable liquid-liquid mirrors. *Lab Chip*, 14(4):737–43, 2014.

[57] J. COOPER MCDONALD and GEORGE M. WHITESIDES. Poly(dimethylsiloxane) as a material for fabricating microfluidic devices. *Accounts of Chemical Research*, 35(7):491–499, 2002.

[58] J. Dietvorst, J. Goyvaerts, T. N. Ackermann, E. Alvarez, X. Munoz-Berbel, and A. Llobera. Microfluidic-controlled optical router for lab on a chip. *Lab Chip*, 19(12):2081–2088, 2019.

[59] R. Urteaga, L. N. Acquaroli, R. R. Koropecki, A. Santos, M. Alba, J. Pallares, L. F. Marsal, and C. L. Berli. Optofluidic characterization of nanoporous membranes. *Langmuir*, 29(8):2784–9, 2013.

[60] Richard Zeltner, Shangran Xie, Riccardo Pennetta, and Philip St J. Russell. Broadband, lensless, and optomechanically stabilized coupling into microfluidic hollow-core photonic crystal fiber using glass nanospike. *ACS Photonics*, 4(2):378–383, 2017.

[61] R. Lima, S. Wada, S. Tanaka, M. Takeda, T. Ishikawa, K. Tsubota, Y. Imai, and T. Yamaguchi. In vitro blood flow in a rectangular pdms microchannel: experimental observations using a confocal micro-piv system. *Biomed Microdevices*, 10(2):153–67, 2008.

[62] D. R. Potter and E. R. Damiano. The hydrodynamically relevant endothelial cell glycocalyx observed in vivo is absent in vitro. *Circ Res*, 102(7):770–6, 2008.

[63] I. Fernandez-Cuesta, A. Llobera, and M. Ramos-Payan. Optofluidic systems enabling detection in real samples: A review. *Anal Chim Acta*, 1192:339307, 2022.

[64] A. Stambaugh, J. W. Parks, M. A. Stott, G. G. Meena, A. R. Hawkins, and H. Schmidt. Optofluidic multiplex detection of single sars-cov-2 and influenza a antigens using a novel bright fluorescent probe assay. *Proc Natl Acad Sci U S A*, 118(20):e2103480118, 2021.

[65] Y. Shi, K. T. Nguyen, L. K. Chin, Z. Li, L. Xiao, H. Cai, R. Yu, W. Huang, S. Feng, P. H. Yap, J. Liu, Y. Zhang, and A. Q. Liu. Trapping and detection of single viruses in an optofluidic chip. *ACS Sens*, 6(9):3445–3450, 2021.

[66] G. Persichetti, I. A. Grimaldi, G. Testa, and R. Bernini. Multifunctional optofluidic lab-on-chip platform for raman and fluorescence spectroscopic microfluidic analysis. *Lab Chip*, 17(15):2631–2639, 2017.

[67] J. Liu, W. Xu, A. Zhu, H. Kang, Y. Cao, and F. Long. Reusable optofluidic point-of-care testing platform with lyophilized specific antibody for fluorescence detection of cholylglycine in serum. *Mikrochim Acta*, 187(8):439, 2020.

[68] H. E. Parker, S. Sengupta, A. V. Harish, R. R. G. Soares, H. N. Joensson, W. Margulis, A. Russom, and F. Laurell. A lab-in-a-fiber optofluidic device using droplet microfluidics and laser-induced fluorescence for virus detection. *Sci Rep*, 12(1):3539, 2022.

[69] S. Dochow, M. Becker, R. Spittel, C. Beleites, S. Stanca, I. Latka, K. Schuster, J. Kobelke, S. Unger, T. Henkel, G. Mayer, J. Albert, M. Rothhardt, C. Krafft, and J. Popp. Raman-on-chip device and detection fibres with fibre bragg grating for analysis of solutions and particles. *Lab Chip*, 13(6):1109–13, 2013.

[70] Jeongan Choi, Jiwon Lee, and Jae Hee Jung. Fully integrated optofluidic sers platform for real-time and continuous characterization of airborne microorganisms. *Biosensors and Bioelectronics*, 169:112611, 2020.

[71] Jonathan JS Rickard, Valentina Di-Pietro, David J Smith, David J Davies, Antonio Belli, and Pola Goldberg Oppenheimer. Rapid optofluidic detection of biomarkers for traumatic brain injury via surface-enhanced raman spectroscopy. *Nature biomedical engineering*, 4(6):610–623, 2020.

[72] Jiuchuan Guo, Fanyu Zeng, Jinhong Guo, and Xing Ma. Preparation and application of microfluidic sers substrate: Challenges and future perspectives. *Journal of Materials Science Technology*, 37:96–103, 2020.

[73] R. Pardehkhorram, F. Alshawawreh, V. R. Goncales, N. A. Lee, R. D. Tilley, and J. J. Gooding. Functionalized gold nanorod probes: A sophisticated design of sers immunoassay for biodetection in complex media. *Anal Chem*, 93(38):12954–12965, 2021.

[74] J. Jeon, N. Choi, H. Chen, J. I. Moon, L. Chen, and J. Choo. Sers-based droplet microfluidics for high-throughput gradient analysis. *Lab Chip*, 19(4):674–681, 2019.

[75] C. Li, G. Bai, Y. Zhang, M. Zhang, and A. Jian. Optofluidics refractometers. *Micromachines (Basel)*, 9(3):136, 2018.

[76] Shimeng Chen, Yun Liu, Qingxu Yu, and Wei Peng. Microcapillary-based integrated lspr device for refractive index detection and biosensing. *Journal of Lightwave Technology*, 38(8):2485–2492, 2020.

[77] Jixuan Wu, Ye Li, Binbin Song, Cheng Zhang, Qian Wang, Xinliang Gao, and Kaixing Huang. Microstructured optical fiber based on surface plasmon resonance for dual-optofluidic-channel sensing. *Plasmonics*, 17(5):1965–1971, 2022.

[78] N. Chen, M. Chang, X. Lu, J. Zhou, and X. Zhang. Photonic crystal fiber plasmonic sensor based on dual optofluidic channel. *Sensors (Basel)*, 19(23):5150, 2019.

[79] Yun-Chu Chen, Jing-Jie Chen, Yang-Jyun Hsiao, Cheng-Zhe Xie, Chien-Chung Peng, Yi-Chung Tung, and Yih-Fan Chen. Plasmonic gel films for time-lapse lspr detection of hydrogen peroxide secreted from living cells. *Sensors and Actuators B: Chemical*, 336:129725, 2021.

[80] X. Fan and I. M. White. Optofluidic microsystems for chemical and biological analysis. *Nat Photonics*, 5(10):591–597, 2011.

[81] Y. Shi, Z. Li, P. Y. Liu, B. T. T. Nguyen, W. Wu, Q. Zhao, L. K. Chin, M. Wei, P. H. Yap, X. Zhou, H. Zhao, D. Yu, D. P. Tsai, and A. Q. Liu. On-chip optical detection of viruses: A review. *Adv Photonics Res*, 2(4):2000150, 2021.

[82] D. Barshilia, L. K. Chau, and G. E. Chang. Low-cost planar waveguide-based optofluidic sensor for real-time refractive index sensing. *Opt Express*, 28(19):27337–27345, 2020.

[83] I. C. Liu, P. C. Chen, L. K. Chau, and G. E. Chang. Optofluidic refractive-index sensors employing bent waveguide structures for low-cost, rapid chemical and biomedical sensing. *Opt Express*, 26(1):273–283, 2018.

[84] J. Tang, G. Qiu, X. Zhang, and J. Wang. A 3d-cascade-microlens optofluidic chip for refractometry with adjustable sensitivity. *Lab Chip*, 21(19):3784–3792, 2021.

[85] M. Oliva-Ramírez, J. Gil-Rostra, F. Yubero, and A. R. González-Elipe. Robust polarization active nanostructured 1d bragg microcavities as optofluidic label-free refractive index sensor. *Sensors and Actuators B: Chemical*, 256:590–599, 2018.

[86] E. Eriksson, J. Scrimgeour, A. Granéli, K. Ramser, R. Wellander, J. Enger, D. Hanstorp, and M. Goksör. Optical manipulation and microfluidics for studies of single cell dynamics. *Journal of Optics A: Pure and Applied Optics*, 9(8):S113–S121, 2007.

[87] D. E. Lucchetta, F. Simoni, N. Sheremet, V. Reshetnyak, and R. Castagna. Shape-driven optofluidic rotational actuation. *The European Physical Journal Plus*, 136(4):1–9, 2021.

[88] Bradley S. Schmidt, Allen H. J. Yang, David Erickson, and Michal Lipson. Optofluidic trapping and transport on solid core waveguides within a microfluidic device. *Opt Express*, 15(22):14322–14334, 2007.

[89] A. H. Yang, S. D. Moore, B. S. Schmidt, M. Klug, M. Lipson, and D. Erickson. Optical manipulation of nanoparticles and biomolecules in sub-wavelength slot waveguides. *Nature*, 457(7225):71–5, 2009.

[90] Ni Chen, Youlin Xu Di Jiang, and Tang Wenlai. Application of viscoelastic fluid in passive particle manipulation technologies. *Progress in Chemistry*, 32(5):519, 2020.

[91] Haitao Zhao, Lip Ket Chin, Yuzhi Shi, Patricia Yang Liu, Yi Zhang, Hong Cai, Eric Peng Huat Yap, Wee Ser, and Ai-Qun Liu. Continuous optical sorting of nanoscale biomolecules in integrated microfluidic-nanophotonic chips. *Sensors and Actuators B: Chemical*, 331:129428, 2021.

[92] Dan Yuan, Say Hwa Tan, Ronald Sluyter, Qianbin Zhao, Sheng Yan, Nam-Trung Nguyen, Jinhong Guo, Jun Zhang, and Weihua Li. On-chip microparticle and cell washing using coflow of viscoelastic fluid and newtonian fluid. *Analytical chemistry*, 89(17):9574–9582, 2017.

[93] A. Ashkin. Acceleration and trapping of particles by radiation pressure. *Physical Review Letters*, 24(4):156–159, 1970.

[94] A. Ashkin, J. M. Dziedzic, J. E. Bjorkholm, and Steven Chu. Observation of a single-beam gradient force optical trap for dielectric particles. *Opt Lett*, 11(5):288–290, 1986.

[95] Yuanjie Yang, Yu-Xuan Ren, Mingzhou Chen, Yoshihiko Arita, and Carmelo Rosales-Guzmán. Optical trapping with structured light: a review. *Advanced Photonics*, 3(03):034001–034001, 2021.

[96] J. L. Killian, F. Ye, and M. D. Wang. Optical tweezers: A force to be reckoned with. *Cell*, 175(6):1445–1448, 2018.

[97] A. A. M. Bui, A. V. Kashchuk, M. A. Balanant, T. A. Nieminen, H. Rubinsztein-Dunlop, and A. B. Stilgoe. Calibration of force detection for arbitrarily shaped particles in optical tweezers. *Sci Rep*, 8(1):10798, 2018.

[98] G. Gouesbet and G. Gréhan. Generalized lorenz-mie theory for a sphere with an eccentrically located spherical inclusion. *Journal of Modern Optics*, 47(5):821–837, 2000.

[99] Karel Svoboda and Steven M. Block. Optical trapping of metallic rayleigh particles. *Opt Lett*, 19(13):920–932, 1994.

[100] M. Jorgolli, T. Nevill, A. Winters, I. Chen, S. Chong, F. F. Lin, M. Mock, C. Chen, K. Le, C. Tan, P. Jess, H. Xu, A. Hamburger, J. Stevens, T. Munro, M. Wu, P. Tagari, and L. P. Miranda. Nanoscale integration of single cell biologics discovery processes using optofluidic manipulation and monitoring. *Biotechnol Bioeng*, 116(9):2393–2411, 2019.

[101] Carlo Bradac. Nanoscale optical trapping: A review. *Advanced Optical Materials*, 6(12):1800005, 2018.

[102] Jian Zhou and Ian Papautsky. Fundamentals of inertial focusing in microchannels. *Lab on a Chip*, 13(6):1121–1132, 2013.

[103] Chuchuan Hong, Sen Yang, Ivan I Kravchenko, and Justus C Ndukaife. Electrothermoplasmonic trapping and dynamic manipulation of single colloidal nanodiamond. *Nano Letters*, 21(12):4921–4927, 2021.

[104] Weiqiang Ding, Tongtong Zhu, Lei-Ming Zhou, and Cheng-Wei Qiu. Photonic tractor beams: a review. *Advanced Photonics*, 1(2):024001–024001, 2019.

[105] O. Brzobohatý, V. Karásek, M. Šiler, L. Chvátal, T. Čižmár, and P. Zemánek. Experimental demonstration of optical transport, sorting and self-arrangement using a 'tractor beam'. *Nature Photonics*, 7(2):123–127, 2013.

[106] Vladlen Shvedov, Arthur R. Davoyan, Cyril Hnatovsky, Nader Engheta, and Wieslaw Krolikowski. A long-range polarization-controlled optical tractor beam. *Nature Photonics*, 8(11):846–850, 2014.

[107] Nikolay V Petrov, Bogdan Sokolenko, Maksim S Kulya, Andrei Gorodetsky, and Aleksey V Chernykh. Design of broadband terahertz vector and vortex beams: I. review of materials and components. *Light: Advanced Manufacturing*, 3:1–19, 2022.

[108] Hongwen Ren, Yi-Hsin Lin, and Shin-Tson Wu. Linear to axial or radial polarization conversion using a liquid crystal gel. *Applied Physics Letters*, 89(5):051114, 2006.

[109] Y. Zhang, W. Shi, Z. Shen, Z. Man, C. Min, J. Shen, S. Zhu, H. P. Urbach, and X. Yuan. A plasmonic spanner for metal particle manipulation. *Sci Rep*, 5(1):1–9, 2015.

[110] Z. Shen, H. Liu, S. Zhang, Y. C. Shen, B. Zhang, and S. Luo. Optical manipulation of rayleigh particles by metalenses-a numerical study. *Appl Opt*, 58(21):5794–5799, 2019.

[111] Ram Nandan Kumar, Subhasish Dutta Gupta, Nirmalya Ghosh, Ayan Banerjee, Igor V. Minin, Sylvain Lecler, and Vasily N. Astratov. Manipulation of mesoscopic particles using a structured beam in optical tweezers. *SPIE*, pages 94–105, 2022.

[112] M. Li, S. Yan, B. Yao, Y. Liang, and P. Zhang. Spinning and orbiting motion of particles in vortex beams with circular or radial polarizations. *Opt Express*, 24(18):20604–12, 2016.

[113] Emma Eriksson, Jonas Enger, Bodil Nordlander, Nika Erjavec, Kerstin Ramser, Mattias Goksör, Stefan Hohmann, Thomas Nyström, and Dag Hanstorp. A microfluidic system in combination with optical tweezers for analyzing rapid and reversible cytological alterations in single cells upon environmental changes. *Lab on a Chip*, 7(1):71–76, 2007.

[114] Q. Chen, A. Jian, Z. Li, and X. Zhang. Optofluidic tunable lenses using laser-induced thermal gradient. *Lab Chip*, 16(1):104–11, 2016.

[115] Y. Sun and X. Fan. Optical ring resonators for biochemical and chemical sensing. *Anal Bioanal Chem*, 399(1):205–11, 2011.

[116] Alemayehu Nana Koya, Joao Cunha, Tian-Long Guo, Andrea Toma, Denis Garoli, Tao Wang, Saulius Juodkazis, Dan Cojoc, and Remo Proietti Zaccaria. Novel plasmonic nanocavities for optical trapping-assisted biosensing applications. *Advanced Optical Materials*, 8(7):1901481, 2020.

[117] A. N. Grigorenko, N. W. Roberts, M. R. Dickinson, and Y. Zhang. Nanometric optical tweezers based on nanostructured substrates. *Nature Photonics*, 2(6):365–370, 2008.

[118] C. Min, Z. Shen, J. Shen, Y. Zhang, H. Fang, G. Yuan, L. Du, S. Zhu, T. Lei, and X. Yuan. Focused plasmonic trapping of metallic particles. *Nat Commun*, 4(1):2891, 2013.

[119] P. Muhlschlegel, H.-J. Eisler, O. J. F. Martin, B. Hecht, and D. W. Pohl. Resonant optical antennas. *Sci Rep*, 308(5728):1607–1609, 2005.

[120] Mathieu L. Juan, Maurizio Righini, and Romain Quidant. Plasmon nano-optical tweezers. *Nature Photonics*, 5(6):349–356, 2011.

[121] Mohsen Samadi, Pooya Alibeigloo, Abolfazl Aqhili, Mohammad Ali Khosravi, Farahnaz Saeidi, Shoaib Vasini, Mostafa Ghorbanzadeh, Sara Darbari, and Mohammad Kazem Moravvej-Farshi. Plasmonic tweezers: Towards nanoscale manipulation. *Optics and Lasers in Engineering*, 154:107001, 2022.

[122] Khalil Mokri and Mohammad Hazhir Mozaffari. Numerical design of a plasmonic nanotweezer for realizing high optical gradient force. *Optics Laser Technology*, 119:105620, 2019.

[123] Nicolò Maccaferri, Grégory Barbillon, Alemayehu Nana Koya, Guowei Lu, Guillermo P. Acuna, and Denis Garoli. Recent advances in plasmonic nanocavities for single-molecule spectroscopy. *Nanoscale Advances*, 3(3):633–642, 2021.

[124] G. Volpe, R. Quidant, G. Badenes, and D. Petrov. Surface plasmon radiation forces. *Phys Rev Lett*, 96(23):238101, 2006.

[125] Domna G. Kotsifaki and Síle Nic Chormaic. Plasmonic optical tweezers based on nanostructures: fundamentals, advances and prospects. *Nanophotonics*, 8(7):1227–1245, 2019.

[126] M. Righini, G. Volpe, C. Girard, D. Petrov, and R. Quidant. Surface plasmon optical tweezers: tunable optical manipulation in the femtonewton range. *Phys Rev Lett*, 100(18):186804, 2008.

[127] G. C. Messina, X. Zambrana-Puyalto, N. Maccaferri, D. Garoli, and F. De Angelis. Two-state switchable plasmonic tweezers for dynamic manipulation of nano-objects. *Nanoscale*, 12(15):8574–8581, 2020.

[128] Weihua Zhang and Olivier J. F. Martin. A universal law for plasmon resonance shift in biosensing. *ACS Photonics*, 2(1):144–150, 2014.

[129] M. Gullans, T. G. Tiecke, D. E. Chang, J. Feist, J. D. Thompson, J. I. Cirac, P. Zoller, and M. D. Lukin. Nanoplasmonic lattices for ultracold atoms. *Phys Rev Lett*, 109(23):235309, 2012.

[130] T. Shoji and Y. Tsuboi. Plasmonic optical tweezers toward molecular manipulation: Tailoring plasmonic nanostructure, light source, and resonant trapping. *J Phys Chem Lett*, 5(17):2957–67, 2014.

[131] K. Y. Chen, A. T. Lee, C. C. Hung, J. S. Huang, and Y. T. Yang. Transport and trapping in two-dimensional nanoscale plasmonic optical lattice. *Nano Lett*, 13(9):4118–22, 2013.

[132] K. Wang, E. Schonbrun, P. Steinvurzel, and K. B. Crozier. Trapping and rotating nanoparticles using a plasmonic nano-tweezer with an integrated heat sink. *Nat Commun*, 2(1):469, 2011.

[133] W. Zhang, L. Huang, C. Santschi, and O. J. Martin. Trapping and sensing 10 nm metal nanoparticles using plasmonic dipole antennas. *Nano Lett*, 10(3):1006–11, 2010.

[134] B. J. Roxworthy, K. D. Ko, A. Kumar, K. H. Fung, E. K. Chow, G. L. Liu, N. X. Fang, and Jr. Toussaint, K. C. Application of plasmonic bowtie nanoantenna arrays for optical trapping, stacking, and sorting. *Nano Lett*, 12(2):796–801, 2012.

[135] Tatsuya Shoji, Junki Saitoh, Noboru Kitamura, Fumika Nagasawa, Kei Murakoshi, Hiroaki Yamauchi, Syoji Ito, Hiroshi Miyasaka, Hajime Ishihara, and Yasuyuki Tsuboi. Permanent fixing or reversible trapping and release of dna micropatterns on a gold nanostructure using continuous-wave or femtosecond-pulsed near-infrared laser light. *Journal of the American Chemical Society*, 135(17):6643–6648, 2013.

[136] Haoran Wei, Seyyed M. Hossein Abtahi, and Peter J. Vikesland. Plasmonic colorimetric and sers sensors for environmental analysis. *Environmental Science: Nano*, 2(2):120–135, 2015.

[137] M. Righini, P. Ghenuche, S. Cherukulappurath, V. Myroshnychenko, F. J. Garcıa de Abajo, and R. Quidant. Nano-optical trapping of rayleigh particles and escherichia coli bacteria with resonant optical antennas. *Nano Lett*, 9(10):5, 2009.

[138] Holger Fischer and Olivier J. F. Martin. Engineering the optical response of plasmonic nanoantennas. *Opt Express*, 16(12):11, 2008.

[139] Brian J Roxworthy and Kimani C Toussaint. Femtosecond plasmonic optical tweezers using gold bowtie nanoantenna arrays. In *Frontiers in Optics*, page FW1G. 3. Optica Publishing Group, 2012.

[140] Chuchuan Hong, Sen Yang, and Justus C. Ndukaife. Optofluidic control using plasmonic tin bowtie nanoantenna. *Optical Materials Express*, 9(3):953–964, 2019.

[141] B. J. Roxworthy and Jr. Toussaint, K. C. Femtosecond-pulsed plasmonic nanotweezers. *Sci Rep*, 2(1):1–6, 2012.

[142] Yasuyuki Tsuboi, Tatsuya Shoji, Noboru Kitamura, Mai Takase, Kei Murakoshi, Yoshihiko Mizumoto, and Hajime Ishihara. Optical trapping of quantum dots based on gap-mode-excitation of localized surface plasmon. *The Journal of Physical Chemistry Letters*, 1(15):2327–2333, 2010.

[143] Mariko Toshimitsu, Yuriko Matsumura, Tatsuya Shoji, Noboru Kitamura, Mai Takase, Kei Murakoshi, Hiroaki Yamauchi, Syoji Ito, Hiroshi Miyasaka, Atsushi Nobuhiro, Yoshihiko Mizumoto, Hajime Ishihara, and Yasuyuki Tsuboi. Metallic-nanostructure-enhanced optical trapping of flexible polymer chains in aqueous solution as revealed by confocal fluorescence microspectroscopy. *The Journal of Physical Chemistry C*, 116(27):14610–14618, 2012.

[144] Zhongbo Yan, Ming Xia, Pei Zhang, and Ya-Hong Xie. Self-aligned trapping and detecting molecules using a plasmonic tweezer with an integrated electrostatic cell. *Advanced Optical Materials*, 5(5):1600329, 2017.

[145] EdwardH Synge. Xxxviii. a suggested method for extending microscopic resolution into the ultra-microscopic region. *The London, Edinburgh, and Dublin Philosophical Magazine and Journal of Science*, 6(35):356–362, 1928.

[146] Mathieu L. Juan, Reuven Gordon, Yuanjie Pang, Fatima Eftekhari, and Romain Quidant. Self-induced back-action optical trapping of dielectric nanoparticles. *Nature Physics*, 5(12):915–919, 2009.

[147] A. A. Al Balushi, A. Kotnala, S. Wheaton, R. M. Gelfand, Y. Rajashekara, and R. Gordon. Label-free free-solution nanoaperture optical tweezers for single molecule protein studies. *Analyst*, 140(14):4760–78, 2015.

[148] Xue Han, Viet Giang Truong, and Síle Nic Chormaic. Efficient microparticle trapping with plasmonic annular apertures arrays. *Nano Futures*, 2(3):035007, 2018.

[149] Xue Han, Viet Giang Truong, Prince Sunil Thomas, and Síle Nic Chormaic. Sequential trapping of single nanoparticles using a gold plasmonic nanohole array. *Photonics Research*, 6(10):981–986, 2018.

[150] F. I. Baida and D. Van Labeke. Three-dimensional structures for enhanced transmission through a metallic film: Annular aperture arrays. *Physical Review B*, 67(15):155314, 2003.

[151] A. A. Saleh and J. A. Dionne. Toward efficient optical trapping of sub-10-nm particles with coaxial plasmonic apertures. *Nano Lett*, 12(11):5581–6, 2012.

[152] D. Yoo, K. L. Gurunatha, H. K. Choi, D. A. Mohr, C. T. Ertsgaard, R. Gordon, and S. H. Oh. Low-power optical trapping of nanoparticles and proteins with resonant coaxial nanoaperture using 10 nm gap. *Nano Lett*, 18(6):3637–3642, 2018.

[153] Xiaowei Li, Qiaofeng Tan, Benfeng Bai, and Guofan Jin. Non-spectroscopic refractometric nanosensor based on a tilted slit-groove plasmonic interferometer. *Opt Express*, 19(21):20691–20703, 2011.

[154] A. A. Saleh, S. Sheikhoelislami, S. Gastelum, and J. A. Dionne. Grating-flanked plasmonic coaxial apertures for efficient fiber optical tweezers. *Opt Express*, 24(18):20593–603, 2016.

[155] Reuven Gordon. Metal nanoapertures and single emitters. *Advanced Optical Materials*, 8(20):2001110, 2020.

[156] S. Ghosh and A. Ghosh. Next-generation optical nanotweezers for dynamic manipulation: From surface to bulk. *Langmuir*, 36(21):5691–5708, 2020.

[157] Y. Zhang, C. Min, X. Dou, X. Wang, H. P. Urbach, M. G. Somekh, and X. Yuan. Plasmonic tweezers: for nanoscale optical trapping and beyond. *Light Sci Appl*, 10(1):59, 2021.

[158] Xiaolei Shi, Lambertus Hesselink, and Robert L. Thornton. Ultrahigh light transmission through a c-shaped nanoaperture. *Opt Lett*, 28(15):1320–1322, 2003.

[159] Xiaolei Shi and Lambertus Hesselink. Design of a c aperture to achieve 10 resolution and resonant transmission. *Opt Soc Am B*, 21(7):1305–1317, 2004.

[160] J. A. Matteo, D. P. Fromm, Y. Yuen, P. J. Schuck, W. E. Moerner, and L. Hesselink. Spectral analysis of strongly enhanced visible light transmission through single c-shaped nanoapertures. *Applied Physics Letters*, 85(4):648–650, 2004.

[161] P. Hansen, Y. Zheng, J. Ryan, and L. Hesselink. Nano-optical conveyor belt, part i: Theory. *Nano Lett*, 14(6):2965–70, 2014.

[162] Y. Zheng, J. Ryan, P. Hansen, Y. T. Cheng, T. J. Lu, and L. Hesselink. Nano-optical conveyor belt, part ii: Demonstration of handoff between near-field optical traps. *Nano Lett*, 14(6):2971–6, 2014.

[163] Mohammad Asif Zaman, Punnag Padhy, Paul C. Hansen, and Lambertus Hesselink. Dielectrophoresis-assisted plasmonic trapping of dielectric nanoparticles. *Physical Review A*, 95(2):023840, 2017.

[164] H. Tan, H. Hu, L. Huang, and K. Qian. Plasmonic tweezers for optical manipulation and biomedical applications. *Analyst*, 145(17):5699–5712, 2020.

[165] D. Gao, W. Ding, M. Nieto-Vesperinas, X. Ding, M. Rahman, T. Zhang, C. Lim, and C. W. Qiu. Optical manipulation from the microscale to the nanoscale: fundamentals, advances and prospects. *Light Sci Appl*, 6(9):e17039, 2017.

[166] Y. Ren, Q. Chen, M. He, X. Zhang, H. Qi, and Y. Yan. Plasmonic optical tweezers for particle manipulation: Principles, methods, and applications. *ACS Nano*, 15(4):6105–6128, 2021.

[167] Jennifer E Curtis, Brian A Koss, and David G Grier. Dynamic holographic optical tweezers. *Optics communications*, 207(1-6):169–175, 2002.

[168] David G Grier. A revolution in optical manipulation. *nature*, 424(6950):810–816, 2003.

[169] D. E. Smalley, E. Nygaard, K. Squire, J. Van Wagoner, J. Rasmussen, S. Gneiting, K. Qaderi, J. Goodsell, W. Rogers, M. Lindsey, K. Costner, A. Monk, M. Pearson, B. Haymore, and J. Peatross. A photophoretic-trap volumetric display. *Nature*, 553(7689):486–490, 2018.

[170] Xianzhong Chen, Ming Chen, Muhammad Qasim Mehmood, Dandan Wen, Fuyong Yue, Cheng-Wei Qiu, and Shuang Zhang. Longitudinal multifoci metalens for circularly polarized light. *Advanced Optical Materials*, 3(9):1201–1206, 2015.

[171] Song Gao, Chul-Soon Park, Changyi Zhou, Sang-Shin Lee, and Duk-Yong Choi. Twofold polarization-selective all-dielectric trifoci metalens for linearly polarized visible light. *Advanced Optical Materials*, 7(21):1900883, 2019.

[172] Calum Williams, Yunuen Montelongo, and Timothy D. Wilkinson. Plasmonic metalens for narrowband dual-focus imaging. *Advanced Optical Materials*, 5(24):1700811, 2017.

[173] R. Ahmed and H. Butt. Strain-multiplex metalens array for tunable focusing and imaging. *Adv Sci (Weinh)*, 8(4):2003394, 2021.

[174] Y. Bao, Q. Jiang, Y. Kang, X. Zhu, and Z. Fang. Enhanced optical performance of multifocal metalens with conic shapes. *Light Sci Appl*, 6(10):e17071, 2017.

[175] W. Wang, Z. Guo, K. Zhou, Y. Sun, F. Shen, Y. Li, S. Qu, and S. Liu. Polarization-independent longitudinal multi-focusing metalens. *Opt Express*, 23(23):29855–66, 2015.

[176] S. Tian, H. Guo, J. Hu, and S. Zhuang. Dielectric longitudinal bifocal metalens with adjustable intensity and high focusing efficiency. *Opt Express*, 27(2):680–688, 2019.

[177] W. T. Chen, A. Y. Zhu, V. Sanjeev, M. Khorasaninejad, Z. Shi, E. Lee, and F. Capasso. A broadband achromatic metalens for focusing and imaging in the visible. *Nat Nanotechnol*, 13(3):220–226, 2018.

[178] S. Sun, K. Y. Yang, C. M. Wang, T. K. Juan, W. T. Chen, C. Y. Liao, Q. He, S. Xiao, W. T. Kung, G. Y. Guo, L. Zhou, and D. P. Tsai. High-efficiency broadband anomalous reflection by gradient meta-surfaces. *Nano Lett*, 12(12):6223–9, 2012.

[179] Mohammadreza Khorasaninejad, Wei Ting Chen, Robert C. Devlin, Jaewon Oh, Alexander Y. Zhu, and Federico Capasso. Metalenses at visible wavelengths diffraction-limited focusing and subwavelength resolution imaging. *Appl Opt*, 352(6290):6, 2016.

[180] Mohammadreza Khorasaninejad, Zhujun Shi, Alexander Y Zhu, Wei-Ting Chen, Vyshakh Sanjeev, Aun Zaidi, and Federico Capasso. Achromatic metalens over 60 nm bandwidth in the visible and metalens with reverse chromatic dispersion. *Nano letters*, 17(3):1819–1824, 2017.

[181] M. Khorasaninejad, W. T. Chen, A. Y. Zhu, J. Oh, R. C. Devlin, D. Rousso, and F. Capasso. Multispectral chiral imaging with a metalens. *Nano Lett*, 16(7):4595–600, 2016.

[182] S. Wang, P. C. Wu, V. C. Su, Y. C. Lai, C. Hung Chu, J. W. Chen, S. H. Lu, J. Chen, B. Xu, C. H. Kuan, T. Li, S. Zhu, and D. P. Tsai. Broadband achromatic optical metasurface devices. *Nat Commun*, 8(1):187, 2017.

[183] Z. Li, M. H. Kim, C. Wang, Z. Han, S. Shrestha, A. C. Overvig, M. Lu, A. Stein, A. M. Agarwal, M. Loncar, and N. Yu. Controlling propagation and coupling of waveguide modes using phase-gradient metasurfaces. *Nat Nanotechnol*, 12(7):675–683, 2017.

[184] Xiao Fu, Haowen Liang, and Juntao Li. Metalenses: from design principles to functional applications. *Frontiers of Optoelectronics*, 14(2):170–186, 2021.

[185] M. Khorasaninejad and F. Capasso. Metalenses: Versatile multifunctional photonic components. *Science*, 358(6367):eaam8100, 2017.

[186] S. C. Malek, H. S. Ee, and R. Agarwal. Strain multiplexed metasurface holograms on a stretchable substrate. *Nano Lett*, 17(6):3641–3645, 2017.

[187] Adeel Afridi, Josep Canet-Ferrer, Laurent Philippet, Johann Osmond, Pascal Berto, and Romain Quidant. Electrically driven varifocal silicon metalens. *ACS Photonics*, 5(11):4497–4503, 2018.

[188] W. Bai, P. Yang, J. Huang, D. Chen, J. Zhang, Z. Zhang, J. Yang, and B. Xu. Near-infrared tunable metalens based on phase change material ge2se2te5. *Sci Rep*, 9(1):5368, 2019.

[189] Haejun Chung and Owen D. Miller. Tunable metasurface inverse design for 80144° angular deflection. *ACS Photonics*, 7(8):2236–2243, 2020.

[190] F. He, K. F. MacDonald, and X. Fang. Continuous beam steering by coherent light-by-light control of dielectric metasurface phase gradient. *Opt Express*, 28(20):30107–30116, 2020.

[191] D. Wintz, P. Genevet, A. Ambrosio, A. Woolf, and F. Capasso. Holographic metalens for switchable focusing of surface plasmons. *Nano Lett*, 15(5):3585–9, 2015.

[192] T. Badloe, I. Kim, Y. Kim, J. Kim, and J. Rho. Electrically tunable bifocal metalens with diffraction-limited focusing and imaging at visible wavelengths. *Adv Sci (Weinh)*, 8(21):e2102646, 2021.

[193] Bingshuang Yao, Xiaofei Zang, Yang Zhu, Dahai Yu, Jingya Xie, Lin Chen, Sen Han, Yiming Zhu, and Songlin Zhuang. Spin-decoupled metalens with intensity-tunable multiple focal points. *Photonics Research*, 9(6):1019–1032, 2021.

[194] H. Markovich, II Shishkin, N. Hendler, and P. Ginzburg. Optical manipulation along an optical axis with a polarization sensitive meta-lens. *Nano Lett*, 18(8):5024–5029, 2018.

[195] Jianfa Zhang, Kevin F. MacDonald, and Nikolay I. Zheludev. Controlling light-with-light without nonlinearity. *Light: Science Applications*, 1(7):e18–e18, 2012.

[196] Maria Papaioannou, Eric Plum, João Valente, Edward TF Rogers, and Nikolay I Zheludev. Two-dimensional control of light with light on metasurfaces. *Light: Science & Applications*, 5(4):e16070–e16070, 2016.

[197] Xu Fang, Kevin F. MacDonald, and Nikolay I. Zheludev. Controlling light with light using coherent metadevices: all-optical transistor, summator and invertor. *Light: Science Applications*, 4(5):e292–e292, 2015.

[198] F. He, K. F. MacDonald, and X. Fang. Coherent illumination spectroscopy of nanostructures and thin films on thick substrates. *Opt Express*, 26(10):12415–12424, 2018.

[199] Ziying Zhang, Xueqian Zhang, Yuehong Xu, Xieyu Chen, Xi Feng, Meng Liu, Quan Xu, Ming Kang, Jiaguang Han, and Weili Zhang. Coherent chiral-selective absorption and wavefront manipulation in single-layer metasurfaces. *Advanced Optical Materials*, 9(3):2001620, 2020.

[200] A. Xomalis, I. Demirtzioglou, E. Plum, Y. Jung, V. Nalla, C. Lacava, K. F. MacDonald, P. Petropoulos, D. J. Richardson, and N. I. Zheludev. Fibre-optic metadevice for all-optical signal modulation based on coherent absorption. *Nat Commun*, 9(1):182, 2018.

[201] Fei He, Yu Feng, Hailong Pi, Jize Yan, Kevin F. MacDonald, and Xu Fang. Coherently switching the focusing characteristics of all-dielectric metalenses. *Optics Express*, 30(15):27683–27693, 2022.

[202] H. Zhang, M. Kang, X. Zhang, W. Guo, C. Lv, Y. Li, W. Zhang, and J. Han. Coherent control of optical spin-to-orbital angular momentum conversion in metasurface. *Adv Mater*, 29(6):1604252, 2017.

[203] Ming Kang, Huifang Zhang, Xueqian Zhang, Quanlong Yang, Weili Zhang, and Jiaguang Han. Interferometric control of dual-band terahertz perfect absorption using a designed metasurface. *Physical Review Applied*, 9(5):054018, 2018.

[204] Z. Zhang, M. Kang, X. Zhang, X. Feng, Y. Xu, X. Chen, H. Zhang, Q. Xu, Z. Tian, W. Zhang, A. Krasnok, J. Han, and A. Alu. Coherent perfect diffraction in metagratings. *Adv Mater*, 32(36):e2002341, 2020.

[205] D. Lin, A. L. Holsteen, E. Maguid, G. Wetzstein, P. G. Kik, E. Hasman, and M. L. Brongersma. Photonic multitasking interleaved si nanoantenna phased array. *Nano Lett*, 16(12):7671–7676, 2016.

[206] D. Lin, A. L. Holsteen, E. Maguid, P. Fan, P. G. Kik, E. Hasman, and M. L. Brongersma. Polarization-independent metasurface lens employing the pancharatnam-berry phase. *Opt Express*, 26(19):24835–24842, 2018.

[207] Y. Li, S. Liu, D. Sun, M. Luo, X. Qi, S. Zhao, and Z. Ma. Single-layer multitasking vortex-metalens for ultra-compact two-photon excitation sted endomicroscopy imaging. *Opt Express*, 29(3):3795–3807, 2021.

[208] Chunmei Zhang, Fuyong Yue, Dandan Wen, Ming Chen, Zhengren Zhang, Wei Wang, and Xianzhong Chen. Multichannel metasurface for simultaneous control of holograms and twisted light beams. *ACS Photonics*, 4(8):1906–1912, 2017.

[209] B. H. Chen, P. C. Wu, V. C. Su, Y. C. Lai, C. H. Chu, I. C. Lee, J. W. Chen, Y. H. Chen, Y. C. Lan, C. H. Kuan, and D. P. Tsai. Gan metalens for pixel-level full-color routing at visible light. *Nano Lett*, 17(10):6345–6352, 2017.

[210] A. Arbabi, E. Arbabi, S. M. Kamali, Y. Horie, S. Han, and A. Faraon. Miniature optical planar camera based on a wide-angle metasurface doublet corrected for monochromatic aberrations. *Nat Commun*, 7(1):13682, 2016.

[211] B. Groever, W. T. Chen, and F. Capasso. Meta-lens doublet in the visible region. *Nano Lett*, 17(8):4902–4907, 2017.

[212] Amir Arbabi, Ehsan Arbabi, Yu Horie, Seyedeh Mahsa Kamali, and Andrei Faraon. Planar metasurface retroreflector. *Nature Photonics*, 11(7):415–420, 2017.

[213] J. E. Baker, R. P. Badman, and M. D. Wang. Nanophotonic trapping: precise manipulation and measurement of biomolecular arrays. *Wiley Interdiscip Rev Nanomed Nanobiotechnol*, 10(1):e1477, 2018.

[214] David Erickson, Xavier Serey, Yih-Fan Chen, and Sudeep Mandal. Nanomanipulation using near field photonics. *Lab on a Chip*, 11(6):995–1009, 2011.

[215] Onofrio M Maragò, Philip H Jones, Pietro G Gucciardi, Giovanni Volpe, and Andrea C Ferrari. Optical trapping and manipulation of nanostructures. *Nature nanotechnology*, 8(11):807–819, 2013.

[216] X. Yang, Y. Liu, R. F. Oulton, X. Yin, and X. Zhang. Optical forces in hybrid plasmonic waveguides. *Nano Lett*, 11(2):321–8, 2011.

[217] O. G. Helleso, P. Lovhaugen, A. Z. Subramanian, J. S. Wilkinson, and B. S. Ahluwalia. Surface transport and stable trapping of particles and cells by an optical waveguide loop. *Lab Chip*, 12(18):3436–40, 2012.

[218] M. Soltani, J. Lin, R. A. Forties, J. T. Inman, S. N. Saraf, R. M. Fulbright, M. Lipson, and M. D. Wang. Nanophotonic trapping for precise manipulation of biomolecular arrays. *Nat Nanotechnol*, 9(6):448–52, 2014.

[219] S. Lin, E. Schonbrun, and K. Crozier. Optical manipulation with planar silicon microring resonators. *Nano Lett*, 10(7):2408–11, 2010.

[220] Yangcheng Li, Oleksiy V. Svitelskiy, Alexey V. Maslov, David Carnegie, Edik Rafailov, and Vasily N. Astratov. Giant resonant light forces in microspherical photonics. *Light: Science Applications*, 2(4):e64–e64, 2013.

[221] N. Descharmes, U. P. Dharanipathy, Z. Diao, M. Tonin, and R. Houdre. Single particle detection, manipulation and analysis with resonant optical trapping in photonic crystals. *Lab Chip*, 13(16):3268–74, 2013.

[222] T. van Leest and J. Caro. Cavity-enhanced optical trapping of bacteria using a silicon photonic crystal. *Lab Chip*, 13(22):4358–65, 2013.

[223] S. H. Wu, N. Huang, E. Jaquay, and M. L. Povinelli. Near-field, on-chip optical brownian ratchets. *Nano Lett*, 16(8):5261–6, 2016.

[224] Zhe Xu, Wuzhou Song, and Kenneth B. Crozier. Optical trapping of nanoparticles using all-silicon nanoantennas. *ACS Photonics*, 5(12):4993–5001, 2018.

[225] J. Kim. Joining plasmonics with microfluidics: from convenience to inevitability. *Lab Chip*, 12(19):3611–23, 2012.

[226] A. Cuche, A. Canaguier-Durand, E. Devaux, J. A. Hutchison, C. Genet, and T. W. Ebbesen. Sorting nanoparticles with intertwined plasmonic and thermo-hydrodynamical forces. *Nano Lett*, 13(9):4230–5, 2013.

[227] M. Wang, C. Zhao, X. Miao, Y. Zhao, J. Rufo, Y. J. Liu, T. J. Huang, and Y. Zheng. Plasmofluidics: Merging light and fluids at the micro-/nanoscale. *Small*, 11(35):4423–44, 2015.

[228] J. J. Baumberg, J. Aizpurua, M. H. Mikkelsen, and D. R. Smith. Extreme nanophotonics from ultrathin metallic gaps. *Nat Mater*, 18(7):668–678, 2019.

[229] P. Genevet, J. Lin, M. A. Kats, and F. Capasso. Holographic detection of the orbital angular momentum of light with plasmonic photodiodes. *Nat Commun*, 3(1):1278, 2012.

[230] Xu Fang, Ming Lun Tseng, Din Ping Tsai, and Nikolay I. Zheludev. Coherent excitation-selective spectroscopy of multipole resonances. *Physical Review Applied*, 5(1):014010, 2016.

[231] X. Fang, K. F. MacDonald, E. Plum, and N. I. Zheludev. Coherent control of light-matter interactions in polarization standing waves. *Sci Rep*, 6(1):31141, 2016.

[232] J. H. Kang, K. Kim, H. S. Ee, Y. H. Lee, T. Y. Yoon, M. K. Seo, and H. G. Park. Low-power nano-optical vortex trapping via plasmonic diabolo nanoantennas. *Nat Commun*, 2(1):582, 2011.

[233] P. T. Lin, H. Y. Chu, T. W. Lu, and P. T. Lee. Trapping particles using waveguide-coupled gold bowtie plasmonic tweezers. *Lab Chip*, 14(24):4647–52, 2014.

[234] Russell A. Jensen, I. Chun Huang, Ou Chen, Jennifer T. Choy, Thomas S. Bischof, Marko Lončar, and Moungi G. Bawendi. Optical trapping and two-photon excitation of colloidal quantum dots using bowtie apertures. *ACS Photonics*, 3(3):423–427, 2016.

[235] Yang Zhao, Amr A. E. Saleh, and Jennifer A. Dionne. Enantioselective optical trapping of chiral nanoparticles with plasmonic tweezers. *ACS Photonics*, 3(3):304–309, 2016.

[236] K. Wang, E. Schonbrun, P. Steinvurzel, and K. B. Crozier. Scannable plasmonic trapping using a gold stripe. *Nano Lett*, 10(9):3506–11, 2010.

[237] K. D. Leake, M. A. Olson, D. Ozcelik, A. R. Hawkins, and H. Schmidt. Spectrally reconfigurable integrated multi-spot particle trap. *Opt Lett*, 40(23):5435–8, 2015.

[238] P. R. Huft, J. D. Kolbow, J. T. Thweatt, and N. C. Lindquist. Holographic plasmonic nanotweezers for dynamic trapping and manipulation. *Nano Lett*, 17(12):7920–7925, 2017.

[239] M. Jiang, G. Wang, W. Jiao, Z. Ying, N. Zou, H. P. Ho, T. Sun, and X. Zhang. Plasmonic non-concentric nanorings array as an unidirectional nano-optical conveyor belt actuated by polarization rotation. *Opt Lett*, 42(2):259–262, 2017.

[240] M. Jiang, G. Wang, W. Xu, W. Ji, N. Zou, H. P. Ho, and X. Zhang. Two-dimensional arbitrary nano-manipulation on a plasmonic metasurface. *Opt Lett*, 43(7):1602–1605, 2018.

[241] J. C. Ndukaife, A. V. Kildishev, A. G. Nnanna, V. M. Shalaev, S. T. Wereley, and A. Boltasseva. Long-range and rapid transport of individual nano-objects by a hybrid electrothermoplasmonic nanotweezer. *Nat Nanotechnol*, 11(1):53–9, 2016.

[242] L. Lin, M. Wang, X. Peng, E. N. Lissek, Z. Mao, L. Scarabelli, E. Adkins, S. Coskun, H. E. Unalan, B. A. Korgel, L. M. Liz-Marzan, E. L. Florin, and Y. Zheng. Opto-thermoelectric nanotweezers. *Nat Photonics*, 12(4):195–201, 2018.

[243] E. Hendry, P. J. Hale, J. Moger, A. K. Savchenko, and S. A. Mikhailov. Coherent nonlinear optical response of graphene. *Phys Rev Lett*, 105(9):097401, 2010.

[244] P. B. Johnson and R. W. Christy. Optical constants of the noble metals. *Physical Review B*, 6(12):4370–4379, 1972.

[245] Kirt R Williams, Kishan Gupta, and Matthew Wasilik. Etch rates for micromachining processing-part ii. *Journal of microelectromechanical systems*, 12(6):761–778, 2003.

[246] C. Pin, J. B. Jager, M. Tardif, E. Picard, E. Hadji, F. de Fornel, and B. Cluzel. Optical tweezing using tunable optical lattices along a few-mode silicon waveguide. *Lab Chip*, 18(12):1750–1757, 2018.

[247] S. Lin and K. B. Crozier. Planar silicon microrings as wavelength-multiplexed optical traps for storing and sensing particles. *Lab Chip*, 11(23):4047–51, 2011.

[248] F. Vollmer and L. Yang. Label-free detection with high-q microcavities: a review of biosensing mechanisms for integrated devices. *Nanophotonics*, 1(3-4):267–291, 2012.

[249] G. Tkachenko, D. Stellinga, A. Ruskuc, M. Chen, K. Dholakia, and T. F. Krauss. Optical trapping with planar silicon metalenses. *Opt Lett*, 43(14):3224–3227, 2018.

[250] Y. Qin, Y. Li, D. Deng, Y. Liu, and M. Sun. Ultracompact biosensor based on a metalens with a longitudinally structured vector beam. *Appl Opt*, 58(16):4438–4442, 2019.

[251] Ming Lun Tseng, Hui-Hsin Hsiao, Cheng Hung Chu, Mu Ku Chen, Greg Sun, Ai-Qun Liu, and Din Ping Tsai. Metalenses: Advances and applications. *Advanced Optical Materials*, 6(18):1800554, 2018.

[252] G. Thalhammer, R. Steiger, S. Bernet, and M. Ritsch-Marte. Optical macro-tweezers: trapping of highly motile micro-organisms. *Journal of Optics*, 13(4):044024, 2011.

[253] Jochen Guck, Revathi Ananthakrishnan, C Casey Cunningham, and Josef KaS. Stretching biological cells with light. *Phys Condens Matter*, 14(4843):15, 2002.

[254] Nicola Bellini, Francesca Bragheri, Ilaria Cristiani, Jochen Guck, Roberto Osellame, and Graeme Whyte. Validation and perspectives of a femtosecond laser fabricated monolithic optical stretcher. *Biomed Opt Express*, 3(10):2658–2668, 2012.

[255] R. An, G. Wang, W. Ji, W. Jiao, M. Jiang, Y. Chang, X. Xu, N. Zou, and X. Zhang. Controllable trapping and releasing of nanoparticles by a standing wave on optical waveguides. *Opt Lett*, 43(16):3901–3904, 2018.

[256] M. Kreysing, D. Ott, M. J. Schmidberger, O. Otto, M. Schurmann, E. Martin-Badosa, G. Whyte, and J. Guck. Dynamic operation of optical fibres beyond the single-mode regime facilitates the orientation of biological cells. *Nat Commun*, 5(1):5481, 2014.

[257] O. Brzobohaty, A. V. Arzola, M. Siler, L. Chvatal, P. Jakl, S. Simpson, and P. Zemanek. Complex rotational dynamics of multiple spheroidal particles in a circularly polarized, dual beam trap. *Opt Express*, 23(6):7273–87, 2015.

[258] M. G. Donato, O. Brzobohaty, S. H. Simpson, A. Irrera, A. A. Leonardi, M. J. Lo Faro, V. Svak, O. M. Marago, and P. Zemanek. Optical trapping, optical binding, and rotational dynamics of silicon nanowires in counter-propagating beams. *Nano Lett*, 19(1):342–352, 2019.

[259] Eric Plum, Kevin F. MacDonald, Xu Fang, Daniele Faccio, and Nikolay I. Zheludev. Controlling the optical response of 2d matter in standing waves. *ACS Photonics*, 4(12):3000–3011, 2017.

[260] Kerstin Avila, David Moxey, Alberto de Lozar, Marc Avila, Dwight Barkley, and Björn Hof. The onset of turbulence in pipe flow. *Sci*, 333(6039):6, 2022.

[261] Vaclav Prajzler, Woohyun Jung, Kyunghwan Oh, Jakub Cajzl, and Pavla Nekvindova. Optical properties of deoxyribonucleic acid thin layers deposited on an elastomer substrate. *Optical Materials Express*, 10(2):421–433, 2020.

[262] Edward D Palik. *Handbook of optical constants of solids*, volume 3. Academic press, 1998.

[263] X. Zhang, J. Qiu, X. Li, J. Zhao, and L. Liu. Complex refractive indices measurements of polymers in visible and near-infrared bands. *Appl Opt*, 59(8):2337–2344, 2020.

[264] Alfred Zajac and Eugene Hecht. *Optics, Fourth Edit*. Pearson Higher Education, 2002.

[265] Max Born and Emil Wolf. *Principles of optics: electromagnetic theory of propagation, interference and diffraction of light*. Elsevier, 2013.

[266] Ye Feng Yu, Alexander Y. Zhu, Ramón Paniagua-Domínguez, Yuan Hsing Fu, Boris Luk'yanchuk, and Arseniy I. Kuznetsov. High-transmission dielectric metasurface with 2 phase control at visible wavelengths. *Laser Photonics Reviews*, 9(4):412–418, 2015.

[267] A Rosenberger, A Münnemann, F Kiendl, G Güntherodt, P Rosenbusch, JAC Bland, G Eggers, and P Fumagalli. Topographic cross talk in reflection mode near-field optical microscopy on patterned structures. *Journal of Applied Physics*, 89(12):7727–7729, 2001.

[268] Ebrahim Karimi, Sebastian A Schulz, Israel De Leon, Hammam Qassim, Jeremy Upham, and Robert W Boyd. Generating optical orbital angular momentum at visible wavelengths using a plasmonic metasurface. *Light: Science & Applications*, 3(5):e167–e167, 2014.

[269] Zile Li, Chen Chen, Zhiqiang Guan, Jin Tao, Sheng Chang, Qi Dai, Ying Xiao, Yuan Cui, Yiqun Wang, Shaohua Yu, et al. Three-channel metasurfaces for simultaneous metaholography and meta-nanoprinting: a single-cell design approach. *Laser & Photonics Reviews*, 14(6):2000032, 2020.

[270] Seyedeh Mahsa Kamali, Ehsan Arbabi, Amir Arbabi, and Andrei Faraon. A review of dielectric optical metasurfaces for wavefront control. *Nanophotonics*, 7(6):1041–1068, 2018.

[271] F. Aieta, P. Genevet, M. A. Kats, N. Yu, R. Blanchard, Z. Gaburro, and F. Capasso. Aberration-free ultrathin flat lenses and axicons at telecom wavelengths based on plasmonic metasurfaces. *Nano Lett*, 12(9):4932–6, 2012.

[272] Dianmin Lin, Pengyu Fan, Erez Hasman, and Mark L. Brongersma. Dielectric gradient metasurface optical elements. *Appl Opt*, 345(6194):6, 2014.

[273] W. T. Chen, M. Khorasaninejad, A. Y. Zhu, J. Oh, R. C. Devlin, A. Zaidi, and F. Capasso. Generation of wavelength-independent subwavelength bessel beams using metasurfaces. *Light Sci Appl*, 6(5):e16259, 2017.

[274] M. Mazilu, D. James Stevenson, F. Gunn-Moore, and K. Dholakia. Light beats the spread: "non-diffracting" beams. *Laser Photonics Reviews*, 4(4):529–547, 2010.

[275] Y. Liang, S. Yan, B. Yao, and M. Lei. Direct observation and characterization of optical guiding of microparticles by tightly focused non-diffracting beams. *Opt Express*, 27(26):37975–37985, 2019.

[276] Dimitrios Tzarouchis and Ari Sihvola. Light scattering by a dielectric sphere: Perspectives on the mie resonances. *Applied Sciences*, 8(2):184, 2018.

[277] Kurt Nassau. *The physics and chemistry of color: the fifteen causes of color*. 2001.

[278] Yasuhiro Harada and Toshimitsu Asakura. Radiation forces on a dielectric sphere in the rayleigh scattering regime. *Opt Commun*, 124(5-6):529–541, 1996.

[279] Julls Adams Stratton. Electromagnetic theory, mcgrow-hill book company. *Inc., New York, and London*, pages 205–207, 1941.

[280] Milton Kerker. *The scattering of light and other electromagnetic radiation*. Elsevier, 2016.

[281] James P. Gordon. Radiation forces and momenta in dielectric media. *Physical Review A*, 8(1):14–21, 1973.

[282] S. Wang, P. C. Wu, V. C. Su, Y. C. Lai, M. K. Chen, H. Y. Kuo, B. H. Chen, Y. H. Chen, T. T. Huang, J. H. Wang, R. M. Lin, C. H. Kuan, T. Li, Z. Wang, S. Zhu, and D. P. Tsai. A broadband achromatic metalens in the visible. *Nat Nanotechnol*, 13(3):227–232, 2018.

[283] H. Liang, Q. Lin, X. Xie, Q. Sun, Y. Wang, L. Zhou, L. Liu, X. Yu, J. Zhou, T. F. Krauss, and J. Li. Ultrahigh numerical aperture metalens at visible wavelengths. *Nano Lett*, 18(7):4460–4466, 2018.

[284] Ruizhi Zuo, Wenwei Liu, Hua Cheng, Shuqi Chen, and Jianguo Tian. Breaking the diffraction limit with radially polarized light based on dielectric metalenses. *Advanced Optical Materials*, 6(21):1800795, 2018.

[285] Nazmi Yilmaz, Aytekin Ozdemir, Ahmet Ozer, and Hamza Kurt. Rotationally tunable polarization-insensitive single and multifocal metasurface. *Journal of Optics*, 21(4):045105, 2019.

[286] Xiaofei Zang, Hongzhen Ding, Yuttana Intaravanne, Lin Chen, Yan Peng, Jingya Xie, Qinghong Ke, Alexey V. Balakin, Alexander P. Shkurinov, Xianzhong Chen, Yiming Zhu, and Songlin Zhuang. A multi-foci metalens with polarization-rotated focal points. *Laser Photonics Reviews*, 13(12):1900182, 2019.

[287] Hyounghan Kwon, Ehsan Arbabi, Seyedeh Mahsa Kamali, MohammadSadegh Faraji-Dana, and Andrei Faraon. Single-shot quantitative phase gradient microscopy using a system of multifunctional metasurfaces. *Nature Photonics*, 14(2):109–114, 2019.

[288] P. Huo, C. Zhang, W. Zhu, M. Liu, S. Zhang, S. Zhang, L. Chen, H. J. Lezec, A. Agrawal, Y. Lu, and T. Xu. Photonic spin-multiplexing metasurface for switchable spiral phase contrast imaging. *Nano Lett*, 20(4):2791–2798, 2020.

[289] C. Chen, W. Song, J. W. Chen, J. H. Wang, Y. H. Chen, B. Xu, M. K. Chen, H. Li, B. Fang, J. Chen, H. Y. Kuo, S. Wang, D. P. Tsai, S. Zhu, and T. Li. Spectral tomographic imaging with aplanatic metalens. *Light Sci Appl*, 8(1):99, 2019.

[290] O. Avayu, E. Almeida, Y. Prior, and T. Ellenbogen. Composite functional metasurfaces for multispectral achromatic optics. *Nat Commun*, 8(1):14992, 2017.

[291] Yilin Wang, Qingbin Fan, and Ting Xu. Design of high efficiency achromatic metalens with large operation bandwidth using bilayer architecture. *Opto-Electronic Advances*, 4(1):20000801–20000815, 2021.

[292] Xiujuan Zou, Gaige Zheng, Quan Yuan, Wenbo Zang, Run Chen, Tianyue Li, Lin Li, Shuming Wang, Zhenlin Wang, and Shining Zhu. Imaging based on metalenses. *PhotoniX*, 1(1):1–24, 2020.

[293] B. Li, W. Piyawattanametha, and Z. Qiu. Metalens-based miniaturized optical systems. *Micromachines (Basel)*, 10(5):310, 2019.

[294] M. Pan, Y. Fu, M. Zheng, H. Chen, Y. Zang, H. Duan, Q. Li, M. Qiu, and Y. Hu. Dielectric metalens for miniaturized imaging systems: progress and challenges. *Light Sci Appl*, 11(1):195, 2022.

[295] Brendan P Cormack, Raphael H Valdivia, and Stanley Falkow. FACS-optimized mutants of the green fluorescent protein (gfp). *Gene*, 173(1):33–38, 1996.

[296] N. Bellini, K. C. Vishnubhatla, F. Bragheri, L. Ferrara, P. Minzioni, R. Ramponi, I. Cristiani, and R. Osellame. Femtosecond laser fabricated monolithic chip for optical trapping and stretching of single cells. *Opt Express*, 18(5):10, 2010.

[297] C. Liberale, G. Cojoc, F. Bragheri, P. Minzioni, G. Perozziello, R. La Rocca, L. Ferrara, V. Rajamanickam, E. Di Fabrizio, and I. Cristiani. Integrated microfluidic device for single-cell trapping and spectroscopy. *Sci Rep*, 3(1):1258, 2013.

[298] Julene Madariaga-Marcos, Roberta Corti, Silvia Hormeño, and Fernando Moreno-Herrero. Characterizing microfluidic approaches for a fast and efficient reagent exchange in single-molecule studies. *Scientific reports*, 10(1):1–12, 2020.

[299] Byunghang Ha, Jinsoo Park, Ghulam Destgeer, Jin Ho Jung, and Hyung Jin Sung. Transfer of microparticles across laminar streams from non-newtonian to newtonian fluid. *Analytical chemistry*, 88(8):4205–4210, 2016.

[300] S. Kedenburg, M. Vieweg, T. Gissibl, and H. Giessen. Linear refractive index and absorption measurements of nonlinear optical liquids in the visible and near-infrared spectral region. *Opt Materials Express*, 2(11):1688–1611, 2012.

[301] Su-8 2000 permanent negative epoxy photoresist. https://microchem.com/su-8-photoresist/su-8-2000-photoresist/. Accessed March 27, 2023.

[302] C.Z. Tan. Determination of refractive index of silica glass for infrared wavelengths by ir spectroscopy. *Non-Crystall Solids*, 223(1-2):158–163, 1998.

[303] K. Zhanghao, X. Chen, W. Liu, M. Li, Y. Liu, Y. Wang, S. Luo, X. Wang, C. Shan, H. Xie, J. Gao, X. Chen, D. Jin, X. Li, Y. Zhang, Q. Dai, and P. Xi. Super-resolution imaging of fluorescent dipoles via polarized structured illumination microscopy. *Nat Commun*, 10(1):4694, 2019.

[304] N. Sultanova, S. Kasarova, and I. Nikolov. Dispersion properties of optical polymers. *Acta Physica Polonica A*, 116(4):585–587, 2009.

[305] IRVING H. MALITSON. Refraction and dispersion of synthetic sapphire. *OSA*, 52(12):3, 1962.

[306] P. Johnson and R. Christy. Optical constants of transition metals: Ti, v, cr, mn, fe, co, ni, and pd. *Physical Review B*, 9(12):5056–5070, 1974.

[307] Z. Liu, X. Gu, J. Hwu, S. Sassolini, and D. L. Olynick. Low-temperature plasma etching of high aspect-ratio densely packed 15 to sub-10 nm silicon features derived from ps-pdms block copolymer patterns. *Nanotechnology*, 25(28):285301, 2014.

[308] H Bilge Yağcı and Hilmi Volkan Demir. "meta-atomless" architecture based on an irregular continuous fabric of coupling-tuned identical nanopillars enables highly efficient and achromatic metasurfaces. *Applied Physics Letters*, 118(8):081105, 2021.

[309] Guangyuan Si, Xiaoxiao Jiang, Jiangtao Lv, Qiongchan Gu, and Fengwen Wang. Fabrication and characterization of well-aligned plasmonic nanopillars with ultrasmall separations. *Nanoscale research letters*, 9(1):1–7, 2014.

[310] Daphne S Bindels, Lindsay Haarbosch, Laura Van Weeren, Marten Postma, Katrin E Wiese, Marieke Mastop, Sylvain Aumonier, Guillaume Gotthard, Antoine Royant, Mark A Hink, et al. mscarlet: a bright monomeric red fluorescent protein for cellular imaging. *Nature methods*, 14(1):53–56, 2017.

[311] Mikhail Drobizhev, Rosana S Molina, and Jacob Franklin. Multiphoton bleaching of red fluorescent proteins and the ways to reduce it. *International journal of molecular sciences*, 23(2):770, 2022.

[312] ME Shaheen, JE Gagnon, and BJ Fryer. Excimer laser ablation of aluminum: influence of spot size on ablation rate. *Laser Physics*, 26(11):116102, 2016.